Gamma-ray bursts

Exploring the population using novel Bayesian techniques

Aksulu, M.D.

Publication date
2021

Document Version
Final published version

Gamma-ray Bursts: Exploring the population using novel Bayesian techniques M.D. Aksulu

Gamma-ray Bursts: Exploring the population using novel Bayesian techniques

Mehmet Deniz Aksulu

Gamma-ray bursts: Exploring the population using novel Bayesian techniques

Mehmet Deniz Aksulu

Contact: aksulumdeniz@gmail.com

Gamma-ray bursts: Exploring the population using novel Bayesian techniques
Thesis, Anton Pannekoek Institute, Universiteit van Amsterdam

Cover by Nurdan Melek Aksulu (melekaksulu@hotmail.com)
Printed by Gildeprint

ISBN: 978-94-6419-383-1

UNIVERSITY OF AMSTERDAM

ANTON PANNEKOEK
INSTITUTE

The research included in this thesis was carried out at the Anton Pannekoek Institute for Astronomy (API) of the University of Amsterdam. It was supported by the Netherlands Research School for Astronomy (NOVA). Support was occasionally provided by the Leids Kerkhoven-Bosscha Fonds (LKBF).

Gamma-ray bursts: Exploring the population using novel Bayesian techniques

ACADEMISCH PROEFSCHRIFT

ter verkrijging van de graad van doctor
aan de Universiteit van Amsterdam
op gezag van de Rector Magnificus
prof. dr. ir. K.I.J. Maex
ten overstaan van een door het College voor Promoties ingestelde commissie,
in het openbaar te verdedigen in de Aula der Universiteit
op vrijdag 17 december 2021, te 11:00 uur

door

Mehmet Deniz Aksulu

geboren te Elazığ

Promotiecommissie:

Promotor(es):	prof. dr. R.A.M.J. Wijers	Universiteit van Amsterdam
Copromotor(es):	dr. H.J. van Eerten	University of Bath
Overige leden:	dr. A.J. van der Horst	George Washington University
	dr. P. Uttley	Universiteit van Amsterdam
	prof. dr. S.B. Markoff	Universiteit van Amsterdam
	dr. P. Mösta	Universiteit van Amsterdam
	prof. dr. A.L. Watts	Universiteit van Amsterdam
	prof. dr. C. Kouveliotou	George Washington University
	prof. dr. L. Kaper	Universiteit van Amsterdam

Faculteit der Natuurwetenschappen, Wiskunde en Informatica

In memory of
dr. M. Sabahattin Özberk

Contents

Chapter 1

Introduction

The stars don't shine upon us
We're in the way of their light.
David Berman

1.1 Overview

The serendipitous discovery of the gamma-ray burst (GRB) phenomenon was possible thanks to the distrust between the United States of America and the Union of Soviet Socialist Republics at the height of the Cold War. With the weaponization of nuclear energy and the demonstrated power of such weapons at the end of the Second World War, an arms race between the powerful countries of the west and the east had begun. Naturally, developing such devastating weapons required much research and testing. As these weapons became more and more powerful, the tests demonstrating the power of these devices also became more and more dangerous. Over growing public health and environmental concerns due to the test detonation of nuclear weapons in a variety of environments; the U.S.A., U.S.S.R. and the United Kingdom followed common sense and decided to restrict the testing of nuclear weapons. They signed the Partial Test Ban Treaty in Moscow on 5 August 1963, which prohibited test detonation of nuclear weapons in any environment but underground. In order to make sure that the U.S.S.R. was compliant, the U.S. developed a group of satellites called *Vela*, which carried X-ray and γ-ray instruments to detect the characteristic double-humped light curve originating from nuclear explosions.

In 1973, Klebesadel et al. (1973) were conducting a search for high-energy emission originating from supernovae by looking at the data gathered by the Vela satellites. They were unable to find any supernova-related emission in the data sets, however they reported the discovery of 16 independent "γ-ray bursts" with durations in the range of 0.1 to 30 seconds. These prompt flashes of γ rays were detected by several of the Vela satellites simultaneously and they were determined to be of cosmic origin. The discovery of GRBs immediately sparked the curiosity of the astrophysical community and many have speculated that the bursts should be of Galactic origin, as otherwise they would require an enormous amount of

1

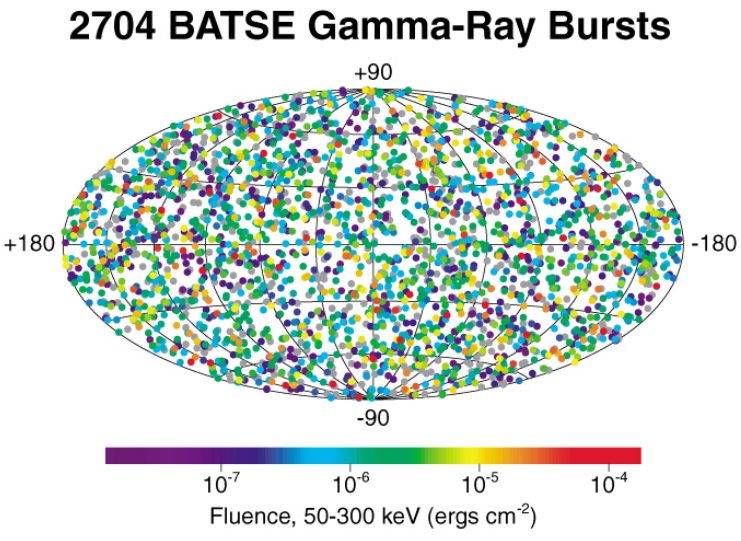

Figure 1.1: Locations and fluences of 2704 GRBs detected by BATSE. The spatial distribution of GRBs is determined to be isotropic, which is consistent with the extra-galactic origin hypothesis. Image credit: NASA.

energy to produce. Given that the detected fluence in γ-rays was reported to be on the order of $\sim 10^{-4}$ erg cm^{-2}, assuming isotropic emission at a redshift $z = 1$ would imply energies $\sim 4 \times 10^{52}$ erg! Thanks to the Burst and Transient Source Experiment (BATSE) aboard the *Compton Gamma Ray Observatory* the number of detected GRBs had increased dramatically and allowed for more robust statistical analysis regarding the origin of GRBs. Meegan et al. (1992) have provided crucial evidence favouring the extra-galactic origin for GRBs. They showed that GRBs are distributed isotropically across the sky, which is inconsistent with the Galactic source hypothesis where one would expect the GRBs to be detected predominantly along the Galactic plane of the Milky Way (see Figure 1.1)[1]. The first BATSE catalogue (Fishman et al., 1994) enabled Kouveliotou et al. (1993) to establish the existence of (at least) two populations of GRBs, based on the duration of the prompt γ-ray flashes. They were able to demonstrate, in a statistically significant manner, that the burst duration distribution had a bi-modal shape with a separation between the two populations at ~ 2 seconds.

As observational evidence gradually started to shed light on the properties of these mysterious γ-ray flashes, there were also endeavours to build a theoretical framework to explain the nature of GRBs. In their seminal work, Lattimer & Schramm (1976) and Eichler et al. (1989) have examined the consequences of neutron star mergers. They proposed that neutron star mergers would lead to nucleosynthesis of heavy elements, neutrino emission, gravitational waves and that these events could comprise a portion of the observed GRB population. It

[1] Although the spatial distribution of GRBs was determined to be isotropic, this was not considered as definitive proof for their cosmological origin at the time. Other hypotheses such as a neutron stars located at a previously unknown Galactic "corona" were suggested to explain the isotropic spatial distribution. See e.g., the Great Debate in 1995.

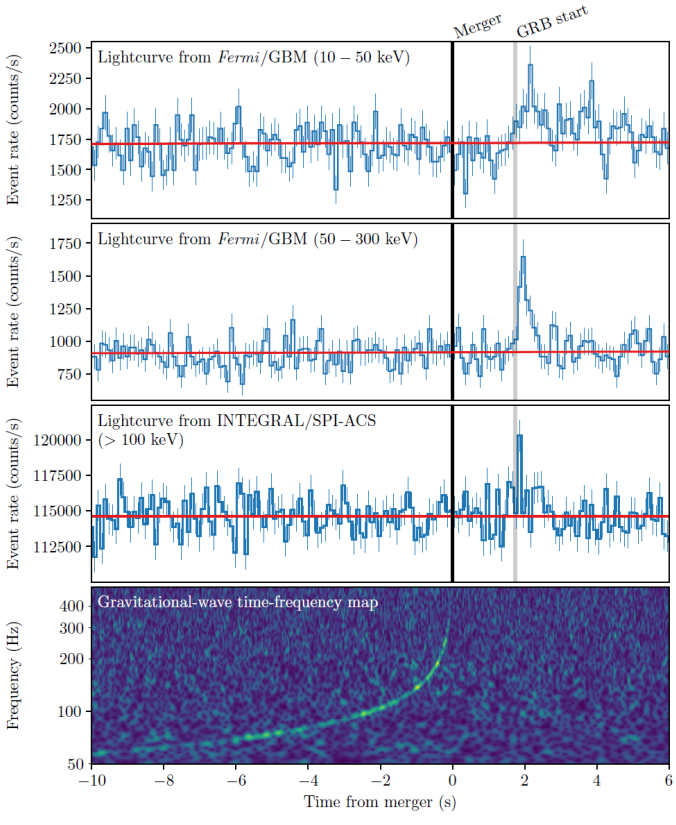

Figure 1.2: The momentous detection of GW/GRB 170817/A. The top two panels show the prompt emission of GRB 170817A as detected by the *Fermi* telescope in two separate bands. The third panel from the top shows the independent detection of GRB 170817A by the *INTEGRAL* telescope. The bottom panel represents the detection of GW 170817 by the LIGO/Virgo collaboration in the form of a waterfall plot. As expected, there is a small delay between gravitational waves and electromagnetic counterpart. Credit: Abbott et al. (2017a).

would take 28 more years before our observational capabilities would catch up to verify most of the claims presented in these studies. On August 17, 2017 the *Fermi Gamma-ray Space Telescope* and *INTEGRAL* detected a short-duration GRB in conjunction with the independent detection of gravitational waves by the advanced Laser Interferometer Gravitational-Wave Observatory (LIGO) and Virgo collaboration (Abbott et al., 2017a,b; Fong et al., 2017). This profound discovery provided strong evidence that neutron star mergers are progenitors of short GRBs as well as marked the beginning of the multi-messenger era in Astronomy (see Figure 1.2). Woosley (1993) proposed that core-collapse supernovae of rapidly-rotating massive stars could be another candidate for the progenitor of GRBs. In 1998, Galama et al. (1998a,b) found the first evidence of supernova/long GRB association by identifying SN 1998bw at the approximate location of GRB 980425.

1

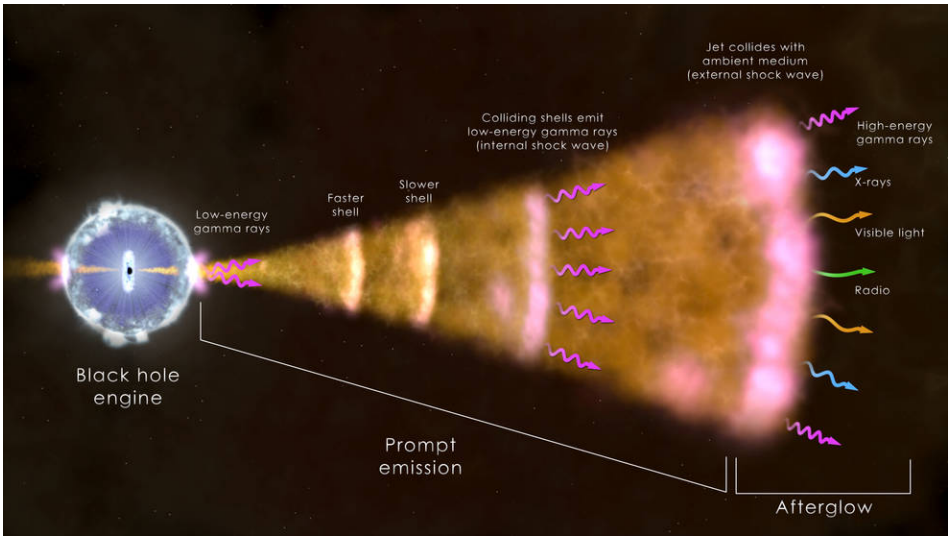

Figure 1.3: Illustration of the different stages of GRBs. They are initially detected as flashes of γ rays (the prompt emission) followed by a long-lived broadband afterglow. Here, the internal shocks model is shown for the prompt phase. Image credit: NASA's Goddard Space Flight Center.

Rees & Mészáros (1992) have laid the foundations for the "fireball" model of GRBs, and argued that a relativistic fireball would inevitably interact with its environment to produce electromagnetic radiation. In Mészáros et al. (1994), the authors considered the relativistic blast wave created by a point explosion moving into the surrounding medium, and how such a process would lead to broadband electromagnetic radiation. Later, van Paradijs et al. (1997) detected the long-awaited first optical counterpart to a GRB. They detected an optical transient consistent with the location of GRB 970228, ~ 21 hours after the initial detection of the γ-ray emission. Moreover, Costa et al. (1997) detected a fading X-ray transient associated with the same GRB. This long-lived broadband emission following the initial burst of γ rays is called the *afterglow* of the GRB. Soon after their discovery, follow-up observations of the afterglow emission proved to be useful to understand the physics of GRBs. Metzger et al. (1997) performed the first spectroscopic measurements of a GRB afterglow (GRB 970508) and proved the extra-galactic origin of GRBs by measuring the redshift for the first time.

To summarize, GRBs are the most energetic explosions in the Universe. They are the product of either the core-collapse of massive stars (associated with long GRBs) or coalescing compact binaries, where at least one of the objects is a neutron star (associated with short GRBs). GRBs are ultra-relativistic collimated outflows powered by a compact central engine. They are initially detected as brief flashes of γ rays, which is called the prompt emission phase of the GRB. As the ultra-relativistic ejecta sweeps up enough mass from the surrounding medium a pair of shocks are created, one of which moves into the ejecta (reverse shock), and the other moves into the circumburst medium (forward shock). In these relativistic shocks, tangled magnetic fields are amplified and charged particles are accelerated, which

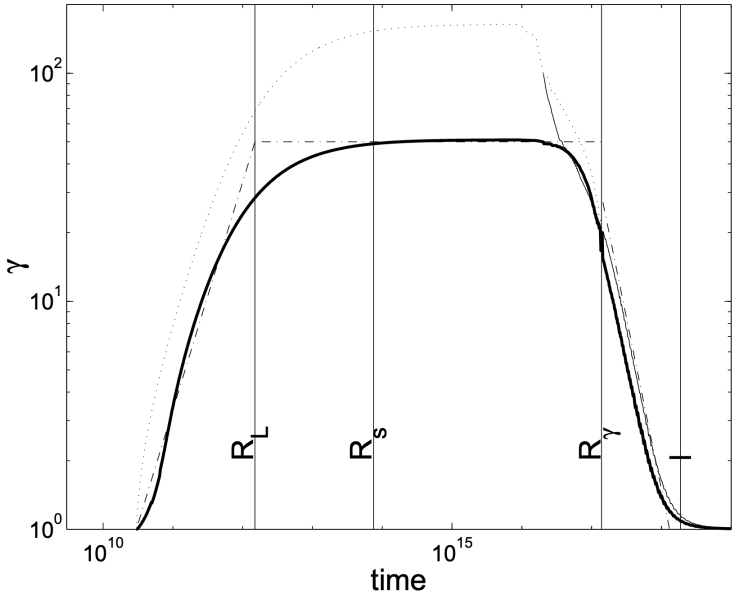

Figure 1.4: Evolution of the bulk Lorentz factor of the ejecta based on hydrodynamic simulations. The reader can see the different stages of the blast wave; the acceleration stage during which Γ rapidly increases, the coasting stage where Γ stays approximately constant, and the deceleration stage. Credit: Kobayashi et al. (1999)

emit synchrotron radiation spanning the entire electromagnetic spectrum. This broadband long-lived emission is called the afterglow of the GRB. See Figure 1.3 for an illustration of the different stages of GRBs. In the following sections, the current theoretical understanding of the physics of GRBs is described. For a complete review of the observational properties and theoretical understanding of GRBs the reader is referred to e.g., Piran (2004); Kumar & Zhang (2015).

1.2 GRB blast waves

In 1986, Paczyński (1986); Goodman (1986) were already investigating the physics of cosmological GRBs. Given the high temporal variability in the prompt emission light curves of GRBs and the fact that they are at cosmological distances, they considered the release of energies on the order of $\sim 10^{51}$ erg into a small volume with radius ~ 10 km within a short amount of time (~ 1 s). Such high energy densities would lead to pair-production which would lead to an, initially, optically thick fireball. As the fireball starts its adiabatic expansion, the bulk Lorentz factor of the flow, Γ, will increase linearly with the blast wave radius as long as the fireball remains optically thick. Following the acceleration stage, once the blast wave reaches the photosphere (at which point it becomes optically thin) it enters the

coasting stage throughout which Γ stays approximately constant. The maximum, coasting, bulk Lorentz factor of the flow is defined as,

$$\Gamma_0 \equiv \frac{E_0}{c^2 M_0}, \tag{1.1}$$

where E_0 is the total explosion energy, c is the speed of light and M_0 is the baryonic mass of the ejecta. As the blast wave ploughs through the circumburst medium, the kinetic energy is imparted to the surrounding material. Once the blast wave collects enough material, i.e., with a mass of M_0/Γ_0, it enters the deceleration stage (Rees & Mészáros, 1992). In this case the deceleration radius of a blast wave, with a coasting Lorentz factor of Γ_0, moving into a medium with constant number density, n, can be expressed as,

$$\begin{aligned} \frac{4}{3}\pi r_{\rm dec}^3 n m_p &= \frac{E_0}{\Gamma_0^2 c^2} \\ \implies r_{\rm dec} &= \left(\frac{3E_0}{4\pi n m_p \Gamma_0^2 c^2}\right)^{1/3}. \end{aligned} \tag{1.2}$$

In the lab-frame of the burster, $r_{dec} = c\,t_{\rm dec,lab}$. Since the blast wave is moving towards the observer with a Lorentz factor Γ_0, the time in the lab-frame can be expressed as $t_{\rm lab} = t_{\rm obs}/(2\Gamma_0^2)$. Once we substitute these expressions in Equation 1.2, the deceleration time in the observer frame can be expressed as,

$$t_{\rm dec} = \left(\frac{3E_0}{32\pi n m_p \Gamma_0^8 c^5}\right)^{1/3}. \tag{1.3}$$

Numerical results for the Lorentz factor evolution of the blast wave can be seen in Figure 1.4 (Kobayashi et al., 1999).

Assuming a more general circumburst number density profile of the form

$$n = A r^{-k}, \tag{1.4}$$

where r is the distance from the centre, the time of deceleration for the blast wave becomes

$$t_{\rm dec} = \left[\frac{(3-k)E_0}{2^{4-k}\pi A m_p \Gamma^{8-2k} c^{5-k}}\right]^{\frac{1}{3-k}}. \tag{1.5}$$

Throughout this thesis, I only consider density profiles with either $k = 0$, which corresponds to a homogeneous, interstellar medium-like (ISM-like) density profile, or $k = 2$, which is representative of the density profile in free stellar winds.

Since the ejecta are optically thick during the acceleration stage, and since the blast wave imparts a large portion of its kinetic energy to the surrounding medium during the deceleration stage, it is expected that the radiative processes governing the observed prompt emission arise during (or at the transition to) the coasting stage. Despite decades of research, the

radiative processes giving rise to the prompt emission are not well understood. There are mainly two models to explain the observed temporal and spectral properties of the prompt emission; the *internal shocks* and *photospheric emission* model. The internal shocks model assumes that the central engine of the GRB will create an outflow with time varying Γ. In such a scenario the outflow consists of regions with different Γ, and the faster material ejected at later times will catch up with the regions with lower Γ (see Figure 1.3 for an illustration). When these shells collide internal shocks are generated in the outflow where a considerable amount of the kinetic energy can be converted into thermal energy (Rees & Mészáros, 1994). In turn, a reasonable fraction of the thermal energy will be deposited into charged particles which can create non-thermal radiation. Depending on the differences of Γ between the colliding shells and the mass of the shells, the maximum expected radiative efficiency of such a process is $\sim 30\,\%$. The photospheric model, on the other hand, assumes low energy near-thermal photons interacting with higher energy electrons below the photosphere i.e., before the ejecta become optically thin. These photons will typically gain energy when they interact with the electrons and if the ejecta become optically thin before the photons and electrons have a chance of completely thermalizing the escaping photons might generate a GRB. None of these models are able to explain all of the observed properties of the prompt emission, and it is likely that a combination of both radiation mechanisms contribute to generating GRBs.

1.3 GRB afterglows

The afterglow emission relays crucial information regarding the physics governing GRBs. It is thanks to the afterglow emission that the cosmological origin of GRBs was conclusively demonstrated (Metzger et al., 1997). Still, the majority of redshift measurements of GRBs are thanks to follow-up observations of the afterglow in optical wavelengths, which allows spectroscopic measurements of absorption lines. Moreover, modelling the afterglow emission allows us to probe the energetics of GRBs, their dynamical evolution, microphysical properties of ultra-relativistic shocks, the environments of GRBs and their progenitors. This thesis is predominantly focused on extracting information from the observed afterglow emission of GRBs.

1.3.1 Dynamics

The blast strength of the first atom bomb explosion in 1945 was deemed classified by the U.S. military. Sedov (1946); Taylor (1950a) presented the dynamical evolution of blast waves created by point explosions. In 1950, Taylor (1950b) was able to infer the (then classified) explosion energy of the 1945 atomic test by utilizing a series of publicly available snapshots of the explosion. This was possible due to the self-similar nature of the blast wave evolution. The so-called Sedov-Taylor (ST) solution has been widely utilized in astronomy to describe Newtonian blast waves, especially for the evolution of supernova remnants. The Blandford-McKee (BM) solution is the relativistic analogue of the Sedov-Taylor solution (Blandford & McKee, 1976). Post-deceleration, the GRB blast wave dynamics is described by the BM solu-

tion as long as the blast wave remains ultra-relativistic. As the blast wave decelerates further, the blast wave dynamics smoothly transitions to the Newtonian Sedov-Taylor solution. For a blast wave which is in a self-similar deceleration stage one can derive some basic scalings for the Γ and r (blast wave radius) evolution;

$$\Gamma \propto t_{\rm obs}^{\frac{k-3}{8-2k}}, \qquad r \propto t_{\rm obs}^{\frac{1}{4-k}}, \tag{1.6}$$

where $t_{\rm obs}$ refers to the time in the observer frame and k is defined as in Equation 1.4. Since it is assumed that the blast wave is moving towards the observer at nearly the speed of light whilst generating the afterglow emission, the emission duration at the observer frame is contracted by a factor of $\sim 2\Gamma^2$. These scalings naturally explain the observed power-law decay of the GRB afterglow light curves.

1.3.1.1 Jet-break

GRBs require an outrageous energy budget considering the cosmological distances where these events take place. It is possible to reduce the required energetics of GRBs, when one considers a *collimated* outflow instead of an isotropic explosion. When it is assumed that the outflow is collimated with a half-opening angle of θ_0 the true energy becomes,

$$E_{\rm true} = E_{\rm iso}(1-\cos\theta_0) \tag{1.7}$$

where $E_{\rm iso}$ is the isotropic-equivalent energy. Rhoads (1999) anticipated the collimated nature of GRB jets and predicted the observational signatures of such beamed outflows. While $\Gamma > 1/\theta_0$ it is impossible to distinguish between an isotropic outflow and a beamed jet. This is because of the fact that the emission is Doppler-beamed towards the observer with an angle of $1/\Gamma$, thus the observer is unable to "see" the edges of the jet when $\Gamma > 1/\theta_0$. Moreover, the blast wave is unable to spread sideways when $\Gamma > 1/\theta_0$ because the edges of the jet are not causally connected. Rhoads (1999) predicted that when $\Gamma \sim 1/\theta_0$ that there should be a steepening in the afterglow light curve, which is called the *jet-break*. Once $\Gamma < 1/\theta_0$, the steepening of the light curve happens due to two reasons:

1. As Γ becomes smaller the observer is able to see more of the emitting regions of the blast wave, and when $\Gamma = 1/\theta_0$ the observer can see the whole emitting region. After which point further decrease of Γ does not increase the size of the emitting region.
2. When $\Gamma = 1/\theta_0$ the edges of the jet become causally connected, which allows the sideways expansion of the blast wave. This leads to Γ decreasing even faster than before due to the fact that the blast wave interacts with more of the circumburst medium.

1.3.2 Radiation

As the GRB blast wave starts to interact with its surrounding medium, a pair of shocks are created. The reverse shock propagates into the ejecta, whereas the forward shock propagates into the circumburst medium. These shocks compress the plasma and amplify ambient mag-

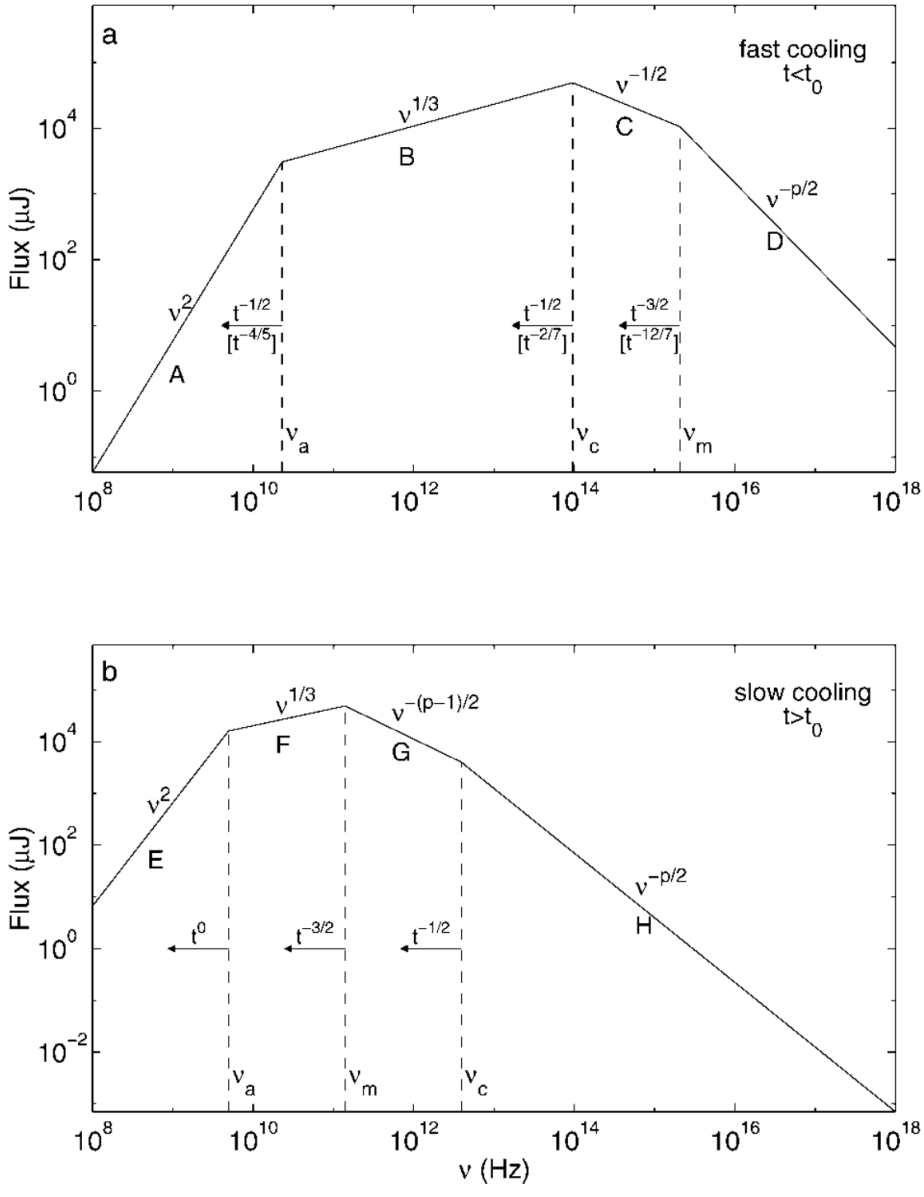

Figure 1.5: Example broadband synchrotron spectra of the GRB afterglow emission. ν_a, ν_m and ν_c represent the self-absorption, injection and cooling break respectively. The upper panel illustrates the fast cooling spectrum ($\nu_m > \nu_c$) whereas the bottom panel shows the slow cooling spectral regime ($\nu_m < \nu_c$). p is the power-law index of the accelerated electron distribution. Credit: Sari et al. (1998)

netic fields. Charged particles are accelerated by scattering back and forth across the shock front in a process called diffusive shock acceleration (Bell, 1978). We denote the fraction of thermal energy going into the magnetic fields and accelerated particles as ϵ_B and ϵ_e, respectively. The energy spectrum of the accelerated particles follows a power law of the form,

$$n_e(\gamma) \propto \gamma^{-p}, \tag{1.8}$$

where p is the power-law index and γ is the Lorentz factor of the individual particles. The distribution has a minimum Lorentz factor of γ_m and a maximum Lorentz factor denoted by $\gamma_{\rm max}$. The integrated energy in the particles hardly depends on $\gamma_{\rm max}$ when $\gamma_{\rm max} \gg \gamma_m$ for $p > 2$. Therefore, $\gamma_{\rm max}$ is usually not taken into account when $p > 2$ to reduce the number of free parameters.

The observed emission is the sum of the synchrotron emission of all accelerated particles. The spectrum can then be described as a broken power-law with several prominent breaks. The *injection break*, ν_m, signifies the contribution of particles with Lorentz factors of γ_m. As the particles emit synchrotron radiation, they lose their energy and cool down. For particles with γ larger than a critical value γ_c, the cooling timescale is shorter than the dynamical timescale, thus, they rapidly lose their energy to synchrotron emission. This introduces another break in the spectrum called the *cooling break*, ν_c. Finally, the *self-absorption* break, ν_a, is the frequency below which the blast wave becomes optically thick. In Figure 1.5 example spectra for different ordering of these break frequencies are shown (Sari et al., 1998).

When low-energy photons interact with high-energy charged particles, they can get up-scattered and gain energy from the particles. In the context of GRB afterglows, it is likely that the emitted lower-energy synchrotron photons would in turn interact with the high-energy particles in a synchrotron self-Compton (SSC) scatering process. This would lead to additional cooling of the particle population and result in high-energy up-scattered photons. In 2019, MAGIC Collaboration et al. (2019a) detected high-energy, TeV photons coincident with GRB 190114C. This marked the first high-confidence detection of TeV emission from a GRB, demonstrating that the afterglow phase is capable of producing very high-energy photons.

1.3.3 Afterglow data sets

The launch of the *Neil Gehrels Swift Observatory* has enabled quick localization of GRBs and therefore the number of GRBs with detected afterglow counterparts has increased dramatically (Gehrels et al., 2004). Furthermore, the on-board X-ray detector (*Swift*-XRT) has revealed the early-time ($\sim$ 1 minute after initial detection of the burst) behaviour and complex features of the X-ray afterglow emission. *Swift*-XRT discovered that the X-ray light curve did not follow just a simple power-law decay but instead included an early steep decay followed by a shallow (plateau) phase with occasional flaring behaviour. This complex temporal evolution at early times could signify energy injection due to late-time central engine activity. Emission originating from the reverse shock can also lead to flaring behaviour.

Broadband follow-up observations are required to properly constrain the locations of the breaks in the afterglow synchrotron spectra (see Figure 1.5). Depending on the adopted triggering strategy, ground/space based observatories perform follow-up observations upon the detection of a GRB. The data set can include various different emission/absorption components, and propagation effects. Persistent emission from the host galaxy can add a time-independent offset to the afterglow light-curves, and needs to be taken into account. Furthermore, dust extinction and absorption in the host galaxy of the GRB will affect the optical/soft X-ray counterparts of the afterglow emission. Interstellar scintillation can cause strong variability in radio wavelengths, especially at early times when the angular size of the blast wave is smaller. Moreover, extra-galactic background light (EBL) attenuation prevents the detection of TeV afterglow emission at large redshifts.

1.4 Numerical afterglow models

Analytical solutions for the blast wave dynamics successfully describe the evolution of GRB jets in asymptotic regimes (see Section 1.3.1). The BM solution is valid as long as the blast wave is ultra-relativistic (i.e., at early-times when $\Gamma \gg 1$) whereas the ST solution is only valid for Newtonian blast waves (i.e, at late times when $\Gamma \sim 1$). It is not straightforward to describe the dynamics of the trans-relativistic regime using simple analytical prescriptions. In the last decade, advancements in numerical methods allowed the study of GRB jet dynamics via detailed relativistic hydrodynamical simulations. To capture the physics of these ultra-relativistic outflows, these simulations need to resolve the blast wave over many orders of magnitudes in space and time. Therefore, advanced numerical techniques such as adaptive mesh refinement (AMR e.g., Zhang & MacFadyen 2009; van Eerten et al. 2010) are required to capture the dynamics of GRB jets spanning from ultra-relativistic to Newtonian regimes. These hydrodynamical simulations also demonstrated that the simple analytical approach to calculate the lateral evolution of the jet (Rhoads, 1999) overestimates the lateral expansion of the blast wave after the jet-break time, $t_{\rm jet}$ (e.g., Zhang & MacFadyen 2009; Wygoda et al. 2011; van Eerten & MacFadyen 2012b). Therefore, to accurately calculate the dynamics at $t_{\rm obs} \gtrsim t_{\rm jet}$, 2D hydrodynamical simulations are required. For a comprehensive review the reader is referred to, e.g., van Eerten (2018).

Throughout this thesis, I make use of numerical models which are based on 2D relativistic hydrodynamical simulations to capture the jet dynamics in a realistic fashion. van Eerten et al. (2012) introduced boxfit, which is a numerical tool capable of producing afterglow light curves and spectra for given burst parameters. To accomplish this, they make use of 2D hydrodynamical simulations performed for GRB jets with different initial opening angles. They make use of scale-invariance to calculate the blast wave dynamics for any given explosion energies and circumburst densities. Once the dynamics of the jet are inferred from the pre-calculated simulation snapshots, boxfit solves radiative transfer equations to calculate observed synchrotron emission at given observer times and bands.

Although boxfit has drastically reduced the computational cost of calculating realistic dynamics for GRB jets, the code still has to solve radiative transfer equations in realtime to

produce light curves and spectra. When performing Bayesian inference to infer burst parameters from afterglow data sets, the model needs to be evaluated more than 100000 times, which makes boxfit impractical to use with large data sets. The numerical code scalefit (Ryan et al. in preparation; Aksulu et al., 2020; Ryan et al., 2015), on the other hand, is able to calculate the afterglow emission in a much more computationally effective manner, while still relying on 2D hydrodynamic simulations. scalefit relies on pre-calculated spectral tables, where the peak spectral flux and the break frequencies (i.e., ν_a, ν_m and ν_c) are stored at various observer time epochs. Furthermore, these tables are generated for various jet opening angles and observer viewing angles. We make use of boxfit to generate these spectral tables. In turn, scalefit makes use of scaling rules (van Eerten & MacFadyen, 2012a) to infer the spectra at given observer times, for different spectral regimes (i.e., different orderings of ν_a, ν_m and ν_c). This eliminates the necessity of solving the radiative transfer equations, and reduces the computational cost of evaluating the model dramatically.

1.5 Gaussian process framework

Although the blast wave model is able to successfully explain the general trends in the observed GRB afterglow emission, the detailed temporal and spectral evolution can often exhibit complex features. These deviations from the models can arise due to physical process which are not included in the models, e.g., reverse shock contribution at early-times, late-time energy injection from the central engine, synchrotron self-Compton processes. Furthermore, as described in Section 1.3.3, GRB afterglow data sets often include instrumental systematics and propagation effects, which further complicate the observed evolution of GRB afterglows.

In Aksulu et al. (2020) (see Chapter 2), we introduce a novel approach to modelling GRB afterglow data sets, by making use of Gaussian processes (GPs) to account for the above described additional systematics. GPs are stochastic processes that define continuous distributions over functions (see e.g., Rasmussen & Williams 2006). GPs are useful tools for regression and classification problems where the underlying mechanism producing the data sets is unknown, which is the case for the systematics included in the GRB afterglow data sets. The GP framework is described as,

$$f\left(t,\nu\right)\sim\mathcal{GP}\left(\mu(t,\nu,\boldsymbol{\phi}),\boldsymbol{\Sigma}(t,\nu,\boldsymbol{\theta})\right), \tag{1.9}$$

where, t and ν are the time and frequency at which the observations are obtained, μ is the mean function of the GP, $\boldsymbol{\Sigma}$ is the covariance matrix, $\boldsymbol{\phi}$ and $\boldsymbol{\theta}$ represent the model parameters and the, so called, *hyperparameters* of the GP model respectively. Thanks to its computational efficiency, we are able to make use of the scalefit numerical model as the mean function of the GP (see Section 1.4). The covariance matrix, $\boldsymbol{\Sigma}$, describes how the data points are correlated over observer time and frequency. $\boldsymbol{\Sigma}$ is calculated based on the chosen *kernel* function and the corresponding hyperparameters of the GP. Throughout this thesis I utilized a *squared-exponential* kernel function, which results in a covariance matrix of the form,

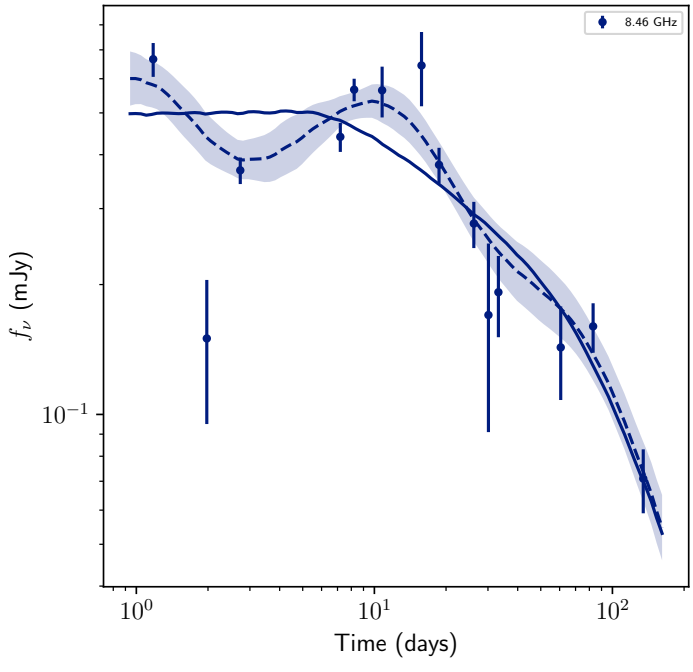

Figure 1.6: Radio afterglow light curve of GRB 000926. The solid line represents the light curve predicted by only the model (scalefit). The dashed line, together with the shaded area, represents the mean and 1–σ uncertainty of the Gaussian process (GP) model. The variability at early times is due to interstellar scintillation. As can be seen, the GP model is able to account for scintillation.

1

$$\mathbf{\Sigma}_{ij} = k(\mathbf{X}_i, \mathbf{X}_j) = A \exp\left[-\frac{1}{2}\sum_{k=1}^{2}\frac{(\mathbf{X}_{ik} - \mathbf{X}_{jk})^2}{l_k^2}\right] + \delta_{ij}\sigma_h^2, \tag{1.10}$$

where, (A, l_1, l_2, σ_h) are the hyperparameters and $\mathbf{X}$ is the feature set (time epochs and frequencies of the observations). Here, A defines the amplitude of the correlation between the observations, whereas (l_1, l_2) respectively define the length scale in time and frequency space over which the data are correlated. σ_h adjusts the amount of white noise present in the data set.

The likelihood function of the GP model is described as,

$$\log \mathscr{L}(\nabla|\mathbf{X}, \boldsymbol{\theta}, \boldsymbol{\phi}) = -\frac{1}{2}\boldsymbol{r}^T\mathbf{\Sigma}^{-1}\boldsymbol{r} - \frac{1}{2}\log|\mathbf{\Sigma}| - \frac{N}{2}\log(2\pi), \tag{1.11}$$

where, $\boldsymbol{r}$ is the residuals of the model with respect to the observations. We marginalize the model parameters and hyperparameters over the likelihood function to obtain robust estimates of the GRB parameters.

In principle the GP component should only explain artifacts in the data set which cannot be accounted for by the model itself, i.e., components which are highly variable in time and/or frequency domains. In order to prevent the GP from modelling components which vary gradually over time and/or frequency (such components should be accounted for by the model), we do not allow (l_1, l_2) parameters to exceed a certain value. In Figure 1.6, an example fit for the radio afterglow of GRB 000926 can be seen, where the variability due to interstellar scintillation is captured by the GP model.

1.6 Outline of thesis

The overarching aim of this thesis is to provide insights regarding the physics of GRBs by constraining their physical parameters, and to probe how these parameters are distributed across the GRB population.

In Chapter 2, we introduce a new method for modelling the afterglow emission of GRBs. The blast wave model is able to explain the general trends in the observed GRB afterglow light curves and spectra. However, as it is the case with every model, the physical realities are more complex. The GRB afterglow data sets contain systematic deviations from our models due to emission mechanisms not included in the models (e.g., synchrotron self-Compton, reverse shock contribution), propagation effects (e.g., interstellar scintillation at radio wavelengths, dust absorption due to the host galaxy) and instrumental effects. When performing Bayesian inference, we find that these systematic deviations lead to underestimated uncertainties on the model parameters when sampling the χ^2 likelihood. We introduce a new method for modelling the afterglow emission, where we make use of Gaussian processes to account for additional systematics in a non-parametric fashion. This new approach results in more robust parameter estimates. We demonstrate the effectiveness of the proposed method using synthetic data sets. Furthermore, we apply this new method on well-studied, archival GRB afterglow data sets, and compare our results with previous studies.

In Chapter 3, we make use of the above mentioned method to model a sample of 26 GRBs. Our sample consists of 22 long GRBs and 4 short GRBs with available, well-sampled, broad-band afterglow data sets. In this study we aim to understand how the various GRB parameters are distributed across the population. We perform model selection between homogeneous and wind-like circumburst media (CBM), using the obtained Bayesian evidence values for each modelling effort. We find that there is an approximately even split between the number of long GRBs in homogeneous and wind-like CBM. As expected, the short GRB sample is consistent with a homogeneous CBM density profile. We look for correlations between the burst parameters and make comparisons between the parameter distributions of long GRBs in homogeneous/wind-like environments and short GRBs. We do not find any significant differences between the kinetic energies of short and long GRBs. Given that short GRBs are much less luminous during the prompt phase, we find that short GRBs are systematically less efficient in producing the prompt γ-ray emission when compared to long GRBs. Furthermore, we find that the inferred density profile for long GRBs in wind-like environments is consistent with the density profiles expected of canonical Wolf-Rayet type stars.

In Chapter 4, we take a different approach to probe the parameter distributions of the GRB population. Instead of modelling individual GRBs, we conduct a population study based on the *Swift* BAT6 sample of long GRBs. We build a numerical tool which is able to generate a synthetic population of GRBs for given parameter distributions, and output distributions of the observables such as detected photon count in γ-rays, redshift, isotropic-equivalent prompt energetics, and afterglow flux values. In order to make a fair comparison between the synthetic population and the observed BAT6 sample, it is crucial to take into account the selection effects. We make use of Bayesian inference in order to infer the distribution parameters of the synthetic population, which successfully reproduces the observed properties of the BAT6 sample. Furthermore, we compare the inferred synthetic population to our previous work, presented in Chapter 3, and find that the parameter distributions agree with each other, especially for GRBs in wind-like environments. We briefly comment on the energetics of GRBs, and the lack of observed jet-breaks in the GRB population. We make a case study based on the famous GRB 130427A, and discuss how the upcoming *ATHENA* mission can help to test the forward shock model.

In Chapter 5, we present the first results for the *Australia Telescope Compact Array* (ATCA) rapid-response mode observations triggered on a short GRB (GRB 181123B). With the beginning of the multi-messenger era in Astronomy, it has become important to quickly follow-up on LIGO/VIRGO detected gravitational wave (GW) events. Such rapid follow-up observations might present improvements on the large uncertainties of positional information for GW events. *ATCA* started observations $\sim$ 12.6 hours after the initial trigger of short GRB 181123B. Although there were no significant detections, *ATCA* was able to obtain upper limits on the afterglow emission. In this study, I led the modelling efforts to understand how such early-time observations can help constrain the physics of GRBs. We demonstrate that even upper limits help to constrain the model parameters. Especially the fraction of thermal energy going into accelerating the charged particles, ϵ_e, can be constrained using these observations.

In Chapter 6, we derive the physical parameters of the "MAGIC" GRB 190114C, which is the first GRB detected in TeV energies. We present new radio follow-up observation obtained by the *Meer Karoo Array Telescope* (MeerKAT) and collect additional observations from the literature in radio/mm-wavelengths, optical, and X-ray bands in order to compile a broad-band data set for the afterglow of GRB 190114C. Furthermore, we make use of the method introduced in Chapter 2 to robustly infer the physical parameters of this exceptional GRB. We find that the accelerated particle distribution exhibits a hard energy distribution with a power law index well below 2, which might be one of the reasons that this GRB emitted TeV photons. We compare the inferred parameters of GRB 190114C with a large sample of long GRBs (see Chapter 3) and find that this GRB constitutes an outlier within the GRB population. This might indicate that TeV emitting GRBs are relatively rare.

Chapter 2

A new approach to modelling gamma-ray burst afterglows: Using Gaussian processes to account for the systematics

M. D. Aksulu, R. A. M. J. Wijers, H. J. van Eerten, A. J. van der Horst

Monthly Notices of the Royal Astronomical Society, 2020, 497, 4, p.4672–4683

Abstract

The afterglow emission from gamma-ray bursts (GRBs) is a valuable source of information to understand the physics of these energetic explosions. The fireball model has become the standard to describe the evolution of the afterglow emission over time and frequency. Thanks to recent developments in the theory of afterglows and numerical simulations of relativistic outflows, we are able to model the afterglow emission with realistic dynamics and radiative processes. Although the models agree with observations remarkably well, the afterglow emission still contains additional physics, instrumental systematics, and propagation effects which make the modelling of these events challenging. In this work, we present a new approach to modelling GRB afterglows, using Gaussian processes (GPs) to take into account systematics in the afterglow data. We show that, using this new approach, it is possible to obtain more reliable estimates of the explosion and microphysical parameters of GRBs. We present fit results for 5 long GRBs and find a preliminary correlation between the isotropic energetics and opening angles of GRBs, which confirms the idea of a common energy reservoir for the kinetic energy of long GRBs.

2.1 Introduction

Gamma-ray bursts (GRBs) are the most energetic explosions in the Universe. They are either the result of the collapse of massive stars (long GRBs) (Woosley, 1993), or of compact object mergers where at least one of the objects is a neutron star (short GRBs) (Eichler et al., 1989); for a review see, e.g. Piran (2004). During these catastrophic events, an ultra-relativistic, collimated outflow is generated by a compact central engine (Rees & Mészáros, 1992). Initially, GRBs are detected as prompt γ-ray flashes. The exact emission mechanism which produces these γ rays is still debated; for a review see, e.g. Kumar & Zhang (2015). As the outflow starts to interact with the circumburst medium, it starts to decelerate and forms a relativistic, collisonless shock where charged particles are accelerated in tangled magnetic fields and emit synchrotron emission across the whole electromagnetic spectrum (Rees & Mészáros, 1992). This emission is called the afterglow of the GRB. It is possible to understand more about the physics of GRBs by modelling the afterglow. The afterglow emission reveals how the dynamics of such relativistic shocks evolve over time as well as the microphysical properties in such extreme acceleration regions (Wijers et al., 1997; Sari et al., 1998; Wijers & Galama, 1999; Panaitescu & Kumar, 2002; Yost et al., 2003).

With the launch of the *Neil Gehrels Swift Observatory* (Gehrels et al., 2004), the detection rate of GRB afterglows has significantly increased. Together with multi-wavelength ground and space based follow-up, and the start of the multi-messenger era, we now have a wealth of data on GRB afterglows (Abbott et al., 2017b; MAGIC Collaboration et al., 2019a). Moreover, recent advancements in afterglow theory and numerical hydrodynamics allow us to model the dynamics and emission mechanism of GRB afterglows much more reliably (van Eerten, 2018). Although the models agree with the general trends of the afterglow data, it is still challenging to get reliable estimates of GRB parameters because of additional physics which is not included in the models (e.g. self-synchrotron Compton scattering effects, reverse shock emission), instrumental systematics, and propagation effects (e.g. scintillation in radio, absorption by the host galaxy gas and dust in the optical and X-ray regimes). All these effects introduce systematic deviations to the afterglow observations, and result in a more complex flux evolution over time and frequency than predicted by the models. Gompertz et al. (2018) have shown that there must be intrinsic errors involved when modelling GRB afterglows, by using closure relations to show that the data exhibits inconsistencies which cannot be explained by the measurement errors. In this work, we show that systematic deviations put unrealistically tight constraints on the model parameters when performing parameter estimation where the likelihood function is only proportional to the χ^2 value.

In this paper we introduce a new approach to fitting GRB afterglow data, by modelling the systematics using Gaussian processes (GPs). This way, the model parameters are not bound by artifacts of systematic deviations, and Bayesian parameter estimation gives more reliable parameter uncertainties. In Section 4.3 we explain the method in detail, in Section 2.3 we present test results with synthetic data sets, and compare to results obtained by conventional modelling. Moreover, in Section 2.4 we apply this method to 5 long GRB afterglow data sets and present the results. In Section 2.5 we further elaborate on the modelling of GRB afterglows, and we conclude in Section 2.6.

2.2 Method

GPs are a generalization of the Gaussian probability distribution, in the sense that, GPs enable us to define a probability distribution over functions instead of variables or vectors (Rasmussen & Williams, 2006). GPs are non-parametric, stochastic processes, and are therefore a useful tool in regression problems where the underlying model of the data is unknown, as is the case for the systematic differences between GRB afterglow models and observations.

In this section we describe a Gaussian process framework for modelling the systematics in the GRB afterglow data sets. We follow the same methodology described in Gibson et al. (2012), where they used the same approach to model transit light curves of exoplanets, which are affected by significant systematics.

2.2.1 GRB afterglow data

In order to solve for the many GRB afterglow model parameters, a well-sampled multi-wavelength data set is required. The data set consists of N flux measurements, $\boldsymbol{y} = (f_{\nu 1}, \ldots, f_{\nu N})^T$, measured at times and frequencies $\mathbf{X} = (\boldsymbol{x}_1, \ldots, \boldsymbol{x}_N)^T = ((t_1, \nu_1)^T, \ldots, (t_N, \nu_N)^T)^T$, where $\mathbf{X}$ is an $N \times 2$ matrix. The reported uncertainties of the flux measurements are expressed as $\boldsymbol{\sigma} = (\sigma_1, \ldots, \sigma_N)^T$.

2.2.2 Gaussian process framework

In this work, we use a GP model to take into account any possible systematics in the GRB afterglow data in a non-parametric fashion, where the systematics are described as,

$$f(t, \nu) \sim \mathcal{GP}(\mu(t, \nu, \phi), \boldsymbol{\Sigma}(t, \nu, \boldsymbol{\theta})), \tag{2.1}$$

where μ is the mean function of the GP (i.e. the afterglow model), $\boldsymbol{\Sigma}$ is the covariance matrix of the GP model, ϕ and $\boldsymbol{\theta}$ represent the GRB parameters and the, so called, *hyperparameters* of the GP model respectively.

The log likelihood of the GP model is described as,

$$\log \mathcal{L}(\nabla | \mathbf{X}, \boldsymbol{\theta}, \phi) = -\frac{1}{2} \boldsymbol{r}^T \boldsymbol{\Sigma}^{-1} \boldsymbol{r} - \frac{1}{2} \log |\boldsymbol{\Sigma}| - \frac{N}{2} \log(2\pi) \tag{2.2}$$

where $\boldsymbol{r}$ is the residual of the afterglow model with respect to the observed flux density values. We define the residual as,

$$\boldsymbol{r} = \log \boldsymbol{y} - \log \boldsymbol{\mu}, \tag{2.3}$$

due to the fact that the measured flux densities vary over orders of magnitudes with time and frequency. In such cases it is common to model the logarithm of the measured values (Snelson et al., 2004). Therefore, we exclude any negative flux measurements from the data sets when modelling.

The covariance matrix, $\mathbf{\Sigma}$, defines how correlated the data points are over observer time and frequency. In order to construct the covariance matrix, a squared-exponential kernel is chosen, over the 2D input space (time and frequency),

$$\mathbf{\Sigma}_{ij} = k(\mathbf{X}_i, \mathbf{X}_j) = A \exp\left[-\frac{1}{2}\sum_{k=1}^{2}\frac{(\mathbf{X}_{ik} - \mathbf{X}_{jk})^2}{l_k^2}\right] + \delta_{ij}\sigma_w^2, \tag{2.4}$$

where A represents the amplitude of the correlations, l_1 and l_2 determine the length scales of the correlations over time and frequency respectively, and σ_w represents the amount of white noise in the data set. These parameters are called the hyperparameters of the GP and need to be marginalized together with the model parameters. The white noise parameter is formulated as $\sigma_w = \sigma_{\log f_\nu}\sigma_h$, where $\sigma_{\log f_\nu}$ is the uncertainty in the logarithm of the flux measurements and σ_h is the hyperparameter which scales the reported uncertainties. Thus, the hyperparameters can be expressed as,

$$\boldsymbol{\theta} = (A, l_1, l_2, \sigma_h)^T. \tag{2.5}$$

In this work, we use the george Python package (Ambikasaran et al., 2015) as the GP framework. george enables us to calculate efficiently the covariance matrix and the GP likelihood even for relatively large data sets and it is designed to be used with any external optimization/sampling algorithm.

2.2.3 Model

We assume a relativistic, collimated, outflow interacting with the circumburst medium (CBM), forming a pair of shocks propagating into the ejecta (short-lived reverse shock) and into the CBM (long-lived forward shock) where charged particles are accelerated and emit synchrotron radiation (Sari et al., 1998; Wijers & Galama, 1999; Granot & Sari, 2002). In this work we only consider the emission originating from the forward shock. The forward shock model has been able to successfully describe the spectral and temporal evolution of GRB afterglows.

In this work, we incorporate scalefit (Ryan et al., 2015, Ryan et al. in prep.), as the mean function of the GP model. scalefit is an afterglow model, which makes use of pre-calculated tables of spectral features (i.e self-absorption break ν_a, injection break ν_m, cooling break ν_c, and peak flux density of the spectrum $f_{\nu,\mathrm{peak}}$) over decades in time and for different observing angles. scalefit takes advantage of scale invariance to calculate the observed flux density for given explosion and microphysical parameters, observer times and frequencies. The model parameters are described as,

$$\boldsymbol{\phi} = (\theta_0, E_{K,\mathrm{iso}}, n_0, \theta_{\mathrm{obs}}, p, \epsilon_B, \bar{\epsilon}_e, \xi_N)^T, \tag{2.6}$$

where θ_0 is the opening angle of the jet, $E_{K,\mathrm{iso}}$ is the isotropic-equivalent kinetic energy of the explosion, n_0 is the circumburst number density, θ_{obs} is the observing angle, p is the power-law index of the accelerated electron population, ϵ_B is the fraction of thermal energy in the magnetic fields, $\bar{\epsilon}_e \equiv \frac{p-2}{p-1}\epsilon_e$ where ϵ_e is the fraction of thermal energy in the accelerated electrons, and ξ_N is the fraction of electrons being accelerated.

boxfit (van Eerten et al., 2012) is used to produce the tables containing the spectral features. boxfit is a GRB afterglow modelling tool, which makes use of pre-calculated hydrodynamics data and solves radiative transfer equations during runtime. Since it relies on hydrodynamics data, it is able to model the dynamics of the blast wave reliably. boxfit has been used to successfully model the broadband emission from various afterglows (see e.g. Guidorzi et al. 2014; Higgins et al. 2019; Kangas et al. 2020), but its computationally expensive repeated radiative transfer calculations are a drawback when implementing boxfit in a sampling algorithm. scalefit instead draws from a table that reproduces the spectral breaks and peak fluxes from boxfit exactly, but approximates the spectral curvature across breaks when reconstructing spectra. Through its approximation of spectral curvature, scalefit avoids the need for repeated radiative transfer calculations and allows for fast computation (for applications, see e.g. Ryan et al. 2015; Zhang et al. 2015). This offers a good compromise between speed and accuracy. In this work, aimed at GPs, we make use of the fact that due to the slight differences in their approach the different modelling tools produce afterglow light curves with different relative systematics, leaving a detailed comparison of the relative merit between the methods for afterglow modelling in general for future work.

2.2.4 Regression

In order to marginalize over the model parameters and the hyperparameters of the GP, we make use of pymultinest (Buchner et al., 2014), which is the Python implementation of the MultiNest nested sampling algorithm (Feroz et al., 2009). Sampling from complex objective functions can be challenging as algorithms can get stuck in local maxima. The main advantage of using pymultinest is that it is able to converge on the global maximum with high efficiency (i.e. relatively small number of function evaluations). For all the presented results, pymultinest is used in the importance sampling mode (Feroz et al., 2019) with mode separation disabled. We use 1000 initial live points and use an evidence tolerance of 0.5 as our convergence criterion. These values are adapted from Feroz et al. (2009).

The fraction of accelerated electrons, ξ_N, is degenerate with respect to $(E_{K,\mathrm{iso}}, n_0, \epsilon_B, \bar{\epsilon}_e)$, where $(E_{K,\mathrm{iso}}, n_0)$ are proportional to $1/\xi_N$, and $(\epsilon_B, \bar{\epsilon}_e)$ are proportional to ξ_N (Eichler & Waxman, 2005). Because of this degeneracy, we fix ξ_N to be 0.10. Canonically, ξ_N is set to unity when modelling GRB afterglows, however, for our sample we find that a smaller value for ξ_N gives more physical results for ϵ_B and $\bar{\epsilon}_e$, since accepting the canonical value results in non-physical parameter values (e.g. $\epsilon_B + \epsilon_e > 1$). Moreover, particle-in-cell simulations have shown that ξ_N can be as low as 0.01, depending on the shock conditions (Sironi & Spitkovsky, 2011).

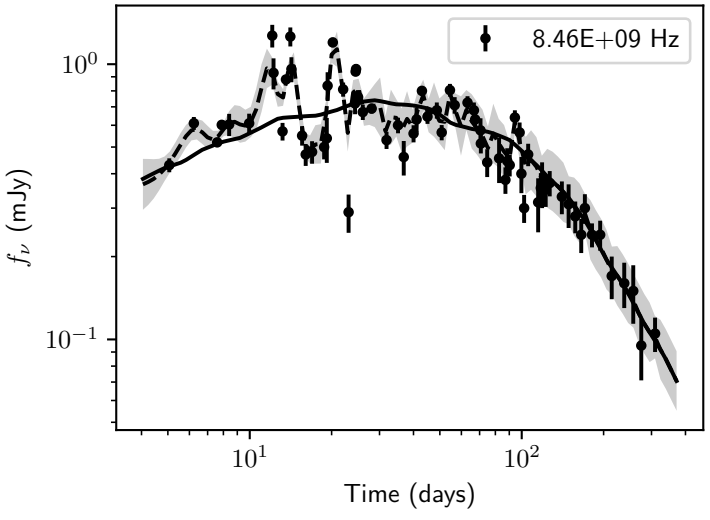

Figure 2.1: Example regression result from modelling GRB 970508 using the GP model. The radio light curve at 8.46 GHz is shown, where the solid line is the scalefit light curve, the dashed line is the mean predicted by the GP model and the shaded area represents the 1-σ uncertainty of the GP model. It can be seen that at early times the data is heavily affected by scintillation, and the systematics are modelled by the GP. The variability in the model (solid line) is due to numerical noise.

Regression is performed by marginalizing over both the hyperparameters and model parameters (see Equations 3.3 and 4.4). In all of the fits presented in this work, we assume that the systematics are uncorrelated over the frequency domain by fixing the hyperparameter l_2 to a very small number. We recognize that this assumption may not hold for regions of the spectrum where the frequency domain is sampled closely (e.g. radio or optical observations at similar frequencies). Also, dust extinction may lead to correlated noise in the frequency space over several decades. However, after correcting for dust extinction, when the data set spans over multiple decades in frequency, the emission in radio, optical and X-rays will not be correlated. In Figure 2.1, we present an example regression result for the radio light curve of GRB 970508, which contains significant variability in radio bands at early times due to interstellar scintillation. It can be seen that over time, as the shock front expands and the source size increases, the variability decreases.

2.3 Application to synthetic data

In order to test the effectiveness of the proposed method, we generate synthetic data sets and try to recover the true parameters by modelling the synthetic data using both the conventional method of sampling the χ^2 likelihood and the proposed method of sampling the GP log likelihood function (Equation 2.2).

Table 2.1: Assumed priors for modelling synthetic data sets.

Parameter range	Prior distribution
$0.01 < \theta_0 < 1.6$	log-uniform
$10^{50} < E_{K,\mathrm{iso}} < 10^{55}$	log-uniform
$10^{-4} < n_0 < 1000$	log-uniform
$0 < \theta_{\mathrm{obs}}/\theta_0 < 2$	uniform
$1.5 < p < 3.0$	uniform
$10^{-7} < \epsilon_B < 0.50$	log-uniform
$10^{-4} < \bar{\epsilon}_e < 10$	log-uniform

Table 2.2: Fit results for the synthetic data set generated using Model 1. The data set contains only white noise as described in Section 2.3. Results from both χ^2 and GP ($\mathcal{GP}$) likelihood sampling are presented. All the uncertainties on the parameters represent the 95% credible interval. Parameter estimations which include and exclude the true parameter value within the 95% credible interval are marked as ✓and ✗, respectively.

Parameter	χ^2	$\mathcal{GP}$	True value
$\boldsymbol{\theta_0}$	$0.0967^{+0.016}_{-0.0061}$ ✓	$0.098^{+0.017}_{-0.029}$ ✓	0.10
$\boldsymbol{\log_{10}(E_{K,\mathrm{iso},53})}$	$0.01^{+0.17}_{-0.21}$ ✓	$-0.04^{+0.23}_{-0.24}$ ✓	0.00
$\boldsymbol{\log_{10}(n_0)}$	$-0.09^{+0.18}_{-0.23}$ ✓	$-0.12^{+0.26}_{-0.32}$ ✓	0.00
$\boldsymbol{\theta_{\mathrm{obs}}/\theta_0}$	$0.29^{+0.17}_{-0.13}$ ✓	$0.27^{+0.26}_{-0.22}$ ✓	0.30
$\boldsymbol{p}$	$2.405^{+0.022}_{-0.018}$ ✓	$2.406^{+0.028}_{-0.042}$ ✓	2.40
$\boldsymbol{\log_{10}(\epsilon_B)}$	$-1.94^{+0.27}_{-0.24}$ ✓	$-1.91^{+0.37}_{-0.34}$ ✓	-2.00
$\boldsymbol{\log_{10}(\bar{\epsilon}_e)}$	$-1.48^{+0.15}_{-0.20}$ ✓	$-1.51^{+0.16}_{-0.15}$ ✓	-1.54

Two sets of synthetic data are generated using scalefit (Model 1 from now on) and boxfit (Model 2 from now on) as the underlying model. The synthetic data sets are generated in radio, optical and X-ray bands and across 10 time epochs, which are log-uniformly separated. The uncertainty fractions are chosen to be 10%, 2%, and 10%, for radio, optical and X-ray bands respectively. The data points are generated by drawing from a Gaussian distribution with the model value (either Model 1 or 2) as the mean and the corresponding uncertainty as the standard deviation.

In this work, we model any type of data set using Model 1 (see Section 3.2.3). Therefore, the synthetic data set generated with Model 1 contains only white noise, whereas the synthetic data set generated with Model 2 also contains systematics with respect to Model 1. This allows us to test the performance of the GP model, both in the absence and presence of systematic differences. For all the synthetic data modelling, we use the same prior for the parameters, which is presented in Table 2.1. We select fiducial GRB parameter values for our synthetic data sets; $(\theta_0, E_{K,\mathrm{iso}}, n_0, \theta_{\mathrm{obs}}/\theta_0, p, \epsilon_B, \epsilon_e) = (0.10, 10^{53}, 1.00, 0.30, 2.4, 10^{-2}, 10^{-1})$.

Tables 2.2 and 2.3 show fit results for both data sets and modelling approaches. As it can be seen in Table 2.2, the GP model and χ^2 sampling perform similarly in the absence of

Table 2.3: Fit results for the synthetic data set generated using Model 2. The data set contains both white noise and systematics as described in Section 2.3. Results from both χ^2 and GP ($\mathcal{GP}$) likelihood sampling are presented. All the uncertainties on the parameters represent the 95% credible interval. Parameter estimations which include and exclude the true parameter value within the 95% credible interval are marked as ✓and ✗, respectively.

Parameter	χ^2	$\mathcal{GP}$	True value
θ_0	$0.03570^{+0.00081}_{-0.00072}$ ✗	$0.071^{+0.062}_{-0.039}$ ✓	0.10
$\log_{10}(E_{K,\mathrm{iso},53})$	$0.519^{+0.034}_{-0.034}$ ✗	$0.57^{+0.87}_{-1.0}$ ✓	0.00
$\log_{10}(n_0)$	$-2.669^{+0.044}_{-0.048}$ ✗	$-0.2^{+1.2}_{-1.3}$ ✓	0.00
$\theta_{\mathrm{obs}}/\theta_0$	$0.641^{+0.033}_{-0.038}$ ✗	$0.70^{+0.46}_{-0.58}$ ✓	0.30
p	$2.469^{+0.014}_{-0.014}$ ✗	$2.33^{+0.11}_{-0.12}$ ✓	2.40
$\log_{10}(\epsilon_B)$	$-0.538^{+0.081}_{-0.081}$ ✗	$-2.0^{+1.5}_{-1.6}$ ✓	-2.00
$\log_{10}(\bar{\epsilon}_e)$	$-1.779^{+0.018}_{-0.017}$ ✗	$-1.96^{+0.46}_{-0.52}$ ✓	-1.54

systematics. Overall, the GP model results in larger parameter uncertainties. When there are systematics involved, the shortcomings of the χ^2 sampling approach stand out. In Table 2.3, we show that the χ^2 sampling technique is unable to recover any of the true parameters, despite inferring small uncertainties on the parameters. On the other hand the GP model is able to recover every parameter within the 95% credible interval.

In Figure 2.2 we show the fit results for all synthetic data sets and modelling approaches in the form of violin plots. Violin plots are a way to visualize the marginalized distributions of parameters in a compact way, where the shaded area represents the normalized histogram of the posterior samples, and the solid bar shows the interquartile range of the distribution. As it can be seen, the GP model results in larger uncertainties, more complex marginal distributions, and more accurate parameter estimations.

In order to investigate further whether sampling the GP likelihood results in more reliable parameter inferences, regardless of the chosen parameters for the synthetic data sets, we generate 100 sets of synthetic data both using Model 1 and Model 2 with randomly chosen GRB parameters. We fit all of the data sets using both the proposed method of GP likelihood sampling and χ^2 sampling. We perform coverage measurements on these fit results to determine how accurate the inferred uncertainties are. Coverage measurements are performed by fitting 100 synthetic data sets and counting how many times the true parameter was recovered for a given confidence region.

In Figure 2.3, we show the coverage measurement results for each GRB parameter both in the presence and absence of systematic deviations. These plots show the fraction of successfully recovered parameters (vertical axis) for a given credible interval [1] (horizontal axis) (Sellentin & Starck, 2019). The black points show the ideally expected coverage, where the error bars are calculated using the binomial uncertainty, given by,

$$\sigma = \sqrt{p(1-p)/N} \tag{2.7}$$

[1] Credible interval is the Bayesian analogue of confidence interval.

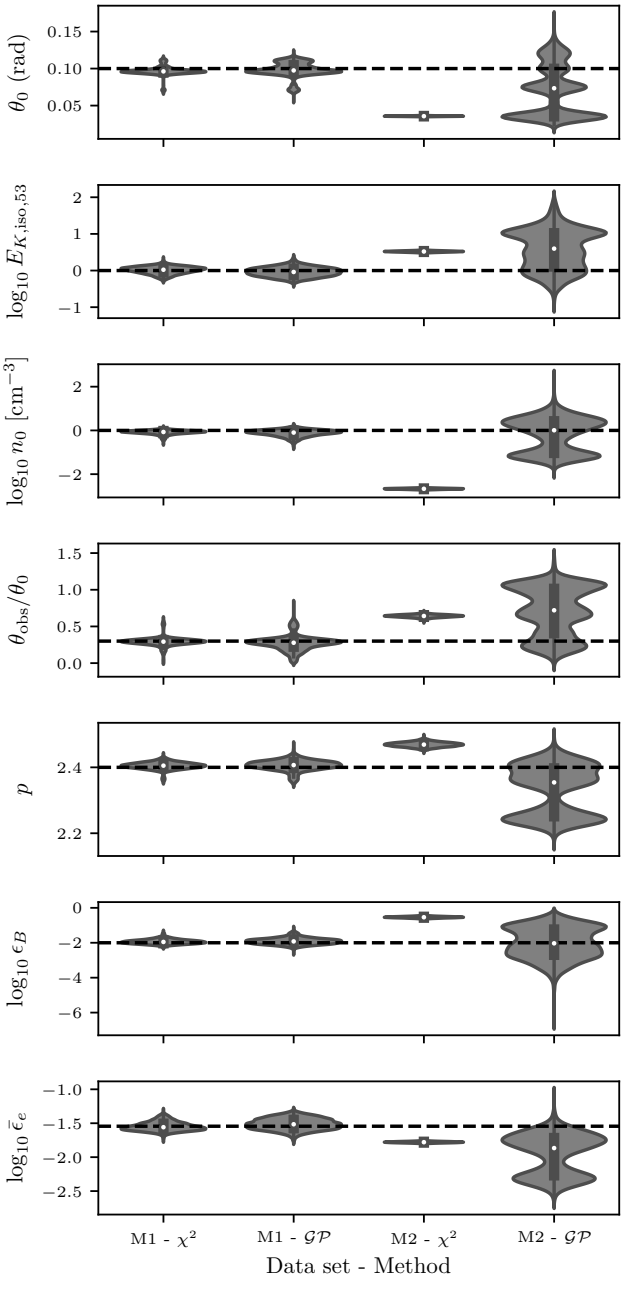

Figure 2.2: Violin plot of the fit results for different synthetic data sets and methods. Data sets which are generated by Model 2 (M2) contain systematics and white noise. Data sets generated with Model 1 (M1) contain no systematics but the same amount of white noise as Model 2. Both data sets are fitted using χ^2 sampling (χ^2) and sampling the GP likelihood in Equation 2.2 ($\mathcal{GP}$). The horizontal dashed lines represent the true parameter values.

Table 2.4: Redshift (z), Galactic foreground extinction ($A_{V,\mathrm{MW}}$), rest-frame host galaxy extinction ($A_{V,\mathrm{host}}$), and the best fit extinction model for the host galaxy of the long GRB sample. MW denotes Milky Way type host extinction, and SMC denotes Small Magellanic Cloud type host extinction (Pei, 1992).

GRB name	z	$A_{V,\mathrm{MW}}$	$A_{V,\mathrm{host}}$	Host type
970508	0.835	~ 0	~ 0	N/A
980703	0.966	0.1891	0.90	MW
990510	1.619	~ 0	0.22	SMC
991208	0.706	0.0512	0.80	MW
991216	1.02	2.016	~ 0	N/A

Table 2.5: Assumed priors for modelling the long GRB sample.

Parameter range	Prior distribution
$0.01 < \theta_0 < 1.6$	log-uniform
$10^{48} < E_{K,\mathrm{iso}} < 10^{55}$	log-uniform
$10^{-4} < n_0 < 1000$	log-uniform
$0 < \theta_{\mathrm{obs}}/\theta_0 < 2$	uniform
$1.0 < p < 3.0$	uniform
$10^{-7} < \epsilon_B < 0.50$	log-uniform
$10^{-5} < \bar{\epsilon_e} < 10$	log-uniform

where p is the probability of containing the true parameter (credible interval) and N is the number of samples (100 in our case). The coverage measurements show that the GP model performs better both in the presence and absence of systematic deviations, as the measured coverage for the GP model is closer to the ideal case. χ^2 sampling underestimates the errors on the parameters, especially for parameters which affect the temporal slope of the light curves (θ_0, θ_{obs} and p). In the presence of systematic deviations, even the GP model underestimates the errors on the parameters, however, less so than χ^2 sampling.

2.4 Application to archival GRB afterglow data

In this section we present fit results for 5 long GRB afterglows for which significant modeling has already been done, namely; GRB 970508, GRB 980703, GRB 990510, GRB 991208 and GRB 991216. We compare our results to previous, multi-wavelength, modelling efforts. In Table 3.1, we present the overall properties of the GRB sample. For this work, we were able to generate scalefit tables for constant density CBM only. Therefore, constant density CBM is assumed when fitting the afterglow data. We use the prior distributions presented in Table 2.5 in our modelling efforts. The inferred parameter distributions for the long GRB sample can be seen in Figure 2.4 in the form of a violin plot.

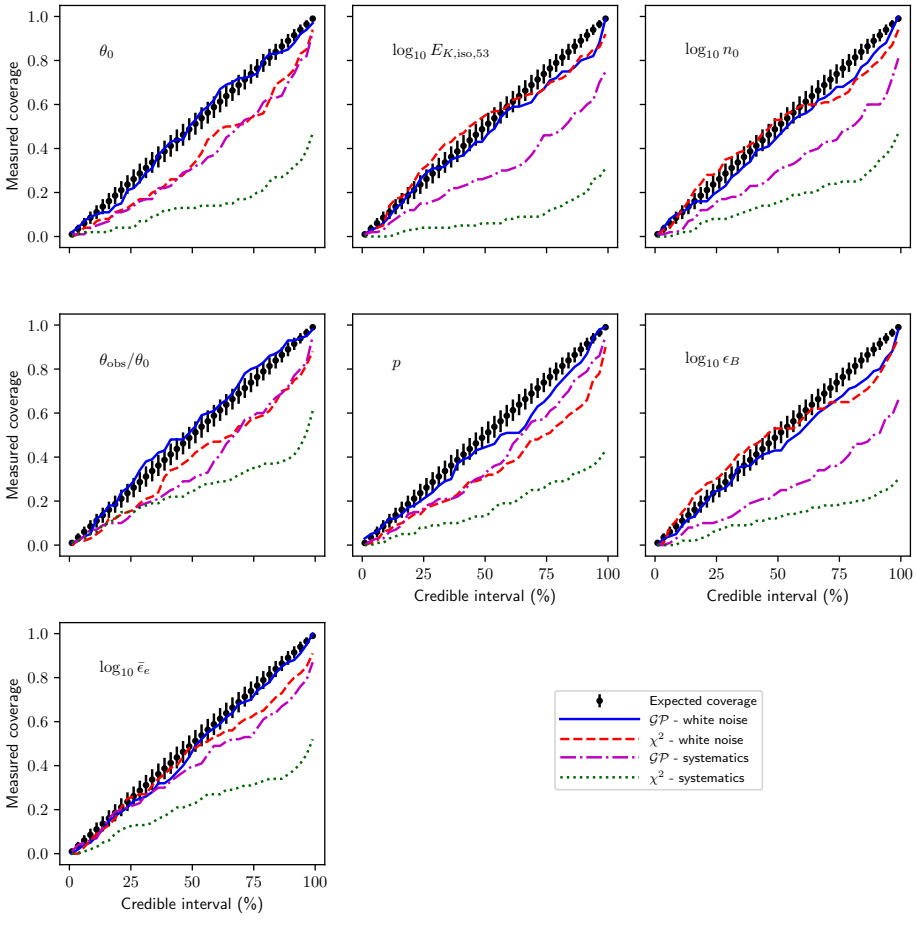

Figure 2.3: Coverage measurement results for GRB parameters. The blue and red lines show the coverage measurement results in the case where the data only contains white noise (synthetic data set generated by Model 1) for GP model regression ($\mathcal{GP}$) and χ^2 sampling, respectively. The magenta and yellow lines show the coverage measurement results in the case where the data contains systematic deviations (synthetic data set generated by Model 2) for GP model regression and χ^2 sampling, respectively. The black points show the ideally expected coverage, where the error bars are calculated using the binomial uncertainty $\sigma = \sqrt{p(1-p)/N}$, where p is the probability of containing the true parameter (credible interval) and N is the number of samples (100 in our case).

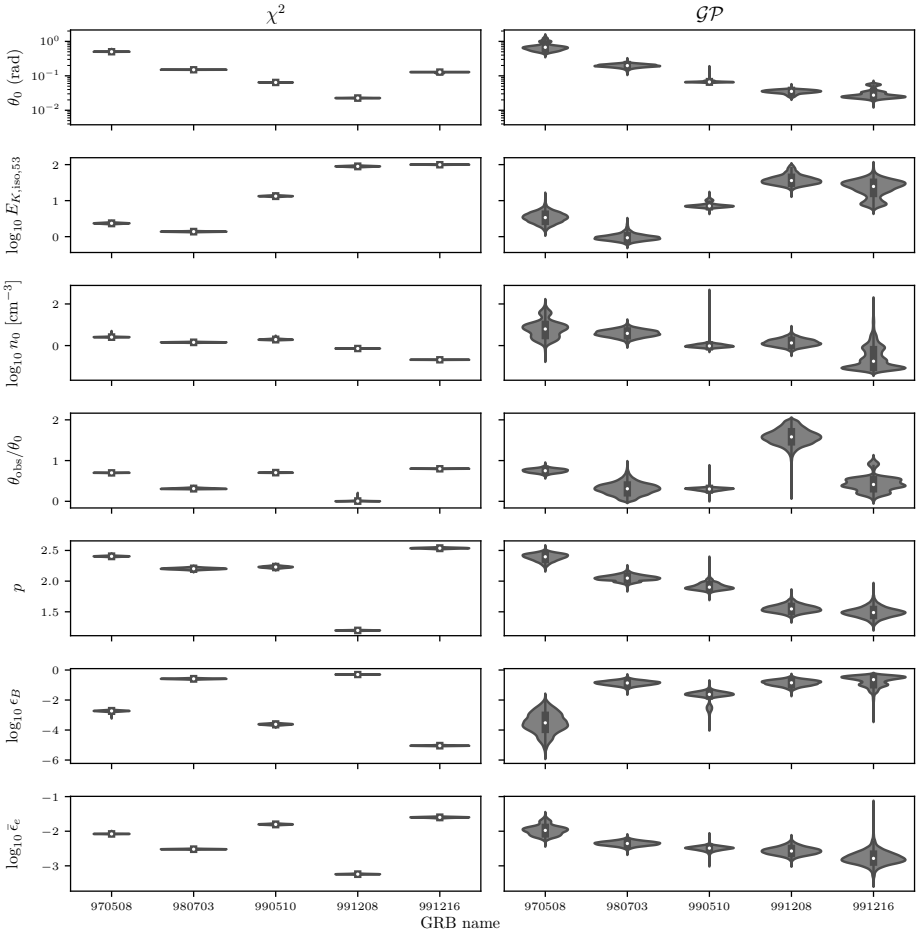

Figure 2.4: Violin plot showing the inferred marginalized distributions of the GRB parameters for the long GRB sample. The panel on the left shows the results for χ^2 sampling whereas the panel on the right shows the results from GP likelihood sampling.

Table 2.6: Fit results for GRB 970508. Results from both χ^2 sampling and GP likelihood sampling ($\mathcal{GP}$) are presented. The uncertainties on the parameters represent the 95% credible interval for columns χ^2 and $\mathcal{GP}$. Columns PK02 and Y03 show results from Panaitescu & Kumar (2002) and Yost et al. (2003), respectively. PK02 did not provide uncertainties on the parameters for this burst. The uncertainties for the Y03 results represent the 68.3% credible interval. All the values taken from previous studies have been converted to the same units. The values have been corrected for our choice of $\xi_N = 0.1$ by multiplying ($E_{K,\mathrm{iso}}$, n_0) by 10 and dividing (ϵ_B, $\bar{\epsilon}_e$) by 10 (see Section 2.2.4).

GRB 970508				
Parameter	χ^2	$\mathcal{GP}$	PK02	Y03
$\boldsymbol{\theta_0}$	$0.5007^{+0.0063}_{-0.0055}$	$0.74^{+0.52}_{-0.28}$	0.32	$0.84^{+0.030}_{-0.030}$
$\boldsymbol{\log_{10}(E_{K,\mathrm{iso},53})}$	$0.370^{+0.027}_{-0.026}$	$0.53^{+0.28}_{-0.28}$	0.597	$0.56^{+0.011}_{-0.011}$
$\boldsymbol{\log_{10}(n_0)}$	$0.407^{+0.028}_{-0.027}$	$0.80^{+0.90}_{-0.69}$	0.87	$0.30^{+0.021}_{-0.045}$
$\boldsymbol{\theta_{\mathrm{obs}}/\theta_0}$	$0.6977^{+0.0055}_{-0.0074}$	$0.750^{+0.093}_{-0.096}$	1.33	0
$\boldsymbol{p}$	$2.404^{+0.013}_{-0.013}$	$2.39^{+0.10}_{-0.12}$	2.18	$2.12^{+0.03}_{-0.008}$
$\boldsymbol{\log_{10}(\epsilon_B)}$	$-2.729^{+0.075}_{-0.077}$	$-3.5^{+1.2}_{-1.4}$	-2.34	$-1.60^{+0.010}_{-0.036}$
$\boldsymbol{\log_{10}(\bar{\epsilon}_e)}$	$-2.078^{+0.011}_{-0.011}$	$-1.97^{+0.30}_{-0.25}$	-2.77	$-2.43^{+0.02}_{-0.015}$

2.4.1 GRB 970508

GRB 970508 exhibits an increase in optical flux at around $\sim$ 1 day after the burst, and starts to decline as a power-law with time. Panaitescu & Kumar (2002) (PK02 from now on) explain the rise in the optical flux by assuming that the jet is viewed off-axis with $\theta_{\mathrm{obs}} \sim 4/3\theta_0$. They find that a wind-like CBM ($n \propto r^{-2}$) suits the observations best. On the other hand, Yost et al. (2003) (Y03 from now on) favor a constant density CBM in their analysis.

In our analysis, we exclude the data points before the peak of the rise in optical wavelengths, and fit the data points which obey the power-law behaviour. We take the observing angle as a free parameter, allowing viewing angles both larger and smaller than the opening angle.

Figure 2.7 shows the light curves for the inferred parameter distribution for the afterglow of GRB 970508 using GP regression. Table 2.6 shows the inferred parameter values. Assuming that the re-brightening in optical bands is due to late-time energy injection from the central engine, the energetics inferred from our modelling will overestimate the initial explosion energy. We find a wide opening angle, $0.74^{+0.52}_{-0.28}$ rad, which is consistent with Y03, who find an opening angle of $0.84^{+0.03}_{-0.03}$ rad. The inferred isotropic kinetic energy by the GP model is consistent with both PK02 and Y03, whereas the χ^2 sampling infers a lower $E_{K,\mathrm{iso}}$ with small uncertainty. Both GP likelihood and χ^2 sampling infer similar p values of $\sim$ 2.4, which is larger than what PK02 and Y03 found.

2.4.2 GRB 980703

Panaitescu & Kumar (2001b) (PK01 from now on) favor a constant density CBM for GRB 980703. Following Vreeswijk et al. (1999), PK01 take the host extinction to be $A_V = 1.45 \pm 0.13$, and find that $p = 3.08$. Y03 also favor a constant density CBM, and find a value of

Table 2.7: Fit results for GRB 980703. Results from both χ^2 sampling and GP likelihood sampling ($\mathcal{GP}$) are presented. See Table 2.6 for detailed explanation.

GRB 980703			
Parameter	χ^2	$\mathcal{GP}$	Y03
θ_0	$0.14990^{+0.00093}_{-0.0011}$	$0.199^{+0.043}_{-0.042}$	$0.234^{+0.02}_{-0.007}$
$\log_{10}(E_{K,\mathrm{iso},53})$	$0.139^{+0.016}_{-0.015}$	$-0.02^{+0.19}_{-0.17}$	$1.07^{+0.028}_{-0.080}$
$\log_{10}(n_0)$	$0.156^{+0.026}_{-0.025}$	$0.58^{+0.33}_{-0.34}$	$2.44^{+0.057}_{-0.049}$
$\theta_{\mathrm{obs}}/\theta_0$	$0.313^{+0.023}_{-0.018}$	$0.31^{+0.28}_{-0.29}$	0
p	$2.202^{+0.026}_{-0.026}$	$2.049^{+0.092}_{-0.094}$	$2.54^{+0.04}_{-0.1}$
$\log_{10}(\epsilon_B)$	$-0.588^{+0.048}_{-0.049}$	$-0.87^{+0.28}_{-0.31}$	$-3.74^{+0.087}_{-0.079}$
$\log_{10}(\bar{\epsilon}_e)$	$-2.520^{+0.015}_{-0.015}$	$-2.36^{+0.13}_{-0.13}$	$-2.02^{+0.065}_{-0.110}$

$A_V = 1.15$ for the host extinction and infer $p = 2.54^{+0.04}_{-0.1}$. In this work we take the host extinction to be $A_V = 0.9$ (Bloom et al., 1998a) and find that $p = 2.05^{+0.10}_{-0.095}$.

The host galaxy of GRB 980703 has a significant contribution to the observed radio and optical emission. We assume that the host galaxy contribution is constant over time and leave the host galaxy flux in radio and optical wavelengths as free parameters.

Figure 2.8 shows the light curves for the inferred parameter distribution for the afterglow of GRB 980703 using GP regression. Table 2.7 shows the inferred parameter values. The GP model infers an opening angle which is consistent with Y03, whereas χ^2 likelihood sampling infers a smaller opening angle. Inferred n_0 and $E_{K,\mathrm{iso}}$ values are significantly smaller than Y03.

2.4.3 GRB 990510

PK01 favor a constant density CBM for the case of GRB 990510. The optical afterglow of GRB 990510 exhibits a break in its temporal evolution at around 1.5 days. This break is interpreted as a jet-break. PK01 find $p = 2.09 \pm 0.03$ using closure relations, which is also consistent with the inferred value from the GP model.

Figure 2.9 shows the light curves for the inferred parameter distribution for the afterglow of GRB 990510 using GP regression. Table 2.8 shows the inferred parameter values. The inferred opening angle is consistent with van Eerten et al. (2012), where they performed a detailed fit using boxfit (vE12) model and found an opening angle $0.075^{+0.002}_{-0.004}$ rad assuming an on-axis observer. On the other hand PK02 find a smaller opening angle $0.054^{+0.001}_{-0.006}$ rad. The GP model predicts a larger ϵ_B value when compared to χ^2 sampling and previous studies.

2.4.4 GRB 991208

Figure 2.10 shows the light curves for the inferred parameter distribution for the afterglow of GRB 991208 using GP regression. Table 2.9 shows the inferred parameter values. The

Table 2.8: Fit results for GRB 990510. Results from both χ^2 sampling and GP likelihood sampling ($\mathcal{GP}$) are presented. The uncertainties on the parameters represent the 95% credible interval for columns χ^2 and $\mathcal{GP}$. Columns PK02 and vE12 show results from Panaitescu & Kumar (2002) and van Eerten et al. (2012). The uncertainties for the PK02 and vE12 results represent the 90% and 68% credible intervals, respectively. All the values taken from previous studies have been converted to the same units. The values have been corrected for our choice of $\xi_N = 0.1$ by multiplying $(E_{K,\mathrm{iso}}, n_0)$ by 10 and dividing $(\epsilon_B, \bar{\epsilon}_e)$ by 10 (see Section 2.2.4). Since PK02 find $p < 2$, the conversion from ϵ_e to the equivalent $\bar{\epsilon}_e$ results in a negative value. Therefore we denote $\log_{10}(\bar{\epsilon}_e)$ as N/A.

GRB 990510				
Parameter	χ^2	$\mathcal{GP}$	PK02	vE12
$\boldsymbol{\theta_0}$	$0.06423^{+0.00078}_{-0.00077}$	$0.0671^{+0.0062}_{-0.0042}$	$0.054^{+0.0017}_{-0.0087}$	$0.075^{+0.002}_{-0.004}$
$\boldsymbol{\log_{10}(E_{K,\mathrm{iso},53})}$	$1.125^{+0.026}_{-0.024}$	$0.870^{+0.18}_{-0.089}$	$0.98^{+0.80}_{-0.21}$	$1.25^{+0.06}_{-0.02}$
$\boldsymbol{\log_{10}(n_0)}$	$0.293^{+0.049}_{-0.042}$	$-0.01^{+0.15}_{-0.13}$	$0.46^{+0.139}_{-0.316}$	$-0.52^{+0.054}_{-0.221}$
$\boldsymbol{\theta_{\mathrm{obs}}/\theta_0}$	$0.705^{+0.014}_{-0.0093}$	$0.297^{+0.057}_{-0.074}$	0	0
$\boldsymbol{p}$	$2.230^{+0.028}_{-0.027}$	$1.91^{+0.12}_{-0.089}$	$1.83^{+0.18}_{-0.01}$	$2.28^{+0.06}_{-0.01}$
$\boldsymbol{\log_{10}(\epsilon_B)}$	$-3.620^{+0.086}_{-0.089}$	$-1.72^{+0.42}_{-1.0}$	$-3.28^{+0.95}_{-1.01}$	$-3.33^{+0.07}_{-0.08}$
$\boldsymbol{\log_{10}(\bar{\epsilon}_e)}$	$-1.803^{+0.026}_{-0.026}$	$-2.49^{+0.11}_{-0.12}$	N/A	$-2.08^{+0.13}_{-0.02}$

inferred p value by the GP model agrees with the results presented in PK02, whereas χ^2 sampling results in a smaller p value.

In our analysis we find a smaller opening angle than PK02 with an extremely off-axis observer angle. The GP regression and χ^2 sampling give significantly different results for microphysical parameters and observer angle.

2.4.5 GRB 991216

Figure 2.11 shows the light curves for the inferred parameter distribution for the afterglow of GRB 991216 using GP regression. Table 2.10 shows the inferred parameter values. PK02

Table 2.9: Fit results for GRB 991208. Results from both χ^2 sampling and GP likelihood sampling ($\mathcal{GP}$) are presented together with literature values. See Table 2.8 for detailed explanation.

GRB 991208			
Parameter	χ^2	$\mathcal{GP}$	PK02
$\boldsymbol{\theta_0}$	$0.02261^{+0.00059}_{-0.00059}$	$0.0350^{+0.0072}_{-0.0088}$	$0.22^{+0.026}_{-0.038}$
$\boldsymbol{\log_{10}(E_{K,\mathrm{iso},53})}$	$1.951^{+0.024}_{-0.024}$	$1.58^{+0.30}_{-0.23}$	$-0.015^{+0.49}_{-0.27}$
$\boldsymbol{\log_{10}(n_0)}$	$-0.1410^{+0.0073}_{-0.0077}$	$0.14^{+0.36}_{-0.32}$	$2.25^{+0.34}_{-0.17}$
$\boldsymbol{\theta_{\mathrm{obs}}/\theta_0}$	$0.0079^{+0.017}_{-0.0083}$	$1.58^{+0.38}_{-0.34}$	0
$\boldsymbol{p}$	$1.1964^{+0.0077}_{-0.0074}$	$1.55^{+0.13}_{-0.12}$	$1.53^{+0.03}_{-0.03}$
$\boldsymbol{\log_{10}(\epsilon_B)}$	$-0.30186^{+0.00086}_{-0.0018}$	$-0.86^{+0.35}_{-0.38}$	$-2.45^{+0.43}_{-0.39}$
$\boldsymbol{\log_{10}(\bar{\epsilon}_e)}$	$-3.241^{+0.017}_{-0.016}$	$-2.57^{+0.23}_{-0.21}$	N/A

Table 2.10: Fit results for GRB 991216. Results from both χ^2 sampling and GP likelihood sampling ($\mathscr{GP}$) are presented together with literature values. See Table 2.8 for detailed explanation.

GRB 991216			
Parameter	χ^2	$\mathscr{GP}$	PK02
θ_0	$0.1268^{+0.0031}_{-0.0095}$	$0.033^{+0.028}_{-0.012}$	$0.047^{+0.006}_{-0.017}$
$\log_{10}(E_{K,\mathrm{iso},53})$	$1.9961^{+0.0041}_{-0.0082}$	$1.34^{+0.36}_{-0.51}$	$0.99^{+0.68}_{-0.31}$
$\log_{10}(n_0)$	$-0.6833^{+0.0094}_{-0.010}$	$-0.60^{+1.0}_{-0.64}$	$1.67^{+0.38}_{-0.20}$
$\theta_{\mathrm{obs}}/\theta_0$	$0.7979^{+0.0071}_{-0.0095}$	$0.43^{+0.54}_{-0.33}$	0
p	$2.536^{+0.016}_{-0.017}$	$1.49^{+0.18}_{-0.16}$	$1.36^{+0.03}_{-0.03}$
$\log_{10}(\epsilon_B)$	$-5.041^{+0.044}_{-0.036}$	$-0.76^{+0.46}_{-0.70}$	$-2.74^{+0.46}_{-0.21}$
$\log_{10}(\bar{\epsilon}_e)$	$-1.601^{+0.025}_{-0.028}$	$-2.77^{+0.42}_{-0.36}$	N/A

find a hard electron distribution with $p = 1.36 \pm 0.03$, which is consistent with the results we get from GP modelling.

GP regression and χ^2 sampling result in very different parameter values for GRB 991216. This is mainly because the optical data contribute to the χ^2 value the most, whereas the radio data has a small contribution to the χ^2. The best fit obtained from χ^2 sampling, despite the fact that it has a smaller χ^2 value than the best fit of the GP model, completely misses the radio data points and therefore is an inadequate representation of the observed emission.

2.5 Discussion

GRBs are thought to be collimated outflows, therefore the isotropic equivalent energies of these events are an overestimation of the true energetics. The true, beaming corrected, energies of these events significantly depend on the geometry of the outflow (i.e. the opening angle),

$$E_K = E_{K,\mathrm{iso}}(1 - \cos\theta_0). \tag{2.8}$$

Previous studies have shown that there is observational evidence that there exists a standard energy reservoir for GRBs. Frail et al. (2001) have measured the opening angle of a sample of GRBs based on achromatic breaks in the afterglow light curve. They have shown that the beaming corrected energy release in γ-rays is narrowly clustered around 5×10^{50} erg. Moreover, Panaitescu & Kumar (2002) have shown, using multi-wavelength afterglow modelling, that the beaming corrected kinetic energy of GRBs are narrowly distributed and vary between 10^{50} to 5×10^{50} erg. Similarly, Berger et al. (2003) have analysed the X-ray afterglow data for a large sample of GRBs with known jet breaks, and have found evidence that the beaming corrected kinetic energy of these events are approximately constant. Note that, these studies are based on pre-*Swift* afterglow observations and therefore might be biased towards more energetic GRBs. After the launch of *Swift*, thanks to improved localization,

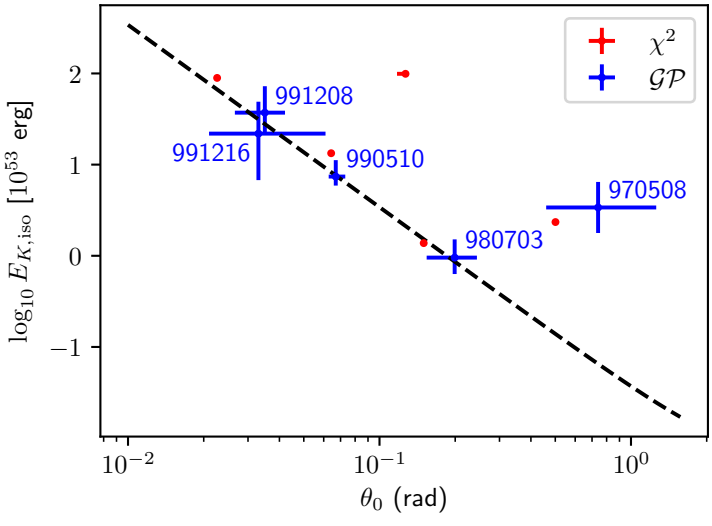

Figure 2.5: Isotropic equivalent kinetic energy ($E_{K\mathrm{iso}}$) dependence on the opening angle (θ_0) inferred from our modelling. The red measurements (χ^2) are obtained by χ^2 sampling and the blue measurements ($\mathcal{GP}$) are obtained by sampling the GP log likelihood function. The dashed black line represents the $E_{K,\mathrm{iso}}(1-\cos\theta_0) = 1.7 \times 10^{51}$ relation. The error bars represent the 95% credible interval.

the number of redshift measurements have increased and other classes of GRBs have been discovered, such as low-luminosity GRBs (ll-GRBs) which exhibit significantly less luminous prompt emission. ll-GRBs might constitute outliers in the overall GRB population and might not conform with the idea of a constant energy reservoir (Liang et al., 2007).

Our analysis also shows a strong correlation between θ_0 and $E_{K,\mathrm{iso}}$. In Figure 2.5, we show the measured opening angles and isotropic energies of our GRB sample. It can be seen that, when the GP model is used for inferring parameters, the measured values suggest that the beaming corrected kinetic energies are approximately the same for long GRBs. GRB 970508 is a clear outlier, which is consistent with the findings of Panaitescu & Kumar (2002). As discussed in Section 2.4.1, GRB 970508 exhibits a re-brightening in optical wavelengths, which could be due to late-time energy injection. This energy injection could account for the overestimation of the isotropic-equivalent kinetic energy of this source, which might imply that the standard energy reservoir applies more strongly to the initial ejecta formation of a GRB than to any later activity of the central engine. Note that the correlation is not apparent when χ^2 sampling is used for parameter estimation.

In Figure 2.6, we show the inferred beaming corrected kinetic energies with 95% credible intervals for the sample GRBs. The inferred E_K in our analysis is $\sim 1.7 \times 10^{51}$ erg, which is about an order of magnitude larger than what previous studies have found. This discrepancy with previous studies is expected as we fix ξ_N to be 0.1 instead of the canonical value of 1.0.

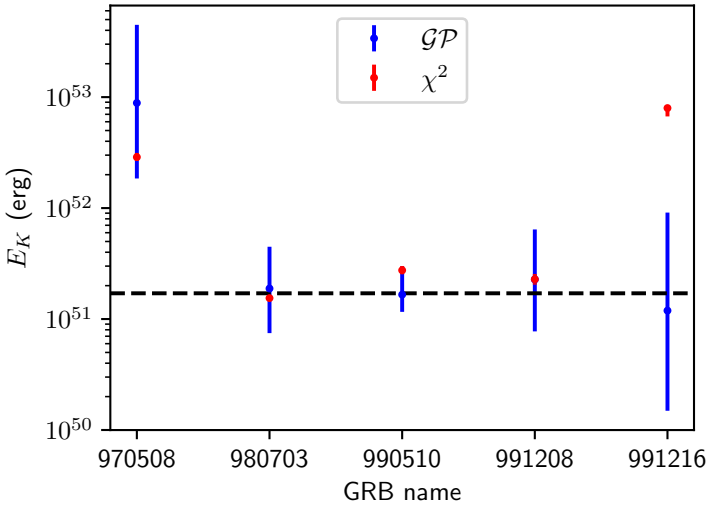

Figure 2.6: Beaming corrected kinetic energies of the long GRB sample. The red measurements (χ^2) are obtained by χ^2 sampling and the blue measurements ($\mathcal{GP}$) are obtained by sampling the GP log likelihood function. The dashed line is the log-average of GRBs 980703, 990510, 991208, 991216, which is equal to 1.7×10^{51} erg. The error bars represent the 95% credible interval.

We also recognise that it is too early to judge whether these few very well studied, well-sampled GRB afterglows are representative of the whole population.

2.6 Conclusion

In this work, we have introduced a novel method for modelling GRB afterglows, where Gaussian processes are used to take into account any systematics between the model and observations in a non-parametric fashion. Using synthetic data sets, we have shown that the GP approach results in more accurate posterior distributions with respect to sampling the χ^2 likelihood.

We model a sample of 5 well-known long GRBs with multi-wavelength coverage (GRBs 970508, 980703, 990510, 991208, 991216), using the scalefit code together with the GP framework. We compare the inferred parameters for each GRB with the literature values and comment upon the parameter distributions of the overall sample. We find a correlation between the isotropic-kinetic energy and opening angle, with GRB 970508 being the only outlier. This correlation, which is consistent with previous studies, suggests that there is a common energy reservoir which drives the dynamics of GRBs.

Acknowledgements

We would like to thank Vatsal Panwar for valuable discussions on Gaussian processes. We would like to thank Dr. Elena Sellentin for her useful tips regarding coverage measurements. We would also like to thank the anonymous referee for their detailed comments. H. J. van Eerten acknowledges partial support by the European Union Horizon 2020 Programme under the AHEAD2020 project (grant agreement number 871158). This work was sponsored by NWO Exact and Natural Sciences for the use of supercomputer facilities.

Appendices

2.A Fit results

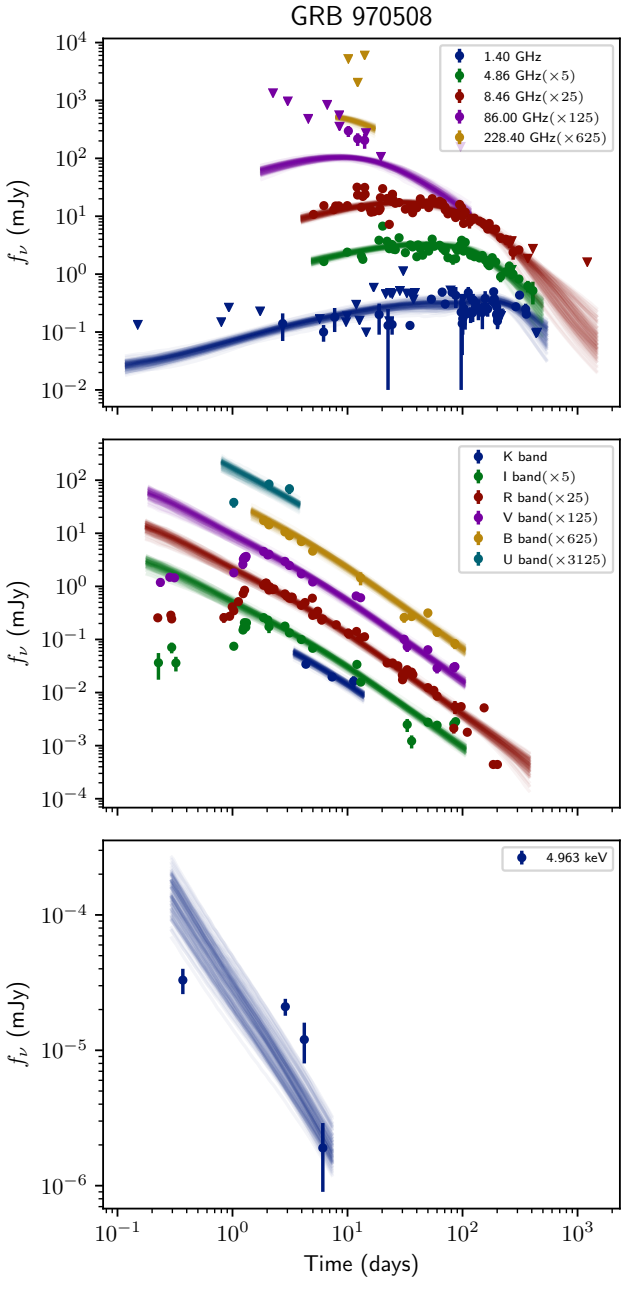

Figure 2.7: Fit result for GRB 970508 by sampling the GP likelihood. Observed flux density values are presented in radio, optical and X-ray bands (upper, middle and lower panel respectively) together with the posterior predictive light curves. Triangles represent 3-σ upper limits. A sample of 100 parameter sets are randomly drawn from the inferred joint probability distribution of the parameters, and scalefit light curves are drawn for each parameter set.

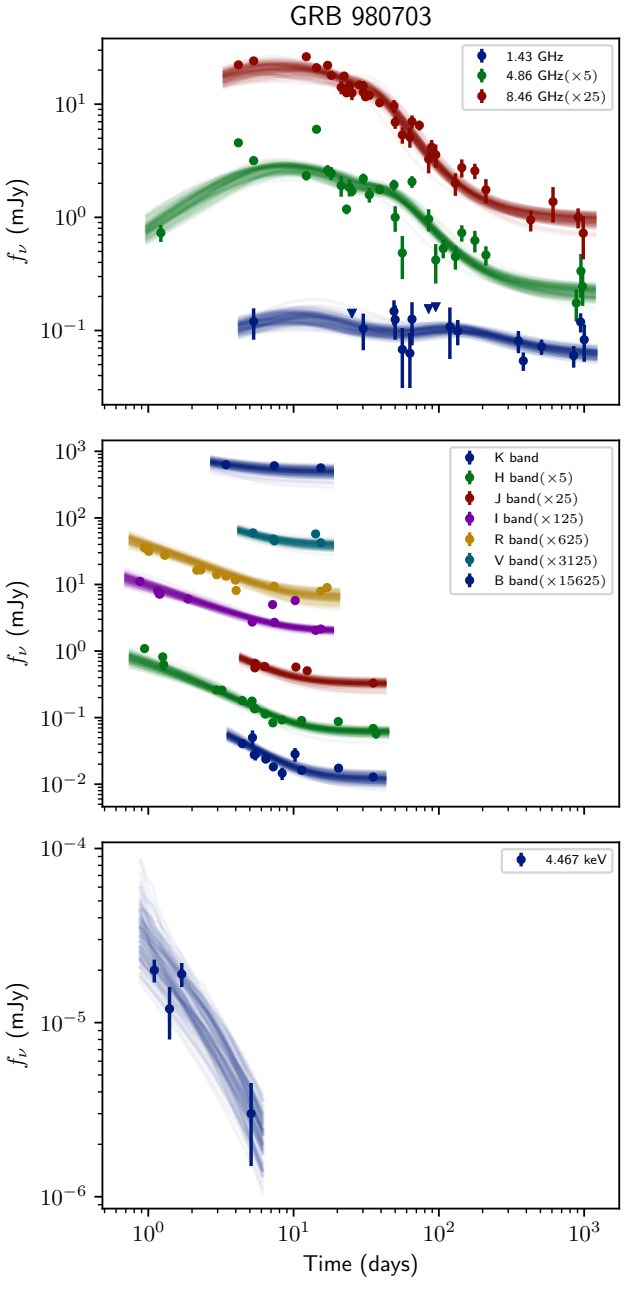

Figure 2.8: Fit result for GRB 980703 by sampling the GP likelihood. Observed flux density values are presented in radio, optical and X-ray bands (upper, middle and lower panel respectively) together with the posterior predictive light curves. Triangles represent 3-σ upper limits. A sample of 100 parameter sets are randomly drawn from the inferred joint probability distribution of the parameters, and scalefit light curves are drawn for each parameter set. The host galaxy contribution in radio and optical is not subtracted.

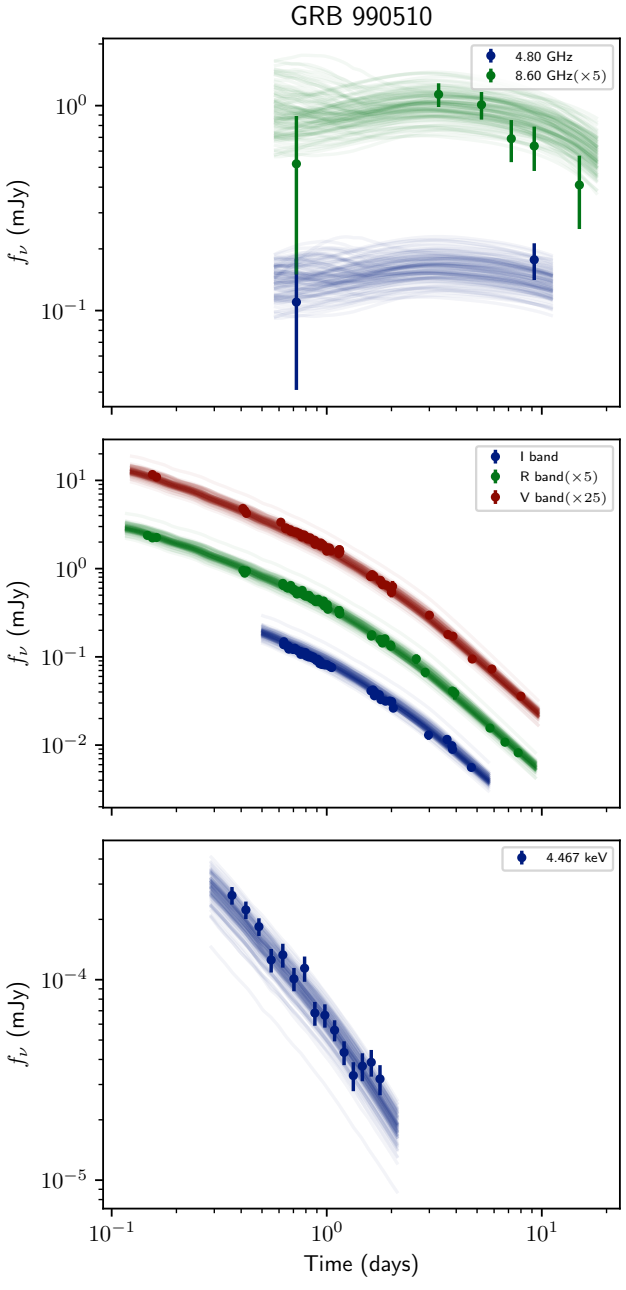

Figure 2.9: Fit result for GRB 990510 by sampling the GP likelihood. Observed flux density values are presented in radio, optical and X-ray bands (upper, middle and lower panel respectively) together with the posterior predictive light curves. A sample of 100 parameter sets are randomly drawn from the inferred joint probability distribution of the parameters, and scalefit light curves are drawn for each parameter set.

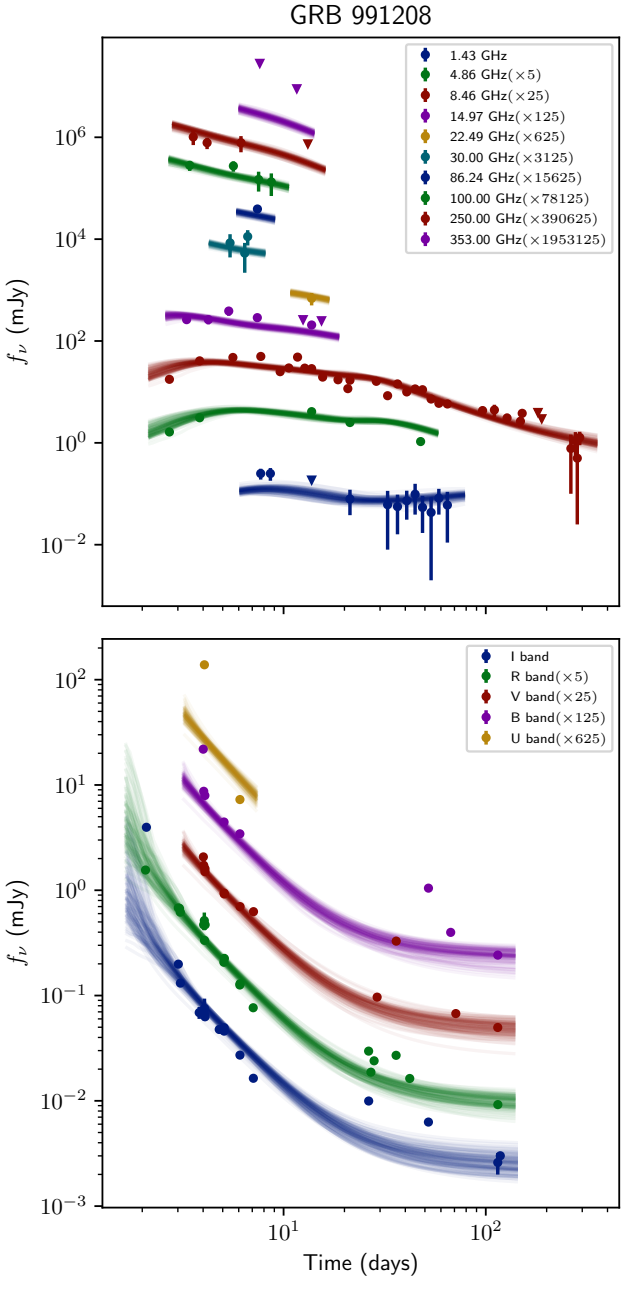

Figure 2.10: Fit result for GRB 991208 by sampling the GP likelihood. Observed flux density values are presented in radio and optical bands (upper and lower panel respectively) together with the posterior predictive light curves. Triangles represent 3-σ upper limits. A sample of 100 parameter sets are randomly drawn from the inferred joint probability distribution of the parameters, and scalefit light curves are drawn for each parameter set. The host galaxy contribution in optical is not subtracted.

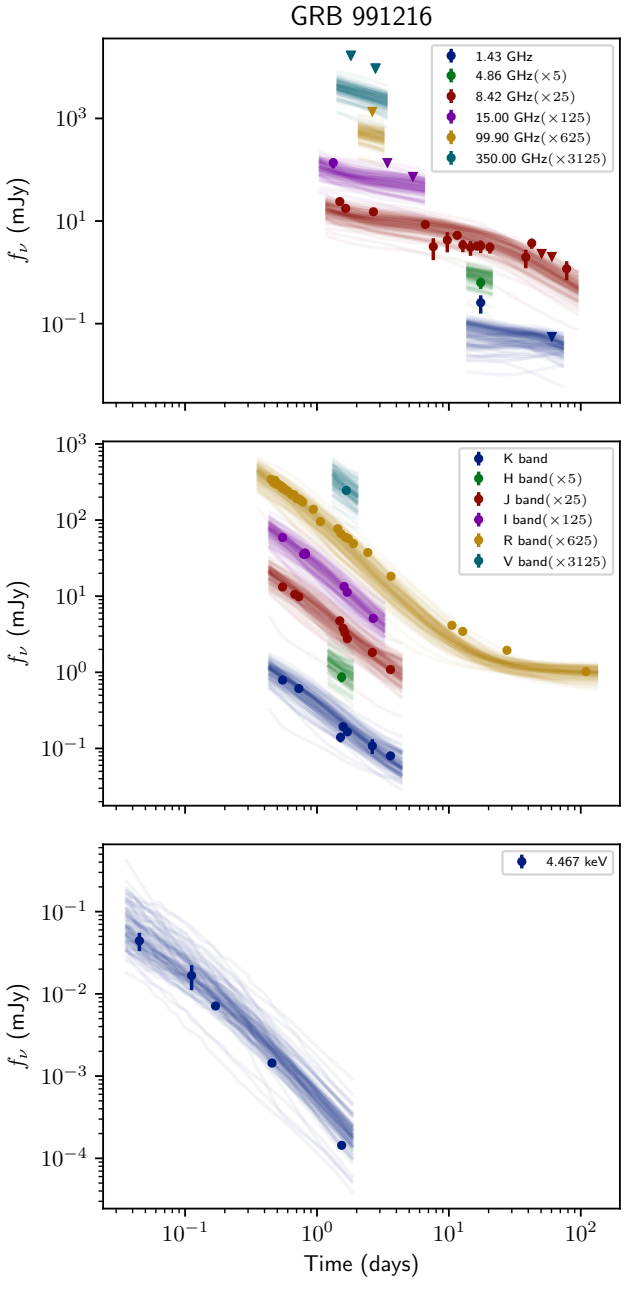

Figure 2.11: Fit result for GRB 991216 by sampling the GP likelihood. Observed flux density values are presented in radio, optical and X-ray bands (upper, middle and lower panel respectively) together with the posterior predictive light curves. Triangles represent 3-σ upper limits. A sample of 100 parameter sets are randomly drawn from the inferred joint probability distribution of the parameters, and scalefit light curves are drawn for each parameter set. The host galaxy contribution in optical is not subtracted.

Chapter 3

Exploring the GRB population: Robust afterglow modelling

M. D. Aksulu, R. A. M. J. Wijers, H. J. van Eerten, A. J. van der Horst

Submitted to the Monthly Notices of the Royal Astronomical Society

Abstract

Gamma-ray bursts (GRBs) are ultra-relativistic collimated outflows, which emit synchrotron radiation throughout the entire electromagnetic spectrum when they interact with their environment. This afterglow emission enables us to probe the dynamics of relativistic blast waves, the microphysics of shock acceleration, and environments of GRBs. We perform Bayesian inference on a sample of GRB afterglow data sets consisting of 22 long GRBs and 4 short GRBs, using the afterglow model scalefit, which is based on 2D relativistic hydrodynamic simulations. We make use of Gaussian processes to account for systematic deviations in the data sets, which allows us to obtain robust estimates for the model parameters. We present the inferred parameters for the sample of GRBs, and make comparisons between short GRBs and long GRBs in constant-density and stellar-wind-like environments. We find that in almost all respects such as energy and opening angle, short and long GRBs are statistically the same. Short GRBs however have a markedly lower prompt γ-ray emission efficiency than long GRBs. We also find that for long GRBs in ISM-like ambient media there is a significant anti-correlation between the fraction of thermal energy in the magnetic fields, ϵ_B, and the beaming corrected kinetic energy. Furthermore, we find no evidence that the mass-loss rates of the progenitor stars are lower than those of typical Wolf-Rayet stars.

3.1 Introduction

Gamma-ray bursts (GRBs) are the most powerful explosions in the Universe. They are ultra-relativistic collimated outflows, which are powered by a compact central object. GRBs are initially observed as brief flashes of γ rays lasting about 0.1–1000 s. These initial brief flashes of high-energy radiation are called the prompt emission of the GRB. The exact emission mechanism of the prompt emission remains elusive, despite decades of dedicated research. GRBs are phenomenologically categorized as short and long GRBs depending on the duration of the prompt emission phase (Kouveliotou et al., 1993). Short GRBs have been associated with compact object mergers where at least one of the objects is a neutron star (Lattimer & Schramm, 1976; Eichler et al., 1989), whereas long GRBs are thought to be results of core-collapse supernovae of massive stars (Woosley, 1993).

As the ejected ultra-relativistic outflow from a GRB starts to interact with the circumburst medium (CBM), a pair of shocks are generated, one of which propagates into the ejecta (reverse shock) and the other propagates into the CBM (forward shock). In these shocks, tangled magnetic fields are amplified and charged particles are accelerated, which results in long-lasting synchrotron emission spanning the whole electromagnetic spectrum (Rees & Mészáros, 1992). This broadband synchrotron emission is observable for several months, even years in some cases, and is called the afterglow emission of the GRB. The afterglow emission provides crucial insights on the energetics and environments of GRBs, the dynamics of relativistic blast waves, and the microphysics of particle acceleration in shocks (Wijers et al., 1997; Sari et al., 1998; Wijers & Galama, 1999; Panaitescu & Kumar, 2002; Yost et al., 2003).

Thanks to missions like the *Neil Gehrels Swift Observatory* (Gehrels et al., 2004) and *Fermi Gamma-ray Space Telescope* (Atwood et al., 2009), the number of detected/localized GRBs has increased and allowed for rapid, ground/space based, broadband follow-up observations of the afterglow emission. Moreover, the start of the multi-messenger era has supplemented our understanding of the physics of GRBs (Abbott et al., 2017b; MAGIC Collaboration et al., 2019a). Besides advances in observational instruments, developments in numerical hydrodynamics and radiative transfer have enabled us to build models with increasing complexity and accuracy (e.g., van Eerten et al. 2012; De Colle et al. 2012; van Eerten & MacFadyen 2013; Ryan et al. 2015; Duffell & Laskar 2018; Wu & MacFadyen 2018; Jacovich et al. 2021). Moreover, advances in statistical methods allow us to perform robust Bayesian inference and obtain reliable parameter estimates (Aksulu et al., 2020). Due to all these developments, we can now model a sample of GRB afterglow data sets, consistently, and investigate the distribution of physical parameters in the GRB population.

Previously, Panaitescu & Kumar (2002); Yost et al. (2003) have performed broadband afterglow modelling, and inferred burst parameters for a sample of long GRBs. Furthermore, Fong et al. (2015) have gathered data for a large number of short GRBs, and inferred their burst parameters based on their afterglow emission. These studies utilized semi-analytic models to reproduce the observed broadband emission; in this study we make use of a model based

on 2D relativistic hydrodynamic simulations. This allows us to capture the dynamics of these energetic events in a more realistic fashion.

In Aksulu et al. (2020) (A20, from now on), we introduced a new method for Bayesian parameter estimation, where we make use of Gaussian processes (GPs) in order to take into account some systematic effects in the data set and physics not included in the model. We showed in A20 that this approach allows us to obtain more robust parameter estimates, whereas the more conventional method of sampling the χ^2 likelihood leads to underestimated uncertainties on the parameters, especially in the presence of systematics. We make use of a modified version of the GP model described in A20, in order to model a sample of 26 GRB afterglow data sets. In Section 4.3 we describe the GRB sample, model, inference approach and details of the regression process. In Section 4.4 we present our results and the inferred physical parameters of the sample. Finally we discuss our findings in Section 4.5 and conclude in Section 4.6. Throughout this work we assume the cosmology as described in Planck Collaboration et al. (2016).

3.2 Method

3.2.1 Sample

Our GRB afterglow sample consists of 26 GRBs with well-sampled, broadband data sets. We relied only on peer-reviewed, published data sets, and converted the reported measurements to mJy units. The main selection criterion for the sample of GRBs has been the availability of broadband afterglow data. 22 out of the 26 GRBs are long GRBs detected between 1997–2014, with published broadband data sets; the time period is set to get a large enough sample. For short GRBs, we found only four with detections in radio, optical and X-ray bands up to the present. We omitted GRBs with non-canonical features in their light curves and include the five GRBs modelled in A20. When possible, we neglect epochs and/or bands for which there is evidence that the emission is dominated by processes which are not included in our model (e.g., early time optical and radio emission from GRB 130427A, which is dominated by reverse shock emission). This does not, of course, in any way represent a well-defined complete sample. We drew the boundary for having enough data somewhat subjectively, and similarly selected data sections in the early light curves suspected of unmodeled physics by eye.

We corrected the observed flux values for Galactic dust extinction using the extinction curve given by Pei (1992). We subtract any persistent emission originating from the host galaxy when possible. We do not correct the data for the dust extinction due to the host galaxy; instead we leave the rest-frame A_V value for the host galaxy as a free parameter (see Section 3.2.3). We present the GRB sample in Table 3.1.

3.2.2 Gaussian process framework

GPs are stochastic processes which can be used for regression and classification problems for which the underlying physical model is unknown (e.g., Rasmussen & Williams 2006).

Table 3.1: The GRB sample for this study. The measured redshift (z) and isotropic equivalent prompt energetics ($E\gamma$, iso) are presented.

	Burst name	z	$E\gamma$, iso/10^{52} (erg)
short GRBs	051221A	0.5465	0.15
	130603B	0.3564	0.21
	140903A	0.351	0.006 ± 0.0003
	200522A	0.5536	0.0084 ± 0.0011
long GRBs	970508	0.835	0.61 ± 0.13
	980703	0.966	6.9 ± 0.8
	990510	1.619	17.8 ± 2.6
	991208	0.706	22.3 ± 0.8
	991216	1.02	67.5 ± 8.1
	000301C	2.04	4.6
	000418	1.118	9.1 ± 1.7
	000926	2.066	27. ± 5.8
	010222	1.477	81. ± 1.
	030329	0.1685	1.66 ± 0.2
	050820A	2.615	97.5 ± 7.7
	050904	6.29	124. ± 7.7
	060418	1.49	12.8 ± 1.
	090328	0.7357	13. ± 3.
	090423	8.26	9.5 ± 2.
	090902B	1.8229	440. ± 30.
	090926A	2.1062	200. ± 5.
	120521C	6.0	8.25 ± 2.
	130427A	0.3399	81.
	130702A	0.145	0.064 ± 0.01
	130907A	1.238	330. ± 10.
	140304A	5.283	12.24 ± 1.4

Following A20 (also see Gibson et al. 2012), we make use of GPs to take into account any systematic deviations from the afterglow model. In this section, we highlight some improvements on the GP model introduced in A20. For clarity we use the same notation as in A20. Vectors and matrices are represented by bold symbols.

The systematics are described by the GP model as,

$$f(t,\nu) \sim \mathcal{GP}\left(\mu(t,\nu,\phi), \mathbf{\Sigma}(t,\nu,\boldsymbol{\theta})\right), \tag{3.1}$$

where t and ν are the time and frequency coordinates in the observer frame, ϕ represents the afterglow model parameters, and $\boldsymbol{\theta}$ represents the hyperparameters of the GP. Since the observer time and frequency change over many orders of magnitude, we work with the logarithm of these coordinates when performing GP regression. The mean function of the GP, μ, is the afterglow model, and $\mathbf{\Sigma}$ is the covariance matrix which describes how the systematics are correlated over t and ν. We adopt a 2D heterogeneous squared-exponential kernel function (e.g., see Rasmussen & Williams 2006) to calculate the covariance matrix,

$$\mathbf{\Sigma}_{ij} = k(\mathbf{X}_i, \mathbf{X}_j) = A \exp\left[-\frac{1}{2}\sum_{k=1}^{2}\frac{(\mathbf{X}_{ik}-\mathbf{X}_{jk})^2}{l_k^2}\right] + \delta_{ij}\sigma_h^2, \tag{3.2}$$

where $\mathbf{X}$ represents the 2D feature set (i.e., observer time and band). The hyperparameters of the GP are defined as,

$$\boldsymbol{\theta} = (A, l_1, l_2, \sigma_h)^T \tag{3.3}$$

where A represents the amplitude of the correlations, l_1 and l_2 determine the length scales of the correlations over time and frequency, respectively, and σ_h represents the amount of white noise in the data set. In A20, the systematics in the data set were assumed to be uncorrelated across different observational bands. Therefore, the hyperparameter l_2 was fixed to be a small number. In this work, we make l_2 a free parameter, thereby allowing the GP model to capture systematics correlated over different observational bands. We refer the reader to A20 for a more detailed explanation of the GP model.

3.2.3 Model

We assume a collimated, ultra-relativistic blast wave moving into a circumburst medium, which need not be uniform; we assume a density profile of the form

$$n = n_{\rm ref}\left(\frac{r}{10^{17}\ {\rm cm}}\right)^{-k}. \tag{3.4}$$

The normalisation is chosen at a radius that often falls within the range sampled by real afterglows. We will not treat k as a fully free parameter, but only allow the 'classic' values of 2 and 0. For $k = 2$, the interpretation of the environment is pretty unambiguous: the blast

wave is in the unshocked, freely expanding part of a massive stellar wind. In that case a more common nomenclature of the parameters is:

$$\rho(r) = \frac{A}{r^2}, \tag{3.5}$$

where r is the distance from the star and A can be expressed as,

$$A = \frac{\dot{M}}{4\pi v_{\rm wind}}. \tag{3.6}$$

Here, $\dot{M}$ is the mass loss rate of the progenitor star and $v_{\rm wind}$ is the wind velocity. For a canonical Wolf-Rayet star with a mass loss rate of $10^{-5}\,M_\odot$/yr and wind velocity of 1000 km/s, $A \sim 5 \times 10^{11}$ g/cm, which value is denoted by A_*. We can simply scale the inferred $n_{\rm ref}$ values to units of A_* using

$$\frac{A}{A_*} = \frac{n_{\rm ref}}{30\,{\rm cm}^{-3}}. \tag{3.7}$$

For $k = 0$ the interpretation of the environment is much more ambiguous. In this case the actually observed afterglow typically covers well under a factor 10 in radius travelled by the blast wave, so any environment in which the density does not change much over a factor few in distance (and within the solid angle hit by the outflow) will do. This could definitely be canonical ISM, but for A_* not too different from 1, a wind bubble around a massive star will contain many solar masses of material and thus the GRB jet will never emerge from it during the normal afterglow phase (the blast wave typically needs to sweep up less than (beamed equivalent of a spherical amount of) $0.1\,{\rm M}_\odot$ of ambient matter to become non-relativistic). However, the bulk of the wind bubble will contain wind that has been shocked against the ISM, and that is uniform enough to fit the $k = 0$ case. Another possibility might be that the star has a significant proper motion through a somewhat dense ISM. In that case most of the wind bubble is swept back, and in the forward hemisphere the blast wave may emerge from the wind into the ISM in time.

The initial Lorentz factor of the blast wave is assumed to be uniform within the opening angle of the jet, i.e. a top hat jet model. We assume that charged particles are accelerated in the forward shock and emit synchrotron emission (Sari et al., 1998; Wijers & Galama, 1999; Granot & Sari, 2002). In this work, we do not take into account emission originating from the reverse shock and thus confine ourselves to fitting the later parts of the afterglow when the reverse shock has passed through the ejecta and the deceleration phase is over; in this limit the value of the initial Lorentz factor of the jet is no longer important and need not (indeed, cannot) be fit. For the 'microphysical' parameters, which describe the spectrum and energy content of the electrons behind the blast wave and the magnetic field in which they move, we use the customary notation: p is the power-law index of the energy distribution of the relativistic electrons, and ϵ_e and ϵ_B are the fractions of post-shock energy density in relativistic electrons and magnetic field, respectively. Only a fraction of all electrons, ξ_N, may be accelerated. When $p \simeq 2$, the total energy in electrons and the value of p become very correlated in the fit, because the blast-wave emission depends on the combination $\bar{\epsilon}_e \equiv \frac{p-2}{p-1}\epsilon_e$.

Therefore we fit for that quantity, and disentangle p and ϵ_e later where possible. Similarly, the fraction of accelerated electrons, ξ_N, is degenerate with respect to $(E_{K,\mathrm{iso}}, n_{\mathrm{ref}}, \epsilon_B, \bar{\epsilon}_e)$, where $(E_{K,\mathrm{iso}}, n_{\mathrm{ref}})$ are proportional to $1/\xi_N$, and $(\epsilon_B, \bar{\epsilon}_e)$ are proportional to ξ_N (Eichler & Waxman, 2005). Because of this degeneracy, we cannot determine ξ_N independently from afterglow light curves and fix it to the canonical value of 1 (for ease of comparison with previous studies).

We make use of the numerical model scalefit (Ryan et al. in preparation; Aksulu et al., 2020; Ryan et al., 2015). scalefit uses pre-calculated tables of spectral features (spectral breaks, peak spectral flux) for a range of different time epochs, opening angles, and observing angles. These tables are generated separately for ISM and wind-like circumburst density profiles using boxfit (van Eerten et al., 2012). boxfit is a numerical code which is able to output flux values for given observer time, frequency, and GRB parameters. The main advantage of boxfit is that the dynamics rely on pre-calculated relativistic hydrodynamic (RHD) simulations. However, since boxfit solves the radiative transfer equations during runtime, it is computationally expensive. Therefore, it is not practical to use boxfit when performing Bayesian inference. Moreover, boxfit does not take into account the effects of synchrotron cooling on the self-absorption break. This may lead to incorrect spectra in certain regimes. scalefit, on the other hand, makes use of pre-calculated spectral features, obtained from boxfit in a valid regime, and utilizes scaling rules (van Eerten & MacFadyen, 2012a) to calculate the spectra for various regimes (i.e. different orderings of the break frequencies). scalefit is valid for all spectral regimes, unlike boxfit, and is computationally inexpensive in comparison (Ryan et al. in preparation). However, scalefit makes assumptions about the sharpness of the spectra around break frequencies, whereas boxfit generates smooth spectra in a self-consistent way.

Additionally, we account for dust extinction due to the host galaxy when calculating the observed flux. For the majority of GRBs in our sample we adopt the Small Magellanic Cloud extinction curve given by Pei (1992). However, for GRBs 000418 (Gorosabel et al., 2003), 010222 (Frail et al., 2002) and 090328 (McBreen et al., 2010) we assume a Starburst type extinction curve (Calzetti et al., 2000). We include the dust extinction due to the host galaxy as a free parameter.

Summarizing, our model parameters are defined as

$$\phi = (\theta_0, E_{K,\mathrm{iso}}, n_{\mathrm{ref}}, \theta_{\mathrm{obs}}, p, \epsilon_B, \bar{\epsilon}_e, \xi_N, A_V)^T, \tag{3.8}$$

where θ_0 is the opening angle of the jet, $E_{K,\mathrm{iso}}$ is the isotropic-equivalent kinetic energy of the explosion, n_{ref} is the normalization factor for the circumburst density profile (see Equation 4.2), θ_{obs} is the observing angle, p is the power-law index of the accelerated electron population, ϵ_B is the fraction of post-shock energy in the magnetic fields, $\bar{\epsilon}_e \equiv \frac{p-2}{p-1}\epsilon_e$ where ϵ_e is the fraction of post-shock energy in the accelerated electrons, ξ_N is the fraction of electrons being accelerated, and A_V is the amount of dust extinction in the rest-frame due to the host galaxy.

Table 3.2: Assumed priors for the GP hyperparameters.

Parameter range	Prior distribution
$10^{-10} < a < 10^{10}$	log-uniform
$10^{-6} < l_1 < 1$	log-uniform
$10^{-6} < l_2 < 1$	log-uniform
$10^{-3} < \sigma_h < 10^{3}$	log-uniform

3.2.4 Regression

In order to obtain posterior distributions for the hyperparameters and model parameters, we make use of nested sampling (Skilling, 2004). Incorporating nested sampling allows us to calculate the evidence with an associated numerical uncertainty, while producing posterior samples as a byproduct. Inferring the Bayesian evidence is instrumental in this study, because it gives us a measure to determine which model explains the data best: a blast wave moving into a homogeneous ($k = 0$) or wind-like ($k = 2$) circumburst medium (see Section 3.2.3).

Following A20, we utilize pymultinest (Buchner et al., 2014), which is a PYTHON package based on the MultiNest nested sampling algorithm (Feroz et al., 2009). For all the presented results, pymultinest is used in the importance sampling mode (Feroz et al., 2019) with mode separation disabled. We use 400 initial live points and use an evidence tolerance of 0.5 as our convergence criterion.

We assume wide priors for a and σ_h, however, the length scale hyperparameters (i.e. l_1 and l_2) are capped at 1 (see Table 3.2), since we do not expect any systematics to be correlated over orders of magnitude (the GP model operates in the log-space). This is important, we found, because if one allows long correlation length scales, the GP can take up features like constant offsets between model and data, or slope differences, which the model should really be capable of fitting. We intend the Gaussian process mostly to take up issues like calibration differences between instruments leading to extra 'noise' within a band, and physical effects that are shorter in time and frequency scale than is included in the model, such as radio scintillation, minor flares, etc.

For all the model parameters we assume uninformative prior distributions, which can be seen in Table 3.3.

Note that we do not take into account any reported upper limits on the afterglow flux when inferring parameters, since upper limit reports typically do not contain enough information to include them in the fitting in a statistically sound way.

3.3 Results

In this section, we present the modelling results for our sample of 26 GRB afterglow data sets (see Table 3.1). We will not discuss individual GRBs in detail, since the objective of our work is to examine the properties of a population of GRB afterglow sources and systematics

Table 3.3: Assumed priors for the physical parameters.

Parameter range	Prior distribution
$0.01 < \theta_0 < 1.6$	log-uniform
$10^{50} < E_{K,\mathrm{iso}} < 10^{56}$	log-uniform
$10^{-3} < n_{\mathrm{ref}} < 1000$	log-uniform
$0 < \theta_{\mathrm{obs}}/\theta_0 < 2$	uniform
$1.0 < p < 3.0$	uniform
$10^{-10} < \epsilon_B < 1.0$	log-uniform
$10^{-10} < \bar{\epsilon}_e < 10$	log-uniform
$0 < A_V < 10$	uniform

of how the properties are distributed and may differ between subclasses. In so doing, we will examine correlations between each pair of fit parameters and distributions of fit parameters between each of a few subclasses. All in all, we make about 50 such comparisons, and therefore we have a fair chance of finding differences or correlations at the few percent probability level by statistical coincidence. To account for this, we will only regard correlations or differences in distributions as firmly significant when the null hypothesis of no correlation or no difference can be excluded at the single-trial p value of 3×10^{-4} or better, and tentative below $p = 1 \times 10^{-3}$. Of course, since we do not have a statistically complete sample, we should not only examine the statistical significances but also the possible effect of biases.

We find that in all cases the best-fit values of the parameters and their 68% credible intervals remain naturally contained within the range set by the priors, and in most cases this is still true for the 95% credible interval.We also find that in individual cases there can be strong correlations between parameter errors due to degeneracies in a specific fit, but we did not find any that were common enough to induce correlations between parameters in the overall population. We also find that for all physical parameters the range of best-fit values is significantly larger than the error regions of the better constrained afterglows. This implies that there are no physical parameters, specifically also not the shock microphysics parameters or the beaming-corrected energy, that prefer a universal value. This is in agreement with previous studies (e.g., Starling et al. 2008; Curran et al. 2009; Ryan et al. 2015), but now for a large and uniformly analysed sample of GRBs.

For our further description of the results, we focus on groups of physical parameters, from the outside in. We begin with the ambient density, since this is the first distinction we make, and it is made in a way somewhat different to the others, by comparing two different model fits. All others are simply free parameters fit within a certain constrained but continuous range. Of these, we first discuss the energy and geometrical parameters (opening angle and viewing angle), and after that the shock microphysics parameters.

Table 3.4: Model selection for the GRB sample. $\mathscr{Z}$ represents the Bayesian evidence. Reported uncertainties represent 1–σ. We select the mode, either homogeneous (ISM) or wind-like environment, with higher inferred evidence values. The evidence values for the preferred model are written in **bold** numerals.

	Burst name	$\ln \mathscr{Z}$ [ISM]	$\ln \mathscr{Z}$ [Wind]	Bayes factor
short GRBs	051221A	-22.79 ± 0.04	-24.26 ± 0.12	4.33
	130603B[(a)]	-21.45 ± 0.05	-21.42 ± 0.03	$\sim 1.$
	140903A	-24.97 ± 0.05	-25.73 ± 0.02	2.15
	200522A	-18.31 ± 0.03	-19.30 ± 0.02	2.68
long GRBs	970508	-99.21 ± 0.12	-92.68 ± 0.31	$> 150.$
	980703	-86.74 ± 0.02	-82.33 ± 0.06	82.80
	990510	279.21 ± 0.02	278.45 ± 0.03	2.15
	991208	-60.33 ± 0.04	-67.63 ± 0.10	$> 150.$
	991216	-5.37 ± 0.04	-4.56 ± 0.03	2.25
	000301C	37.45 ± 0.05	25.30 ± 0.12	$> 150.$
	000418	-55.09 ± 0.04	-49.81 ± 0.05	$> 150.$
	000926	28.31 ± 0.08	34.48 ± 0.04	$> 150.$
	010222	37.34 ± 0.04	31.01 ± 0.02	$> 150.$
	030329	-29.23 ± 0.01	-59.81 ± 0.05	$> 150.$
	050820A	-40.26 ± 0.74	-33.88 ± 0.05	$> 150.$
	050904	-31.20 ± 0.03	-33.30 ± 0.07	8.13
	060418	-11.55 ± 0.06	-19.19 ± 0.02	$> 150.$
	090328	-50.14 ± 0.03	-51.69 ± 0.30	4.71
	090423	-51.42 ± 0.06	-55.97 ± 0.10	94.59
	090902B	-49.39 ± 0.02	-39.78 ± 0.04	$> 150.$
	090926A	-9.68 ± 0.03	-12.24 ± 0.02	12.98
	120521C	-54.96 ± 0.06	-55.50 ± 0.09	1.70
	130427A	324.52 ± 0.08	336.86 ± 0.03	$> 150.$
	130702A	19.45 ± 0.18	8.55 ± 0.68	$> 150.$
	130907A	-135.85 ± 0.01	-141.59 ± 0.02	$> 150.$
	140304A	-60.46 ± 0.04	-57.90 ± 0.04	13.00

(a) For this data set both homogeneous and wind-like models result in similar evidence values. An ISM-type environment is preferred since this is a short GRB and no strong winds are expected due their progenitors.

3.3.1 GRB environment and ambient medium

We do not assume a priori which model, homogeneous or wind-like environment, should be chosen for a given data set. Instead, we model every data set both for homogeneous and wind-like environment models, and choose which one explains the data best. Model selection is performed by comparing the evidence values from both fits. We present the log–evidence values, along with the corresponding Bayes factors, for each modelling effort in Table 3.4. The Bayes factor, i.e. ratio of the evidence values, allows us to quantify the likelihood of the preferred model over the alternative model. A Bayes factor larger than 20 (e.g. Kass & Raftery 1995) suggests a strong preference for the selected model. 15 out 26 GRBs in our sample, all long, have a Bayes factor larger than 20, and 8 out of these GRBs show evidence for a constant density environment. Thus, if we only consider the GRBs with a strong preference, there is an approximately even split between homogeneous and wind-like environments. Starling et al. (2008) have analyzed a sample of 10 GRBs and commented on their CBM density profile. They also find that both ISM-like and wind-like environments are required to explain the observed light curves for their sample of GRBs. Curran et al. (2009) have analyzed the optical and X-ray light curves of 10 GRB afterglows, and arrived at the same conclusion. Schulze et al. (2011) have compiled a sample of 27 *Swift* detected GRBs (including one short GRB), and utilized the observed X-ray and optical afterglow emission to comment on the density profiles of their environments. They are able to determine that 18 GRBs in their sample are consistent with homogeneous environments, and 6 GRBs are consistent with wind-like environments. If we do not restrict ourselves to high Bayes factors, a slightly higher fraction of afterglows favours an ISM solution (16 out of 25, i.e., 64%).

For the short GRB sample the evidence values for both models are closer to each other. This is mainly due to the fact that short GRBs have fewer observations available, and therefore the data sets are less constraining; importantly, none of the short GRBs favour a wind environment, in agreement with the usual notion that they occur in less dense and near-uniform ISM. For short GRB 130603B, the evidence values for homogeneous and wind-like environments are consistent with each other considering the evidence uncertainty. Given that an ISM environment is a priori favoured, we chose that solution.

The wider environment of the GRB is also probed by the host extinction, A_V. This is of course biased to somewhat low values by the fact that we want well-detected optical afterglows, and for short GRBs to somewhat higher values because we need them to lie in regions of not too low density to produce a detectable afterglow. We find that more than half the afterglows have a nonzero A_V with better than 2σ significance, with no significant differences between short and long GRBs or wind and uniform ambient media.

Now that we have found the best ambient-density model for each afterglow, we will look at the other parameters, for which we take the values for the best-fit ambient medium in each case. We present our modelling results for the GRB parameters (including the rest-frame host extinction values, A_V) in Tables 3.5 and 3.6, the short and long GRB sample respectively. In Figures 3.10, 3.11 and 3.12 we present the posterior distribution for each parameter (in the form of a violin plot) together with their 68% credible intervals. The complete set of light

Table 3.5: Inferred physical parameters for the short GRB sample. Reported uncertainties represent the 68% credible interval . k represents the CBM density profile (see Equation 4.2) and is either 0 for homogeneous or 2 for wind-like environments.

	Burst name	$\log_{10}\theta_0$ [rad]	$\log_{10}E_{K,\mathrm{iso}}$ [erg]	$\log_{10}n_{\mathrm{ref}}$	$\theta_{\mathrm{obs}}/\theta_0$	p	$\log_{10}\epsilon_B$	$\log_{10}\bar{\epsilon}_e$	A_V	k
short GRBs	051221A	$-0.98^{+0.13}_{-0.17}$	$54.48^{+0.80}_{-1.69}$	$0.55^{+1.26}_{-1.80}$	$0.92^{+0.11}_{-0.29}$	$1.78^{+0.17}_{-0.10}$	$-2.40^{+0.91}_{-2.17}$	$-5.26^{+2.43}_{-1.25}$	$0.10^{+0.26}_{-0.10}$	0
	130603B	$-0.97^{+0.28}_{-0.54}$	$53.89^{+0.82}_{-1.17}$	$-1.14^{+0.59}_{-1.36}$	$0.83^{+0.13}_{-0.36}$	$2.67^{+0.25}_{-0.38}$	$-4.71^{+1.72}_{-3.85}$	$-0.98^{+0.51}_{-0.56}$	$0.74^{+0.44}_{-0.32}$	0
	140903A	$-1.15^{+0.35}_{-0.22}$	$54.58^{+0.57}_{-1.20}$	$-1.97^{+1.17}_{-0.82}$	$0.41^{+0.26}_{-0.33}$	$2.36^{+0.17}_{-0.53}$	$-7.21^{+3.58}_{-1.82}$	$-1.07^{+0.63}_{-1.98}$	$0.22^{+0.32}_{-0.22}$	0
	200522A	$-0.22^{+0.39}_{-0.31}$	$53.54^{+1.08}_{-0.78}$	$1.94^{+0.51}_{-1.48}$	$0.51^{+0.35}_{-0.20}$	$1.84^{+0.06}_{-0.06}$	$-7.75^{+1.89}_{-1.27}$	$-3.39^{+1.32}_{-1.33}$	$5.29^{+2.79}_{-3.33}$	0

Table 3.6: Inferred physical parameters for the long GRB sample. Reported uncertainties represent the 68% credible interval . k represents the CBM density profile (see Equation 4.2) and is either 0 for homogeneous or 2 for wind-like environments.

	Burst name	$\log_{10}\theta_0$ [rad]	$\log_{10}E_{K,\mathrm{iso}}$ [erg]	$\log_{10}n_{\mathrm{ref}}$	$\theta_{\mathrm{obs}}/\theta_0$	p	$\log_{10}\epsilon_B$	$\log_{10}\bar{\epsilon}_e$	A_V	k
long GRBs	970508	$0.06^{+0.03}_{-0.05}$	$53.20^{+0.22}_{-0.21}$	$2.18^{+0.11}_{-0.14}$	$1.08^{+0.04}_{-0.03}$	$2.57^{+0.05}_{-0.05}$	$-4.39^{+0.38}_{-0.27}$	$-0.49^{+0.05}_{-0.09}$	$0.13^{+0.07}_{-0.05}$	2
	980703	$-0.34^{+0.26}_{-0.20}$	$52.28^{+0.36}_{-0.19}$	$0.50^{+0.25}_{-0.30}$	$0.89^{+0.16}_{-0.55}$	$2.07^{+0.05}_{-0.10}$	$-0.53^{+0.43}_{-0.57}$	$-1.89^{+0.20}_{-0.17}$	$1.01^{+0.16}_{-0.12}$	2
	990510	$-1.16^{+0.03}_{-0.05}$	$52.99^{+0.11}_{-0.08}$	$-0.95^{+0.15}_{-0.35}$	$0.31^{+0.13}_{-0.07}$	$1.93^{+0.06}_{-0.05}$	$-1.25^{+0.42}_{-0.45}$	$-1.54^{+0.09}_{-0.12}$	$0.01^{+0.02}_{-0.01}$	0
	991208	$-1.94^{+0.19}_{-0.06}$	$54.64^{+0.10}_{-0.41}$	$-0.60^{+0.19}_{-0.11}$	$1.05^{+0.41}_{-0.82}$	$1.61^{+0.08}_{-0.06}$	$-0.07^{+0.07}_{-0.16}$	$-1.33^{+0.12}_{-0.11}$	$0.44^{+0.09}_{-0.08}$	0
	991216	$-0.59^{+0.37}_{-0.25}$	$53.71^{+0.23}_{-0.44}$	$1.28^{+0.23}_{-0.52}$	$0.79^{+0.14}_{-0.41}$	$2.14^{+0.20}_{-0.08}$	$-3.61^{+0.54}_{-0.82}$	$-1.27^{+0.23}_{-0.23}$	$0.07^{+0.11}_{-0.06}$	2
	000301C	$-0.69^{+0.03}_{-0.03}$	$52.42^{+0.16}_{-0.08}$	$0.33^{+0.47}_{-0.11}$	$0.07^{+0.04}_{-0.07}$	$1.88^{+0.10}_{-0.06}$	$-0.21^{+0.14}_{-0.78}$	$-1.52^{+0.19}_{-0.07}$	$0.03^{+0.08}_{-0.02}$	0
	000418	$-0.26^{+0.27}_{-0.29}$	$54.47^{+1.00}_{-0.82}$	$1.11^{+0.70}_{-1.12}$	$0.26^{+0.28}_{-0.20}$	$2.38^{+0.15}_{-0.18}$	$-1.91^{+0.52}_{-4.22}$	$-1.59^{+0.45}_{-0.50}$	$1.22^{+0.40}_{-0.29}$	2
	000926	$-0.24^{+0.31}_{-0.28}$	$55.13^{+0.63}_{-0.46}$	$1.99^{+0.79}_{-0.39}$	$0.34^{+0.20}_{-0.33}$	$2.96^{+0.04}_{-0.04}$	$-6.21^{+1.51}_{-1.08}$	$-0.95^{+0.34}_{-0.28}$	$0.20^{+0.05}_{-0.04}$	2
	010222	$-0.40^{+0.05}_{-0.22}$	$53.94^{+0.17}_{-0.15}$	$-2.32^{+0.19}_{-0.17}$	$0.13^{+0.29}_{-0.09}$	$2.62^{+0.03}_{-0.04}$	$-4.18^{+0.52}_{-0.31}$	$-0.47^{+0.06}_{-0.08}$	$0.54^{+0.05}_{-0.05}$	0
	030329	$0.20^{+0.01}_{-0.07}$	$53.04^{+0.10}_{-0.10}$	$2.59^{+0.20}_{-0.18}$	$0.73^{+0.05}_{-0.05}$	$2.62^{+0.02}_{-0.06}$	$-5.58^{+0.38}_{-0.33}$	$-0.76^{+0.08}_{-0.06}$	$0.01^{+0.02}_{-0.01}$	0
	050820A	$-0.44^{+0.24}_{-0.21}$	$53.24^{+0.12}_{-0.11}$	$0.95^{+0.23}_{-0.16}$	$0.70^{+0.10}_{-0.39}$	$2.11^{+0.14}_{-0.07}$	$-1.95^{+0.19}_{-0.49}$	$-1.31^{+0.25}_{-0.18}$	$0.37^{+0.06}_{-0.08}$	2
	050904	$-1.02^{+0.12}_{-0.04}$	$53.31^{+0.28}_{-0.17}$	$1.05^{+0.25}_{-0.87}$	$0.54^{+0.21}_{-0.13}$	$2.11^{+0.08}_{-0.08}$	$-2.07^{+0.50}_{-0.46}$	$-1.54^{+0.13}_{-0.40}$	$0.07^{+0.05}_{-0.03}$	0
	060418	$-0.82^{+0.06}_{-0.07}$	$52.88^{+0.17}_{-0.14}$	$0.23^{+0.56}_{-0.36}$	$0.83^{+0.05}_{-0.06}$	$2.28^{+0.06}_{-0.04}$	$-2.81^{+0.32}_{-0.65}$	$-1.30^{+0.17}_{-0.13}$	$0.17^{+0.05}_{-0.05}$	0
	090328	$-0.68^{+0.20}_{-0.13}$	$53.17^{+0.51}_{-0.86}$	$1.66^{+0.70}_{-0.79}$	$0.94^{+0.23}_{-0.33}$	$2.28^{+0.10}_{-0.18}$	$-3.90^{+1.31}_{-0.89}$	$-1.39^{+0.48}_{-0.37}$	$0.07^{+0.11}_{-0.06}$	0
	090423	$-0.06^{+0.26}_{-0.10}$	$53.46^{+0.50}_{-0.48}$	$2.01^{+0.75}_{-0.62}$	$0.84^{+0.11}_{-0.46}$	$2.16^{+0.17}_{-0.24}$	$-4.81^{+1.48}_{-0.97}$	$-1.41^{+0.35}_{-0.56}$	$0.09^{+0.09}_{-0.07}$	0
	090902B	$0.04^{+0.11}_{-0.34}$	$53.43^{+0.23}_{-0.37}$	$0.50^{+0.58}_{-0.31}$	$0.24^{+0.19}_{-0.22}$	$2.23^{+0.04}_{-0.09}$	$-3.15^{+0.70}_{-0.91}$	$-1.57^{+0.29}_{-0.23}$	$0.07^{+0.06}_{-0.06}$	2
	090926A	$-0.81^{+0.08}_{-0.10}$	$53.09^{+1.17}_{-0.32}$	$0.19^{+2.07}_{-0.26}$	$0.78^{+0.25}_{-0.14}$	$2.24^{+0.08}_{-0.05}$	$-1.57^{+0.41}_{-2.14}$	$-0.93^{+0.28}_{-0.81}$	$0.09^{+0.01}_{-0.01}$	0
	120521C	$-0.91^{+0.11}_{-0.11}$	$52.98^{+0.23}_{-0.16}$	$-0.47^{+0.41}_{-0.29}$	$0.50^{+0.20}_{-0.34}$	$2.88^{+0.12}_{-0.25}$	$-1.10^{+0.37}_{-0.51}$	$-0.84^{+0.16}_{-0.16}$	$0.78^{+0.09}_{-0.09}$	0
	130427A	$-0.23^{+0.25}_{-0.15}$	$52.58^{+0.64}_{-0.17}$	$0.17^{+0.33}_{-0.53}$	$0.20^{+0.34}_{-0.20}$	$2.16^{+0.04}_{-0.05}$	$-2.31^{+0.62}_{-0.94}$	$-1.13^{+0.20}_{-0.25}$	$0.03^{+0.03}_{-0.03}$	2
	130702A	$-0.71^{+0.12}_{-0.05}$	$53.07^{+0.90}_{-0.97}$	$-0.90^{+1.42}_{-0.45}$	$0.04^{+0.11}_{-0.04}$	$1.46^{+0.08}_{-0.04}$	$-0.71^{+0.63}_{-1.24}$	$-7.65^{+2.05}_{-1.89}$	$0.26^{+0.18}_{-0.12}$	0
	130907A	$-1.38^{+0.17}_{-0.05}$	$53.02^{+0.34}_{-0.09}$	$-1.26^{+0.12}_{-0.11}$	$0.88^{+0.23}_{-0.21}$	$1.87^{+0.09}_{-0.09}$	$-0.04^{+0.04}_{-0.10}$	$-1.03^{+0.14}_{-0.18}$	$1.60^{+0.15}_{-0.16}$	0
	140304A	$-1.30^{+0.23}_{-0.07}$	$54.46^{+0.28}_{-0.42}$	$1.96^{+0.57}_{-0.35}$	$1.19^{+0.34}_{-0.13}$	$2.28^{+0.17}_{-0.25}$	$-3.73^{+0.76}_{-0.72}$	$-1.40^{+0.20}_{-0.33}$	$0.41^{+0.11}_{-0.08}$	2

curves and posterior distributions are available as online supplementary material, including results for both homogeneous and wind-like environments for each GRB in our sample.

3.3.2 Energy, opening angle, and viewing angle

In Figures 3.1 and 3.2 we present the parameter values for the GRBs associated with homogeneous and wind-like environments, respectively, in the form of a corner plot. These figures help us to identify any correlations between the burst parameters. The diagonal elements in each figure contain the parameter distributions for the single fit parameters, with different colours for the short (green), long-ISM (blue) and long-wind (red) GRBs.

Opening angle: We do not find a notably different opening angle distribution for short and long GRBs. When a Kolmogorov-Smirnov (KS) test is performed on the inferred opening angle of ISM-like long GRBs and short GRBs, we find a p value of 0.48 for the hypothesis that the two samples are drawn from the same distribution. A KS test checking the consistency of the θ_0 distribution between ISM- and wind-like long GRBs yields we find $p = 0.012$. On its own that might be considered moderate evidence for a difference, but given the many trials (distribution comparisons) in this paper, it is not (see above).

Observer viewing angle: The distribution of the observer viewing angle, $\theta_{\rm obs}$, does not follow a simple form, since it is constrained to be within the jet opening angle (at least at early times), but that is different for each GRB as we have just seen. However, the fractional observer angle distribution, $\theta_{\rm obs}/\theta_0$, does have a simpler form under the top-hat jet assumption, because in that case every direction within the opening angle has the same properties and thus the same brightness at early times: its probability density is linear for $\theta_0 \ll \pi/2$ and a sine function for $\theta_0 = \pi/2$. We show the distribution for the full sample in Figure 3.3, with the two limiting theoretical cases. The observed distribution extends a bit beyond 1, but no values are significantly larger than 1. Even so, KS-comparison with the theoretical distributions gives $p = 0.17$ for accepting the null hypothesis of equality. We conclude that the data are consistent with the top-hat jet hypothesis and do not strongly indicate a structured, more centrally concentrated jet (which would closely resemble a top-hat jet for observers close to the jet axis in any case, e.g., Dalal et al. 2002; Rossi et al. 2002, 2004; Granot & Kumar 2003; Kumar & Granot 2003; Panaitescu & Kumar 2003; Salmonson 2003; Ryan et al. 2020). However, this does argue against the opening angle of the prompt γ-ray emission being significantly narrower than that of the afterglow emission, since all our GRBs are gamma-ray selected, and thus a wider afterglow opening angle would lead to small values of $\theta_{\rm obs}/\theta_0$. This may argue against, or at least significantly constrain so-called 'jet-cocoon' models of GRBs, in which a core jet with quite high initial Lorentz factors ($\Gamma_0 \gtrsim 100$) is surrounded by an energetic cocoon with Lorentz factors of several tens (e.g., Ramirez-Ruiz et al. 2002; Peng et al. 2005). The initial conditions of the simulations underlying our model are already outside the progenitor object. We do not think our afterglow selection has biased us against jet-cocoon cases: if the cocoon only decelerated after our afterglow data start, it would give rise to a late-injection or plateau phase in the afterglow (Granot & Kumar, 2006; van Eerten, 2014), and we have not excluded any afterglows for obvious signs thereof. If the

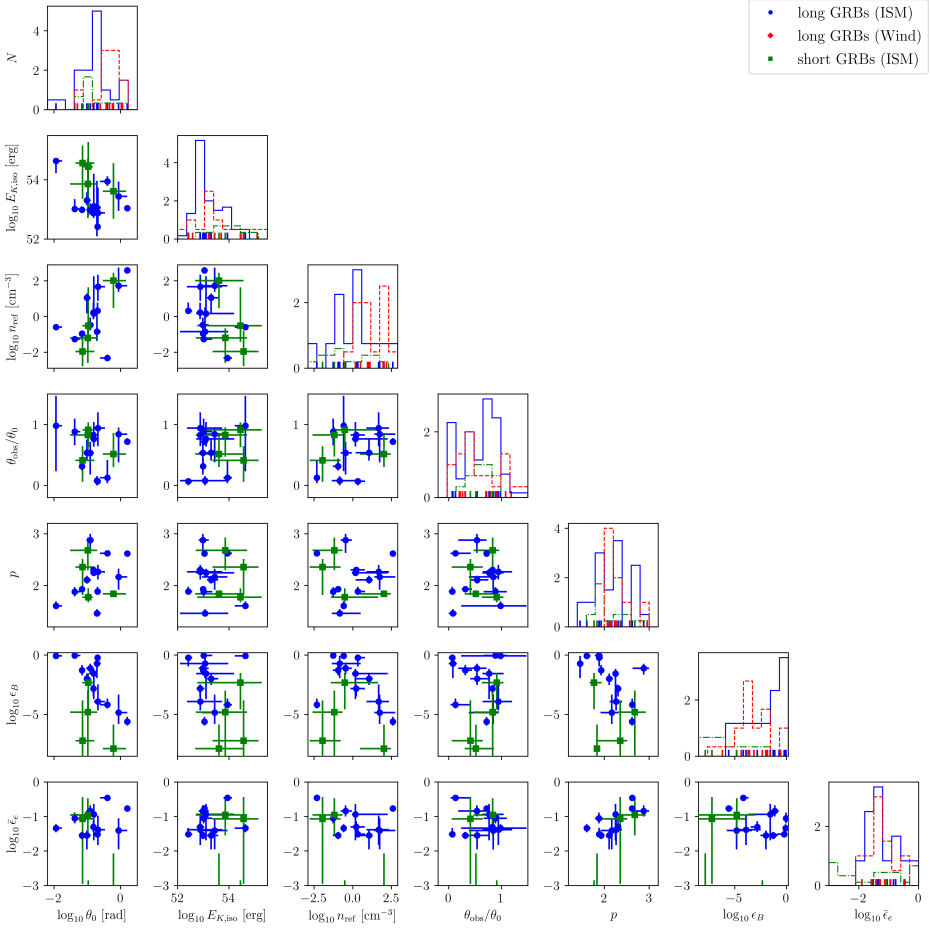

Figure 3.1: Corner plot for the inferred physical parameters of the GRBs associated with constant density environments. Blue circles and green squares represent the inferred parameter value of long GRBs and short GRBs, respectively. The error bars represent the 68% credible limit.

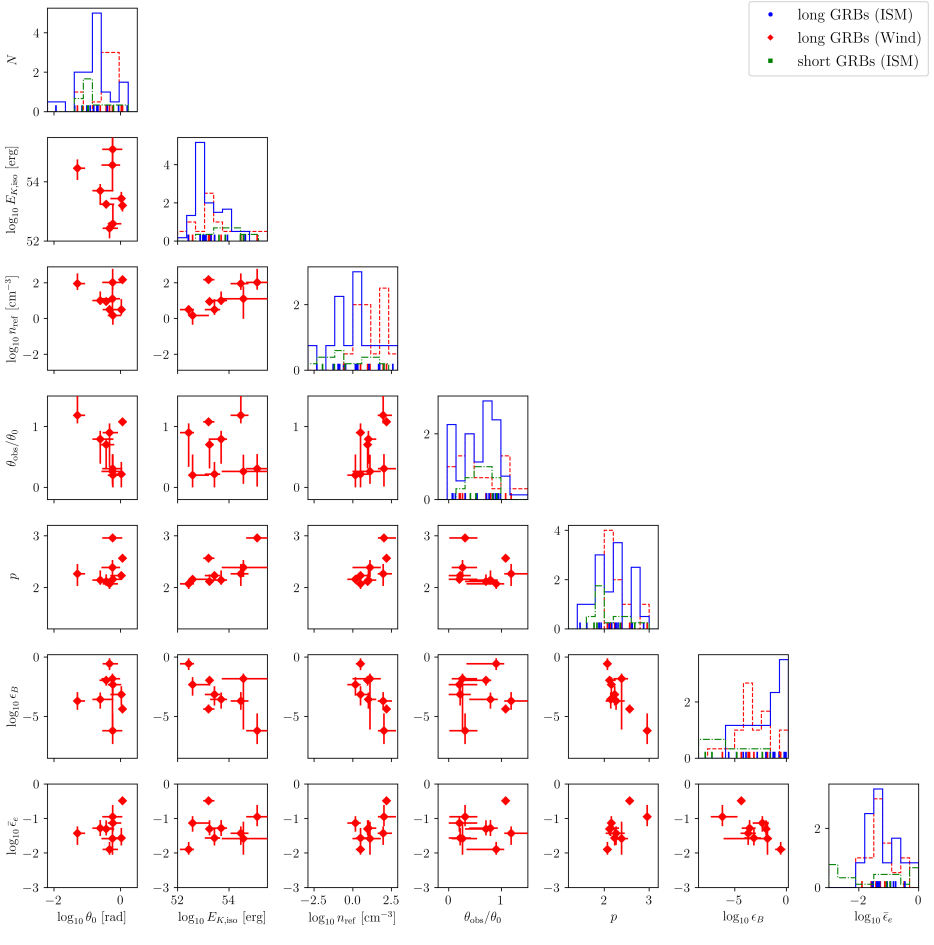

Figure 3.2: Corner plot for the inferred physical parameters of the GRBs associated with wind-like environments. The error bars represent the 68% credible limit.

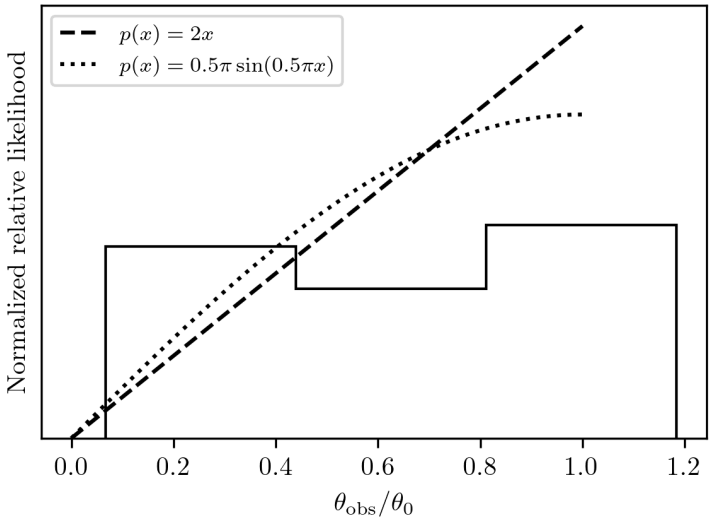

Figure 3.3: Histogram of the inferred $\theta_{\rm obs}/\theta_0$ for the GRB sample. The dotted line represents the analytically expected probability density function for large opening angles ($\theta_0 = \pi/2$ rad), whereas the dashed line represents the probability density function for small opening angles ($\theta_0 \ll \pi/2$ rad).

cocoon decelerated before our afterglow data start, then the tendency to smaller observer angles because of the gamma-ray selection would remain, and we do not see this.

The results on the GRB energy are more complex, and we defer them to the discussion section.

3.3.3 Shock physics parameters

For the shock physics parameters we have to be a bit careful (see Section 3.2.3): in order to avoid too strong degeneracies for $p \simeq 2$, we fit for p and $\bar{\epsilon}_e$, and indeed we do find some cases of $p < 2$. The distribution of p, the power-law index of the shock-accelerated particles, can be seen in Figure 3.4. We find that the p-values are consistent with being drawn from the same distribution for long GRBs and short GRBs. We find a mean value of 2.21 and standard deviation $\sigma_p = 0.36$ for the inferred p values. Curran et al. (2010) have analyzed a large sample of *Swift* detected GRBs to determine the distribution of p. They utilized the reported spectral indices in X rays to determine the p values of their sample, using closure relations. They find that the distribution of p is consistent with a Gaussian distribution with $\mu = 2.36$ and $\sigma = 0.59$; given the errors in both methods, we consider the two results to be consistent. We find three cases where p is significantly less than 2, and thus where a high-energy cutoff to the electron distribution is required to keep the total electron energy finite. In more than half the cases (15), $p = 2$ is included within the 95% confidence region of the fit result, implying that indeed using $\bar{\epsilon}_e$ is required to avoid problems in the fitting process.

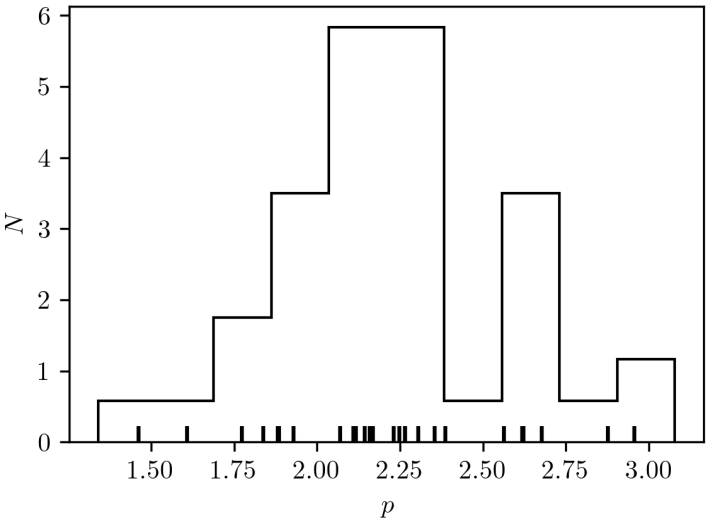

Figure 3.4: Histogram of the inferred p for the GRB sample.

While the short GRBs all have ϵ_B values on the low side, their small number and large error bars prevent us from drawing any strong conclusions in this respect: the KS test results in $p = 0.10$ for the short/long GRB distributions of magnetic-field energy fractions being the same, and similarly we find no evidence for a difference between the long GRBs in ISM and wind environments. What is quite striking though is that ϵ_B ranges over 5–6 decades in value, a much greater range than ϵ_e.

Since ϵ_e is a physically more meaningful measure of the electron energy density, we derive it from the nominal fit values in case $p > 2$. The derived ϵ_e values can be seen in Tables 3.7 and 3.8. In Figure 3.5 we present the ϵ_e distribution of the GRB sample, only for GRBs with inferred mode value of $p > 2$. We find that ϵ_e is never very low and always above 0.1, with some values close to 1. The values for the different subsamples are in good agreement (mean values are 0.34 for homogeneous environment and 0.28 for wind). Beniamini & van der Horst (2017) have demonstrated that it is possible to constrain ϵ_e by measuring the peak flux and peak time of the radio afterglow light curve. By applying this method to a sample of 36 long GRBs, they were able to put upper limits on the scatter of ϵ_e. They find that $\sigma_{\log_{10}\epsilon_e} < 0.31$ for constant density environments, and $\sigma_{\log_{10}\epsilon_e} < 0.26$ for wind-like environments. We find that the standard deviation of ϵ_e for the long GRB sample is $\sigma_{\log_{10}\epsilon_e} = 0.24$ for homogeneous environments and $\sigma_{\log_{10}\epsilon_e} = 0.28$ for wind-like environments. Note that, although the standard deviations of the inferred ϵ_e distributions are consistent with Beniamini & van der Horst (2017), they find lower mean values of 0.15 and 0.13 for ISM-like and wind-like long GRBs, respectively.

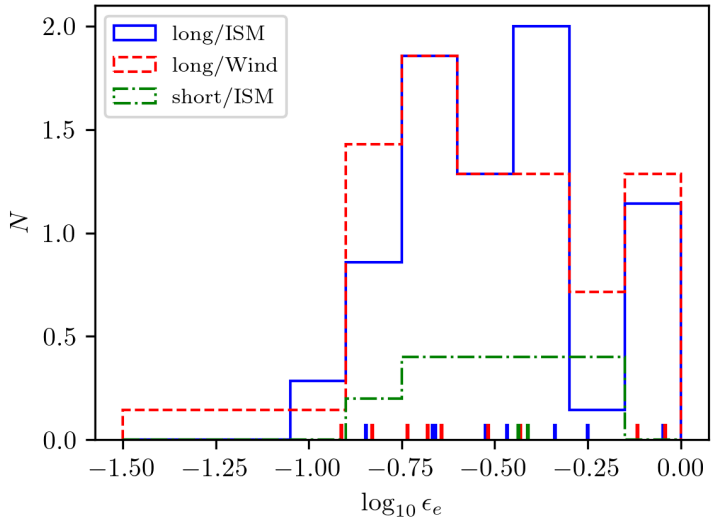

Figure 3.5: Histogram of the inferred ϵ_e for the GRB sample.

3.4 Discussion

3.4.1 GRB environment and ambient medium

The inferred CBM densities for ISM-like long and short GRBs exhibit a wide distribution. The mean value for the circumburst densities of ISM-like long and short GRBs are 1.26 and 0.39 cm^{-3} with standard log-deviations of $\sigma_{\log_{10} n_{\mathrm{ref}}} = (1.32, 1.49)$, respectively, i.e., they cover about 3 decades in density. Given the wide variety of possible massive-star and merger environments, this is not so surprising.

We do not find any pronounced differences between the density distributions for short GRBs and ISM-like long GRBs. Canonically, it is expected that short GRB progenitors should be in lower-density environments than long GRBs. Fong & Berger (2013) report that short GRBs are localized to lie at greater distances from their host galaxy centres when compared to long GRBs. They find that, for short GRBs, the median value of the offset from their galaxian centre is 4.5 kpc, and when compared to the size of their host galaxy the median value of the offset becomes $r/r_{\mathrm{host}} = 1.5$. Note that there is a strong bias in our short GRB sample because we require bright afterglows, and afterglow brightness goes up strongly with ambient density. And indeed, if we check our four short GRBs we find that their environment is quite atypical for the short GRB population: studies of the host galaxies of our four short GRBs show that they do not have a large offset from their host centre. GRB 051221A has been identified to lie in a star-forming galaxy with an estimated normalized offset of $r/r_{\mathrm{host}} = 0.29 \pm 0.04$ (Soderberg et al., 2006). GRB 130603B is associated with a spiral galaxy, and has been localized to a tidally disrupted arm at a distance of 5.4 ± 0.3 kpc from the centre

of the galaxy (de Ugarte Postigo et al., 2014). Troja et al. (2016) find that GRB 140903A lies at a distance of 0.5 ± 0.2 kpc from the centre of its host. Fong et al. (2021) estimate a normalized offset of $r/r_{\rm host} = 0.24 \pm 0.04$ for GRB 200522A. This is quite unlike the full population: Fong et al. (2015) have studied the afterglow emission from a sample of 38 short GRBs and have found that they lie in low-density environments with median densities of $(3\text{–}15) \times 10^{-3}$ cm^{-3}. They also state that 80 to 95% of short GRBs in their sample have densities smaller than 1 cm^{-3}, which is also true for 3 out of 4 GRBs in our short GRB sample within the reported uncertainties. O'Connor et al. (2020) have utilized the X-ray light curves of the *Swift* population of short GRBs to constrain their circumburst environment densities. They assumed fiducial values for the GRB parameters and have found that $\lesssim 16\%$ of the population have densities lower than 10^{-4} cm^{-3}, and that $\gtrsim 30\%$ of the population has densities larger than 10^{-2} cm^{-3}. In other words, our requirement of a well-detected and well-sampled afterglow does seem to have biased our short GRBs to lie in regions similar to those of long GRBs. This means they are not very representative of the whole population of short GRBs. There may be a silver lining to this cloud, in that when discussing their physical parameters in comparison to long GRBs, we can eliminate strong fit-induced correlations with environmental parameters as a potential cause for any differences we find. Also, under the most likely scenario that short GRBs are all mergers, born from a binary long before the merger time, there is no reason to think that the physical properties of the merger and GRB explosion would depend on the medium they happen to be in at the time of merger. Hence, we do not think that this environmental bias makes our GRB sample biased relative to the whole short GRB population in intrinsic parameters.

It would be good again to caution, now quantitatively, that for $k = 0$, the radius of the blast wave scales with observer time as $r \propto t^{1/4}$, which means observations do not cover a wide range of radii. The afterglow starts at the deceleration radius, $r_{\rm dec}$, where half the initial jet energy has been deposited, and transitions into a spherical supernova remnant-like evolution at the non-relativistic radius $r_{\rm NR}$. For typical values these are just under 10^{17} cm and 10^{18} cm, respectively, both scaling as $(E/n)^{1/3}$. Their ratio is $r_{\rm NR}/n_{\rm dec} = 20(\Gamma_0/100)^{-2/3}$, where Γ_0 is the initial jet Lorentz factor. Given that we have few examples where we get close to either end of these regimes, we see that indeed the typical uniform-like afterglow covers only a small range of radii. Therefore, approximate uniformity of the ambient medium is enough, which may apply to many plausible environments.

For long GRBs in wind-like environments, the distribution of $n_{\rm ref}$ has a mean of 14 cm^{-3}, or a mean A value of $0.48\,A_*$, with a standard log-deviation of $\sigma_{\log_{10} n_{\rm ref}} = 0.69$, rather narrower than the density range of the total sample. This indicates that the free-wind parameters we find are indeed similar to canonical values expected of massive Wolf-Rayet stars, the most likely progenitors. It might argue that the likeliest reason for seeing uniform media about equally often is that the reverse shock in the stellar-wind bubble is close enough that in many cases the main afterglow phase is in the shocked wind. For the free-wind case, $r \propto t^{1/2}$, so the afterglow samples a markedly larger range of radii. For canonical values ($\dot{M} = 10^{-5}\,{\rm M}_\odot$/yr, $E = 10^{52}$ erg, $\Gamma_0 = 100$) we find $r_{\rm dec} = 1.5 \times 10^{11}$ cm and $r_{\rm NR} = 1.5 \times 10^{15}$ cm, and since they again scale the same with most parameters, $r_{\rm NR}/r_{\rm dec} = 10^4(\Gamma_0/100)^2$, a large

range indeed even if we see only part of it sampled in the data. Note that for a canonical wind velocity of 1000 km/s, the afterglow phase starts in the wind material that was emitted *less than one hour before the star explodes*, and even in weak winds typically still less than one day. It ends in wind material that was emitted a fraction of a year to a few years before the explosion. GRB afterglows thus do not probe typical mean-life stellar wind parameters, and indicate that even very close to the end of the star's life the wind is similar to that during an average moment in its life. We note that some, especially single-star, GRB scenarios prefer low mass loss rates of the progenitors, and it is known that in low-metallicity environments massive stars do indeed have lower mass loss rates (Vink et al., 2001; Vink & de Koter, 2005); since we find that $A/A_* = 0.48$ on average, our fits do not provide evidence for this. This may agree will with more recent findings that GRBs actually do not prefer low-metallicity environments, other than that they are suppressed in regions with metallicity above solar (Perley et al., 2016; Fynbo et al., 2009, , and references therein). This in turn may favour binary evolution scenarios for the origin of long GRBs (Perley et al., 2016).

These ambient-medium considerations ask for better investigation of scenarios in which the blast wave emerges from the free wind early, since in light of the above this appears difficult, and yet we find half or more of the afterglow fits prefer a uniform-medium solution.

3.4.2 Energy and opening angle

The observed flux of GRB afterglow emission does not directly depend on the true energy of the burst, but rather depends directly on the energy per unit solid angle, or the isotropic equivalent energy, $E_{\rm iso}$. Therefore, to measure the true energetics of these events by afterglow modelling, we need to constrain both the isotropic equivalent energy and the opening angle. The true energy can then be calculated using

$$E_{\rm true} = E_{\rm iso}(1 - \cos\theta_0). \tag{3.9}$$

This equation is valid for both the total energy and for the γ-ray and afterglow kinetic energies separately, provided that the opening of both is the same; we have argued above (Sect. 3.3.2) that this is indeed the case.

In A20, we suggested the existence of a common kinetic energy reservoir for long GRBs, based on a very small sample of only 5 GRBs. For the larger sample in this work, where we have also allowed both wind and ISM ambient media, this no longer holds: in Figure 3.6, we present the inferred isotropic equivalent kinetic energies and opening angles of our long GRB sample. We perform a KS test on the nominal best-fit values for each GRB to determine whether or not the $E_{K,\rm true}$ values for homogeneous and wind-like GRBs are drawn from the same distribution. We find that we can reject the null hypothesis with a p-value of 6.5×10^{-3}, which according to our strict criteria is not significant enough. However, this does not do full justice to the modeling results, since the different GRBs have very different errors on the parameters. So as a potentially more discerning test, we fit for $E_{K,\rm true}$ for GRBs in ISM and wind-like environments separately using the relation in Equation 3.9. The posterior samples of fits results for both groups are shown in Figure 3.6, and do not overlap at all.

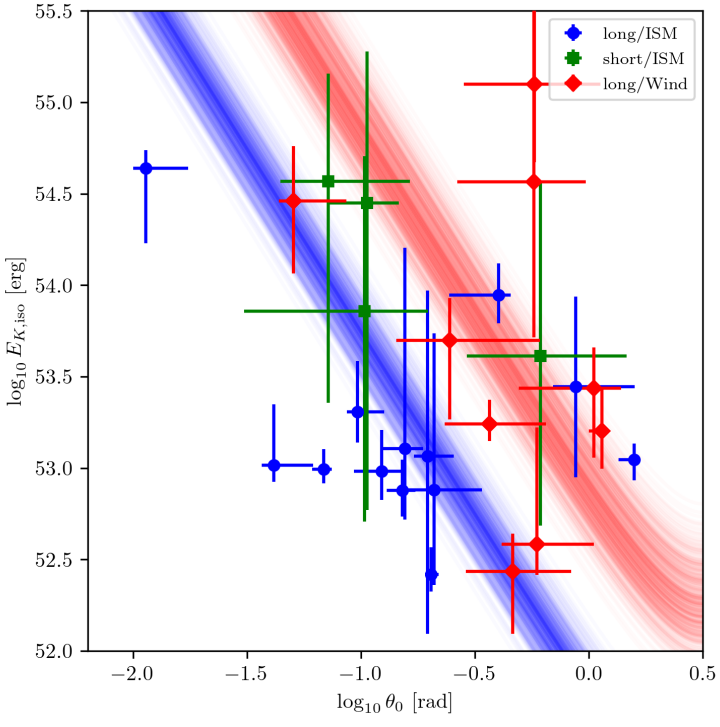

Figure 3.6: Scatter plot of θ_0 and $E_{K,\mathrm{iso}}$ parameters for the long GRB sample. The blue circles and red diamonds represent long GRBs in homogeneous and wind-like environments, respectively. Error bars represent the 68% credible interval. The blue and red lines represent the best-fit results from 500 "iso-energy" curve, $E_{K,\mathrm{iso}} = E_{\mathrm{true}}/(1-\cos\theta_0)$, fits to the inferred parameters. For each fit we sample values from the posterior distribution of the parameters. We find $E_{K,\mathrm{true}} = 2.73^{+0.82}_{-0.77} \times 10^{51}$ for ISM-like long GRBs and $E_{K,\mathrm{true}} = 3.38^{+1.66}_{-1.17} \times 10^{52}$ erg for wind-like long GRBs.

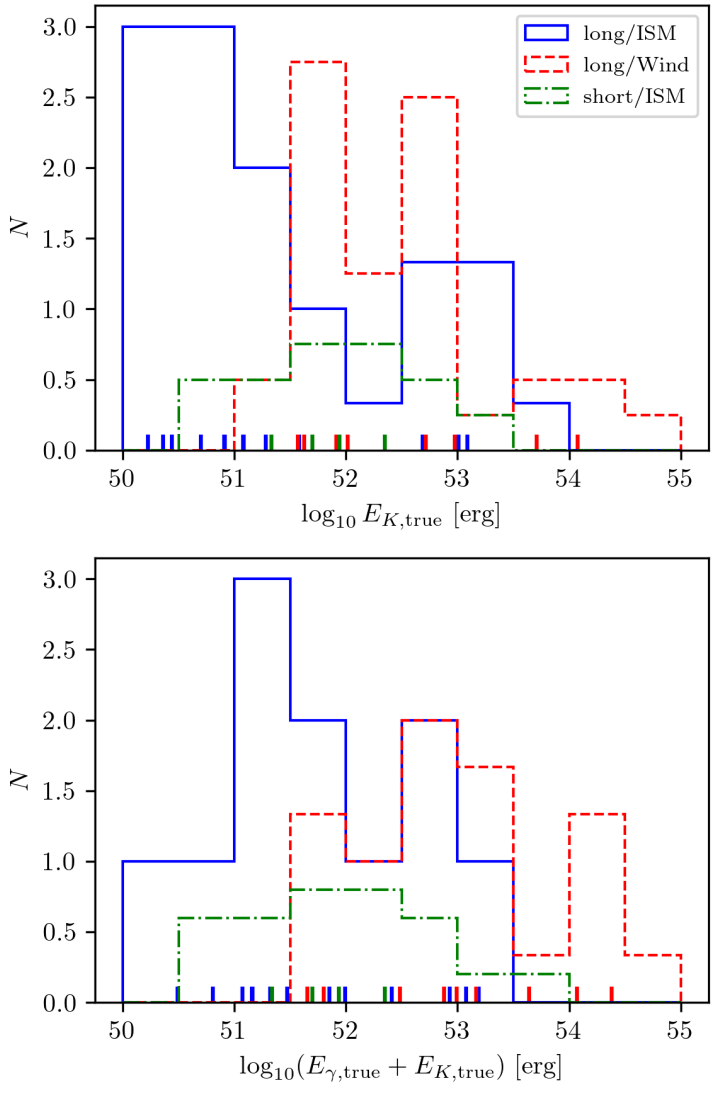

Figure 3.7: Histogram of the inferred energetics for the GRB sample. The upper and lower panels show the histograms for the $E_{K,\mathrm{true}}$ and E_{true} distributions, respectively.

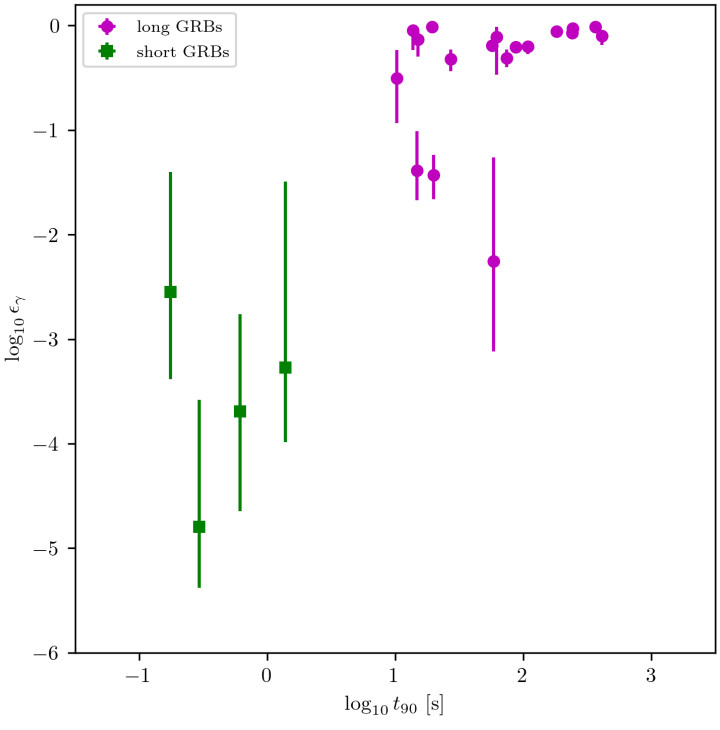

Figure 3.8: Scatter plot of the reported t_{90} and derived ϵ_γ parameters for the short and long GRB sample. The magenta circles and green squares represent long and short GRBs, respectively. Error bars represent the 68% credible interval.

We therefore find that GRBs in wind-like environment are significantly more energetic, with an average $E_{K,\mathrm{true}} = 3.38^{+1.66}_{-1.17} \times 10^{52}$ erg, than GRBs in homogeneous environments with an average $E_{K,\mathrm{true}} = 2.73^{+0.82}_{-0.77} \times 10^{51}$ erg. The histograms of the true kinetic and total energies of the three sub-samples are shown in Figure 3.7. While these again have the disadvantage of making use only of the nominal fit values of the energies rather than all the information in the posterior distribution, they do illustrate some difference between the wind- and ISM-like long GRBs.

The $E_{K,\mathrm{true}}$ distributions for long and short GRBs are consistent with each other. This suggests that the kinetic energy of the explosion is not significantly different between short and long GRBs. However, the measured prompt emission energies are orders of magnitudes lower for short GRBs, which implies that it is the prompt emission efficiency of short GRBs that is lower. The prompt emission efficiency can be defined as

$$\epsilon_\gamma \equiv \frac{E_{\gamma,\mathrm{true}}}{E_{\gamma,\mathrm{true}} + E_{K,\mathrm{true}}}. \tag{3.10}$$

Table 3.7: Derived parameters for the GRB sample. Reported uncertainties represent the 68% credible interval. We calculate ϵ_e values only for GRBs for which the inferred mode of p is larger than 2. Missing values are represented by -. k represents the CBM density profile (see Equation 4.2) and is either 0 for homogeneous or 2 for wind-like environments.

	Burst name	$\log_{10}\epsilon_e$	$\log_{10}E_{K,\mathrm{true}}$ [erg]	$\log_{10}E_{\gamma,\mathrm{true}}$ [erg]	$\log_{10}E_{\mathrm{true}}$ [erg]	$\log_{10}\epsilon_\gamma$	k
short GRBs	051221A	-	$51.33^{+1.45}_{-1.00}$	$48.93^{+0.28}_{-0.35}$	$51.34^{+1.44}_{-0.99}$	$-3.27^{+1.78}_{-0.71}$	0
	130603B	$-0.44^{+0.35}_{-0.39}$	$51.70^{+1.31}_{-1.31}$	$49.05^{+0.58}_{-1.03}$	$51.70^{+1.31}_{-1.30}$	$-2.55^{+1.15}_{-0.84}$	0
	140903A	$-0.41^{+0.29}_{-0.31}$	$51.94^{+0.64}_{-1.20}$	$47.19^{+0.72}_{-0.42}$	$51.94^{+0.64}_{-1.20}$	$-4.79^{+1.21}_{-0.58}$	0
	200522A	-	$52.35^{+1.36}_{-0.72}$	$49.19^{+0.71}_{-0.61}$	$52.35^{+1.45}_{-0.63}$	$-3.69^{+0.93}_{-0.95}$	0
long GRBs	970508	$-0.04^{+0.04}_{-0.08}$	$52.98^{+0.15}_{-0.18}$	$51.55^{+0.06}_{-0.10}$	$52.99^{+0.14}_{-0.18}$	$-1.43^{+0.20}_{-0.23}$	2
	980703	$-0.68^{+0.23}_{-0.29}$	$51.57^{+0.22}_{-0.43}$	$51.86^{+0.50}_{-0.40}$	$51.80^{+0.65}_{-0.13}$	$-0.10^{+0.04}_{-0.09}$	2
	990510	-	$50.36^{+0.12}_{-0.12}$	$50.62^{+0.07}_{-0.10}$	$50.81^{+0.09}_{-0.09}$	$-0.19^{+0.03}_{-0.04}$	0
	991208	-	$50.44^{+0.05}_{-0.04}$	$49.16^{+0.37}_{-0.11}$	$50.49^{+0.04}_{-0.04}$	$-1.32^{+0.38}_{-0.09}$	0
	991216	$-0.52^{+0.29}_{-0.16}$	$52.02^{+0.79}_{-0.61}$	$52.30^{+0.78}_{-0.47}$	$52.48^{+0.72}_{-0.54}$	$-0.13^{+0.07}_{-0.17}$	2
	000301C	-	$50.70^{+0.21}_{-0.08}$	$50.97^{+0.07}_{-0.05}$	$51.16^{+0.10}_{-0.05}$	$-0.20^{+0.04}_{-0.05}$	0
	000418	$-0.91^{+0.43}_{-0.56}$	$53.71^{+0.70}_{-1.27}$	$52.17^{+0.49}_{-0.61}$	$53.64^{+0.77}_{-1.07}$	$-1.60^{+1.05}_{-0.66}$	2
	000926	$-0.64^{+0.39}_{-0.22}$	$54.08^{+0.72}_{-0.72}$	$52.66^{+0.59}_{-0.56}$	$54.07^{+0.69}_{-0.72}$	$-1.66^{+0.40}_{-0.66}$	2
	010222	$-0.05^{+0.05}_{-0.07}$	$52.68^{+0.26}_{-0.37}$	$52.81^{+0.10}_{-0.43}$	$52.93^{+0.31}_{-0.25}$	$-0.31^{+0.08}_{-0.09}$	0

Table 3.8: Continuation of Table 3.7.

	Burst name	$\log_{10}\epsilon_e$	$\log_{10}E_{K,\mathrm{true}}$ [erg]	$\log_{10}E_{\gamma,\mathrm{true}}$ [erg]	$\log_{10}E_{\mathrm{true}}$ [erg]	$\log_{10}\epsilon_\gamma$	k
long GRBs	030329	$-0.34^{+0.07}_{-0.06}$	$53.01^{+0.10}_{-0.18}$	$52.22^{+0.01}_{-0.11}$	$53.08^{+0.08}_{-0.18}$	$-0.88^{+0.10}_{-0.07}$	0
	050820A	$-0.43^{+0.23}_{-0.08}$	$51.93^{+0.54}_{-0.35}$	$52.81^{+0.48}_{-0.39}$	$52.88^{+0.47}_{-0.39}$	$-0.07^{+0.02}_{-0.02}$	2
	050904	$-0.67^{+0.19}_{-0.25}$	$51.28^{+0.14}_{-0.39}$	$51.76^{+0.24}_{-0.09}$	$51.85^{+0.22}_{-0.10}$	$-0.06^{+0.02}_{-0.05}$	0
	060418	$-0.66^{+0.10}_{-0.11}$	$50.92^{+0.22}_{-0.17}$	$51.16^{+0.12}_{-0.14}$	$51.32^{+0.21}_{-0.12}$	$-0.20^{+0.05}_{-0.07}$	0
	090328	$-0.85^{+0.58}_{-0.18}$	$51.58^{+0.50}_{-0.63}$	$51.45^{+0.42}_{-0.24}$	$51.99^{+0.30}_{-0.47}$	$-0.11^{+0.10}_{-0.36}$	0
	090423	$-0.52^{+0.20}_{-0.32}$	$53.09^{+0.70}_{-0.61}$	$52.82^{+0.17}_{-0.47}$	$53.19^{+0.55}_{-0.57}$	$-0.50^{+0.27}_{-0.43}$	0
	090902B	$-0.83^{+0.34}_{-0.11}$	$52.71^{+0.40}_{-0.38}$	$54.36^{+0.28}_{-0.55}$	$54.38^{+0.24}_{-0.57}$	$-0.01^{+0.01}_{-0.02}$	2
	090926A	$-0.25^{+0.25}_{-0.73}$	$51.09^{+1.25}_{-0.27}$	$52.38^{+0.16}_{-0.20}$	$52.41^{+0.37}_{-0.19}$	$-0.05^{+0.04}_{-0.19}$	0
	120521C	$-0.47^{+0.12}_{-0.14}$	$50.91^{+0.21}_{-0.23}$	$50.79^{+0.21}_{-0.24}$	$51.16^{+0.21}_{-0.20}$	$-0.32^{+0.09}_{-0.12}$	0
	130427A	$-0.12^{+0.11}_{-0.32}$	$51.91^{+0.65}_{-0.34}$	$53.14^{+0.49}_{-0.29}$	$53.17^{+0.49}_{-0.30}$	$-0.03^{+0.02}_{-0.04}$	2
	130702A	-	$51.08^{+1.03}_{-0.84}$	$49.08^{+0.23}_{-0.12}$	$51.07^{+1.03}_{-0.79}$	$-2.25^{+0.99}_{-0.86}$	0
	130907A	-	$50.23^{+0.04}_{-0.06}$	$51.45^{+0.34}_{-0.11}$	$51.47^{+0.33}_{-0.10}$	$-0.01^{+0.00}_{-0.01}$	0
	140304A	$-0.73^{+0.12}_{-0.12}$	$51.63^{+0.23}_{-0.19}$	$50.19^{+0.46}_{-0.13}$	$51.65^{+0.23}_{-0.17}$	$-1.39^{+0.38}_{-0.28}$	2

Note: The mode of the distribution of E_{true} is smaller than the mode of the $E_{\gamma,\mathrm{true}}$ for GRB 980703, and it is smaller than $E_{\mathrm{K,true}}$ for GRBs 000418, 000926 and 130702A. This is not due to an error in the analysis, but rather a combined effect due to addition in linear space whilst the distribution is in logarithmic space, and uncertainty in the Gaussian kernel estimator when determining the mode. In any case, the differences are well within the reported uncertainties and do not affect any results.

We present the relevant derived parameters of the GRB sample in Tables 3.7 and 3.8. In Figure 3.8 it can be seen that short GRBs are systematically less efficient than long GRBs. The average value of the inferred ϵ_γ parameters for short and long GRBs are 2.7×10^{-4} and 0.26, respectively. Beniamini et al. (2015) have analyzed the observed flux from 10 long GRBs in X-rays and GeV energies to estimate the energetics of these GRBs. They find that there is a discrepancy between the estimated energies using both bands, where the energy estimated from the GeV flux is significantly larger. They state that this discrepancy can be explained within the forward shock framework by either assuming that the cooling break lies between these two bands or by taking into account Compton cooling effects. As a result they find that the average prompt efficiency value becomes 0.87 for the X-ray estimated energies, and 0.14 for GeV estimated energies. They note that the GeV estimated energetics should be more reliable, and these are consistent with our results. We perform a KS test to determine if the ϵ_γ distribution for long and short GRBs originate from a common distribution. We find that the null hypothesis can be significantly rejected, with $p = 1.3 \times 10^{-4}$, so short GRBs are indeed less efficient γ-ray emitters. However, this analysis does not account for the uncertainties in the ϵ_γ parameter, and relies only on the mode of the posterior distribution.

It is not so clear what might cause this difference in efficiency, and our study does not speak much to this because we examine only the physics of the afterglow. We do note that in the afterglow, the short GRB blast waves have a lower (synchrotron) emission efficiency, because this scales as $\epsilon_e \epsilon_B$, which is lower on average for short GRBs (which have about the same ϵ_e and lower ϵ_B for a given true energy – see below). Whether we should expect that same difference to exist for the internal shocks that cause the prompt emission (or whether those are even dominated by synchrotron emission) is unclear, however. In Gottlieb et al. (2019), the authors find that the main factor determining the radiative efficiency is the amount of baryon loading. Since our findings indicate that short GRBs are less efficient, this could also mean that baryon loading in short GRB jets is more prominent. Gottlieb et al. (2021a) (see also Gottlieb et al., 2020, 2021b) have performed RMHD simulations to investigate how the prompt emission features (variability, spectrum and efficiency) vary for hydrodynamic/magnetized jets with intermittent/continuous central engine activity. They have found that magnetized/intermittent jets are the most likely candidate for GRBs, as they yield high prompt efficiencies and are consistent with observed spectral/temporal features. They also note that, for hydrodynamic/intermittent jets, the efficiency drops below 1%. As the degree of magnetization increases the mixing processes become less efficient and lead to higher ϵ_γ values.

In order to test whether or not the inferred energetics for the GRBs are feasible, we make use of the total beaming corrected energies, $E_{\rm true} \equiv E_{K,\rm true} + E_{\gamma,\rm true}$. Assuming that the jet is powered by the rotational energy of a Kerr black hole (e.g. Blandford & Znajek 1977), it is possible to estimate the total jet energy from the mass $M_{\rm BH}$ and rotation parameter a of the black hole as

$$E_{\rm true} = \epsilon_{\rm jet} E_{\rm rot} = \epsilon_{\rm jet} f(a) M_{\rm BH} c^2, \tag{3.11}$$

where $E_{\rm rot}$ is the rotational energy of the central black hole. Taking not too aggressive values $a = 0.9$ and $\epsilon_{\rm jet} = 0.1$ (e.g., Lee et al. 2000; McKinney 2005), we get $E_{\rm true} \simeq 0.015 M_{\rm BH} c^2$.

Table 3.9: Correlation significance results for the Jackknife re-sampling. The upper panel shows p-value estimates for the whole long GRB sample, the middle panel takes into account only the long GRBs in ISM-like environments, and the bottom panel is for the long GRBs in wind-like environments.

	Anti-/correlation	p-value Minimum	Maximum	Average
long GRBs	ϵ_B–$E_{K,\mathrm{true}}$	1.22×10^{-7}	2.28×10^{-4}	4.65×10^{-5}
	θ_0–ϵ_B	6.85×10^{-4}	0.010	4.18×10^{-3}
	ϵ_B–$E_{K,\mathrm{iso}}$	0.011	0.48	0.12
ISM-like	ϵ_B–$E_{K,\mathrm{true}}$	4.74×10^{-6}	1.28×10^{-4}	3.66×10^{-5}
	θ_0–ϵ_B	1.71×10^{-4}	6.12×10^{-3}	1.60×10^{-3}
	ϵ_B–$E_{K,\mathrm{iso}}$	0.10	0.99	0.82
Wind-like	ϵ_B–$E_{K,\mathrm{true}}$	0.011	0.68	0.21
	θ_0–ϵ_B	0.55	0.99	0.87
	ϵ_B–$E_{K,\mathrm{iso}}$	9.03×10^{-3}	0.37	0.12

The short and long GRBs with the highest inferred beaming corrected energies are GRBs 200522A and 090902B, respectively, with best-fit values of 2.2×10^{52} and 2.4×10^{54} erg. Using Equation 3.11, the implied mass of the central black hole can be inferred as > 0.19 and $> 23.73\ M_\odot$ for GRBs 200522A and 090902B, neither of which presents a significant difficulty for the favourite source models.

3.4.3 ϵ_B–$E_{K,\mathrm{true}}$, θ_0–ϵ_B anti-correlations

We find that θ_0 and $E_{K,\mathrm{true}}$ are strongly correlated with each other for both wind-like and ISM-like long GRBs; this does not, however, have any new meaning. It is simply the result of the fact that E_{true} is derived from E_{iso} via the opening angle, and that the distribution of E_{iso} is fairly narrow, whereas that of θ_0 is wider. Hence, this correlation is largely due to the fact that we are correlating θ_0 with itself, and we even find that the best-fit slope shows $E_{\mathrm{K,true}} \propto \theta_0^{1.7}$, quite close to the theoretically expected $E \propto \theta^2$ one would get for a single-valued E_{iso} with a range of values of $\theta_0 \ll 1$.

We do however find a strong and significant anti-correlation between ϵ_B and $E_{K,\mathrm{true}}$ for the sample of long GRBs. In Figure 3.9 we demonstrate this anti-correlation. We find that the fraction of energy lost to amplifying magnetic fields systematically decreases as the measured beaming corrected kinetic energy gets larger. When we perform a Pearson r correlation test we find a p-value of 10^{-5}, strongly rejecting the null hypothesis that they are uncorrelated. We fit correlation lines by repeatedly sampling from the posterior distributions of the parameters and obtaining the best fit lines for each iteration. The ϵ_B–$E_{K,\mathrm{true}}$ relation can be described as a power-law with index $\alpha = -0.53^{+0.07}_{-0.04}$. Alternatively, we can of course regard this correlation as due to an $\epsilon_B - \theta_0$ relation. The ϵ_B–θ_0 relation can be described as a power-law with index $\alpha = -2.19^{+0.35}_{-0.37}$. We also checked for a possible correlation between

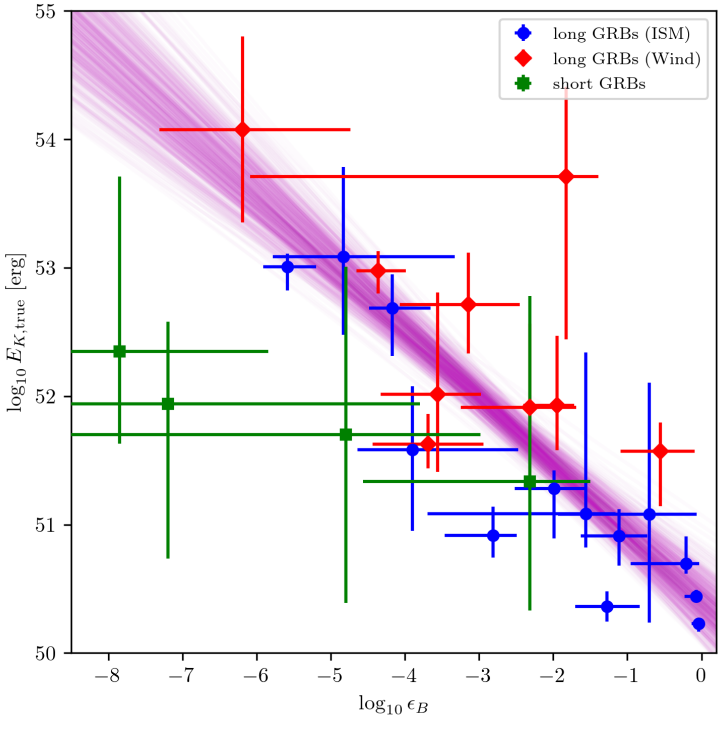

Figure 3.9: Scatter plot of ϵ_B and $E_{K,\mathrm{true}}$ parameters for the GRB sample. The blue circles, red diamonds, and green squares represent ISM-like long GRBs, wind-like long GRBs and short GRBs, respectively. Error bars represent the 68% credible interval. The magenta lines represent the best-fit results from 500 linear fits to the inferred parameters. For each fit we sample values from the posterior distribution of the parameters. The inferred slope is $\alpha = -0.53^{+0.07}_{-0.04}$.

ϵ_B and $E_{K,\mathrm{iso}}$; it is not significant. This may be somewhat surprising, since we think of the energy fractions in electrons and magnetic field to be set very locally at the shock, and thus correlate better with $E_{K,\mathrm{iso}}$, which scales with the local energy per unit area at the shock.

Since the number of GRBs in either sample is small, we use a Jackknife resampling test to check the robustness of these correlations due to outliers. The results can be seen in Table 3.9, and show that the significant correlations are robust. However, they also reveal are rather strong difference between the two subclasses: the correlations are not significant in the wind-like GRBs and very strongly significant in the ISM-likes. The significance of the result for the total population is therefore entirely due to that of the ISM-like GRBs. This is puzzling, since it unclear how the correlation between these two blast wave parameters would come to depend on the shape of the ambient density distribution.

3.4.4 Caveats

First of all, it is not straightforward to infer population distributions from uncertain measurements. When creating histograms, we spread the inferred parameter values across bins which span over the 68% credible region. Since it is not correct to combine posterior samples from separate modelling efforts, the histograms presented in this study are mostly for illustrative purposes. Although this still relays valuable information about the GRB population, it would be valuable to account for the uncertainties in a statistically valid manner (e.g., Hogg et al. 2010).

Second, it is not possible to compile an unbiased sample of well-sampled afterglows, because a variety of instrumental biases and observer choices enter into the determination of which GRBs to follow up extensively and for which such followup is successful. Therefore, the inferred GRB population will likely not cover all of the physical parameter space. We have commented above on whether we estimate this has a significant influence on our conclusions. While we accounted for the small sample size of especially short GRBs when stating significances, it is still good to bear in mind that our short GRBs are especially unrepresentative of the total population of short GRBs (though, as we noted, there is no clear expectation that this this would bias the intrinsic properties of this subset of short GRBs, for which we draw the most marked conclusions.)

3.5 Conclusion

We have studied a sample of 26 GRB afterglows (as well as the total prompt γ-ray energy emitted), which was biased to enabling detailed afterglow physics studies, i.e., towards having well-sampled radio, optical, and X-ray light curves. While this largely excludes the most obscured GRBs (due to optical extinction) and GRBs in low-density regions (i.e., most short GRBs), we argue that there are quite a few conclusions about GRB physics that are not strongly affected by those biases:

1. All physical parameters have intrinsic distributions of significant width, i.e., none have a 'standard' value that is almost the same for all GRBs, or even within a subsample (short, long-ISM, or long-wind; Sect. 4.4).
2. Short GRBs prefer uniform ambient densities, in agreement with theoretical expectations and previous studies (Sect. 3.3.1).
3. Long GRBs have about equal likelihood of wind-like and uniform ambient media. A massive star progenitor is expected to impact the environment of the burst, suggesting a wind-like medium to be more likely. We note that even a massive star wind environment can be close to homogeneous at scales probed by the afterglow observations, but that this is not the most natural outcome for typical parameters (Sect. 3.4.1).
4. The wind strengths for the wind-like long GRBs favour canonical mass loss parameters of massive Wolf-Rayet stars, the most likely progenitors, and specifically do not indicate a bias towards low mass loss rates, as required by some GRB models (Sect. 3.4.1).
5. We do not find evidence for different jet opening angles between long and short GRBs (Sect. 3.3.2).
6. The observer viewing angles are consistent with top-hat jets, and with the opening angles of the prompt γ-ray emission and early afterglow emission being the same. This may significantly constrain so-called 'jet-coccoon' models of GRBs (Sect. 3.3.2).
7. We find a distribution of slopes of the energy distribution of accelerated electrons, p, that is consistent with previous studies; it contains only a few examples where $p < 2$ significantly, but many where it is close enough to 2 to warrant caution in fitting p and ϵ_e (Sect. 3.3.3).
8. The values of ϵ_e are all in the range $0.1 - 1$, with no significant differences between short/long or wind/uniform samples (Sect. 3.3.3).
9. The true total energies of long and short GRBs are similar, implying that the relative faintness of short GRBs in γ rays is due to their lower γ-ray emission efficiency (Sect. 3.4.2).
10. While the total energies of GRB blast waves do not have standard values, they are smaller on average by an order of magnitude for ISM-like long GRBs than for wind-like ones (Sect. 3.4.2).
11. Some required gamma-ray efficiencies of GRBs are close to 1, which is a challenging value for current prompt emission theories (Sect. 3.4.2).
12. There is a strong and significant correlation for ISM-like long GRBs between the magnetic field energy at the shock and the true total kinetic energy of the blast wave. It is surprising that this same correlation does not exist for the wind-like GRBs (Sect. 3.4.3).

Acknowledgements

This work was carried out on the Dutch national e-infrastructure with the support of SURF Cooperative. H. J. van Eerten acknowledges partial support by the European Union Horizon 2020 Programme under the AHEAD2020 project (grant agreement number 871158).

Data Availability

A reproduction package including the data underlying this article will be made available at Zenodo with DOI: 10.5281/zenodo.5035173.

Appendices

3.A Posterior distributions for the free physical parameters

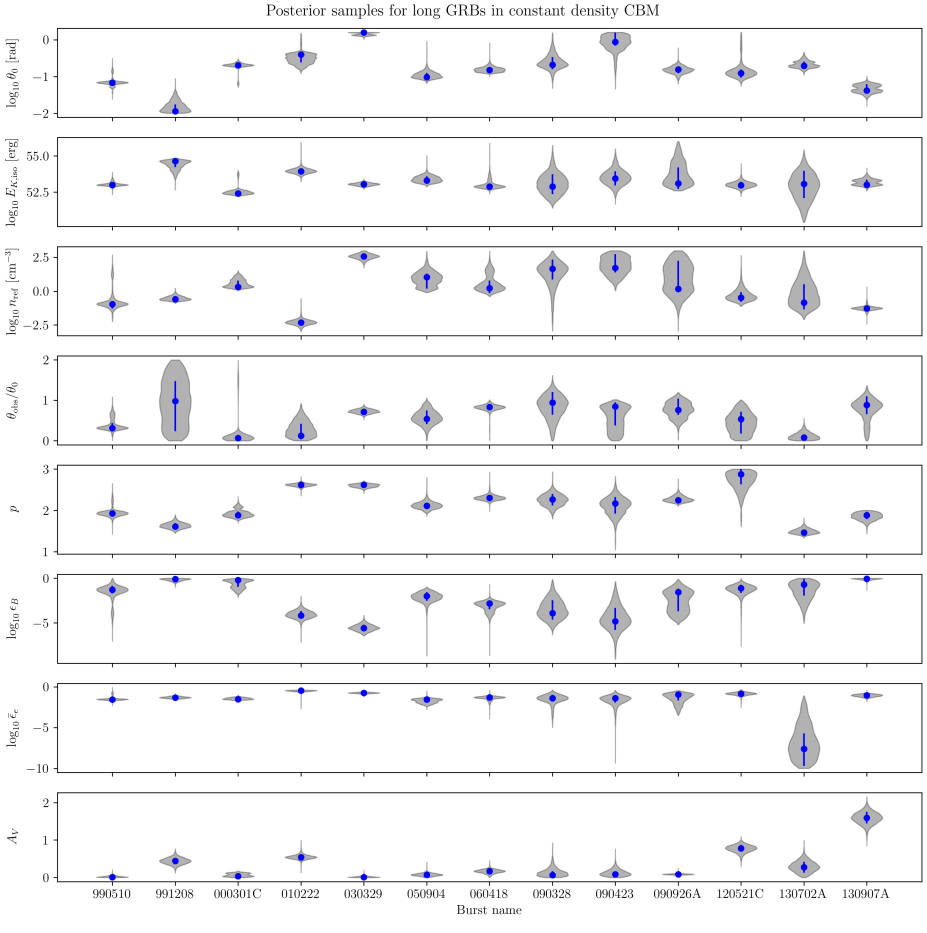

Figure 3.10: Violin plots representing the obtained posterior distributions of the free physical parameters for the long GRB sample associated with a constant density environment. The shaded areas represent the density of the posterior samples and circles represent the mean value. Error bars represent the 68% credible interval.

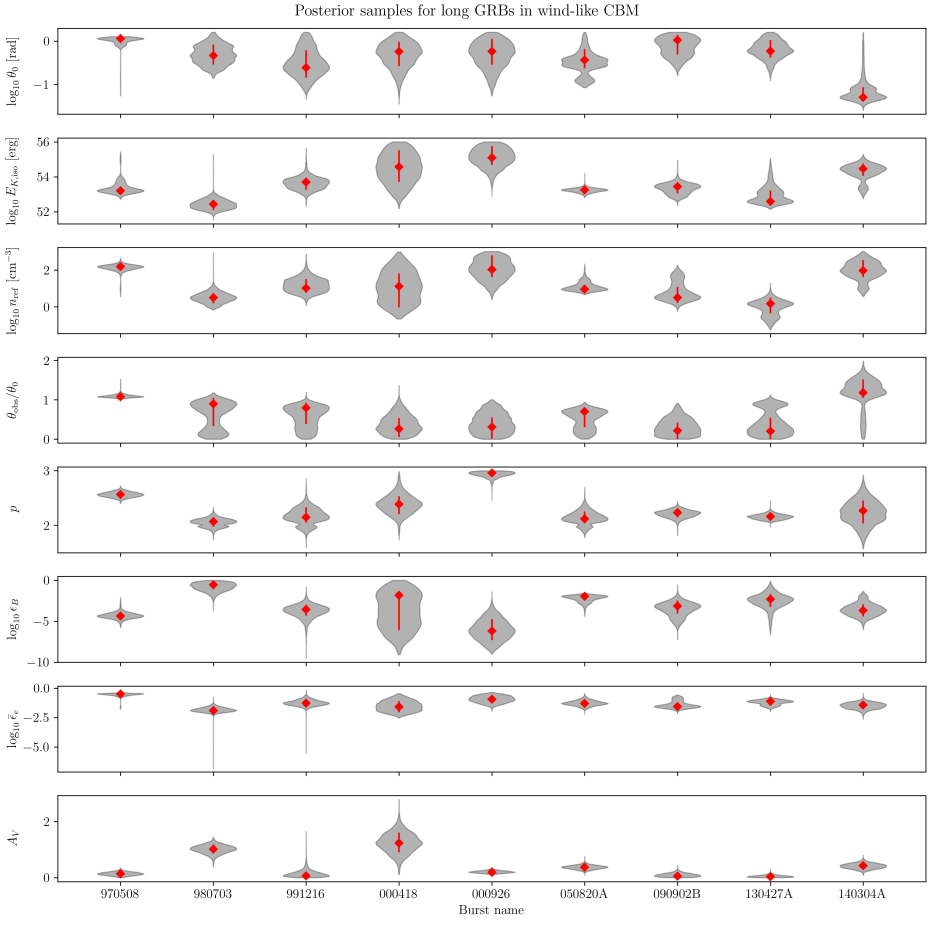

Figure 3.11: Violin plots representing the obtained posterior distributions of the free physical parameters for the long GRB sample associated with a wind-like environment. The shaded areas represent the density of the posterior samples and diamonds represent the mean value. Error bars represent the 68% credible interval.

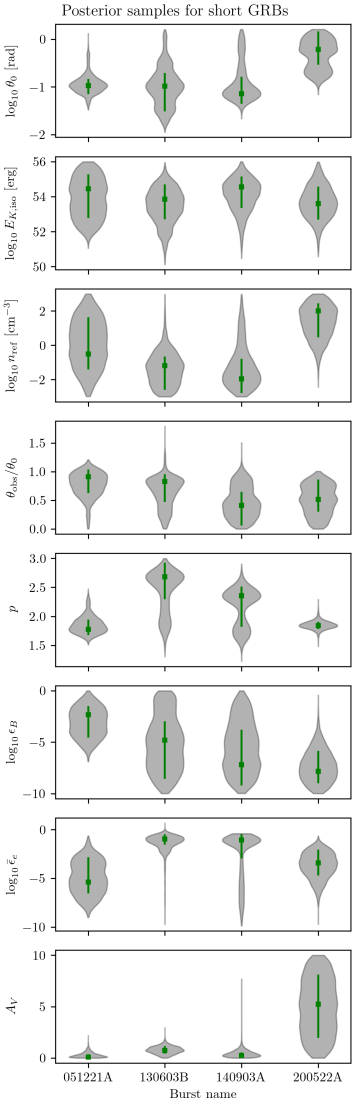

Figure 3.12: Violin plots representing the obtained posterior distributions of the free physical parameters for the short GRB sample. The shaded areas represent the density of the posterior samples and squares represent the mean value. Error bars represent the 68% credible interval.

Chapter 4

Exploring the long GRB population: A population synthesis study

M. D. Aksulu, M. De Pasquale, J. Japelj, H. J. van Eerten, R. A. M. J. Wijers

Submitted to the Monthly Notices of the Royal Astronomical Society

Abstract

In this paper we derive physical properties of a sample of gamma-ray bursts with limited afterglow data, namely the *Swift* BAT6 sample. We use the fact that its gamma-ray selection is well defined and that it is reasonably complete in redshift to perform a population synthesis study, in which we use Bayesian inference to constrain the distributions of physical parameters by fitting the observed distributions of brightness in X rays, optical, and radio as predicted by the numerical afterglow model scalefit. We are able to generate a synthetic population of long GRBs which is consistent with the observed properties of the BAT6 sample. We find that the synthetic population is mostly consistent with previous individual modelling efforts, especially when we assume a wind-like density profile for the circumburst environment. We find that most of the burst parameters of the long GRB population span a large range of values, which is consistent with previous studies. The beaming-corrected kinetic energy of the population is centred around $\sim 10^{52}$ erg with a spread of $\sigma_{\log_{10} E_{K,\mathrm{true}}} \sim 1.2$. We also use the results to show that it is not very rare that GRBs have parameters for which the light curve is a very long break-free power law, such as seen in GRB 130427A.

4.1 Introduction

Gamma-ray bursts (GRBs) are the most energetic explosions in the Universe. They are ultra-relativistic collimated outflows powered by a central compact object. Initially, GRBs are detected as prompt flashes of high-energy radiation that last between 0.1-1000 s. The radiative processes governing the so-called "prompt" phase of GRBs are not yet well-understood. After the prompt phase, when the blast wave starts to interact with the surrounding medium, ultra-relativistic shocks are formed where charged particles get accelerated and emit synchrotron radiation. This "afterglow" radiation spans the entire electromagnetic spectrum and can be observed for days or in some cases even years (Rees & Mészáros, 1992). GRBs are phenomenologically categorized as short and Long GRBs depending on the duration of the prompt phase (Kouveliotou et al., 1993). Long GRBs, which have a duration $t_{90} \gtrsim 2\,\mathrm{s}$, are thought to be the result of core-collapse supernovae of massive stars (Woosley, 1993), whereas short-GRBs have been associated with compact object mergers where at least one of the objects is a neutron star (Lattimer & Schramm, 1976; Eichler et al., 1989).

The afterglow emission of GRBs allows us to probe their energetics, the environments of the progenitor, and the microphysical properties of ultra-relativistic shocks. With the launch of *Neil Gehrels Swift Observatory* in 2004 the localization of GRBs has improved significantly, allowing for follow-up observations of the afterglow with both ground and space-based instruments (Gehrels et al., 2004). Previous studies have utilized the fireball model to infer the burst parameters of individual GRBs based on extensive multi-wavelength afterglow observations (Panaitescu & Kumar, 2002; Yost et al., 2003; Aksulu et al., 2021). In this study, we employ a different method to probe the parameter distributions of the GRB population. Instead of utilizing broadband, high-cadence afterglow data sets to model a relatively small sample of GRBs, we make use of a larger sample of GRBs with a limited number of afterglow flux measurements and well-understood selection biases. We conduct a population synthesis study to reproduce the observed features of such a sample, and perform Bayesian inference to determine the distributions for the burst parameters of the long GRB population. This has the advantage of allowing us to use a rather larger sample of GRBs than is available for detailed individual study, and also one that has somewhat wel understood selection effects. Also, it allows us directly to fit distributions of parameters of the population as a whole. Ghirlanda et al. (2012) performed a population synthesis study to constrain the jet opening angle, θ_0, and the initial bulk Lorentz factor, Γ_0, based on the observed prompt features of the GRB population. Later on, in Ghirlanda et al. (2015), they utilized the obtained distributions to infer the afterglow flux distribution of the GRB population to investigate the detection rates of "orphan" afterglows. However, they assume canonical values for the microphysical parameters, and are unable to reproduce the observed X-ray afterglow flux distribution in conjunction with the optical and radio distributions. In this study, we assume log-/normal distributions for the burst parameters, and leave the distribution mean and standard deviations as free parameters. We perform Bayesian inference, based on the target distributions of the chosen long GRB sample, to obtain posterior distributions for the distribution parameters, and we repeat the procedure for both GRBs in homogeneous and wind-like environments.

Furthermore, we make comparisons between results from individual modelling efforts and the population synthesis.

In Section 4.2 we introduce the sample of long GRBs as well as the target distributions which need to be reproduced by the synthetic population. In Section 4.3, we give a detailed description of the utilized method to generate a synthetic population of GRBs, consistent with the observed features of our sample. In Section 4.4, we present the results of our analysis and compare the obtained parameter distributions with individual GRB afterglow modelling results. In Section 4.5 we comment on the implications of the population study and conclude in Section 4.6.

4.2 Target sample

In order to determine the underlying parameter distribution of the long GRB population, we need a reference sample of GRBs with well-understood selection biases. We will use the observables of this sample as our target distributions. In this work we make use of the BAT6 sample as the target population (Salvaterra et al., 2012). This is a flux complete sample (in the prompt emission phase) of long GRBs which have a selection criterion of having at least 2.6 photons s^{-1} cm^{-2} flux in the 15-150 keV Swift/BAT band. The sample has a high redshift completeness level of 88%.

We gather the prompt emission features and afterglow measurements for the BAT6 sample to create target distributions for the observables of the GRB population. The isotropic-equivalent energy emitted in γ-rays, $E_{\gamma,\mathrm{iso}}$, and the rest-frame energy at which the prompt spectrum peaks, $E_{\mathrm{peak,rest}}$, of the BAT6 sample have been collected from Nava et al. (2012). We collect the peak photon count in the 15-150 keV band from the *Swift*/BAT catalogue (Lien et al., 2016). The X-ray flux values of the afterglow emission at 11 and 24 hours have been collected from the *Swift*/XRT catalogue (Evans et al., 2009). We convert the flux values in the 0.3-10 keV *Swift*/XRT band to units of mJy. We make use of the reported average photon index to calculate the flux at the geometric centre of the *Swift*/XRT band (~ 1.3 keV). Furthermore, we correct for absorption by making use of the ratio of the reported average absorbed and unabsorbed flux values. The data for the R-band observations at 11 hours were obtained from Ghirlanda et al. (2015), upon request from the authors (also see Melandri et al. 2014). The radio observations (8.4 GHz) at various time epochs for the BAT6 sample are presented in Ghirlanda et al. (2013). Since the radio observations are not taken at the same time epoch for all of the GRBs, when we try to reproduce the radio afterglow flux distribution we select a random time epoch from the observation times of the BAT6 sample, for each synthetic GRB. The BAT6 sample of long GRBs along with their corresponding observables are presented in Tables 4.8 and 4.9, and the reader can refer to e.g., Figures 4.3 and 4.4 to see the cumulative histograms of the target distributions. Missing values are simply excluded from the target distributions, which could introduce biases especially for the radio afterglow distribution (see Section 4.5.4).

4.3 Method

4.3.1 Calculating Gamma-ray photon flux

In order to take into account the selection criterion of the BAT6 sample, we need to calculate the photon flux in gamma rays. However, since we do not have a physical model for the prompt emission of GRBs, we need to rely on a series of assumptions and observed correlations to calculate the photon flux. In this work, we follow the reasoning of Ghirlanda et al. (2012).

- The isotropic equivalent gamma-ray energies, $E_{\gamma,\mathrm{iso}}$, for the BAT6 sample are presented in Nava et al. (2012). Since the observed $E_{\gamma,\mathrm{iso}}$ distribution will differ from the intrinsic distribution of the population (due to the selection criterion), we define the intrinsic $E_{\gamma,\mathrm{iso}}$ distribution as a free distribution.
- Following Ghirlanda et al. (2012), we assume that the prompt emission light curve is a simple triangle and deduce the peak luminosity using $L_{\mathrm{peak}} = 2E_{\gamma,\mathrm{iso}}(1+z)/T_{90}$. Where T_{90} is the burst duration, which is drawn from a log-normal distribution centred at 27.5 s and with a standard deviation 0.35. The peak bolometric flux is then computed using $F_{\mathrm{bol}} = L_{\mathrm{peak}}/4\pi d_L^2$.
- Since we need the photon flux within a certain band (15-150 keV), we need to assume a spectral shape. In this work we assume a Band function for the spectral shape (Band et al., 1993),

$$\begin{aligned} N_E(E) &= A\left(\frac{E}{100\ \mathrm{keV}}\right)^{\alpha} \exp\left(-\frac{E}{E_{\mathrm{peak}}}\right) \quad \text{for } (\alpha-\beta)E_{\mathrm{peak}} \leq E, \\ &= A\left[\frac{(\alpha-\beta)E_{\mathrm{peak}}}{100\ \mathrm{keV}}\right]^{\alpha-\beta} \exp(\beta-\alpha)\left(\frac{E}{100\ \mathrm{keV}}\right)^{\beta} \\ &\qquad \text{for } (\alpha-\beta)E_{\mathrm{peak}} > E. \end{aligned} \tag{4.1}$$

  We assume spectral slopes $\alpha = -1$ and $\beta = -2.3$, corresponding to typical observed values (Kaneko et al., 2006; Sakamoto et al., 2011).
- In order to normalize the spectrum in Equation 4.1, we also need to assume a value for E_{peak}. We make use of the phenomenological correlation between $E_{\gamma,\mathrm{iso}}$ and $E_{\mathrm{peak,rest}}$ (Amati relation: Amati et al. 2002) to determine $E_{\mathrm{peak,rest}}$ for any given $E_{\gamma,\mathrm{iso}}$. We draw the $E_{\mathrm{peak,rest}}$ value from the correlation as described by Nava et al. (2012): $\log_{10} E_{\mathrm{peak,rest}}$ is drawn from a normal distribution with mean $0.61 \log_{10} E_{\gamma,\mathrm{iso}} - 29.6$ and standard deviation 0.25. We calculate the observed spectral peak energy $E_{\mathrm{peak}} = E_{\mathrm{peak,rest}}/(1+z)$.
- We calculate the normalization factor, A (Equation 4.1), by integrating $EN_E(E)$ from 0 to ∞ and equate this expression to F_{bol}. Now, that we have normalized the spectrum, we are able to infer the photon flux.

To summarize, we are able to calculate the observed photon count within a given band (15 to 150 keV in our case) for a population of GRBs, given a distribution of $E_{\gamma,\mathrm{iso}}$. This enables us

to discard the GRBs which do not meet the selection criterion of the BAT6 sample from our population. We adopt a log-normal distribution for $E_{\gamma,\mathrm{iso}}$ throughout this work. We note that our assumption that all GRBs have the same spectral shape is a big simplification; but the fact that we leave the distribution of the GRB energy free can absorb some of the variation induced by the spectral properties; also we are not aware of correlations between afterglow properties and prompt emission spectral shape that would make it especially important to include spectral variability in this study.

4.3.2 Afterglow model

In order to compare the observed flux distribution of the afterglow of the BAT6 sample to the synthetic population we need an afterglow model. We assume an ultra-relativistic blast wave moving into the CBM (circumburst medium) to create a shock-front where charged particles are accelerated in tangled magnetic fields, emitting synchrotron radiation (Sari et al., 1998; Wijers & Galama, 1999; Granot & Sari, 2002). We assume that the CBM has a density profile of the form,

$$n = n_{\mathrm{ref}} \left(\frac{r}{10^{17}\ \mathrm{cm}} \right)^{-k}\ \mathrm{cm}^{-3}. \tag{4.2}$$

Here, r is the distance from the central object, n_{ref} is the normalization at 10^{17} cm, and k determines the density profile. In this study, we only consider the cases where $k = 0$, which corresponds to an homogeneous environment, and $k = 2$, which can be interpreted as a free-stellar-wind environment. We assume that the blast wave has an opening angle of θ_0 and an initial isotropic-equivalent energy of $E_{K,\mathrm{iso}}$. The fraction of thermal energy going into accelerating the charged particles is denoted by ϵ_e. We assume that the particles are accelerated to a power-law distribution with a power-law index of p. In this case, the emission properties directly depend on

$$\bar{\epsilon}_e \equiv \frac{p-1}{p-2}\epsilon_e, \tag{4.3}$$

therefore we directly consider $\bar{\epsilon}_e$ in our model to allow $p < 2$ values in the synthetic GRB population. Furthermore, the energy density of the magnetic fields is determined via ϵ_B, which describes the fraction of thermal energy going into the magnetic fields. A fraction, ξ_N of all the electrons are accelerated. In this study we assume $\xi_N = 1$, since this parameter is degenerate with respect to ($E_{K,\mathrm{iso}}$, n_{ref}, ϵ_B, $\bar{\epsilon}_e$) (Eichler & Waxman, 2005).

In this work, we make use of the numerical model scalefit (Ryan et al. in preparation; Aksulu et al., 2021, 2020; Ryan et al., 2015), which makes use of pre-calculated tables of spectral features (spectral breaks, peak spectral flux) for a range of different time epochs, opening angles, and observing angles. These tables are created using the numerical model boxfit (van Eerten et al., 2012), which is directly based on 2D hydrodynamic simulations to capture the dynamics of the blast wave in a realistic fashion. The main disadvantage of boxfit is that it needs to solve radiative transfer equations at runtime, which makes boxfit computationally expensive. Furthermore, contrary to scalefit which makes use of scaling rules to calculate the spectra for different regimes (van Eerten & MacFadyen, 2012a), boxfit is not valid in all spectral regimes (e.g., it does not take into account cooling when calculating the self-

Table 4.1: Free distributions which describe the GRB population. For all the parameters we assume a log-normal distribution, except for p for which we assume a normal distribution. See Sections 4.3.1 and 4.3.2 for parameter definitions.

Parameter	Distribution	
$\log_{10} E_{\gamma,\mathrm{iso}}$	$\mathcal{N}(\mu,\sigma^2)$	normal
$\log_{10} \epsilon_\gamma$	$\mathcal{N}(\mu,\sigma^2)$	normal
$\log_{10} \theta_0$	$\mathcal{N}(\mu,\sigma^2)$	normal
$\log_{10} n_{\mathrm{ref}}$	$\mathcal{N}(\mu,\sigma^2)$	normal
p	$\mathcal{N}(\mu,\sigma^2)$	normal
$\log_{10} \bar{\epsilon}_e$	$\mathcal{N}(\mu,\sigma^2)$	normal
$\log_{10} \epsilon_B$	$\mathcal{N}(\mu,\sigma^2)$	normal

absorption break frequency, whereas in scalefit the spectral regimes where this plays a role are accessible through scaling relations, see Ryan et al. in prep.).

4

To summarize, we are able to calculate the expected afterglow flux for any given GRB with parameters,

$$\phi = (\theta_0, E_{K,\mathrm{iso}}, n_{\mathrm{ref}}, \theta_{\mathrm{obs}}, p, \epsilon_B, \bar{\epsilon}_e, \xi_N, z)^T. \tag{4.4}$$

In order to generate a population of GRBs in a self-consistent manner, we need to relate the prompt emission phase to the afterglow phase. To accomplish this, instead of assuming an independent distribution for $E_{K,\mathrm{iso}}$, we define,

$$\epsilon_\gamma \equiv \frac{E_{\gamma,\mathrm{iso}}}{E_{K,\mathrm{iso}} + E_{\gamma,\mathrm{iso}}}, \tag{4.5}$$

which describes the radiative efficiency of the prompt phase and correlates the afterglow emission features to the prompt emission features.

4.3.3 Generating the population

In this section, we describe the procedure for generating a population of GRBs in compliance with the selection criterion of the BAT6 sample. As detailed in Sections 4.3.1 and 4.3.2 we have 7 free distributions that shape the population of GRBs (see Table 4.1).

To generate a GRB population with n_{pop} number of GRBs, we start by sampling $E_{\gamma,\mathrm{iso}}$ values from a given distribution. For each sample, we calculate the photon count at the detector, and continue sampling new values of $E_{\gamma,\mathrm{iso}}$ until we satisfy the selection criterion of > 2.6 ph s^{-1} cm^{-2} in the 15-150 keV observing band. This means that the given distribution for $E_{\gamma,\mathrm{iso}}$ is the *intrinsic* distribution for the GRB population. As we account for the selection criterion, the $E_{\gamma,\mathrm{iso}}$ distribution for the observed GRB population will differ from the intrinsic distribution. Once we have a GRB with "detectable" prompt emission (and an associated $E_{\gamma,\mathrm{iso}}$ value), we sample from the given distributions for the afterglow parameters. The afterglow emission is coupled to the prompt features only via the ϵ_γ parameter,

while $n < n_{\rm pop}$ **do**
  Sample t_{90};
  detected = False;
  while *!detected* **do**
    Sample z and determine d_L as described in Section 4.3.4.1;
    Sample $E_{\gamma,\rm iso}$ from a given distribution;
    Sample $E_{\rm peak,rest}$ using the Amati relation and calculate the observed $E_{\rm peak} = E_{\rm peak,rest}/(1+z)$;
    Calculate photon flux as described in Section 4.3.1;
    if *photon flux >= 2.6* **then**
      detected = True;
    end
  end
  Sample ϵ_γ, θ_0, $n_{\rm ref}$, p, ϵ_B and $\bar{\epsilon}_e$ from given distributions;
  Determine $E_{K,\rm iso}$ using the relation in Equation 4.5;
  Sample $\theta_{\rm obs}$ following the assumptions in Section 4.3.4.2;
  Add parameter set to population;
  $n++$;
end

Algorithm 1: Generating a population with $n_{\rm pop}$ GRBs.

as this parameter together with the chosen $E_{\gamma,\rm iso}$ value, determines the $E_{K,\rm iso}$ of the burst. In this study, we do not account for any selection effects on the afterglow emission. Therefore, any given distributions for the afterglow parameters (including ϵ_γ) should be interpreted as *observed* distributions.

We repeat the procedure, outlined above, until we have $n_{\rm pop}$ number of GRBs in the population. The pseudo-code for generating a synthetic population of GRBs can be found in Algorithm 1.

4.3.4 Assumptions

4.3.4.1 Redshift distribution

The intrinsic redshift distribution of the population is adapted from Ghirlanda et al. (2012). The GRB formation rate, $\psi(z)$, is given by,

$$\psi(z) = e(z)R(z) \tag{4.6}$$

where $e(z)$, the ratio of the GRB rate density to star formation rate, is taken from Salvaterra et al. (2012) as $e(z) = (1+z)^{1.7}$. $R(z)$, the star formation rate fitted to data, is taken from Li (2008) as,

$$R(z) = \frac{0.0157 + 0.118z}{1 + (z/3.23)^{4.66}}\ \mathrm{M_\odot yr^{-1} Mpc^{-3}}. \tag{4.7}$$

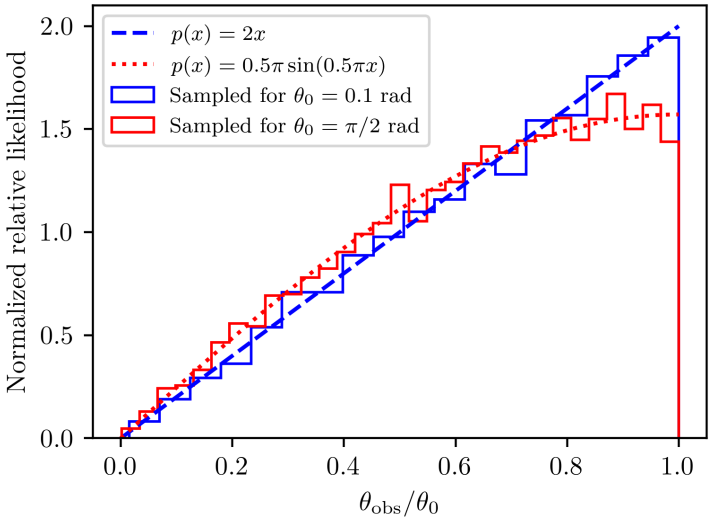

Figure 4.1: Histogram of 10000 numerically sampled $\theta_{\rm obs}/\theta_0$ values. The blue histogram along with the blue line (dashed) represent the sampled and analytically expected probability distribution for $\theta_0 \ll \pi/2$. The red histogram along with the red line (dotted) represent the sampled and analytically expected probability distribution for $\theta_0 \sim \pi/2$

Thus, the GRB formation rate becomes,

$$\psi(z) = (1+z)^{1.7} \frac{0.0157 + 0.118z}{1 + (z/3.23)^{4.66}} \, \mathrm{M_\odot yr^{-1} Mpc^{-3}}. \tag{4.8}$$

After we have sampled the redshift, we assume the cosmology described in Planck Collaboration et al. (2016) to calculate the luminosity distance. Since the calculation of the luminosity distance is computationally expensive, we make use of a pre-calculated z-d_L table and interpolate between the values.

4.3.4.2 Observer angle distribution

In this study, we assume that the observing angles of the GRBs are within their opening angle, θ_0. The observing angle, $\theta_{\rm obs}$, distribution is obtained by using purely geometrical arguments. We rely on the fact that, assuming the cone of the jet is within the observer field of view (i.e. $\theta_{\rm obs} < \theta_0$), the probability distribution of $\theta_{\rm obs}$ becomes,

$$p(\theta_{\rm obs}) = N \sin \theta_{\rm obs} \tag{4.9}$$

where, N is the normalization constant obtained by integrating $p(\theta_{\rm obs})$ from 0 to θ_0. It is straightforward to calculate the cumulative distribution function and sampling $\theta_{\rm obs}$. The probability distribution for $\theta_{\rm obs}/\theta_0$ can be expressed as a linear function for $\theta_0 \ll \pi/2$, and

becomes a sinusoidal function for $\theta_0 \sim \pi/2$. In principle, this probability distribution represents the *intrinsic* distribution for the viewing angle. We assume that, as long as the observer angle is within the cone of the jet, the observed prompt emission flux does not depend on $\theta_{\rm obs}$. Therefore we are able to use Equation 4.9 to directly sample $\theta_{\rm obs}$ values for the synthetic population. In Figure 4.1 the expected probability density function for the fractional observing angle can be seen.

4.3.5 Bayesian inference

In this section, we describe the adopted methodology for inferring the free parameter distributions, shown in Table 4.1, based on the observed prompt and afterglow emission properties of the BAT6 sample.

In order to obtain posterior distributions for the distribution parameters (μ and σ in Table 4.1), we make use of nested sampling (Skilling, 2004). We utilize pymultinest (Buchner et al., 2014), which is a PYTHON package based on the MultiNest nested sampling algorithm (Feroz et al., 2009). Throughout this work, pymultinest is used in the importance sampling mode (Feroz et al., 2019) with mode separation disabled. We use 400 initial live points and use an evidence tolerance of 0.5 as our convergence criterion.

In order to perform Bayesian inference to determine the underlying parameter distributions of the GRB population, we first need to establish a likelihood function, over which we can marginalize the distribution parameters. As can be seen in Table 4.1, each free distribution is defined by two parameters (i.e., μ and σ), which leaves us with 14 free parameters in total. We use k-sample Anderson-Darling (AD) test statistics to evaluate the fitness of our solution. The AD-test statistics is basically the weighted (to give emphasis to the tails of the distribution and to account for different sample sizes) sum of the square differences between two empirical cumulative distributions, and allows us to quantify whether or not two discrete data samples are drawn from the same distribution. We make use of the k-sample AD-test method included in the SciPy PYTHON package (Virtanen et al., 2020), which is based on Scholz & Stephens (1987).

The log-likelihood function then becomes,

$$\ln \mathscr{L} = -\sum_{i=1}^{k} \mathscr{A}\mathscr{D}(\mathrm{f}_{\mathrm{obs},i}, \mathrm{f}_{\mathrm{synth},i}), \tag{4.10}$$

where, $\mathrm{f}_{\mathrm{obs},i}$ and $\mathrm{f}_{\mathrm{synth},i}$ represent the $i^{\rm th}$ component of the observed and synthesized feature sets, and k is the total number of features. To calculate the AD statistics, we generate a population of 50 GRBs at each iteration, which is similar to the number of GRBs in the BAT6 sample.

Since the prompt features (i.e., *observed* $E_{\gamma,\rm iso}$, peak photon count and $E_{\rm peak}$) and the selected redshift of a given GRB only depend on the *intrinsic* $E_{\gamma,\rm iso}$ distribution, we perform Bayesian inference in two phases. In the first phase, we infer the *intrinsic* $E_{\gamma,\rm iso}$ distribution based on the prompt emission features, and create a table of *detected* GRBs. This table is used in the

Table 4.2: Priors for the free distribution parameters in Phase I. The distributions are defined in Table 4.1

Distribution	Prior range	
$\log_{10} E_{\gamma,\mathrm{iso}}$ [erg]	$49 < \mu < 55$	uniform
	$4 \times 10^{-3} < \sigma < 2.17$	log-uniform

second phase to assign redshifts and $E_{\gamma,\mathrm{iso}}$ values to the GRBs in the synthetic population. This allows us to skip the inner "while" loop in the second phase, when fitting for the afterglow parameters.

4.3.5.1 Phase I: Modelling the prompt features

In phase I, we only fit for the distribution parameters of $E_{\gamma,\mathrm{iso}}$ for given target distributions of z, $E_{\gamma,\mathrm{iso}}$, $E_{\mathrm{peak,rest}}$, and the peak photon count (N_{ph}). In this case, the feature set (i.e., f) in Equation 4.10 is defined as,

$$\mathrm{f} = \left(\mathrm{E}_{\gamma,\mathrm{iso}}, \mathrm{z}, \mathrm{N}_{\mathrm{ph}}\right). \tag{4.11}$$

This phase corresponds to the inner "while" loop shown in Algorithm 1, and therefore does not require calculating the afterglow emission for the population of GRBs. This reduces the computational cost of this phase. The assumed priors for the free parameters can be seen in Table 4.2.

Once we obtain posterior distributions for the mean and standard deviation of the intrinsic $E_{\gamma,\mathrm{iso}}$ distribution, we are able to create a table containing parameters for the "detected" GRB population (with $N_{\mathrm{ph}} > 2.6$ ph s^{-1}cm^{-2}). To create this table, we generate a population of 50 GRBs for every posterior sample and record the parameter sets ($E_{\gamma,\mathrm{iso}}$, z, $E_{\mathrm{peak,rest}}$) of these GRBs for later use.

4.3.5.2 Phase II: Modelling the afterglow features

In the second phase, we fit for the afterglow parameters (including ϵ_γ) for the given afterglow measurements of the BAT6 sample. In this case, the feature set (i.e., f) in Equation 4.10 is defined as,

$$\mathrm{f} = \left(\mathrm{f}_{\nu,\mathrm{X-ray\ 11h}}, \mathrm{f}_{\nu,\mathrm{X-ray\ 24h}}, \mathrm{f}_{\nu,\mathrm{R-band}}, \mathrm{f}_{\nu,\mathrm{radio}}\right). \tag{4.12}$$

The assumed priors for the free parameters can be seen in Table 4.3.

In this phase, we skip the inner "while" loop shown in Algorithm 1, and instead make use of the table generated in Phase I to determine the prompt features of each GRB (e.g., $E_{\gamma,\mathrm{iso}}$, z). This ensures that each drawn GRB is consistent with the selection criterion of the BAT6 sample. This greatly accelerates the Bayesian inference procedure.

Table 4.3: Priors for the free distribution parameters in Phase II. The distributions are defined in Table 4.1

Distribution	Prior range	
$\log_{10} \epsilon_\gamma$	$-2 < \mu < 0$	uniform
	$4 \times 10^{-3} < \sigma < 2.17$	log-uniform
$\log_{10} \theta_0$ [rad]	$-2 < \mu < 0.2$	uniform
	$4 \times 10^{-3} < \sigma < 2.17$	log-uniform
$\log_{10} n_{\rm ref}$ [cm^{-3}]	$-3 < \mu < 3$	uniform
	$4 \times 10^{-3} < \sigma < 2.17$	log-uniform
p	$1 < \mu < 3$	uniform
	$10^{-2} < \sigma < 5$	log-uniform
$\log_{10} \epsilon_B$	$-10 < \mu < 0$	uniform
	$4 \times 10^{-3} < \sigma < 2.17$	log-uniform
$\log_{10} \bar{\epsilon}_e$	$-10 < \mu < 0$	uniform
	$4 \times 10^{-3} < \sigma < 2.17$	log-uniform

4.4 Results

In this section we present the results from the Bayesian inference procedure. We marginalize the free distribution parameters as described in Section 4.3.5. We perform 3 fits in total: Phase I where we fit for the prompt features and apply the selection criterion, Phase II where we fit for the afterglow features. We perform Phase II for homogeneous and wind-like environments separately. Aksulu et al. (2021) (A21 from now on) have performed robust Bayesian inference on a sample of 26 broadband GRB afterglow data sets, of which 22 are long GRBs. They applied model selection based on the evidence values to determine the CBM density profile; either homogeneous ($k = 0$) or wind-like ($k = 2$). A21 use the same model, scalefit, in combination with Gaussian processes to account for any systematics in the afterglow data sets. Since they make use of the same afterglow model, it is useful to make comparisons between results from individual modelling of a sample of GRBs, and the population synthesis results from this study. Throughout this section we comment on the similarities and differences between the results from these two different approaches. We perform Kolmogorov-Smirnov (KS) tests between parameter distributions obtained from the population synthesis and results from A21 to determine the probability of rejecting the null hypothesis that the samples are drawn from the same distribution. We make of order 30 such comparisons and therefore consider any p-value below 3×10^{-4} to be significant.

The inferred parameters for Phase I can be seen in Table 4.4. The corresponding posterior distribution is presented in Figure 4.2 in the form of a corner plot. We would like to emphasise that the results in Table 4.4 represent the parameters for the *intrinsic* $E_{\gamma,\rm iso}$ distribution of the long GRB population. The posterior predictive distributions for the observables can be seen in Figure 4.3.

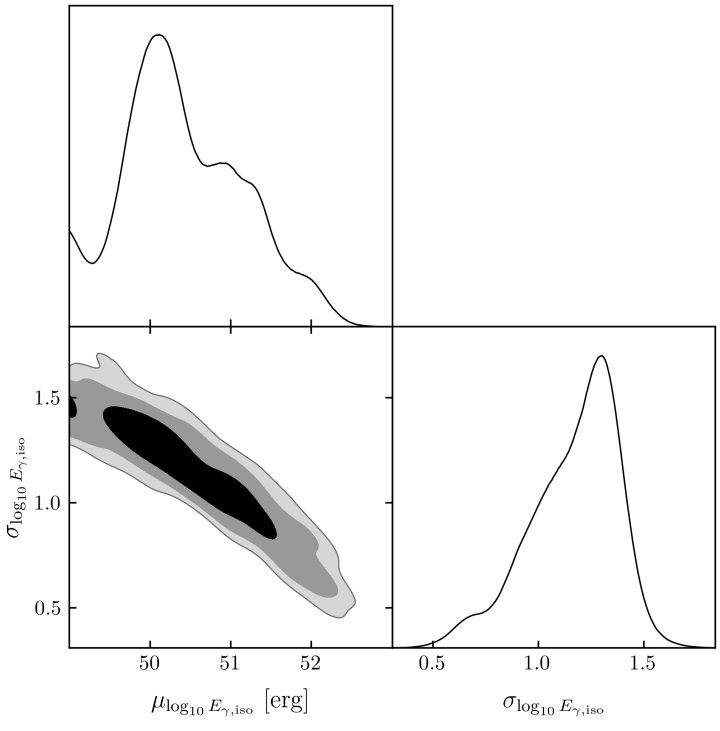

Figure 4.2: Posterior distributions for the mean and standard deviation of the $E_{\gamma,\mathrm{iso}}$ distribution. The parameters are as defined in Table 4.1. As expected, the mean and the width of the distribution are correlated.

Table 4.4: Inferred parameter modes and the corresponding 68% credible regions for Phase I. The parameters are as defined in Table 4.1.

Distribution	Parameter	
$\log_{10} E_{\gamma,\mathrm{iso}}$ [erg]	μ	$50.13^{+0.93}_{-0.54}$
	σ	$1.30^{+0.12}_{-0.26}$

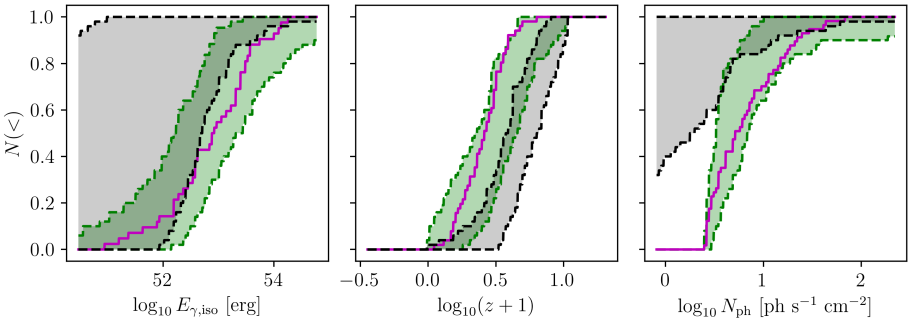

Figure 4.3: Posterior predictive results for Phase I. Cumulative histograms for the observables of Phase I are shown. The solid line (magenta) represents the measured features of the BAT6 sample. The green shaded area represents the posterior predictive of the inference results for the detected population, whereas the intrinsic population is represented by the grey shaded area. The reader can see how the intrinsic distributions get modified by the selection criterion. We randomly draw 1000 posterior samples and generate a population of 50 GRBs for each sample to determine the shaded regions.

4

Table 4.5: Inferred parameter modes and the corresponding 68% credible regions for Phase II. The parameters are as defined in Table 4.1.

Distribution	Parameter	ISM-like	Wind-like
$\log_{10}\epsilon_\gamma$	μ	$-1.37^{+0.60}_{-0.31}$	$-0.79^{+0.30}_{-0.58}$
	σ	$0.02^{+0.04}_{-0.01}$	$0.02^{+0.04}_{-0.01}$
$\log_{10}\theta_0$ [rad]	μ	$-0.76^{+0.47}_{-0.47}$	$-0.29^{+0.26}_{-0.58}$
	σ	$0.04^{+0.08}_{-0.03}$	$0.04^{+0.12}_{-0.04}$
$\log_{10} n_{\mathrm{ref}}$ [cm^{-3}]	μ	$-0.29^{+0.73}_{-0.72}$	$0.67^{+0.93}_{-0.88}$
	σ	$0.04^{+0.10}_{-0.04}$	$0.03^{+0.10}_{-0.02}$
p	μ	$1.69^{+0.14}_{-0.09}$	$2.23^{+0.12}_{-0.50}$
	σ	$0.02^{+0.02}_{-0.01}$	$0.02^{+0.02}_{-0.01}$
$\log_{10}\epsilon_B$	μ	$-2.02^{+1.15}_{-0.83}$	$-1.94^{+1.18}_{-2.03}$
	σ	$0.04^{+0.11}_{-0.03}$	$0.03^{+0.09}_{-0.03}$
$\log_{10}\bar{\epsilon}_e$	μ	$-3.61^{+1.11}_{-0.72}$	$-1.98^{+0.86}_{-0.59}$
	σ	$0.02^{+0.06}_{-0.02}$	$0.02^{+0.05}_{-0.02}$

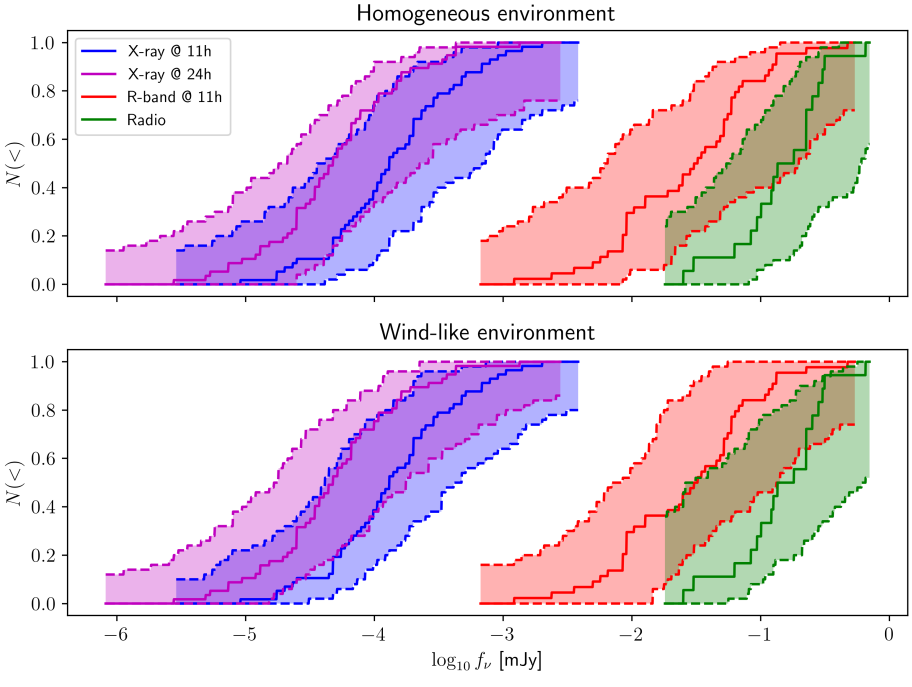

Figure 4.4: Posterior predictive results for Phase II. Cumulative histograms for the observables of Phase II are shown. The solid line represents the measured features of the BAT6 sample. The shaded area represents the posterior predictive of the inference results. We randomly draw 1000 posterior samples and generate a population of 50 GRBs for each sample to determine the shaded regions. The upper and lower panels show results for homogeneous and wind-like CBM, respectively.

The procedures for Phase II are performed twice, for GRBs in homogeneous and wind-like environments. In each case we assume the same type of environment for all of the GRBs in the population. In reality, previous studies have shown that the long GRB population should include both types of environment (e.g., Starling et al. 2008; Curran et al. 2009; Schulze et al. 2011; Aksulu et al. 2021). In principle it is possible to generate a "mixed" population of GRBs which include both homogeneous and wind-like environments. However, this would increase the number of required parameters as each environment type would have different distributions for the burst parameters. In this work, we consider each environment type separately. The inferred parameters for Phase II can be seen in Table 4.5 both for homogeneous/ISM-like and wind-like CBM. The corresponding posterior distributions are presented in Figures 4.10 and 4.11 for homogeneous and wind-like environments, respectively. The posterior predictive distributions for the observables can be seen in Figure 4.4. In Figures 4.12 and 4.13 we also present the multi-dimensional corner plot of the posterior predictive distribution for the afterglow observations. These multi-dimensional plots demonstrate that the synthetic population is able to recover most of the correlations in the observables, except for the R-band/X-ray afterglow correlation. The synthetic population finds a much stronger correlation in the R-band/X-ray plane than what is observed in the BAT6 sample. This indicates that future studies incorporating multi-dimensional k-sample tests in the likelihood function might be able to constrain the GRB population even further. However, this is not within the scope of this work. We are not able to determine which environment type explains the data best, and therefore do not favour one model over the other on the grounds of fit quality.

The inferred parameter values for Phase II exhibit large uncertainties for the mean and relatively small values/uncertainties for the standard deviation of the distributions (see Table 4.5). This is because, in this study, we assume that the underlying parameter distributions for the GRB population are independent from each other. However, when we marginalize over the distribution parameters, we find that there are strong correlations between some of the burst parameters (see Figures 4.10 and 4.11). These correlations force the sampling algorithm towards small σ values and highly correlated μ values to be able to reproduce the observed distributions of the BAT6 sample. Due to this effect, the inferred σ values do not necessarily represent the spread of the underlying parameter distribution. To infer the "real" spread for the burst parameters, we sample a certain number of parameter sets from the posterior distribution and generate 50 GRBs for each parameter set. We combine the GRB populations, generated from each of these posterior samples, to obtain the total population of GRBs, which we call the "posterior predictive" population. The mean and standard deviation for the burst parameters can be estimated using the posterior predictive, which are presented in Table 4.6 along with measurement results from A21. As can be seen in Figures 4.10 and 4.11, the resulting posterior predictive population exhibits strong correlations between parameters. In principle, one could assume correlated parameter distributions by fitting a complete covariance matrix, but that would give too many free parameters to constrain with the data set we have available.

Table 4.6: Mean and standard deviations of burst parameters for the posterior predictive synthetic populations. We generate 50 GRBs per sample for a random selection of 1000 posterior samples. Values from Aksulu et al. (2021) are also given for comparison.

Distribution		Homogeneous		Wind-like	
		This work	A21	This work	A21
$\log_{10}\epsilon_\gamma$	μ	−1.19	−0.49	−0.99	−0.71
	σ	0.44	0.62	0.42	0.73
$\log_{10}\theta_0$ [rad]	μ	−0.70	−0.80	−0.57	−0.37
	σ	0.46	0.53	0.44	0.38
$\log_{10} n_{\rm ref}\,[\rm cm^{-3}]$	μ	−0.20	0.10	0.89	1.16
	σ	0.90	1.32	0.90	0.69
p	μ	1.76	2.15	2.07	2.32
	σ	0.17	0.39	0.28	0.27
$\log_{10}\epsilon_B$	μ	−2.20	−2.17	−2.80	−3.07
	σ	1.13	1.83	1.59	1.55
$\log_{10}\bar{\epsilon}_e$	μ	−3.29	−1.67	−2.23	−1.29
	σ	0.97	1.74	1.03	0.38

In the following sections, we take a detailed look at the inferred parameter distributions of the GRB population. In order to obtain posterior predictive populations for homogeneous and wind-like GRBs, we randomly sample 1000 posterior samples (both for phase I and II) and generate 50 GRBs per sample. In the end, we obtain a population of 50 000 GRBs both for homogeneous and wind-like environments. This procedure is necessary because generating each parameter independently from the best-fit distribution would ignore the highly important correlations between them. Throughout this section, we test the null hypothesis that two distributions are equal using a Kolmogorov-Smirnov (KS) test, and present the resulting p-value.

4.4.1 GRB environment and ambient medium

The environments of GRBs provide valuable information regarding the progenitors of these energetic explosions. In Figure 4.5 we present the CBM density histograms for the synthetic population and measurement results from A21, both for homogeneous and wind-like environments.

Assuming a homogeneous density profile, we find that the particle density of the CBM has a mean of $0.63\,\rm cm^{-3}$ with a wide scatter of $\sigma_{\log_{10} n_{\rm ref}} = 0.90$. These results remain consistent with multi-wavelength afterglow modelling results from A21, as demonstrated by the KS-probability: $p = 0.45$.

Assuming a wind-like density profile, we find that the particle density of the CBM (at a reference distance, see Section 4.3.2) has a mean of $7.76\,\rm cm^{-3}$ with a scatter of $\sigma_{\log_{10} n_{\rm ref}} = 0.90$. These results are also consistent with multi-wavelength afterglow modelling results

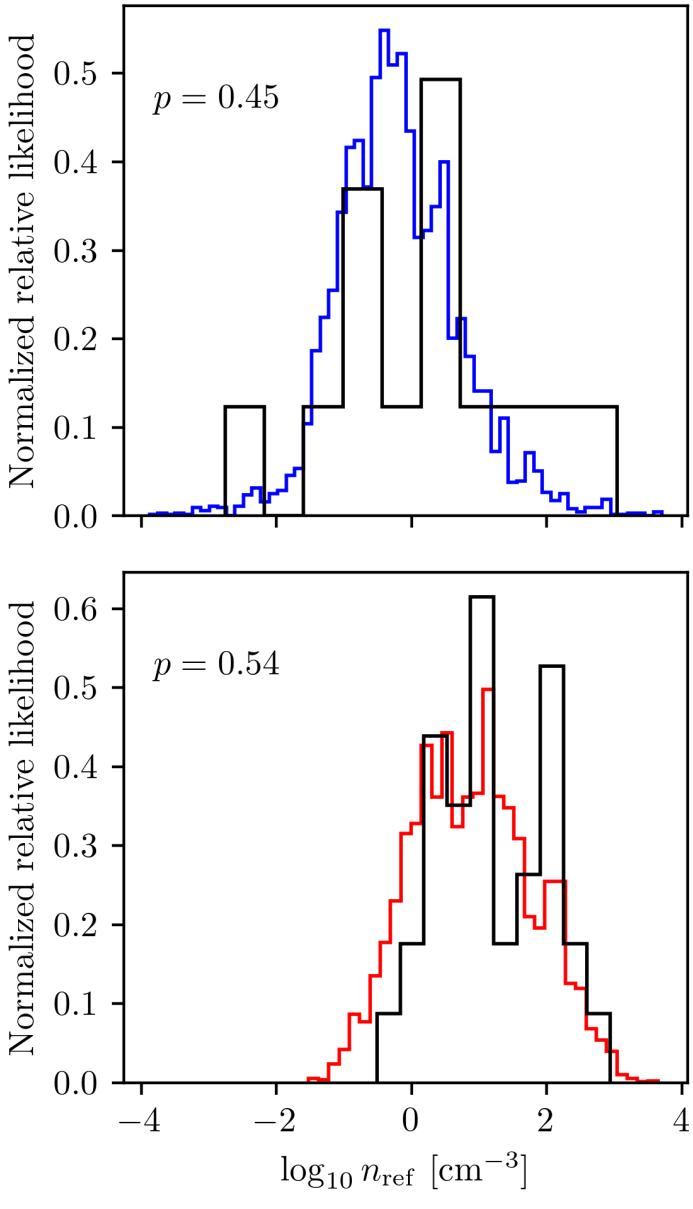

Figure 4.5: Histograms for the CBM density distribution. The upper panel shows the results for the synthetic population (blue) along with the measured values from A21 (black), assuming homogeneous CBM. The lower panel shows the results for the synthetic population (red) along with the measured values from A21 (black), assuming wind-like CBM. The p-values with which we can reject the null hypothesis that the samples from A21 and population synthesis are drawn from the same distribution are presented in the respective sub-plots.

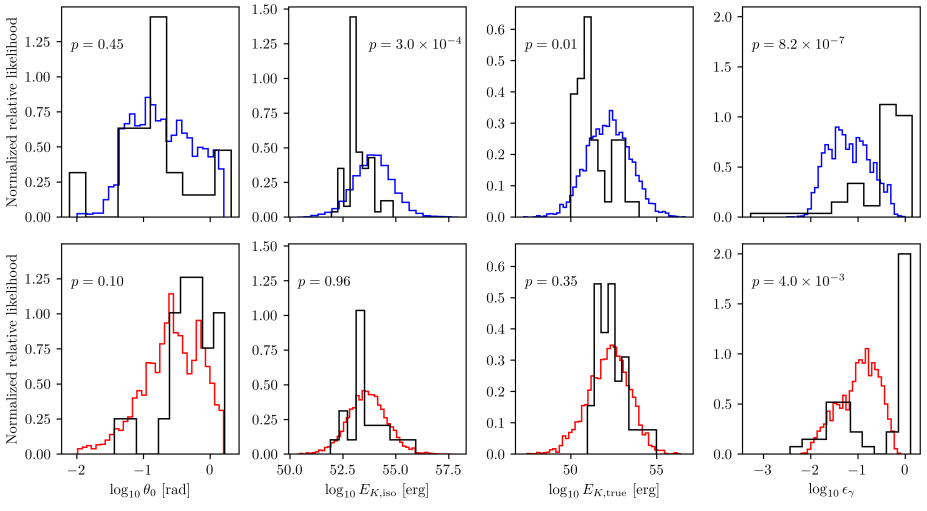

Figure 4.6: Histograms for the opening angle (θ_0), isotropic equivalent kinetic energy ($E_{K,\mathrm{iso}}$), beaming-corrected kinetic energy ($E_{K,\mathrm{true}}$), and prompt efficiency (ϵ_γ). The upper panel shows the results for the synthetic population (blue) along with the measured values from A21 (black), assuming homogeneous CBM. The lower panel shows the results for the synthetic population (red) along with the measured values from A21 (black), assuming wind-like CBM. The p-values with which we can reject the null hypothesis that the samples from A21 and population synthesis are drawn from the same distribution are presented in the respective sub-plots.

from A21 (KS test $p = 0.54$). For the wind-like case, it is more intuitive to express the CBM density as,

$$\rho(r) = \frac{A}{r^2} \tag{4.13}$$

where $A = \dot{M}/(4\pi v_{\mathrm{wind}})$. For a typical Wolf-Rayet type star with wind velocities of 1000 km s^{-1} and a mass-loss rate of 10^{-5} M$_\odot$ yr^{-1}, $A = 5.0 \times 10^{11}$ g cm^{-1}, which is denoted by $A_\star$. We can scale the inferred n_{ref} values to units of $A_\star$ using

$$\frac{A}{A_\star} = \frac{n_{\mathrm{ref}}}{30\,\mathrm{cm}^{-3}}. \tag{4.14}$$

In this notation, our mean density corresponds to $A = 0.26\,A_\star$ for the progenitor wind, a bit lower than, but consistent with $A = 0.48 A_\star$ found by A21. We note that this value is typically found in individual and group studies of GRBs (e.g., Cenko et al., 2011, , and references therein).

4.4.2 Opening angle and Energy

The observed afterglow flux directly depends on the isotropic-equivalent kinetic energy of the explosion; to understand the true energetics of these events we make use of the beaming-corrected energy, which is defined as,

$$E_{K,\mathrm{true}} \equiv E_{K,\mathrm{iso}}(1-\cos\theta_0) \tag{4.15}$$

($\simeq E_{K,\mathrm{iso}}\theta_0^2/2$, of course, for small θ_0). In Figure 4.6, we present the distributions of θ_0, $E_{K,\mathrm{iso}}$, beaming-corrected kinetic energy ($E_{K,\mathrm{true}}$), and prompt efficiency (ϵ_γ) for the synthetic population and the measurement results from A21, both for homogeneous and wind-like environments.

We find a mean of 0.27 rad and a scatter of $\sigma_{\log_{10}\theta_0} = 0.44$ for the opening angle distribution of the synthetic population in wind-like CBM. For GRBs in homogeneous environments the mean and scatter of the θ_0 distribution is 0.20 rad and $\sigma_{\log_{10}\theta_0} = 0.46$, respectively. When we perform a KS-test to determine whether or not the synthetic population is consistent with the inferred θ_0 distribution in A21, we find p-values of 0.45 and 0.10 for GRBs in homogeneous and wind-like environments, indicating that the two results are consistent.

We find similar $E_{K,\mathrm{iso}}$ distributions, with a mean of $(8.3, 4.9) \times 10^{53}$ erg and a scatter of $\sigma_{\log_{10}E_{K,\mathrm{iso}}} = (0.90, 0.91)$, for GRBs in homogeneous and wind-like environments, respectively. The $E_{K,\mathrm{iso}}$ distribution for the synthetic GRB population in homogeneous environments is not consistent with the measured values from A21, right at our threshold significance of $p = 3 \times 10^{-4}$; we see that this is due to the population synthesis requiring higher energies than the fits in A21 by about a factor 10 on average. However, for GRBs in wind-like environments, the inferred $E_{K,\mathrm{iso}}$ distribution is quite consistent with the measured values from A21, with $p = 0.96$.

The beaming-corrected kinetic energy distributions for GRBs in homogeneous and wind-like environments have means of $(1.62, 1.66) \times 10^{52}$ erg with a scatter of $\sigma_{\log_{10}E_{K,\mathrm{true}}} = (1.25, 1.20)$, so they are very similar for the two environments. There is some discrepancy with A21 for the homogeneous environment, but not significantly so ($p = 0.01$). For the wind-like environment, the results agree with A21 ($p = 0.35$).

The distribution for the fraction of energy emitted in gamma rays (ϵ_γ) spans the same range for both environments, with a mean of $(0.06, 0.10)$ with a standard deviation of $\sigma_{\log_{10}\epsilon_\gamma} = (0.44, 0.42)$ for synthetic populations in homogeneous and wind-like environments, respectively. Here the results are most discrepant with the findings of A21 on individual fits. Those results much more often required gamma-ray emission fractions quite close to one. For the homogeneous environment the discrepancy is very significant ($p = 8.2 \times 10^{-7}$); for the wind-like environment ($p = 4.0 \times 10^{-3}$) it is below our threshold for calling a significant discrepancy.

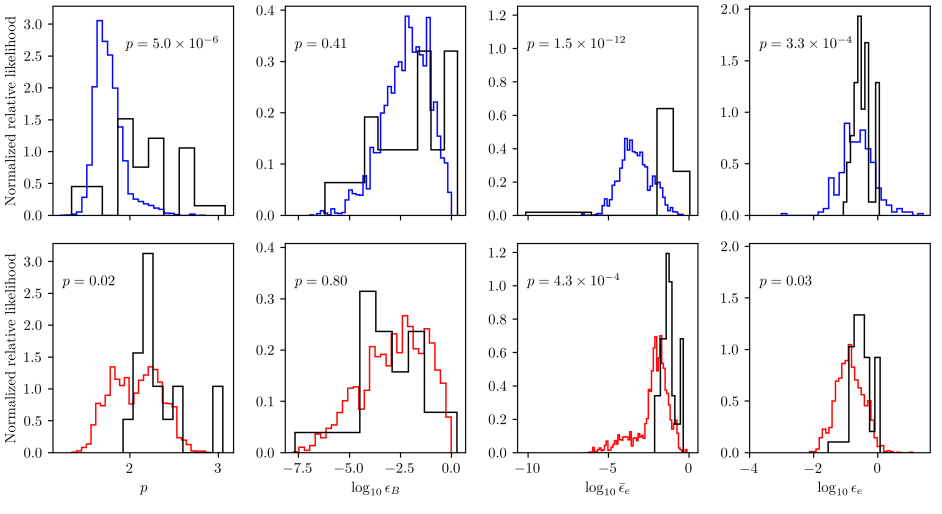

Figure 4.7: Histograms for the power-law index of the accelerated electrons (p), fraction of energy in the accelerated particles ($\bar{\epsilon}_e$, ϵ_e) and magnetic fields (ϵ_B). The upper panel shows the results for the synthetic population (blue) along with the measured values from A21 (black), assuming homogeneous CBM. The lower panel shows the results for the synthetic population (red) along with the measured values from A21 (black), assuming wind-like CBM. The p -values with which we can reject the null hypothesis that the samples from A21 and population synthesis are drawn from the same distribution are presented in the respective sub-plots. We remind the reader that the distributions of ϵ_e are generated from the subsample of cases where $p > 2$, which is small for the homogeneous CBM.

4.4.3 Shock physics parameters

In Figure 4.7, we present the p, ϵ_B, $\bar{\epsilon}_e$, and ϵ_e distributions of the synthetic population and measurement results from A21, both for homogeneous and wind-like environments.

The distribution of the power-law index for the accelerated particles, p, has a mean of $(1.76, 2.07)$ and a scatter of $\sigma_p = (0.17, 0.28)$ for synthetic GRBs in homogeneous and wind-like environments, respectively. For populations in both types of environment we find that a significant portion of GRBs have $p < 2$. This is especially evident for GRBs in homogeneous environments, where the vast majority of the population has $p < 2$, much more strongly than in the corresponding individual fits in A21, with $p = 5 \times 10^{-6}$. This result is quite important, since p is usually assumed to be slightly larger than 2 in both simulations and analysis of GRB afterglows (Curran et al., 2010, e.g.,). For the wind-like environment, the population synthesis outcome also has more low electron index values than the corresponding case in A21, but the discrepancy is not significant ($p = 0.02$).

The fraction of thermal energy in the magnetic fields, ϵ_B, exhibits a wide distribution for synthetic populations in both types of environment. We find that the ϵ_B distribution has a mean of $(6.3, 1.6) \times 10^{-3}$ and a width of $\sigma_{\log_{10}\epsilon_B} = (1.13, 1.59)$ for GRBs in homogeneous and wind-like environments. The inferred ϵ_B distributions for both environment types are consistent with the broadband afterglow modelling results from A21 ($p = 0.41$ and 0.80, respectively), and is also broadly consistent with the values assumed or derived in other studies (Panaitescu & Kumar, 2002, 2001a, e.g.,).

The $\bar{\epsilon}_e$ distribution has a mean of $(5.1, 59) \times 10^{-4}$ with a standard deviation of $\sigma_{\log_{10}\bar{\epsilon}_e} = (0.97, 1.03)$ for GRBs in homogeneous and wind-like environments. By definition (see Section 4.3.2), the $\bar{\epsilon}_e$ parameter is correlated with p. As mentioned above, the p distribution inferred via population synthesis differs from the modelling results in A21, therefore, it is not surprising that the $\bar{\epsilon}_e$ distribution also differs from what is presented in A21. For GRBs in homogeneous CBM we find considerably lower values for $\bar{\epsilon}_e$ with $p = 1.5 \times 10^{-12}$. GRBs in wind-like environments also exhibit lower $\bar{\epsilon}_e$ values when compared to A21, however, the differences are more moderate with $p = 4.3 \times 10^{-4}$. It is also informative to take a look at the inferred ϵ_e distribution, as this parameter is physically more meaningful. However, we are only able to calculate ϵ_e values for the portion of the GRB population with $p > 2$ (see Section 4.3.2), and for the homogeneous CBM case this is only a small tail of the overall distribution, so the comparison should be taken with a grain of salt. For the ϵ_e distribution, we find a mean of $(0.23, 0.14)$ with a standard deviation of $\sigma_{\log_{10}\epsilon_e} = (0.54, 0.44)$ for GRBs in homogeneous and wind-like environments. Beniamini & van der Horst (2017) showed that it is possible to constrain ϵ_e using measurements of the peak of the radio afterglow light curve. They gathered radio afterglow measurements for a sample of 36 long GRBs and inferred that $\mu_{\epsilon_e} = (0.15, 0.13)$ and $\sigma_{\log_{10}\epsilon_e} < (0.31, 0.26)$, for GRBs in homogeneous and wind-like environments. Although we infer similar mean values for ϵ_e, the inferred spread for ϵ_e is larger, but at least for the wind-like case, our findings are within range of earlier findings. Specifically, for the straightforward cases where $p > 2$, we find values of ϵ_e around

0.1, which is similar to those found or assumed in earlier studies. It is the many cases where we find $p < 2$ that require further thought.

4.5 Discussion

4.5.1 Homogeneous vs. wind-like environments

Individual modelling efforts of broadband GRB afterglow data sets have shown time after time that some GRBs favour homogeneous CBM density profiles, whereas others favour wind-like environments (see A21, and references therein). The most accepted progenitor models for long GRBs, core-collapse of massive stars, would naturally lead to wind-like density profiles due to prominent stellar winds. However, there are some scenarios where homogeneous environments can be understood within the massive star progenitor framework. As the stellar wind propagates into the circumstellar medium, the reverse shock will move into the ejected stellar material, homogenizing the circumstellar medium. The density profile of such a shocked-wind environment would be close to homogeneous. Furthermore, if the progenitor star has super-sonic motion relative to the ISM, a GRB jet might punch through the bow-shock and start its deceleration phase within the ISM. However, as we noted in A21, these scenarios will typically require $A_\star << 1$, very high stellar runaway velocities, and/or very high ambient ISM densities, and so they are perhaps in significant tension with our current understanding of GRB progenitors.

Nonetheless, purely based on the population fits in this study, we find that it is possible to reproduce the observed features of the BAT6 sample assuming either homogeneous or wind-like density profiles. We do not find any strong evidence favouring one model over the other. However, it is noteworthy that there is significantly more tension between the synthetic GRB population and individual modelling results when we assume homogeneous density profiles. For wind-like GRBs, the different inference techniques result in similar parameter distributions. Of course the sample of GRBs used in A21 is not in any way a statistically well-defined sample, and so the result need not agree.

4.5.2 Shock physics parameters

The accelerated particles exhibit a significantly harder spectrum with on average lower power-law indices, p, for synthetic GRBs in homogeneous environments, compared to the modelling results from A21. However, the differences for GRBs in wind-like environments are not significant. Curran et al. (2010) found a relatively wide distribution for p centred around 2.36 with a standard deviation of 0.59. The inferred synthetic population assuming homogeneous CBM, exhibit p values consistently lower than 2. Such hard electron distributions would significantly increase the synchrotron radiation efficiency. For GRBs in wind-like environments, the p distribution still extends to values lower than 2 more than in A21, but not nearly as extremely. These results point to two avenues of further research. The first is that they compound the impression already noted above that homogeneous environments are in tension with what we know from other avenues of inquiry, and so perhaps despite

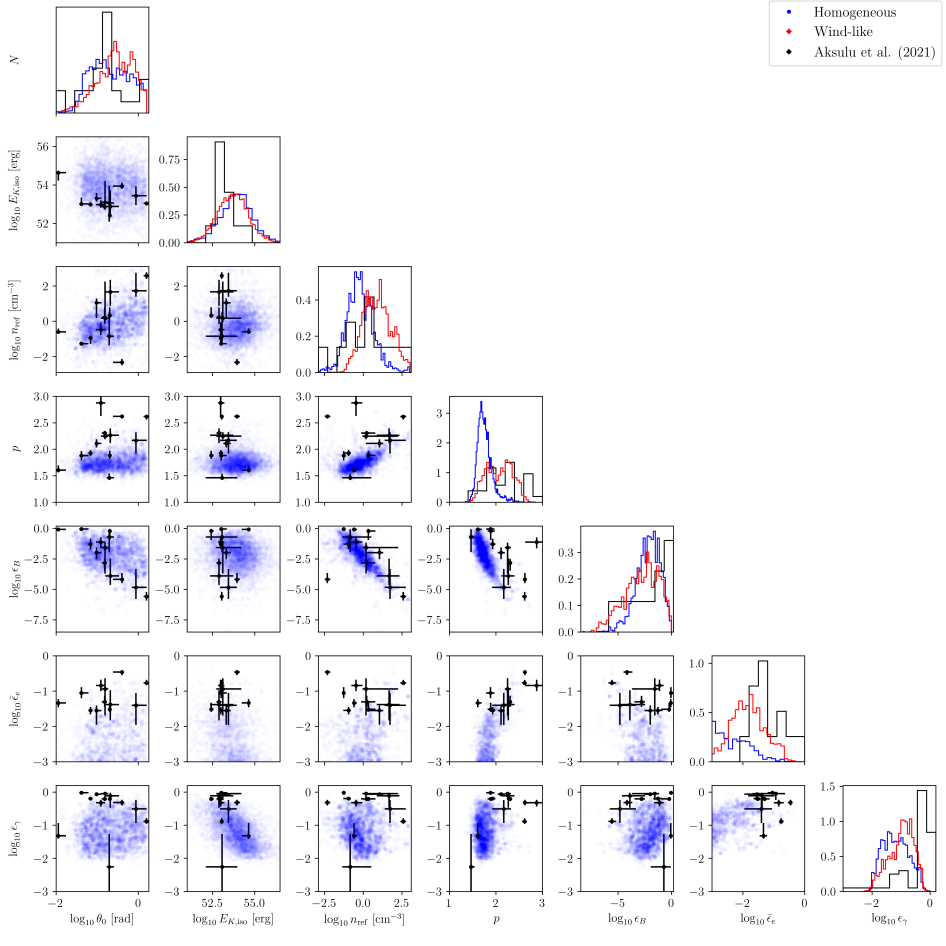

Figure 4.8: The parameter distributions for the synthetic population and broadband afterglow modelling efforts. The blue points represent the posterior predictive synthetic population assuming homogeneous environment. The black points are taken from Aksulu et al. (2021), which represent broadband afterglow modelling results favouring homogeneous environments. The red histogram represents the synthetic population in wind-like environments. The error bars represent the 68% credible interval.

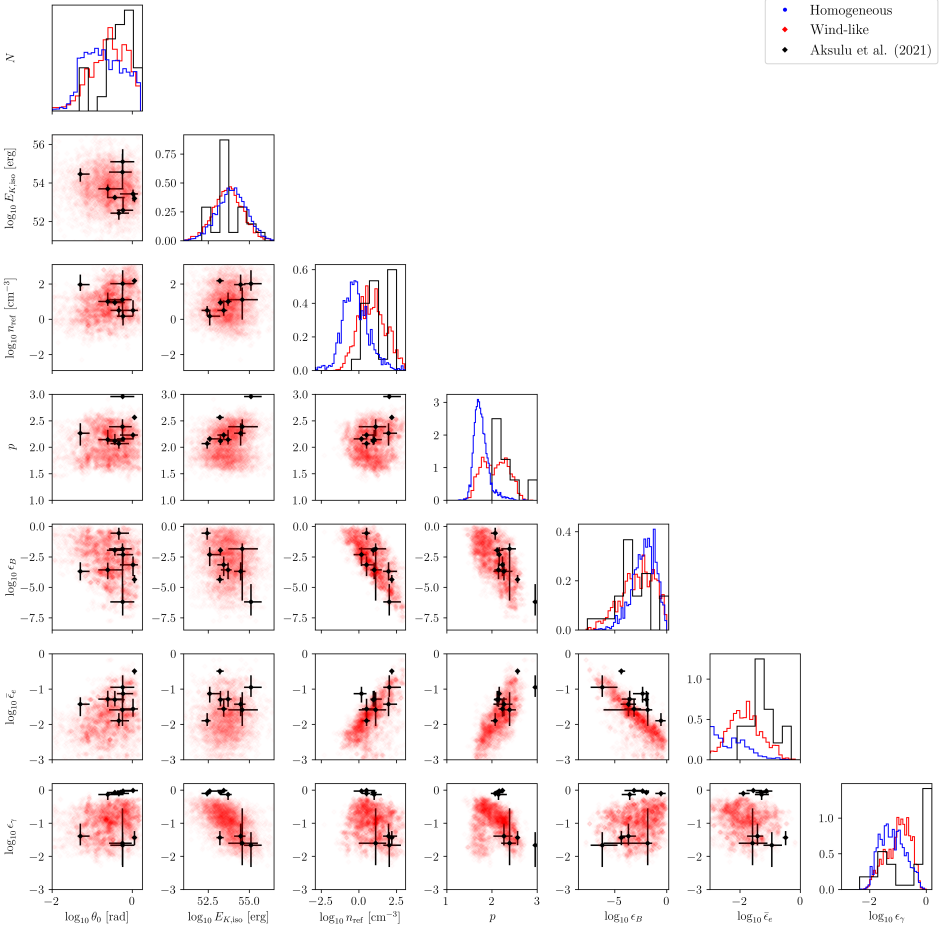

Figure 4.9: The parameter distributions for the synthetic population and broadband afterglow modelling efforts. The red points represent the posterior predictive synthetic population assuming wind-like environment. The black points are taken from Aksulu et al. (2021), which represent broadband afterglow modelling results favouring wind-like environments. The blue histogram represents the synthetic population in homogeneous environments. The error bars represent the 68% credible interval.

their acceptable fit quality per se we may need to consider discarding them. The second is that we require better understanding of the shock physics, especially whether a likely acceleration mechanism would predict frequent cases of $p < 2$, and if so, how one might model and constrain the energetics of the accelerated electron population.

We should iterate again that the fact that the energy fractions ϵ_e and ϵ_B approach unity in the fits is not in and of itself concerning. We have fitted parameter sets $(E_{K,\mathrm{iso}}, n_{\mathrm{ref}}, \epsilon_B, \bar{\epsilon}_e)$ here under the assumption that the fraction of electrons in the pre-shock medium that are accelerated into the post-shock high-energy power law distribution that we see emitting synchrotron radiation, ξ_N, is unity. However, as shown by Eichler & Waxman (2005), any parameter set $(E_{K,\mathrm{iso}}/\xi_N, n_{\mathrm{ref}}/\xi_N, \epsilon_B\xi_N, \bar{\epsilon}_e\xi_N, \xi_N)$ will give exactly the same dynamical and spectral evolution for any allowed $\xi_N < 1$. This degeneracy is of course why we cannot fit for ξ_N separately. Importantly, the physical constraints on the values of the energy fractions are that $\epsilon_B\xi_N < 1$ and $\epsilon_e\xi_N < 1$. Since it is quite plausible that $\xi_N \ll 1$, having one or both the ϵ's approach or even exceed unity in the fits may be allowed. This is true of course only to the extent that the required upward adjustments of the total energy and ambient density are still plausible. From the corner plots, we see there is room for that: for both assumed ambient medium models the highest values of ϵ_B are at the lower end of the densities, and highest energies are also mostly avoided by the high ϵ_B values. But the space is not more than about a factor 10. Similarly, for $\bar{\epsilon}_e$, there is also some room, except in one case of the A21 fits. So perhaps overall there is room for lowering ξ_N to about 0.1 before we get into tension with density and energetics, but not much more. This is in itself interesting, since it provides insight from external physical constraints into what ξ_N might be even though we cannot directly fit for it in the models.

4.5.3 Prompt efficiency

Detailed modelling of individual GRB afterglow data sets often results in energetics that indicate a prompt radiative efficiency $\epsilon_\gamma \sim 1$. Such high radiative efficiencies are difficult to explain for currently proposed radiation mechanisms. The population synthesis results indicate much more modest values for the prompt efficiency, when compared to the individual modelling results in A21. When we perform a KS-test for GRBs in homogeneous environments we are able to reject that the ϵ_γ vales are drawn from the same distribution as A21 with a p-value of 8.2×10^{-7}. The wind-like GRBs, on the other hand, result in a p-value of 4×10^{-3}, which we do not consider significant. Once again, the fact that the two samples have rather different selection effects can play a role in this discrepancy. From a physical viewpoint, lowering ξ_N can also come to the rescue here, since it increases the blast wave energy. The emitted gamma-ray energy is an observational result, and thus unchanged, so it lowers the required gamma-ray emission efficiency.

4.5.4 Robustness of the analysis

To investigate the robustness of our method with respect to the availability of broadband observations, we repeat the regression process for Phase II, as described in Section 4.3, by

Table 4.7: Mean and standard deviations of burst parameters for the posterior predictive synthetic populations when we neglect the R-band or radio afterglow data. We generate 50 GRBs per sample for a random selection of 1000 posterior samples. We include results for when we neglect the R-band and Radio afterglow data in our modelling.

Distribution		Homogeneous	(without)		Wind-like	(without)	
		All bands	R-band	Radio	All bands	R-band	Radio
$\log_{10}\epsilon_\gamma$	μ	−1.19	−1.10	−1.09	−0.99	−1.30	−1.14
	σ	0.44	0.45	0.45	0.42	0.41	0.48
$\log_{10}\theta_0$ [rad]	μ	−0.70	−0.64	−0.62	−0.57	−0.57	−0.64
	σ	0.46	0.46	0.46	0.44	0.44	0.44
$\log_{10} n_{\rm ref}\,[{\rm cm}^{-3}]$	μ	−0.20	−0.11	−0.62	0.89	0.99	0.73
	σ	0.90	1.27	1.46	0.90	0.92	1.07
p	μ	1.76	1.83	1.84	2.07	1.98	2.11
	σ	0.17	0.24	0.22	0.28	0.22	0.34
$\log_{10}\epsilon_B$	μ	−2.20	−2.88	−2.15	−2.80	−3.80	−2.61
	σ	1.13	1.41	1.22	1.59	1.90	1.47
$\log_{10}\bar{\epsilon}_e$	μ	−3.29	−3.03	−2.89	−2.23	−2.64	−2.36
	σ	0.97	1.40	1.02	1.03	1.06	1.23

excluding the R-band and radio afterglow observations, one at a time. The resulting parameter distributions from these fits are presented in Table 4.7. The posterior predictive distributions for the observables are presented in Figures 4.14 and 4.15 for missing R-band and radio data, respectively. The reader can see that the afterglow flux distributions cover a much wider range when the corresponding observing band is not included as a target distribution during the Bayesian inference procedure. This indicates a less constrained population of GRBs. However, as can be seen in Table 4.7, the distributions do not change drastically when we exclude R-band or radio data from the target distributions, which demonstrates that the results are not very much affected by missing data. The exception is the effect of missing optical data on ϵ_B: the mean value changes quite a bit, even by a factor 10 in the wind-like fits. This could be caused by the fact that lack of optical data especially hinders constraining the location of the cooling break, which is sensitive to ϵ_B.

4.5.5 Energetics, missing jet breaks, and GRB 130427A-like events

A study of the energetics of the explosion may be used to indicate the progenitor system. In 2001, a study of a moderate number of GRB light curves with their jet break times led (Frail et al., 2001) to find that the average prompt gamma-ray energy was always of the order of a few 10^{50} erg, similar to the energy produced in a SN II explosion. Successive studies in the *Swift* years have found that the distribution of GRB energies is much wider (Racusin et al., 2009), and several events had energy larger that 10^{51} erg (Cenko et al., 2011, e.g.,). The result of this work indicates that the average *beaming-corrected* kinetic energy in GRB afterglows ranges widely, with values 10^{50} - 10^{55} erg and also on average higher than these studies. There are two broad classes of scenario to explain the engine of a GRB.

One is the collapsar scenario, in which stellar matter, via a disk or torus, feeds the core of the star collapsed into a black hole and, via jets, powers a collimated explosion. The other scenario assumes that the core collapses in a newly born rapidly spinning magnetar, which again powers an explosion. The amount of explosion energy that can be delivered by each depends on rather complex physics, but roughly scales with the mass-energy of the central object. Most of the energies we derive are consistent with both cases, though the extreme high end probably requires the collapsar scenario, in which the central object mass is an order of magnitude higher. In Fig 4.6, no two populations are visible in the energetics. For the population synthesis we did not allow for that possibility in the model, but in the A21 results it could have emerged. However, this does not argue for a single mechanism for the energetics, since the range is much wider than the difference between their means, likely indicating that the energy conversions in both allow a wide range of outcomes.

4.5.5.1 GRB 130427A-like events

In their work, A21 gather that the brightest GRB of the last 30 years, GRB 130427A, possesses a relatively large opening angle $\theta_0 = 33^{+27}_{-9}$ degrees and a true kinetic energy, corrected for beaming, of $\simeq 10^{52}$ erg. Neither the opening angle nor the beaming-corrected kinetic energy appear particularly noteworthy in this study. We note though that, as De Pasquale et al. (2016) and A21 themselves pointed out, a kinetic energy $\simeq 10^{52}$ erg would imply an implausibly high gamma-ray efficiency $\epsilon_\gamma \simeq 0.99$ (but note our earlier caution that a lower ξ_N can fix this).

What makes GRB 130427A rather unique is that there is no sign of a steepening of the X-ray light-curve despite the fact that it was so bright that extends to 3 years after the GRB (formal 95% lower limit to the time of a break: 61 Ms), indicating that any jet break might be very late. As a result, its $E_{\rm true}$ should be considered a lower limit and the efficiency an upper limit. And in principle, there are conditions in the forward shock model for which we would basically never see a jet break. Since the jet break time in wind environment is at an epoch

$$\theta_{\rm jet} = \left(\frac{t_{\rm jet}}{1+z}\right)^{1/4} \left(\frac{E_{\rm K,iso,53}}{A_\star}\right)^{1/2} {\rm d} \tag{4.16}$$

(Chevalier & Li 2000), an event with a large semi-opening angle $\theta_{\rm jet} \simeq 0.6$ rad, $E_{\rm K,iso} = 10^{53}$ erg, $A_\star \simeq 0.01$ would theoretically lead to a jet break time of $\sim 10^5$ days. On the other hand, the distance of the ejecta reached at that time and thus the minimum size of the stellar wind bubble in this case is theoretically given by the formula

$$R = 16\, E^{1/2}_{K,iso,53} A^{-1/2}_{\star,-1} \left(\frac{t_6}{1+z}\right)^{1/2} {\rm pc}; \tag{4.17}$$

with the same parameter values above, we would have $R \simeq 30$ pc. To our knowledge, we do not detect such large stellar wind bubbles around single stars[1].

[1] Obviously, such ejecta could become non-relativistic first, but the example is indicative.

There is a link between the properties of the stellar wind and the density of the pre-explosion constant density medium. The radius of the region shaped by stellar wind, where density decreases as radius r^{-2}, is:

$$r_{\rm t} \simeq \dot{M}_{-5}^{1/3} n_{0,2}^{-1/2} \ {\rm pc} \tag{4.18}$$

(De Pasquale et al. 2016; Fryer et al. 2006), where n is the pre-wind density. It is easy to derive that $r_{\rm t} \simeq 20\,{\rm pc}$ requires a dense wind [1] ($A_\star > 10$) and external ISM density below $1\,{\rm cm}^{-3}$ (which is not high for star forming regions), and the upper limit by De Pasquale et al of $t = 60\,{\rm Ms}$. We thus take $r_{\rm t} \lesssim 20\,{\rm pc}$. Putting this value in equation 4.17, we find

$$13 \gtrsim E_{\rm K,iso,53}^{1/2} A_{\star,-1}^{-1/2} \left(\frac{t_6}{1+z} \right)^{1/2}. \tag{4.19}$$

In order to understand what fraction of GRBs have similar X-ray light curves to GRB 130427A, we generate a population 50 000 GRBs, by randomly sampling 1000 posterior samples and generating 50 GRBs per sample. Moreover, we select GRBs which satisfy the conditions

1. a jet-break at the earliest 90 Ms after the burst,
2. an observed afterglow X-ray flux at 90 Ms which is larger or equal to GRB 130427A, i.e., 2.9×10^{-7} mJy at 1 keV
3. and a "realistic" blast wave radius which is smaller than 15.3 pc (50 ly).

We find that, given the above conditions, $\sim$ 6% of the detected long GRBs in wind-like environments should have similar features to GRB 130427A. When we relax the condition for the blast wave radius (iii), we find that the number of GRBs with late-time jet-breaks and high X-ray flux doubles to $\sim$ 14%. In this analysis we assumed an on-axis observer when calculating $t_{\rm jet}$. If one assumes large observer angles (which is realistically the case), the number of GRBs with large $t_{\rm jet}$ should be even larger. Our study thus suggests that GRB 130427A is certainly not common, but neither is it particularly rare.

In the case of the values found by A21 and GRB 130427A, we have $E_{\rm K,iso,53}^{1/2} A_{\star,-1}^{-1/2} (\frac{t_6}{1+z})^{1/2} \simeq 5.4$. Thus, these parameters do not violate Eq. 4.19 and the fact that we do not see a jet break is consistent with the forward shock model until the limit on the jet break time were raised by another factor 5 or so. It is important to keep in mind that for such extreme parameters the validity of the above equations also ends, specifically because they assume the jet is still ultra-relativistic when it breaks. By equating the swept-up wind mass to $E_{\rm K,iso}/c^2$, we find that this requires a radius less than

$$r_{\rm NR} = 5.7 E_{\rm K,iso,53} \left(\frac{A}{A_\star} \right)^{-1} {\rm pc}. \tag{4.20}$$

At $r = r_{\rm NR}$, the ejecta enter the non-relativistic expansion. In this case, the forward shock model predicts that the decay slope of the X-ray afterglow would also change, creating a

[1] Strictly speaking, $\dot{M}_{-5} = 1$ implies $A_\star = 1$ only if the stellar wind has a speed of $1000\,{\rm km\,s^{-1}}$. However, Eq. 4.18 depends on $\dot{M}^{1/3}$ only, so we can take this rough equality if the wind speed is within a factor few of the reference value.

break in the light-curve. For GRB 130427A, $r_{\rm NR}$ corresponds to about 3 pc, similar to the jet break limit we have derived, and so either a jet break or a break to the non-relativistic regime could plausibly come first in this case. This does indicate that future X-ray facilities such as ATHENA (Nandra et al., 2013), with sensitivities approaching $\sim 10^{-16}$ erg cm^{-2} s^{-1}, will be able to probe both these transitions in a plausible number of GRB afterglows, and thus test the validity of the forward shock model on which our works are based.

4.6 Conclusion

In this study, we developed a method to produce populations of GRBs, which are consistent with the observed features of the BAT6 sample.

1. The dynamics, energetics and environments of the inferred population are in line with broadband modelling results. All of the inferred parameter distributions are relatively wide and do not support the idea that there is a single value for the whole population.
2. When we assume homogeneous environments, there is significant tension between the population synthesis and broadband modelling results for the shock physics parameters. The differences are marginal for GRBs in wind-like environments.
3. The prompt efficiency inferred from population synthesis is on average lower when compared to A21, for both type of CBM density profiles. In the case homogeneous environments there is a significant difference between individual modelling and population synthesis results.
4. A significant fraction of GRBs have a power-law index $p < 2$ for the accelerated particle distributions; for ISM-like environments, it is even the vast majority.
5. $\sim 6\%$ of GRBs in wind-like environments should exhibit a jet-break at late-times $t > 90$ Ms consistent with the observed light curve of GRB 130427A.
6. Future, more sensitive, observatories *Max: like ATHENA* will be invaluable at testing the forward shock model by probing the jet-breaks and/or transrelativistic phase at late times (several years after the burst).

Acknowledgements

This work was carried out on the Dutch national e-infrastructure with the support of SURF Cooperative. H. J. van Eerten acknowledges partial support by the European Union Horizon 2020 Programme under the AHEAD2020 project (grant agreement number 871158). MDP thanks Istanbul University Bilimsel Araştırma Projeleri (BAP) project no. 30901, "Studying GRB Physics with Athena, ESA's next flagship mission". MDP thanks Mr. M. D. Ilhan as well.

Appendices

Table 4.8: The observed features of the BAT6 sample. In this table we present the measured redshifts (z), isotropic-equivalent γ-ray energies ($E_{\gamma,\mathrm{iso}}$), spectral peak energies in the rest-frame ($E_{\mathrm{peak,rest}}$), and measured photon count in the 15-150 keV band of the Swift/BAT instrument. We also present the measured flux values of the afterglow emission in X-rays, R-band and radio bands. The R-band measurements have been corrected for dust extinction. We omit any upper limits in this table. Missing values are denoted by "-". See Section 4.2 for details.

Burst name	z	$E_{\gamma,\mathrm{iso}}/10^{52}$ (erg)	$E_{\mathrm{peak,rest}}$ (keV)	Photon count (ph $\mathrm{s}^{-1}\mathrm{cm}^{-2}$)	X-ray $f_\nu \times 10^3$ (μJy) @ 11h	@ 24h	R-band f_ν (μJy) @ 11h	Radio f_ν (μJy)
050318	1.440	1.69 ± 0.17	115 ± 27	3.16 ± 0.20	57.10	12.74	61	-
050401	2.900	40.60 ± 0.84	499 ± 117	11.80 ± 1.18	247.47	82.49	4	122 ± 33
050416A	0.650	0.09 ± 0.01	26 ± 4	4.88	75.46	37.50	9	260 ± 55
050525A	0.610	2.32 ± 0.06	127 ± 6	41.70 ± 0.94	102.68	30.98	53	63
050802	1.710	-	-	2.56 ± 0.35	73.24	26.98	32	-
050922C	2.200	3.74 ± 0.37	416 ± 118	7.06 ± 0.33	48.56	13.40	46	140 ± 42
060206	4.050	4.10 ± 0.21	409 ± 116	2.79 ± 0.17	49.20	25.76	133	-
060210	3.910	25.30 ± 1.90	574 ± 187	2.70 ± 0.28	422.45	149.00	7	-
060306	3.500	8.26 ± 1.12	315 ± 135	5.96 ± 0.36	112.98	49.21	-	-
060614	0.130	0.25 ± 0.10	55 ± 45	11.40 ± 0.78	388.59	139.75	122	-
060814	1.920	30.70 ± 2.97	750 ± 245	7.27 ± 0.28	236.59	71.28	-	-
060904A	-	-	-	4.87 ± 0.20	65.30	25.96	-	-
060908	1.880	4.41 ± 0.18	426 ± 207	3.03 ± 0.25	17.93	5.72	9	-
060912A	0.940	-	-	8.42 ± 0.46	21.58	9.57	10	-
060927	5.470	7.56 ± 0.46	459 ± 90	2.70 ± 0.17	9.23	2.93	9	-
061007	1.260	101.00 ± 1.40	965 ± 27	15.20 ± 0.41	84.54	25.91	54	-
061021	0.350	0.46 ± 0.08	1046 ± 485	6.11 ± 0.26	262.03	108.32	36	-
061121	1.310	27.20 ± 1.87	1402 ± 185	20.90 ± 0.51	546.25	165.78	29	304 ± 48
061222A	2.090	-	-	3.49 ± 0.08	718.50	275.83	-	285 ± 68
070306	1.500	-	-	4.14 ± 0.24	840.25	201.32	-	-
070328	-	-	-	4.21 ± 0.24	179.65	58.94	-	-
070521	1.350	-	-	6.59 ± 0.28	112.91	21.34	-	-
071020	2.150	8.65 ± 1.53	1013 ± 204	8.31 ± 0.26	202.66	68.63	6	186 ± 26
071112C	0.820	-	-	-	24.53	7.47	9	-
071117	1.330	-	-	11.00 ± 0.41	59.22	26.99	-	-
080319B	0.940	142.00 ± 3.00	1307 ± 43	24.80 ± 0.50	288.41	64.89	67	232 ± 42
080319C	1.950	14.60 ± 2.60	1752 ± 504	5.14 ± 0.34	145.83	38.98	20	-
080413B	1.100	1.65 ± 0.06	163 ± 34	18.30 ± 0.85	152.14	69.83	52	86 ± 36

Table 4.9: Continuation of Table 4.8.

Burst name	z	$E_{\gamma,\mathrm{iso}}/10^{52}$ (erg)	$E_{\mathrm{peak,rest}}$ (keV)	Photon count (ph $\mathrm{s}^{-1}\mathrm{cm}^{-2}$)	X-ray $f_\nu \times 10^3$ (μJy) @ 11h	@ 24h	R-band f_ν (μJy) @ 11h	Radio f_ν (μJy)
080430	0.770	-	-	2.63 ± 0.18	195.63	81.49	59	-
080602	-	-	-	2.83 ± 0.24	2060.98	1445.05	-	-
080603B	2.690	9.41 ± 2.45	376 ± 214	3.53 ± 0.17	202.17	105.38	70	-
080605	1.640	22.10 ± 0.88	665 ± 48	19.60 ± 0.62	138.50	35.39	34	-
080607	3.040	186.00 ± 10.00	1691 ± 169	23.00 ± 1.10	50.01	16.02	1	-
080613B	-	-	-	2.74 ± 0.18	-	-	-	-
080721	2.590	121.00 ± 10.00	1785 ± 223	6.35 ± 0.35	477.85	150.46	62	-
080804	2.200	11.40 ± 0.40	810 ± 45	3.01 ± 0.46	48.20	20.44	13	-
080916A	0.690	0.92 ± 0.03	208 ± 11	2.67 ± 0.16	116.92	45.55	10	-
081007	0.530	0.17 ± 0.01	61 ± 15	2.75 ± 0.36	138.16	55.46	26	320 ± 30
081121	2.510	30.50 ± 2.60	608 ± 42	4.19 ± 1.01	304.48	99.53	50	-
081203A	2.100	35.00 ± 12.80	1541 ± 756	2.78 ± 0.21	26.85	7.86	110	-
081221	2.260	-	-	17.30 ± 0.51	205.49	75.23	-	97 ± 38
081222	2.770	25.20 ± 2.30	630 ± 31	7.46	205.77	55.00	5	-
090102	1.550	21.40 ± 0.40	1174 ± 38	5.38 ± 0.80	136.92	44.78	10	-
090201	-	-	-	14.60 ± 1.05	328.04	111.82	-	-
090424	0.540	3.97 ± 0.08	250 ± 3	69.40	720.19	348.74	131	673 ± 39
090709A	-	-	-	7.69 ± 0.29	505.22	163.45	-	-
090715B	3.000	21.30 ± 3.00	536 ± 164	3.73 ± 0.19	93.68	37.24	24	231 ± 47
090812	2.450	40.50 ± 5.30	2023 ± 663	3.57 ± 0.20	90.64	36.71	2	104 ± 43
090926B	1.240	3.96 ± 0.06	212 ± 4	3.10 ± 0.34	57.19	24.34	11	-
091018	0.970	0.80 ± 0.09	55 ± 26	9.70 ± 0.41	103.11	33.23	39	-
091020	1.710	7.96 ± 1.16	507 ± 68	4.17 ± 0.23	122.49	41.46	138	230 ± 42
091127	0.490	1.61 ± 0.03	51 ± 2	44.30 ± 2.78	1435.42	441.67	231	-
091208B	1.060	1.97 ± 0.06	246 ± 15	15.10 ± 1.06	113.16	48.28	26	-
100615A	-	-	-	5.37 ± 0.20	1112.05	430.42	-	-
100621A	0.540	4.35 ± 0.48	146 ± 23	12.70 ± 0.27	948.21	364.47	502	130 ± 24
100728B	2.106	2.98 ± 0.13	404 ± 29	3.37	17.70	5.29	13	-
110205A	2.220	55.90 ± 5.30	715 ± 238	3.57	44.53	13.32	77	26 ± 2
110503A	1.613	18.00 ± 1.40	572 ± 50	29.70 ± 1.39	195.46	67.23	62	31 ± 3

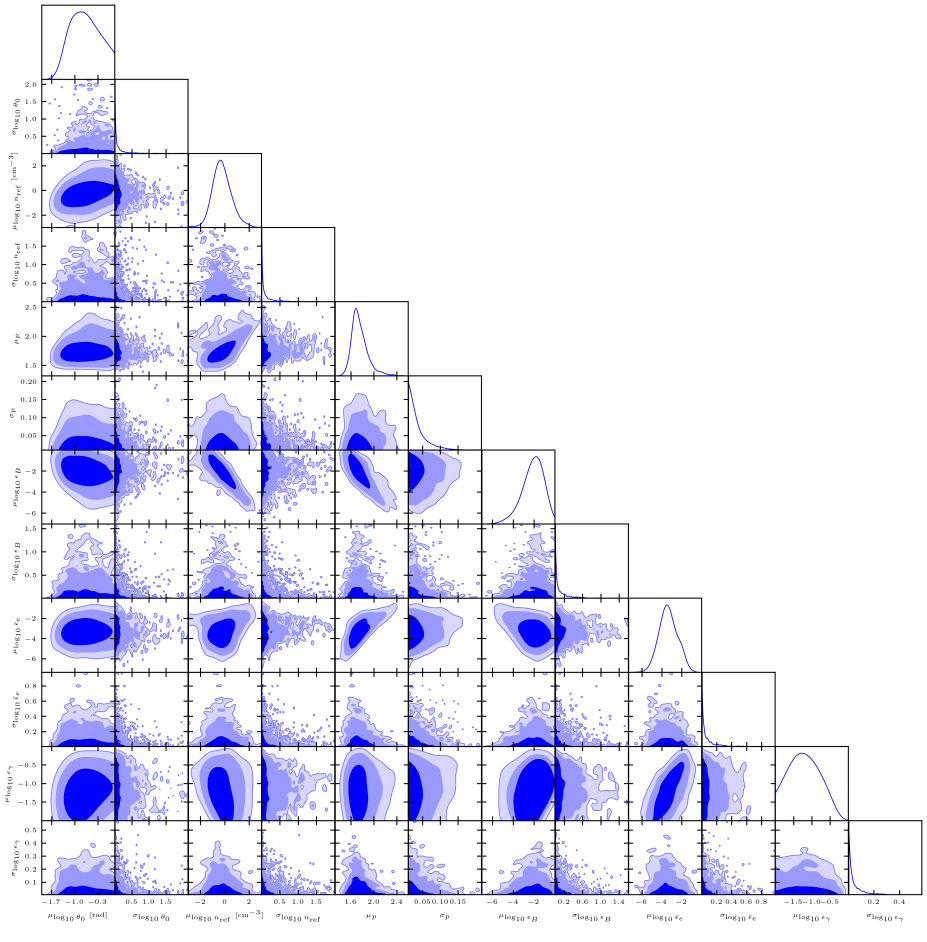

Figure 4.10: Posterior distributions for the Phase II parameters assuming homogeneous environment for the GRB population. The parameters are as defined in Table 4.1.

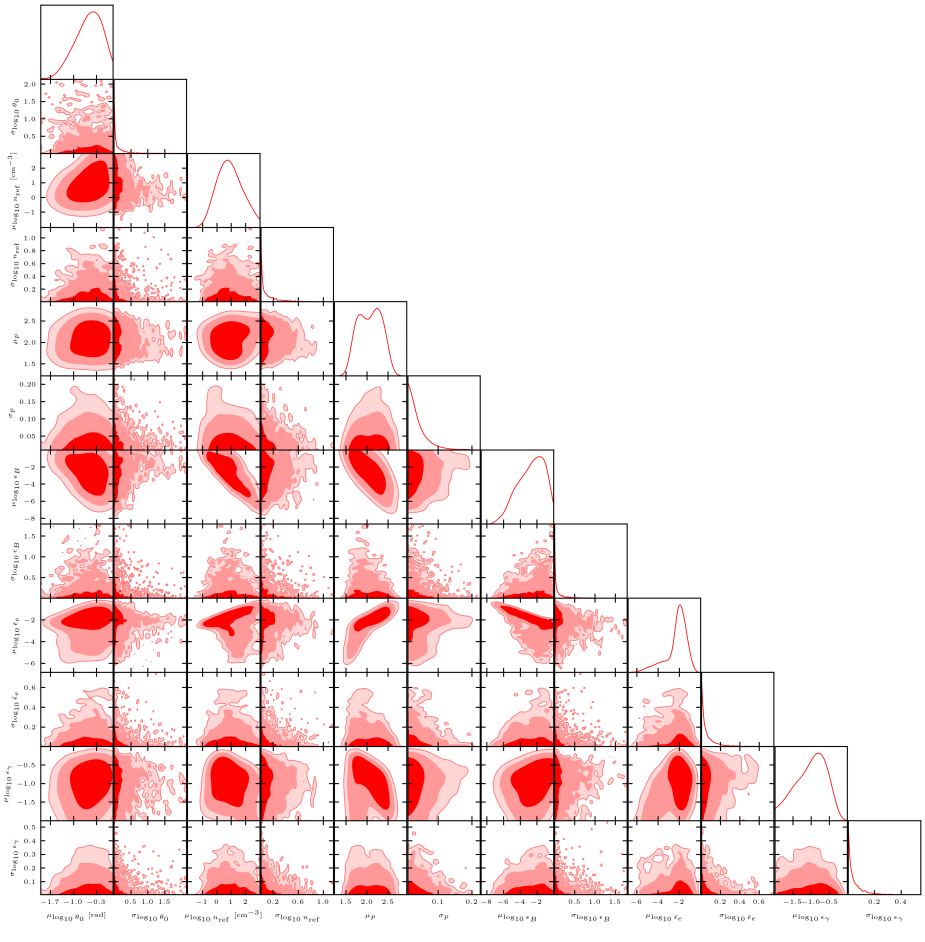

Figure 4.11: Posterior distributions for the Phase II parameters assuming wind-like environment for the GRB population. The parameters are as defined in Table 4.1.

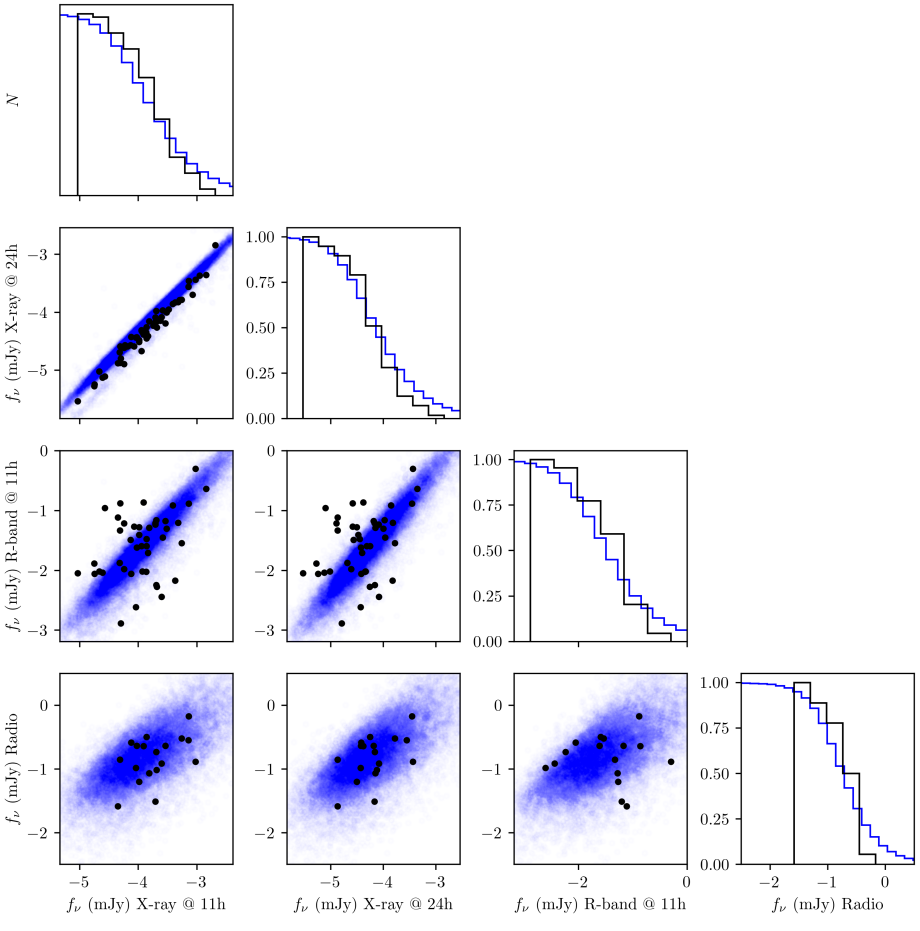

Figure 4.12: Posterior predictive results for Phase II in the form of a corner plot assuming homogeneous CBM. We combine the population observables from a randomly selected sample of 500 posterior samples. For each posterior sample we generate 50 GRBs. The $\log_{10}$ of the flux values are presented. Black points represent the BAT6 sample observables, whereas the blue points represent the synthetic population.

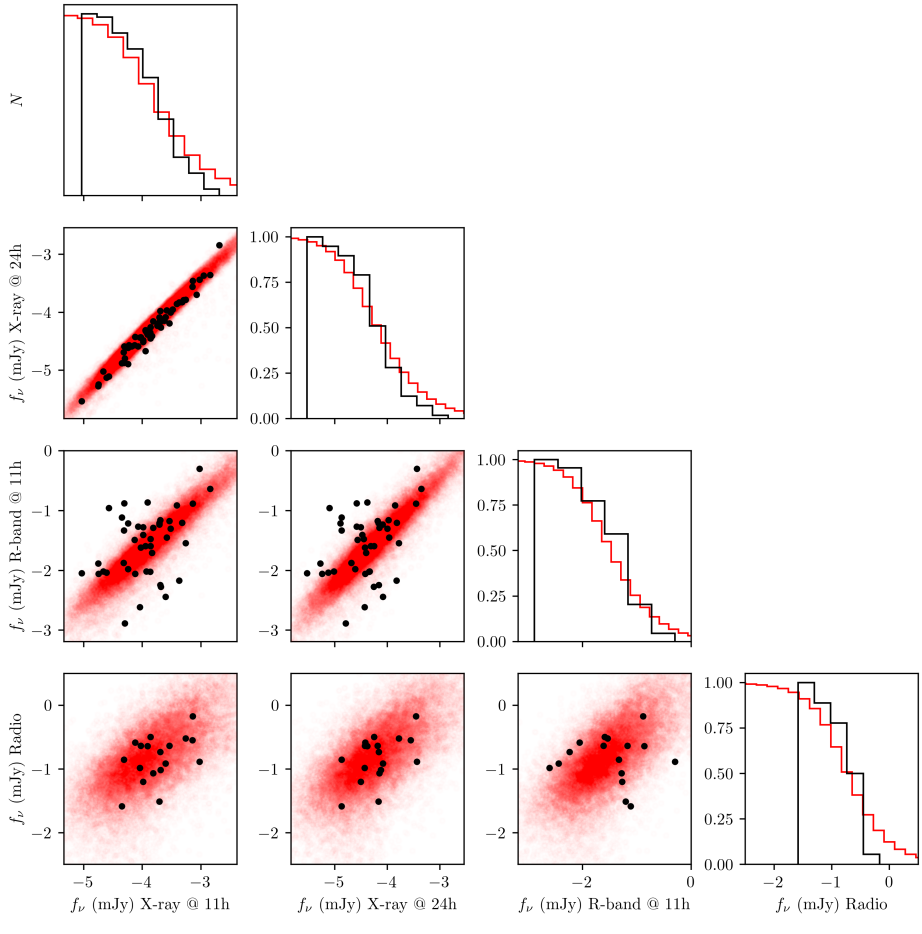

Figure 4.13: Same as Figure 4.12, however, for wind-like CBM.

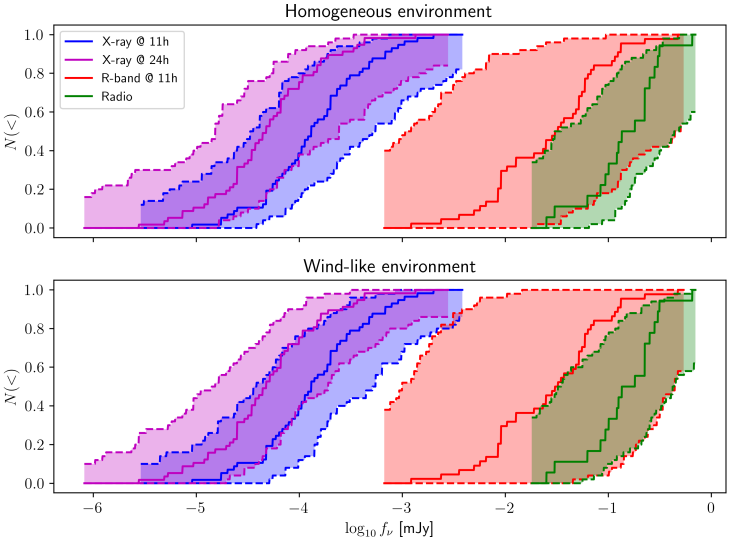

Figure 4.14: Posterior predictive results for Phase II, without accounting for the optical afterglow counterpart.

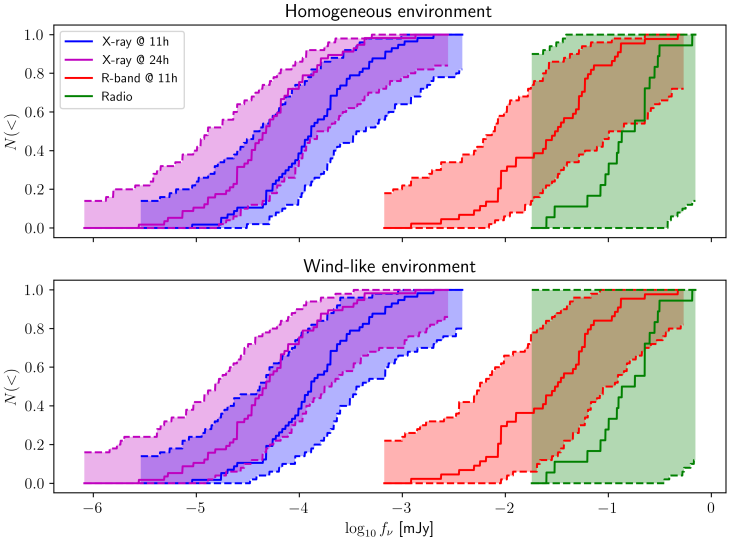

Figure 4.15: Same as Figure 4.14, this time we neglect the radio afterglow counterpart instead of the optical.

Chapter 5

Rapid-response radio observations of short GRB 181123B with the Australia Telescope Compact Array

G. E. Anderson, M. E. Bell, J. Stevens, M. D. Aksulu, J. C. A. Miller-Jones, A. J. van der Horst, R. A. M. J. Wijers, A. Rowlinson, A. Bahramian, P. J. Hancock, J.-P. Macquart, S. D. Ryder, R. M. Plotkin

Monthly Notices of the Royal Astronomical Society, 2021, 503, 3, p.4372–4386

Abstract

We introduce the Australia Telescope Compact Array (ATCA) rapid-response mode by presenting the first successful trigger on the short-duration gamma-ray burst (GRB) 181123B. Early-time radio observations of short GRBs may provide vital insights into the radio afterglow properties of Advanced LIGO- and Virgo-detected gravitational wave events, which will in turn inform follow-up strategies to search for counterparts within their large positional uncertainties. The ATCA was on target within 12.6 hr post-burst, when the source had risen above the horizon. While no radio afterglow was detected during the 8.3 hr observation, we obtained force-fitted flux densities of 7 ± 12 and $15 \pm 11 \mu$Jy at 5.5 and 9 GHz, respectively. Afterglow modelling of GRB 181123B showed that the addition of the ATCA force-fitted radio flux densities to the *Swift*-XRT detections provided more stringent constraints on the fraction of thermal energy in the electrons ($\log \epsilon_e = -0.75^{+0.39}_{-0.40}$ rather than $\log \epsilon_e = -1.13^{+0.82}_{-1.2}$ derived without the inclusion of the ATCA values), which is consistent with the range of typical ϵ_e derived from GRB afterglow modelling. This allowed us to predict that the forward shock may have peaked in the radio band ~ 10 days post-burst, producing detectable radio emission $\gtrsim 3-4$ days post-burst. Overall, we demonstrate the potential for extremely rapid radio follow-up of transients and the importance of triggered radio observations for constraining GRB blast wave properties, regardless of whether there is a detection, via the inclusion of force-fitted radio flux densities in afterglow modelling efforts.

5.1 Introduction

The first gravitational wave (GW) detection of a binary neutron star (BNS) merger, GW170817, by the Advanced LIGO and Virgo (aLIGO/Virgo) facilities, was an eagerly awaited event (Abbott et al., 2017b). Such a merger was predicted to produce a multi-wavelength electromagnetic afterglow radiating from radio to gamma-rays, and GW170817 did not disappoint (Abbott et al., 2017c; Andreoni et al., 2017). The most conspicuous predicted counterpart was the prompt ejection of collimated, short-lived gamma-ray emitting jets, similar to the observed short gamma-ray burst (SGRB, gamma-ray durations < 2 s; Narayan et al., 1992) phenomenon, which is one of the two main classes of gamma-ray burst (GRB; Norris et al., 1984; Dezalay et al., 1992; Kouveliotou et al., 1993) detected by the *Neil Gehrels Swift Observatory* (hereafter *Swift*; Gehrels et al., 2004) Burst Alert Telescope (BAT) and the *Fermi Gamma-ray Space Telescope* (hereafter *Fermi*) Gamma-ray Burst Monitor (GBM; Meegan et al., 2009). The other dominant population known as long GRBs (LGRBs) typically have durations > 2 s and are attributed to core collapse supernovae (e.g. Galama et al., 1998b; Bloom et al., 1998b). It was therefore the near-simultaneous detection of GW170817 and GRB 170817A (the latter of which was a SGRB detected by *Fermi*; Abbott et al., 2017c) and the late-time radio and X-ray follow-up confirming the presence of an off-axis jet (e.g. Mooley et al., 2018; Ghirlanda et al., 2019; Troja et al., 2019b) that strongly supported the link between BNS mergers and SGRBs.

The detection of the electromagnetic counterpart to a aLIGO/Virgo-detected BNS merger is of great importance as it enables the localisation of the source, along with providing complementary information such as an independent distance measurement, insight into the central engine, the energy released, and the final merger remnant. However, the initial localisation of a GW event by aLIGO/Virgo is tens to hundreds of square degrees, making it difficult to search for counterparts. We therefore introduce a method designed to exploit the established link between GW-detected BNS mergers and SGRBs by using the Australia Telescope Compact Array (ATCA) rapid-response mode to trigger on *Swift*-detected SGRBs.

While the radio emission from SGRBs is usually short-lived ($\lesssim 2$ days; Fong et al., 2015), the ATCA rapid-response mode is capable of being on-source within 10 minutes. By rapidly responding to *Swift* SGRB triggers, ATCA can become a new diagnostic tool for uncovering the range of radio behaviour shown by SGRBs to help interpret what to look for from GW events that have off-axis gamma-ray jets. As targeted observations can usually reach deeper sensitivities than wide-field surveys, ATCA observations can provide a template of the radio brightness and timing properties of BNS mergers, which will in-turn inform the follow-up strategies of the next era of aLIGO/Virgo GW events by wide-field radio telescopes, such as Australian instruments like the Murchison Widefield Array (MWA; Tingay et al., 2013) and the Australian Square Kilometre Array Pathfinder (ASKAP; Johnston et al., 2008).

The jet launched during an SGRB is expected to produce a radio afterglow as predicted by the fireball model (Cavallo & Rees, 1978; Rees & Mészáros, 1992). In this model, the relativistic ejecta interact with the circumstellar medium (CSM) producing a forward shock that accelerates electrons and generates synchrotron emission. Reverse shock synchrotron

emission, produced by the shock that propagates back into the post-shock ejecta, may also be observed depending on the density of the CSM and the ejecta. The broadband spectrum produced by the jet interactions in the GRB afterglow is described by the peak flux and 3 characteristic frequencies (ν_m, the minimum electron energy frequency; ν_{sa}, the synchrotron self-absorption frequency; and ν_c, the electron cooling frequency), which evolve over time (Sari et al., 1998; Wijers & Galama, 1999; Granot et al., 1999). Only early-time radio observations are able to properly constrain 2 of these 3 frequencies (ν_m and ν_{sa}), and also disentangle the reverse and forward shock components. By combining ATCA observations with multi-wavelength observations to perform SED modelling, these parameters can be derived, thus providing information about the blast wave kinetic energy, the CSM density, the magnetic field energy density and the power law electron energy distribution (Sari et al., 1998; Wijers & Galama, 1999; Granot et al., 1999). Limits on the linear polarisation of the reverse shock can also provide information on the jet magnetic field structure (Granot & van der Horst, 2014). Early-time radio observations of SGRBs are also sensitive to temporal steepening from the jet-break (Sari et al., 1999), which constrains the jet opening-angle used to calculate the true energy released (and therefore merger BNS/GW event rates, e.g. Fong et al., 2014, 2015; de Ugarte Postigo et al., 2014). Even early-time non-detections in the radio band can allow us to make predictions about when the forward-shock emission may peak, which can inform the cadence and duration of follow-up radio observations, potentially optimising the success of a late-time detection as we demonstrate in this paper. In addition, sensitive, multi-frequency, high-cadence radio observations may allow us to distinguish between more exotic emission models caused by the ejection of neutron star material or the propagation of shocks caused by the merger event, which may produce non- to ultra-relativistic omnidirectional radio emission (e.g. Nakar & Piran, 2011; Kyutoku et al., 2014). It is therefore crucial to obtain early-time radio observations (within minutes to days) of a larger sample of SGRBs to better characterise the timescales and frequencies necessary for understanding the range of behaviours we might expect from GW radio counterparts.

There are also several BNS merger models that suggest a short-lived, supramassive and highly magnetised neutron star (NS) or "magnetar", supported by rotation, can exist for a short time ($< 10^4$ s) before finally forming a stable magnetar or further collapsing into a black hole (BH, e.g. Usov, 1992; Zhang & Mészáros, 2001; Falcke & Rezzolla, 2014; Zhang, 2014). Evidence for such merger products comes from the detection of a "plateau phase" in some SGRB X-ray light curves between $\sim 10^2 - 10^4$ s post-burst, where this departure from power-law decay indicates ongoing energy injection (Rowlinson et al., 2013). Such merger remnant scenarios may be sources of prompt, coherent radio emission (see Rowlinson et al., 2016, for a review). However, no continuous monitoring of the radio behaviour has yet been performed at GHz frequencies during the plateau phase. Such detections or upper limits could constrain different central engine models as has been done at late-times (e.g. Fong et al., 2016).

Only eight SGRBs have published detections in the radio band to date: GRB 050724A, 051221A, 130603B, 140903A, 141212A, 150424A, 160821B and 200522A (Berger et al., 2005; Soderberg et al., 2006; Fong et al., 2014, 2015, 2017; Troja et al., 2016; Zhang et al.,

2017; Troja et al., 2019a; Lamb et al., 2019; Fong et al., 2021). Note that this does not include GW170817 as it had a far more off-axis outflow than standard cosmological SGRBs so the corresponding radio afterglow was detected much later when the ejecta had moved into our line-of-sight (Mooley et al., 2018). Out of a sample of > 70 radio-observed SGRBs, only $\sim 10\%$ have been detected in the radio band at GHz frequencies (Fong et al., 2021). This low detection rate may be due to an observed fast rise in radio emission with a potentially short radio afterglow lifetime. For example, 7 of the 8 radio-detected SGRBs were detected within 1 day post-burst, at least half of which faded below detectability within ~ 2 days (see Figure 5.1). Given these short timescales, it is possible the radio emission is frequently dominated by the reverse-shock (as was the case for GRB 051221A; Soderberg et al., 2006) since simulations of BNS mergers demonstrate forward shock radio emission may evolve over days to weeks (Hotokezaka et al., 2016) as is also the case for many LGRBs (e.g. van der Horst et al., 2008, 2014). If we instead compare the radio-detected sample to those SGRBs that were initially observed at radio wavelengths < 1 day post-burst, this gives a much higher radio detection rate of $\sim 30\%$ (Fong et al., 2015). However, while the first four radio-detected SGRBs showed initial flux densities of > 0.1 mJy/beam at GHz frequencies, few of the other < 1 day post-burst pre-2016 observations had sufficient sensitivity to detect a predicted peak flux density of $\sim 40\mu$ Jy/beam at 10 GHz for an SGRB at an average redshfit of $z = 0.5$ with an expected CSM density of $n_0 \sim 0.1\,\mathrm{cm}^{-3}$ (Berger, 2014). In fact, the four most recent radio-detected SGRBs peak at $\lesssim 40\mu$ Jy/beam.

The small sample of radio detected SGRBs therefore provides limited knowledge of their radio afterglow brightnesses and timescales, and is insufficient for deriving the energy outputs and environmental properties of the population through multi-wavelength modelling. It is therefore vital to perform both rapid and sensitive radio follow-up observations of SGRBs to capture these short-lived and faint events. The key to achieving this is through the use of rapid-response (also known as triggering) systems, where a telescope has the ability to automatically respond to a transient alert, and either repoint at the event or update its observing schedule to begin observations when the source has risen above the horizon. Rapid-response radio telescopes have been in use since the 1990's (for example see Green et al., 1995; Dessenne et al., 1996; Bannister et al., 2012; Palaniswamy et al., 2014; Kaplan et al., 2015) but predominantly at low radio frequencies (100 MHz to 2.3 GHz), with the majority of experiments being designed to search for prompt, coherent radio emission. However, until recently, the only high frequency (> 5 GHz) rapid-response program designed to target incoherent (synchrotron) radio emission from GRBs has been run on the Arcminute Microkelvin Imager (AMI) Large Array (LA), known as ALARRM (the AMI-LA Rapid Response Mode), which has been active since 2012 (Staley et al., 2013; Anderson et al., 2018b). It was only through ALARRM that it was possible to be on-source fast enough to detect the rise and peak in the reverse-shock radio emission at 15 GHz from GRB 130427A within 1 day post-burst, which also represents one of the earliest radio detections of a GRB to date (Anderson et al., 2014). In addition, the radio catalogue of AMI observations of 139 GRBs (12 were short GRBs but non-detections), the majority of which were automatically triggered on using the rapid-response mode within 1 day post-burst, was the first representative sample of GRB radio properties that was unbiased by multi-wavelength selection criteria (Anderson et al.,

2018b). This work revealed that possibly up to $\sim 44-56\%$ of *Swift*-detected LGRBs have a radio counterpart (down to $\sim 0.1-0.15$ mJy/beam), with the increase in detection rate from previous studies ($\sim 30\%$; Chandra & Frail, 2012) likely being due to the AMI rapid-response mode, which allows observations to begin while the reverse-shock is contributing to the radio afterglow. This program has motivated the installation of a rapid-response mode on the ATCA.

Here we present the first triggered observation of a SGRB using the new ATCA rapid-response mode. ATCA is an ideal instrument for performing triggered radio follow-up of *Swift* SGRBs due to its high sensitivity and broadband receivers that provide simultaneous multi-frequency coverage. The ATCA response times (which can be as short as minutes) have the potential to be much faster than the current median SGRB response of the Karl G. Jansky Very Large Array (VLA; ~ 24.7 hrs), which rely on manually scheduling target-of-opportunity observations (Fong et al., 2015). In Section 2, we describe the ATCA rapid-response system from the observer interaction (front-end) level and the observatory (back-end) level. In Section 3, we describe the triggered ATCA observation and data reduction of GRB 181123B, and corresponding results. This is followed by a comparison of our radio limits for GRB 181123B to the sample of radio-detected SGRBs and a discussion of the parameter space that the triggered ATCA observations are probing in Section 4. Finally, we perform modelling of the GRB 181123B afterglow and thus demonstrate the usefulness of obtaining early-time (within 1 day) radio observations of an SGRB (regardless of whether or not there is a detection) to place constraints on the GRB physics.

5.2 ATCA rapid-response mode

ATCA is a six element, 22 m dish, East-West interferometer based in New South Wales in Australia. Its maximum baseline length is 6 km and it is capable of observing in multiple, broad frequency bands with full polarisation, and in a variety of array configurations. ATCA is currently equipped with the Compact Array Broadband Backend (CABB; Wilson et al., 2011), which has a 2 GHz bandwidth that is capable of observing in two frequency bands simultaneously with tunable receivers that operate between 1.1-105 GHz.

Since 2017 April 18, ATCA has been capable of rapidly responding to transient alerts. The rapid-response mode can trigger using the 16 cm, 4 cm and 15 mm receivers, corresponding to a usable frequency range of $1.1-25$ GHz, and can observe in any CABB mode. In the following, we describe both the observer front-end and the observatory back-end of this new triggering system.

5.2.1 VOEvent parsing/front-end

The front-end software we use to interface with the ATCA rapid-response system (VO_ATCA)[1] is designed to trigger on Virtual Observatory Events (VOEvent; Seaman et al. 2011), which are the standard format for broadcasting machine readable astronomical alerts related to

[1] https://github.com/mebell/vo_atca

transient events. A VOEvent package contains all the required data (in XML format) that allow automated decisions to be made in real-time given certain keywords and parameters. VOEvents are brokered via the 4 Pi Sky VOEvent Broker (Staley & Fender, 2016) and the COMET VOEvent client (Swinbank, 2014). These packages allow us to listen to multiple VOEvent streams, including those broadcast by *Swift*. We use the PYTHON package VOVENTPARSE (Staley, 2014) as the main tool to read the VOEvents and to extract the required information to be assessed by the triggering algorithm.

Upon receiving a *Swift* VOEvent, the ATCA VOEvent parser uses the keyword GRB_IDENTIFIED = TRUE to initially identify a GRB packet. Packets containing STARTRACK_LOST_LOCK=TRUE are ignored as it means that *Swift* has lost its celestial position-lock so such an alert is unlikely to be from a real transient. While the observatory back-end prevents the telescope from overriding for sources that are too far north (see Section 5.2.2), we impose an additional declination cut-off for all SGRBs north of $+15^{\circ}$ to ensure the potential for > 8 hr integrations for the triggered observations.

On passing these stages, the parser then assesses the duration of the trigger so that SGRB candidates can be identified. However, on the short timescales following the alert, and with growing uncertainty as the GRB burst duration increases, it is difficult to classify *Swift* GRBs as short or long in an automated way. A rigorous classification of the GRB requires human inspection of the data, which is only published online on the Gamma-ray Coordinates Network Circulars (GCN) Archive,[1] usually between 10 mins and 1 hr post-burst and therefore not via a VOEvent. To account for this, we implemented a three-tiered system to flexibly respond to different GRB durations and therefore filter for those events more likely to be SGRBs. The keyword INTEG_TIME (the length of time for the transient signal to reach a significant threshold) parameter is used as an estimator of the incoming GRB's true duration.

- GRBs with INTEG_TIME<0.257 s have a high probability of being SGRBs so the VOEvent parser will automatically submit these triggers to the observatory and alert team members via text and email of the override observation.
- With durations 0.257 s <INTEG_TIME < 1.025 s, we have implemented a "wait-to-proceed" algorithm as the probability of the GRB being a SGRB decreases with increasing INTEG_TIME. In this case, we issue email and text alerts so that team members can check the GCN Archive for adequate verification of the GRB classification. If the GRB is confirmed to be short, then the duty team member responds "YES" to the detection email, and this email reply is read by an algorithm (via the Google email Application Programming Interface[2]) that then proceeds with submitting the trigger to ATCA, resulting in an override observation. This provides an easy interface to assess and submit triggers via a mobile phone, which can receive SMS alerts and allow responding to emails away from a computer.
- If INTEG_TIME>1.025 s then we presume that the GRB is long and we do not proceed with submitting a trigger to override the telescope.

[1] https://gcn.gsfc.nasa.gov/gcn3_archive.html
[2] https://developers.google.com/gmail/api

After the parser (or duty team member) has successfully identified the event as an SGRB, our algorithm then searches the ATCA calibrator database for a nearby and suitable phase calibrator. It then automatically builds a schedule file (we use the ATCA scheduler software CABB-SCHEDULE-API)[1] for a 12-hour observation of the GRB in the requested frequency band (for GRB triggering we currently use the 4 cm receiver), which has interleaved phase calibrator observations every 20 minutes. Note that the total exposure time is also limited by how far the GRB is above the horizon at the time of the trigger. The schedule file and override request is then submitted to the observatory where it is assessed for submission to the observing queue by the ATCA back-end.

5.2.2 Observatory back-end

Time on the ATCA is scheduled into two 6-month long semesters, and the order of observations in each semester is set months in advance. This is done to allow the project investigators, who are also responsible for conducting the observations, to plan their activities. A rapid-response system is not easily compatible with this mode of operation.

Nevertheless, demand for the telescope to quickly respond to events has been steadily rising. In 2016, roughly 10% of telescope time was given to NAPA (Non A-priori Assignable) or ToO (Target of Opportunity) projects, while in 2019 this figure had risen to 19%. For a NAPA project, a science case is given to the time assignment committee (TAC), which ranks its significance against the other projects for that semester. Provided the science is considered compelling, these projects are allowed to displace time from other projects during the semester, with the philosophy being that were we to know during the scheduling process when an event would happen, a compelling project would have been scheduled to observe it.

Rapid-response NAPAs operate in the same way. A scientific justification must be supplied to the TAC, who must agree that rapid response is warranted. The observatory then supplies an authentication Javascript Web Token (JWT) to the project, and assists the investigators to test their automatic triggering system.

A web service is provided so that the trigger to start observations can be sent from any internet-connected device. A Python library (ATCA-RAPID-RESONSE-API) is also available to make it easier to send requests to this service.[2] All requests must contain a valid schedule file, and must nominate the target coordinates and a nearby phase calibrator.

Upon receipt of a trigger, the web service tries to schedule the observation as soon as possible. If the source is above the horizon and the user-nominated minimum useful observing time can be obtained before the source sets, the current and subsequent observations can be displaced and the system can start the observations within 2 seconds of the trigger's arrival. Within that time, emails are sent to the projects that will be displaced, and to the triggering team, describing the new order of the scheduling. The schedule is also altered as necessary to add a scan on a flux density calibrator at an opportune time, and potentially to shorten

[1] https://github.com/ste616/cabb-schedule-api
[2] https://github.com/ste616/atca-rapid-response-api

the observations to fit the available time. At all times, the emphasis is to move the telescope to the target coordinates as quickly as possible.

The service can also provide an immediate rejection should no suitable time be found for the observation. For example, if no available time can be found up to 100 hours in the future (generally because the request was made during a time when the array is shutdown for maintenance or participating in VLBI observing), the observations are rejected and the proposal team are notified. While no explicit limit is set for the source declination, sources too far north may not be available for the user-nominated minimum useful observing time, and will thus be rejected.

If the web service can schedule the observations, a separate service then takes over, and takes control of the observing control software. Some more checks are made to see if the array can be used for observing, and will delay the start of the observations if the weather conditions are unsuitable. This service also monitors the observations for interruptions due to weather, equipment failure and human intervention. Rudimentary responses are pre-programmed for any such eventuality. The service stops once the observations have finished, the target sets, or the observations are cancelled, whichever comes first. Control of the telescope then goes to the investigators whose project was scheduled to be running at this end time.

A more complete guide to the operation of the rapid-response system is provided in the ATCA Users Guide.[1]

5.2.3 Triggering performance

Since the commencement of the program, we have worked with the observatory to improve the success of SGRB triggered observations with ATCA, which involved extensive system and software debugging. Many SGRBs were missed due to the telescope being in uninterruptible modes such as maintenance, reconfiguration, participating in VLBI or operating in an incompatible correlator mode (the latter has since been resolved).

Our original override strategy involved triggering on all *Swift* GRBs with INTEG_TIME$<$ 1.025 s as SGRBs have been detected with INTEG_TIME up to 1.024 s. However, as mentioned in Section 5.2.1, the majority of events within this timescale are LGRBs. *Swift* data requires a human in the loop to classify the event as long or short, which is usually based on the duration and the hardness of the event (note that SGRBs often produce higher energy prompt emission than LGRBs) and are only published on the GCN Archive up to an hour post-burst (also note that the distinction between events with durations between $1-2$ s can be tenuous and has led to discussions regarding intermediate GRB classes; e.g. Mukherjee et al., 1998; Horváth, 1998; Huja et al., 2009; de Ugarte Postigo et al., 2011). This original strategy therefore resulted in several false ATCA triggers, most of which were identified and cancelled before the telescope was overridden as there was additional lead time before the event in question had risen above the horizon. However, there were a few instances where some data was collected on LGRBs. Recent edits to the VOEvent parsing of event timescales

[1] https://www.narrabri.atnf.csiro.au/observing/users_guide/html/atug.html

using the keyword INTEG_TIME, which are described in Section 5.2.1 have resulted in a significant reduction in ATCA triggers of LGRB contaminants.

When ATCA receives a trigger of an event that is above the horizon, the main limitation to the response time is the telescope slew speed. On receiving the VOEvent via the parsing code, it takes $2-3$ s for the observation to be queued and the subsequent maximum observing time calculated. Following a *Swift* alert on the long GRB 190519A (Ukwatta et al., 2019), ATCA was on target and observing the event in 2 min and 39 s. Other response times range between $3-6$ min post-burst, which make the ATCA rapid-response system competitive with other triggering facilities such as AMI (e.g. Anderson et al., 2018b) yet is also based in the Southern Hemisphere, has more collecting area, a larger number of frequency bands, polarisation capabilities, and (in some configurations) better angular resolution.

5.2.4 Short GRB experimental design

The majority of GRBs detected by *Swift*-BAT are LGRBs, with SGRBs (in this case events with $T_{90} \leq 2$ s including those found in ground analysis) only accounting for $\sim 7-8\%$ (this is based on event numbers between 2017 and 2019 using the *Swift* GRB Look-up Table,[1] where T_{90} is the time between 5 and 95% of the fluence being emitted). We therefore expect $\sim 5-10$ SGRBs to be detected by *Swift* per year, and therefore predict $\lesssim 2$ will be observable with ATCA (below a Declination cut-off of $+15$ deg) during an observing semester.

Our rapid-response observations are performed using the 4 cm receiver, which has dual 2 GHz windows that are usually centered at 5.5 and 9 GHz, which is the most sensitive ATCA band. This choice is based on several factors: the full-width half-maximum of the primary beam encompasses the initial *Swift*-BAT positional uncertainty of newly detected GRBs (1-4 arcmin; Barthelmy et al., 2005), it is largely immune to atmospheric instabilities, and is less disrupted by RFI than other ATCA bands. In addition, as synchrotron emission from GRB reverse and forward shocks peaks earlier and brighter with increasing frequency, the 4 cm band (5.5/9 GHz) is optimal for ensuring the source will be bright but not peaking before the telescope is on-target.

As mentioned in Section 5.1, the radio afterglows from SGRBs are usually detected within 1 day post-burst (e.g. Fong et al., 2015), which strongly motivates our need for the ATCA rapid-response mode. The triggered observations are designed to observe between $2-12$ h (depending on how long the source is above the horizon following the trigger). As previous SGRB radio studies have shown that the radio afterglow has already switched-on within $4-16$ h post-burst (e.g. Anderson et al., 2018b), a ≤ 12 hr observation allows us to track the rapid rise in emission with a sensitivity of $\sim 60\,\mu$Jy (3σ) on one hour timescales.[2] This means that any delays of ≤ 1 hr related to waiting for the GRB classification does not affect the rapid-response science goal (see Section 5.2.1). A ≤ 12 hr track also ensures some periods of simultaneous *Swift* X-ray Telescope (XRT, observing band between $0.3-10$ keV; Lien et al., 2018) observations, which is essential for modelling the spectral energy distribution

[1] https://swift.gsfc.nasa.gov/archive/grb_table/
[2] https://www.narrabri.atnf.csiro.au/myatca/interactive_senscalc.html

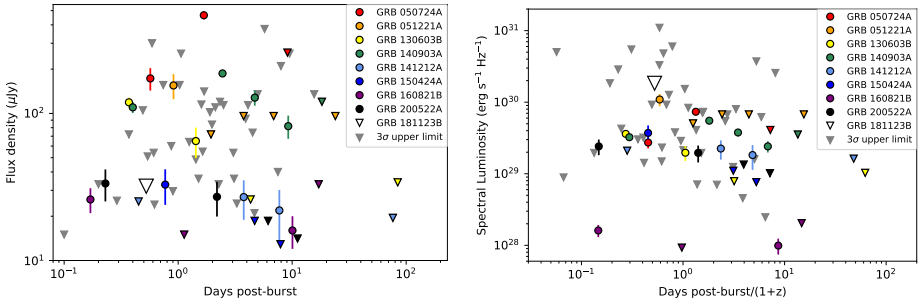

Figure 5.1: Radio light curves of SGRB radio detections (1σ error bars) and 3σ upper-limits observed at frequencies between 6 and 10 GHz. Left: Radio flux density vs days post-burst and Right: k-corrected spectral luminosity vs days post-burst in the rest-frame. The 9 GHz upper-limit of GRB 181123B is depicted as a large white triangle. For those GRBs without a known redshift we assume $z = 0.5$. The 3σ upper limits of those SGRBs that were observed but not detected in the radio band are depicted as grey triangles. References for all radio flux densities and redshifts for radio-detected SGRBs: Berger et al. (2005), Fox et al. (2005), Prochaska et al. (2005), Soderberg et al. (2006), de Ugarte Postigo et al. (2014), de Ugarte Postigo et al. (2014), Cucchiara et al. (2014), Chornock et al. (2014), Fong et al. (2014), Fong et al. (2015), Troja et al. (2019a), Lamb et al. (2019), Paterson et al. (2020), Fong et al. (2021). All radio upper limits shown in grey were taken from Fong et al. (2015, see references therein).

(SED), and for exploring the radio properties associated with the plateau phase (e.g. see our modelling in Section 5.4.1).

Following the triggered, rapid-response observation, we also request three ~ 4 hr follow-up observations in the 4 cm band to occur between $1-3$, $4-6$, and $8-12$ days post-burst, which can reach a sensitivity of $30\,\mu$Jy (3σ). While 3 of the previous radio-detected SGRBs faded below detectability within 2 days post-burst, the other 2 were detected up to 10 days post-burst (see Figure 5.1), thus motivating this more long-term monitoring of any triggered candidate.

5.3 ATCA observations of GRB 181123B

Swift-BAT detected the short GRB 181123B at 05:33:03 UT (trigger=873186), which was rapidly detected in the X-rays by the *Swift*-XRT and localised to the position α(J2000.0) = $12^{\rm h}17^{\rm m}28\overset{\rm s}{.}05$ and δ(J2000.0) = $+14^\circ35'52\overset{''}{.}4$ with a 90% confidence of $1\overset{''}{.}8$ (Osborne et al., 2018). Further optical and near-infrared follow-up detected a source coincident with the *Swift*-XRT position (Fong et al., 2018; Paterson & Fong, 2018; Paterson et al., 2018), resulting in the identification of the host galaxy at redshift $z = 1.754$ and the detection of the optical afterglow to GRB 181123B ($i = 25.1$ mag at 9.1 h post-burst; Paterson et al., 2020). This makes GRB 181123B one of only three SGRBs at $z > 1.5$ (Paterson et al., 2020).

On receiving the VOEvent trigger, ATCA was automatically scheduled to begin observations on 2018 Nov 23 at 18:07:24.9 UT (12.6 h post-burst) for 8.3 h (Anderson et al., 2018a), when the GRB had risen above the horizon (minimum elevation of 12 deg). On this date, ATCA was in the 6B array configuration, and the triggered observations were taken in the

Table 5.1: ATCA observations of GRB 181123B at 5.5 and 9 GHz, which began on 2018 Nov 23 at 18:07:24.9 UT (12.6 h post-burst) for 8.3 h.

Frequency (GHz)	3σ Upper-limit (μJy/beam)	Forced-fit flux density (μJy/beam)
5.5	34	7 ± 12
9.0	32	15 ± 11

4 cm band, with the dual 2 GHz bandwidth windows centered at 5.5 and 9 GHz. The observation pointing was at the initial BAT position, which was 1.2 arcmin offset from the final *Swift*-XRT position of GRB 181123B. Note that we requested no follow-up ATCA observations due to the imminent reconfiguration and correlator reprogramming, with many subsequent programmes having priority.

The ATCA rapid-response observation was reduced and analysed with the radio reduction software MIRIAD (Sault et al., 1995) using standard techniques. Flux and bandpass calibration were conducted using PKS 1934-638 and phase calibration with PKS 1222+216. Several rounds of phase and amplitude self calibration were also applied (this was possible due to the nearby bright field source FIRST J121731.7+143953; Helfand et al., 2015). In order to obtain the most robust flux density upper limits at the position of the GRB, we used MFCLEAN to create a clean model of the sources in the field (manually drawing clean boxes) and subtracted this model from the visibilities. A primary beam correction was then applied due to the 1.2 arcmin offset between the pointing centre and the best known GRB position from the *Swift*-XRT. GRB 181123B was not detected, and the final 3σ upper-limits can be found in Table 5.1.

As we know the precise location of GRB 181123B to within the ATCA beam, we also report the peak force-fitted flux density at both 5.5 and 9 GHz in Table 5.1. These were calculated using the task IMFIT to force-fit a Gaussian to the beam that was fixed at the *Swift*-XRT position of the GRB (errors are the 1σ rms). The advantage of quoting the force-fitted flux density over an upper-limit is that such a measurement also accounts for the presence of nearby sources, as well as variations in the noise across the image. The data were also divided into 3 h and 1 h timescales and then re-imaged to search for evidence of emission that may have switched on nearer the end of the observation; however none was detected.

5.4 Discussion

In this section, we first demonstrate that our radio flux density limits for GRB 181123B are consistent and competitive with previous studies of the radio-detected SGRB population. This is followed by afterglow modelling to demonstrate the importance of obtaining early-time radio observations (regardless of whether there is a detection) to better constrain the properties of the blast wave.

In Figure 5.1, we show the light curves of SGRBs observed in the radio band between 6 and 10 GHz. The 8 radio-detected SGRBs are colour-coded with 3σ upper-limits represented by triangles. The 3σ upper limits of those SGRBs observed but not detected in the radio band have been plotted as grey triangles. The ATCA 9 GHz 3σ upper-limit of GRB 181123B is shown as a large white triangle. In the left panel of Figure 5.1, we have plotted the observed radio flux density vs days post-burst, whereas in the right panel we have plotted the spectral luminosity vs days post-burst in the rest frame, assuming a redshift of $z = 0.5$ (Berger, 2014) for those events with no known redshift. When converting the flux (F) to luminosity (L), a k-correction was also applied such that $L = 4\pi F d_L^2 (1+z)^{\alpha-\beta-1}$ erg s^{-1} Hz^{-1}, where d_L is the luminosity distance for the redshift z (assuming ΛCDM cosmology with $H_0 = 68$ km s^{-1} Mpc^{-1} and $\Omega_m = 0.3$; Planck Collaboration et al., 2016), and α and β are the temporal and spectral indices defined as $F \propto t^{\alpha}\, \nu^{\beta}$ (Bloom et al., 2001). We assume $\alpha = 0$ and $\beta = 1/3$, which are appropriate for an optically thin, post-jet-break light curve (see Chandra & Frail, 2012).

From Figure 5.1 we can see that the ATCA flux limit for GRB 181123B is extremely competitive and consistent with the most constraining lower-limits. Using formalism by Granot & Sari (2002), Berger (2014) showed that if we assume fiducial parameters for SGRBs, along with typical microphysical parameters for LGRBs, the expected peak flux density at a redshift of $z = 0.5$ is $F_\nu \sim 40\mu$ Jy at ~ 10 GHz for an ambient medium density of $n_0 = 0.1$ cm^{-3}. Our 3σ sensitivity at 9 GHz was 32μ Jy, and therefore sensitive enough to detect emission from a GRB with the above properties, however, it is important to note that some GRB microphysical and macrophysical parameters like the kinetic energy and the CSM density can vary by several orders of magnitude (Granot & van der Horst, 2014).

The luminosity light curves in Figure 5.1 show the 3σ upper-limit for GRB 181123B at ~ 1 day post-burst (in the rest frame). Given the very high redshift of GRB 181123B, even these sensitive ATCA observations would not have detected the radio counterpart to the seven SGRBs detected at early times (within a day post-burst in the rest frame) if they were placed at $z = 1.754$. We therefore cannot draw any further comparisons between the physical properties of the radio-detected GRB sample and GRB 181123B based on luminosity alone and require more detailed multi-wavelength light curve modelling (see Section 5.4.1).

5.4.1 Modelling constraints

In this section, we model the afterglow of GRB 181123B in order to explore how early-time (< 1 day) radio observations of SGRBs can help to constrain the dynamical and microphysical parameters of such blast waves in the context of the fireball model. Using the redshift derived from the identification of the host galaxy of GRB 181123B ($z = 1.754$; Paterson et al., 2020), we model the force-fitted flux density values at the *Swift*-XRT position of the GRB from our ATCA observations together with the *Swift*-XRT light curve (Evans et al., 2009, 2010). We have chosen to use the force-fitted flux measurements plus errors in our modelling as it allows us to assign a likelihood to a predicted model flux for a set of model parameters, which is not possible with an upper limit (for some examples of where radio force-fitted

flux measurements are quoted and used in afterglow modelling see Galama et al., 1998c; Kulkarni et al., 1999; van der Horst et al., 2011, 2015).

For this modelling, we have chosen to only consider the forward-shock component to minimise complexity, particularly as we are dealing with a small number of data points. As previously mentioned, the reverse-shock could be dominant at early times ($\lesssim 1$ day) in the radio band as has been observed for some SGRBs (e.g. Soderberg et al., 2006; Lamb et al., 2019; Troja et al., 2019a). Given that the reverse-shock evolves to lower frequencies more rapidly than the forward-shock and we have no radio detection, our modelling depends primarily on the X-ray detections, which are always dominated by the forward-shock, thus motivating our model choice. Our afterglow fitting also does not rule out a reverse shock contribution. We therefore assume a spherical, relativistic, blast wave interacting with the circumburst medium and generating synchrotron emission. Since SGRBs are known to occur in homogeneous, low density environments (median densities of $n_0 \approx (3-15) \times 10^{-3}$ cm^{-3} with $\approx 80-95\%$ of events being situated in environments of $n_0 < 1$ cm^{-3}; Fong et al., 2015), we assume a constant density circumburst medium.

We use the boxfit code to model the afterglow emission (van Eerten et al., 2012). boxfit makes use of pre-calculated hydrodynamics data to calculate the dynamics of the blast wave, and solves radiative transfer equations on the go. Since in this work we assume a spherical blast wave, we fix the opening angle (θ_0) to $\pi/2$. We then use the C++ implementation of the MultiNest nested sampling algorithm, which is a Bayesian inference tool, to determine the posterior distributions of the free parameters (Feroz et al., 2009). The free parameters of our model are defined as:

- $E_{K,\rm iso}$: Isotropic equivalent kinetic energy in units of erg.
- n_0: Circumburst medium number density in units of cm^{-3}.
- p: Power-law index of the accelerated electron distribution, such that $N(\gamma) \propto \gamma^{-p}$, with some minimum Lorentz factor γ_m (Wijers & Galama, 1999).
- ϵ_B: Fraction of thermal energy in the magnetic fields.
- ϵ_e: Fraction of thermal energy in the electrons.

In order to demonstrate how the inclusion of early-time radio data helps to further constrain the dynamical and microphysical parameters (when combined with *Swift*-XRT observations and regardless of whether or not there is a radio detection), we model the afterglow of GRB 181123B with and without the ATCA force-fitted fluxes and compare the posterior distributions of the free parameters. In both fits, we use the same prior for the free parameters (Table 5.2) and the resulting best fit values in Table 5.3 are set with the lowest chi-squared value in the posterior.

Light curves for the posterior predictive distribution when the ATCA force-fitted flux density values are included in the modelling, together with the best fit, can be found in Figure 5.2. Given that the modelling of the X-ray detections of GRB 181123B alone suggests an energetic solution, the inclusion of radio information aids to pull down the overall fit so that at both 5.5 and 9 GHz, the best fit light curves are clustered around the ATCA force-fitted flux den-

sities. While the resulting model is consistent with the *Swift* Ultraviolet/Optical Telescope (UVOT; Roming et al., 2005) upper-limits (Oates & Lien, 2018), it over-predicts the Galactic extinction corrected i-band flux reported by (Paterson et al., 2020) by a factor of ~ 3 or 1.2 magnitudes. At this high redshift, an i-band detection indicates the afterglow emission was produced at ultraviolet wavelengths in the rest frame, and would therefore be quite prone to extinction by dust. Given our model does not consider extinction, intrinsic or otherwise, this over-prediction may therefore not be unreasonable. However, our i-band prediction is much higher than the host optical extinction calculated by Paterson et al. (2020) from photometric observations ($A_V = 0.23$) or calculated from their observed excess hydrogen column density (N_H; derived from X-ray afterglow spectral modelling), which is known to scale to optical extinction (Güver & Özel, 2009), predicting $A_V = 0.38$. There are also other potential sources of optical and infrared emission from SGRBs such as a kilonova from r-process radiative decay (e.g. Metzger et al., 2010), which our model does not include. However, such emission usually does not dominate over the afterglow until > 1 d post-burst (e.g. Tanvir et al., 2013).

As can be seen in Table 5.3, the inclusion of the ATCA force-fitted fluxes in our modelling allows for much better constraints to be placed on ϵ_e (see also Figure 5.5, which shows a comparison between the marginal distributions of the parameters for both cases - modelling with and without the ATCA data). The rest of the parameters are consistent between both modelling experiments but the $E_{K,\mathrm{iso}}$ is on the brighter end of known SGRBs (Fong et al., 2015). Our findings are consistent with those by Beniamini & van der Horst (2017), who have shown that the flux density and time of the GRB radio light curve peak can be used to particularly constrain ϵ_e. We also note that our constraint on ϵ_e is also consistent (within the 95% credible interval) with the distribution of ϵ_e $(0.13 - 0.15)$ found through the analysis of 36 GRB radio afterglows performed by Beniamini & van der Horst (2017). The predicted radio peak also suggests that at later times ($\gtrsim 3 - 4$ days post-burst), the forward shock radio emission from GRB 181123B may have been detectable at 5.5 and 9 GHz with ≥ 4 hr ATCA integrations (see Figure 5.2). Therefore, the inclusion of early-time radio data in GRB afterglow modelling (regardless of whether or not there is a detection), together with an X-ray light curve, allows us to predict the forward shock peak radio flux density, thus constraining the fraction of shock energy in the relativistic electrons (ϵ_e). Paterson et al. (2020) also derived these same afterglow parameters for GRB 181123B but assumed fixed values of $\epsilon_e = 0.1$ and $\epsilon_B = 0.1$ or 0.01. While our parameters are far less constrained, our values for $E_{K,iso}$ and n_0 (as well as ϵ_e and ϵ_B) are consistent with Paterson et al. (2020) within the 95% credible intervals. However, our value range for p was higher and did not overlap with the range derived by Paterson et al. (2020). Note that our value range for p is more consistent with those calculated for radio-detected SGRBs (see Section 5.4.2).

5.4.1.1 Robustness of the results for more complicated models

The aim of the modelling analysis presented in Section 5.4.1 is to demonstrate how early-time radio data (even a non-detection) can help to constrain physical parameters in the framework of the fireball model. However, the presence of a plateau feature in many GRB

Table 5.2: Assumed priors for the free parameters for all modelling efforts.

Parameter range	Prior distribution
$10^{49} < E_{K,\mathrm{iso}}\ (\mathrm{erg}) < 10^{54}$	log-uniform
$10^{-4} < n_0\ (\mathrm{cm}^{-3}) < 10$	log-uniform
$2.0 < p < 3.5$	uniform
$10^{-7} < \epsilon_B < 0.50$	log-uniform
$10^{-4} < \epsilon_e < 0.50$	log-uniform

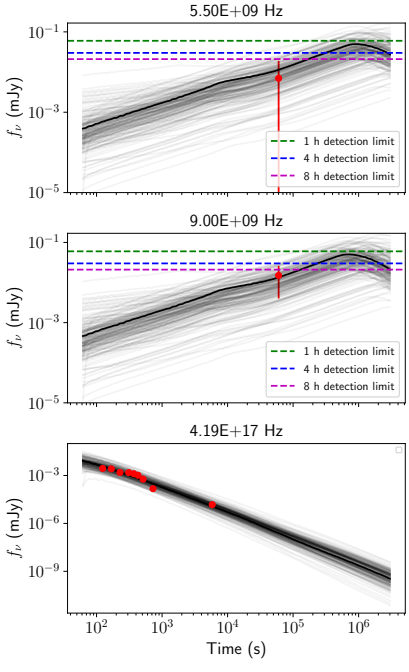

Figure 5.2: Fit result for the afterglow light curves of GRB 181123B at ATCA observing frequencies 5.5 GHz (top panel) and 9.0 GHz (middle panel), and with the *Swift*-XRT (0.3−10 keV; bottom panel) when the ATCA data are included (in this case the force-fitted flux densities; red data point and error bar plotted on the 5.5 and 9.0 GHz light curves). The plotted values in the *Swift*-XRT light curve (also red data points) were downloaded via the *Swift* Burst Analyser (Evans et al., 2010). For each of the three frequency bands, 200 light curves are drawn by sampling the inferred posterior distribution of the parameters. The solid line represents the best fit model. The horizontal dashed lines show the 3-σ detection limit for various ATCA integration times.

Table 5.3: Fit results for GRB 181123B for when the ATCA force-fitted data are excluded, included or the ATCA force-fitted mean is lowered by an order of magnitude. The errors on the parameters represent the 95% credible interval. It can be seen that when the ATCA data are included, ϵ_e is better constrained.

Parameter name	ATCA data excluded	ATCA data included	Lower ATCA forced fit
$\log_{10} E_{K,\mathrm{iso}}$	$52.4^{+1.4}_{-1.6}$	$52.0^{+1.5}_{-1.2}$	$51.5^{+1.1}_{-0.85}$
$\log_{10} n_0$	$-0.4^{+1.4}_{-1.5}$	$-0.5^{+1.4}_{-1.4}$	$-1.1^{+1.4}_{-1.3}$
p	$2.92^{+0.42}_{-0.37}$	$2.90^{+0.42}_{-0.38}$	$2.97^{+0.38}_{-0.39}$
$\log_{10} \epsilon_B$	$-2.9^{+2.5}_{-3.2}$	$-3.0^{+2.7}_{-3.5}$	$-2.5^{+2.1}_{-2.3}$
$\log_{10} \epsilon_e$	$-1.13^{+0.82}_{-1.2}$	$-0.75^{+0.39}_{-0.40}$	$-0.60^{+0.30}_{-0.35}$

X-ray light curves indicates that energy injection and more complex emission mechanisms are at play beyond a simple forward and reverse shock. One of the main interpretations of X-ray plateaus observed from SGRBs is likely an energy injection signature from a potentially short-lived, supramassive, highly magnetised, rapidly rotating neutron star remnant, often referred to as a 'magnetar' (e.g. Zhang & Mészáros, 2001; Yu & Huang, 2007; Rowlinson et al., 2013). In fact, Gompertz et al. (2015) has performed broad-band modelling of SGRBs that includes energy injection from the spin-down of such a magnetar. Alternatively, Leventis et al. (2014) were able to demonstrate that X-ray plateaus could be explained by the combined emission from the reverse and forward shock, provided that the blast wave is in the thick shell regime, and such a reverse shock would also lead to an additional emission component in radio and optical wavelengths. In the case of GRB 181123B, the X-ray light curve of the afterglow shows evidence of a plateau phase at early times that Sarin et al. (2020) and Rowlinson et al. (2020) have interpreted as energy injection from an unstable magnetar that collapsed a few hundred seconds following its formation. While many models have been proposed in the literature to describe the X-ray light curve behaviour of GRBs, our limited radio data-set means that an exhaustive analysis of these complex models is beyond the scope of this paper. Nonetheless, it is worth exploring whether the constraints we have derived from our simple forward shock model are still meaningful if we introduce additional free parameters.

In the following we investigate how the inclusion of the ATCA data affects the posterior of modelling efforts that also include energy injection. We therefore incorporate energy injection into boxfit, which is modelled by varying the isotropic equivalent kinetic energy ($E_{K,\mathrm{iso}}$) as a power-law in time. In this case, $E_{K,\mathrm{iso}}$ is described as:

$$E = \begin{cases} E_0 & t \leq t_{\mathrm{inj}} \\ E_0 (t/t_{\mathrm{inj}})^{\alpha} & t_{\mathrm{inj}} < t \leq t_{\mathrm{inj}} + dt_{\mathrm{inj}} \\ E_0 (1 + dt_{\mathrm{inj}}/t_{\mathrm{inj}})^{\alpha} & t_{\mathrm{inj}} + dt_{\mathrm{inj}} < t \end{cases} \tag{5.1}$$

where the three additional parameters are defined as:

- t_{inj}: Start time of the energy injection in seconds (s).

Table 5.4: Assumed priors for the energy injection parameters for all modelling efforts.

Parameter range	Prior distribution
$8.64 < t_{\rm inj}$ (s) $< 4.32 \times 10^5$	log-uniform
$8.64 < dt_{\rm inj}$ (s) $< 4.32 \times 10^5$	log-uniform
$0.0 < \alpha < 2.0$	uniform

- $dt_{\rm inj}$: Duration of energy injection in seconds (s).
- α: Power-law index of the energy injection.

The assumed prior distributions for the energy injection parameters can be seen in Table 5.4. We use the same priors as before for all other burst parameters (Table 5.2).

The resulting best-fit parameters for the afterglow modelling of GRB 181123B that includes energy injection for the cases when the ATCA force-fitted flux densities are included and excluded can be found in Table 5.5, with the resulting light curves for the posterior predictive distribution, together with the best fit model plotted in Figure 5.3. Due to the limited multi-wavelength coverage of the afterglow, we are not able to place tight constraints on the energy injection parameters. However, note that ϵ_e continues to be well constrained when ATCA data are included, even with a more complex model with additional parameters (see Figure 5.6, which shows the marginal distributions of the parameters for the energy injection cases when ATCA data are included and excluded). In addition, Figure 5.7 compares the obtained marginalized distribution for the GRB parameters (omitting the energy injection parameters) for the two modelling cases that include the ATCA data: with and without including energy injection. It can be seen that the resulting parameter values common between both fits are consistent within the 95% credible intervals despite different model complexities. However, while the model is consistent with the *Swift*-UVOT upper-limits, it over-predicts the i-band detection (Paterson et al., 2020), which demonstrates the limitations of our modelling.

The modelling of GRB 181123B shows that early-time radio observations, regardless of whether they are detections or non-detections, are able to constrain the fraction of thermal energy in the accelerated electrons, ϵ_e, beyond what is possible with just the *Swift*-XRT X-ray light curve data. Our modelling also predicted that observations at later times (1-10 days) may have resulted in a detection of the forward shock, which would further constrain the GRB parameters.

To test how the dependencies between the parameters in our model are affected by the mean of the forced fitted values, we ran an additional fit using boxfit (without energy injection) where we lowered the mean of the ATCA force-fitted flux density values by an order of magnitude. Table 5.3 shows the resulting inferred parameters with the best fit light curves shown in Figure 5.4. The main effect of lowering the mean value of the force-fitted ATCA flux densities on the parameters was to decrease the mean value of the circumburst medium density (n_0) and increase the fraction of thermal energy in the magnetic fields (ϵ_B) by a

Table 5.5: Fit results for GRB 181123B for when the ATCA force-fitted data are excluded and included, with energy injection also included in our modelling. The errors on the parameters represent the 95% credible interval. It can be seen that when the ATCA data are included, ϵ_e is better constrained.

Parameter name	ATCA data excluded	ATCA data included
$\log_{10} E_{K,\mathrm{iso}}$	$51.8^{+1.9}_{-1.3}$	$51.4^{+1.7}_{-0.91}$
$\log_{10} n_0$	$-0.7^{+1.6}_{-1.7}$	$-0.9^{+1.7}_{-1.8}$
p	$3.08^{+0.42}_{-0.47}$	$3.16^{+0.35}_{-0.50}$
$\log_{10} \epsilon_B$	$-1.9^{+1.6}_{-3.5}$	$-2.1^{+1.9}_{-4.0}$
$\log_{10} \epsilon_e$	$-1.01^{+0.70}_{-1.2}$	$-0.66^{+0.35}_{-0.39}$
$\log_{10} t_{\mathrm{inj}}$ (days)	$-1.23^{+1.7}_{-0.91}$	$-1.32^{+1.8}_{-0.84}$
$\log_{10} dt_{\mathrm{inj}}$ (days)	$-1.2^{+1.8}_{-2.3}$	$-1.1^{+1.8}_{-2.3}$
α	$0.86^{+0.94}_{-0.77}$	$0.88^{+0.92}_{-0.76}$

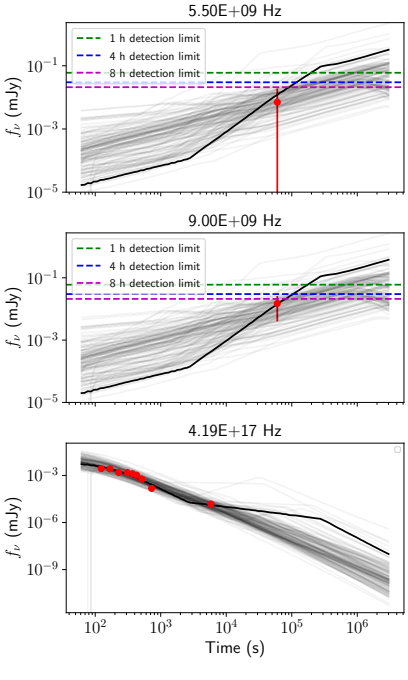

Figure 5.3: As for Figure 5.2 but with energy injection incorporated into our modelling.

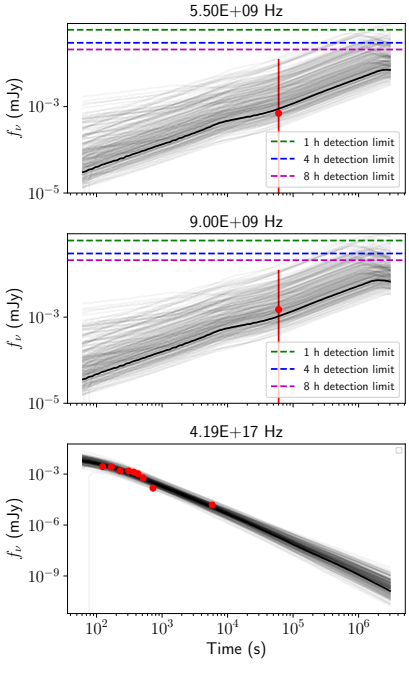

Figure 5.4: As for Figure 5.2 but with the ATCA forced-fitted flux densities lowered by an order of magnitude.

similar amount (factor of $\sim 3-4$) when compared to the results from fitting the original force-fitted ATCA flux densities. However, note that all parameters presented in Table 5.3 that were derived from including ATCA force-fitted flux densities in our modelling still agree within the 95% credible intervals of the modelling performed without the ATCA information. The reduction in the ATCA force-fitted mean flux densities also indicate that the predicted peak forward shock emission in the radio band would be delayed and also drop below the ATCA 3σ detection limits (see Figure 5.4) when compared to the fit performed with the measured force-fitted flux densities shown in Figure 5.2.

Overall, our analysis demonstrates the importance of quoting force-fitted flux density values for radio transients over just reporting 3σ upper-limits, which is traditional in most fields of astrophysics. If only upper-limits are reported then it is not always possible to incorporate this information into some modelling analyses (e.g. like our GRB afterglow modelling), which means we are throwing away important data that could further constrain the physics of an event or source. Finally, the inclusion of early-time radio force-fitted flux densities allows us to make predictions about the time and brightness of the forward shock peak in the radio band, which can inform late-time radio follow-up strategies.

5.4.2 Comparisons of GRB 181123B to radio-detected SGRBs

We now compare our parameter constraints on the micro- and macro-physical properties of GRB 181123B resulting from our modelling to those obtained for other radio-detected GRBs. For this comparison, we only focus on the parameters derived from our forward-shock modelling using boxfit with the inclusion of the ATCA data (see Table 5.3). Six of the eight radio-detected SGRBs have constraints on the same parameters (e.g. Table 5.2) through afterglow modelling (GRB 050724A, 051221A, 130603B, 140903A, 160821B, GRB 200522A; Berger et al., 2005; Soderberg et al., 2006; Fong et al., 2014; Pandey et al., 2019; Troja et al., 2016; Zhang et al., 2017; Troja et al., 2019a; Lamb et al., 2019; Fong et al., 2021). The advantage of these modelling efforts was that these events had extensive multi-wavelength data (radio, infrared, optical, X-ray) so the afterglow analysis led to stringent constraints on these parameters and in many cases, an estimate of the gamma-ray jet opening angle, which has important implications for rate calculations. While the parameters we derived for GRB 181123B were far less constrained, our 95% credible intervals agree with those values derived for the six SGRBs mentioned above, but the upper limits in our prediction for both n_0 and p are much higher overall. In fact, our derived accelerated electron distribution is steeper than that usually expected for GRBs ($\boldsymbol{p = 2.90^{+0.42}_{-0.38}}$) but not unreasonably so. Overall, as previously mentioned, the inclusion of ATCA force-fitted flux densities within 1 day post-burst have allowed us to place reasonable constraints on ϵ_e.

5.5 Conclusions

In this paper, we introduce the ATCA rapid-response observing mode by presenting results from the first successful SGRB trigger on GRB 181123B. This new mode of operations allows the telescope to automatically and rapidly respond to transient alerts broadcast via VOEvents, causing the active observing programme to be interrupted to allow for time-critical observations of transient phenomena. Successful triggers on LGRBs (see Section 5.2.3) have demonstrated that if the source is above the horizon, the ATCA can be on target and observing the event as fast as 3 minutes post-burst, allowing us to probe this early-time radio regime over a wide range of frequencies ($1.1 - 25$ GHz) with full polarisation, and in a variety of array configurations.

The ATCA rapid-response observations of GRB 181123B began 12.6 hr post-burst, as soon as the target had risen above the horizon, collecting 8.3 h of data at 5.5 and 9 GHz. While no radio emission was detected from GRB 181123B, we quote force-fitted flux densities, which enabled more constraining GRB afterglow modelling to be performed then would usually be possible with just X-ray data from *Swift*-XRT. The addition of early-time radio data in the modelling allowed us to obtain more stringent constraints on the fraction of thermal energy in the electrons behind the shock wave (ϵ_e), which in turn allowed us to predict the peak in the forward shock radio afterglow emission around ~ 10 days post-burst. This modelling indicates that $\gtrsim 3 - 4$ days post-burst, the radio afterglow of GRB 181123B may have been detectable with a ≥ 4 hr ATCA integration.

Our results demonstrate the importance of including early-time radio observations in afterglow modelling efforts for constraining GRB blast wave properties and predicting the late-time peak in the radio forward shock, regardless of whether or not there is a detection, provided that force-fitted flux densities are quoted rather than upper-limits in the case of a non-detection.

This project also demonstrates the importance of implementing rapid-response observing systems on radio telescopes to probe a new parameter space in transient science. Early-time radio observations of SGRBs can allow us to distinguish between different sources of early-time synchrotron afterglow emission (e.g. Kyutoku et al., 2014) and even detect prompt and persistent coherent signals predicted to be produced during the compact merger and from the merger remnant (e.g. Rowlinson & Anderson, 2019). Detections from rapid-response radio observations will provide crucial insight into the radio brightness and timescales we might expect from aLIGO/Virgo-detected merging BNSs or NS-BH systems, which will aid in our search for electromagnetic counterparts in the large GW positional error regions. Other science cases include LGRBs, which may show bright, early-time radio emission from the reverse shock (e.g. Anderson et al., 2014) and flare stars, which have shown simultaneous high-energy and radio flaring behaviour (e.g. Fender et al., 2015).

Finally, our efforts running rapid-response programs on ATCA act as an excellent test for transient observing strategies with the SKA. It is only through the utilisation of a rapid-response system that we can exploit the SKA to study early-time BNS and BH-NS merger physics down to sub-micro-Jansky levels.

Acknowledgements

We thank the referee for their careful reading of the manuscript and recommendations. GEA is the recipient of an Australian Research Council Discovery Early Career Researcher Award (project number DE180100346) and JCAM-J is the recipient of Australian Research Council Future Fellowship (project number FT140101082) funded by the Australian Government.

The Australia Telescope Compact Array (ATCA) is part of the Australia Telescope National Facility, which is funded by the Australian Government for operation as a National Facility managed by CSIRO. This work made use of data supplied by the UK *Swift* Science Data Centre at the University of Leicester and the *Swift* satellite. *Swift*, launched in November 2004, is a NASA mission in partnership with the Italian Space Agency and the UK Space Agency. *Swift* is managed by NASA Goddard. Penn State University controls science and flight operations from the Mission Operations Center in University Park, Pennsylvania. Los Alamos National Laboratory provides gamma-ray imaging analysis.

The ATCA rapid-response front-end software makes use of COMET (Swinbank, 2014) and VOEVENT-PARSE (Staley & Fender, 2016) to process the incoming VOEvents. Both the front-end (VO_ATCA)[1] and back-end (ATCA-RAPID-RESONSE-API)[2] software for ATCA rapid-response triggering rely on the ASTROPY, a community-developed core Python package for Astronomy

[1] https://github.com/mebell/vo_atca
[2] https://github.com/ste616/atca-rapid-response-api

(The Astropy Collaboration et al., 2013; Astropy Collaboration et al., 2018), NUMPY (van der Walt et al., 2011) and SCIPY (Jones et al., 2001) python modules. This research also makes use of MATPLOTLIB (Hunter, 2007). This research has made use of NASA's Astrophysics Data System. This research has made use of SAOImage DS9, developed by Smithsonian Astrophysical Observatory. This research has made use of the VizieR catalogue access tool (Ochsenbein et al., 2000) and the SIMBAD database (Wenger et al., 2000), operated at CDS, Strasbourg, France.

Data Availability Statement

The unprocessed ATCA visibility datasets are public and can be accessed via the ATCA online archive (https://atoa.atnf.csiro.au/) under project code C3204 and PI G Anderson. The reduced images of these observations have been uploaded to Zenodo (Anderson, 2021).

Appendices

5.A Marginalised parameter distributions for different model fits

The following Figures 5.5, 5.6 and 5.7 show the marginalised parameter distributions for different modelling tests performed in Section 5.4.1.

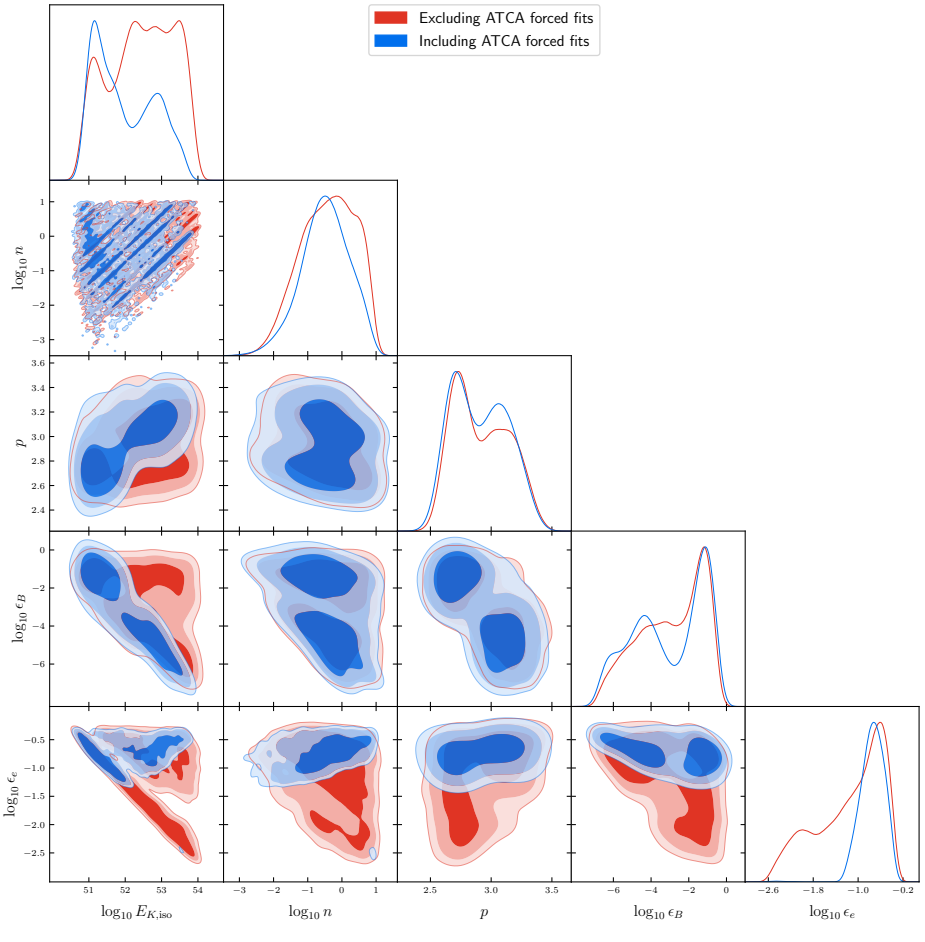

Figure 5.5: The corner plot for the marginalized parameter distributions resulting from forward-shock modelling of the GRB 181123B afterglow using boxfit. The red distributions show the modelling results when the ATCA force-fitted flux densities are not included in the data set and the blue distributions show the results for when the ATCA data are included.

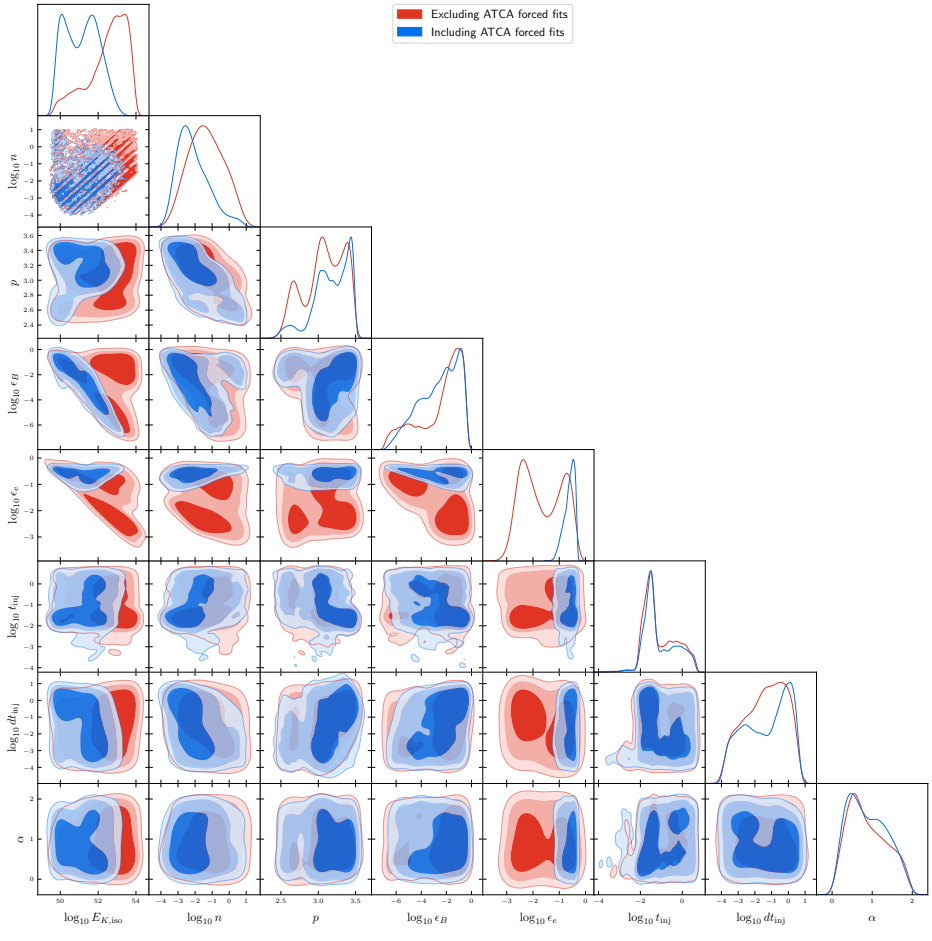

Figure 5.6: As for Figure 5.5 but with energy injection included in the model.

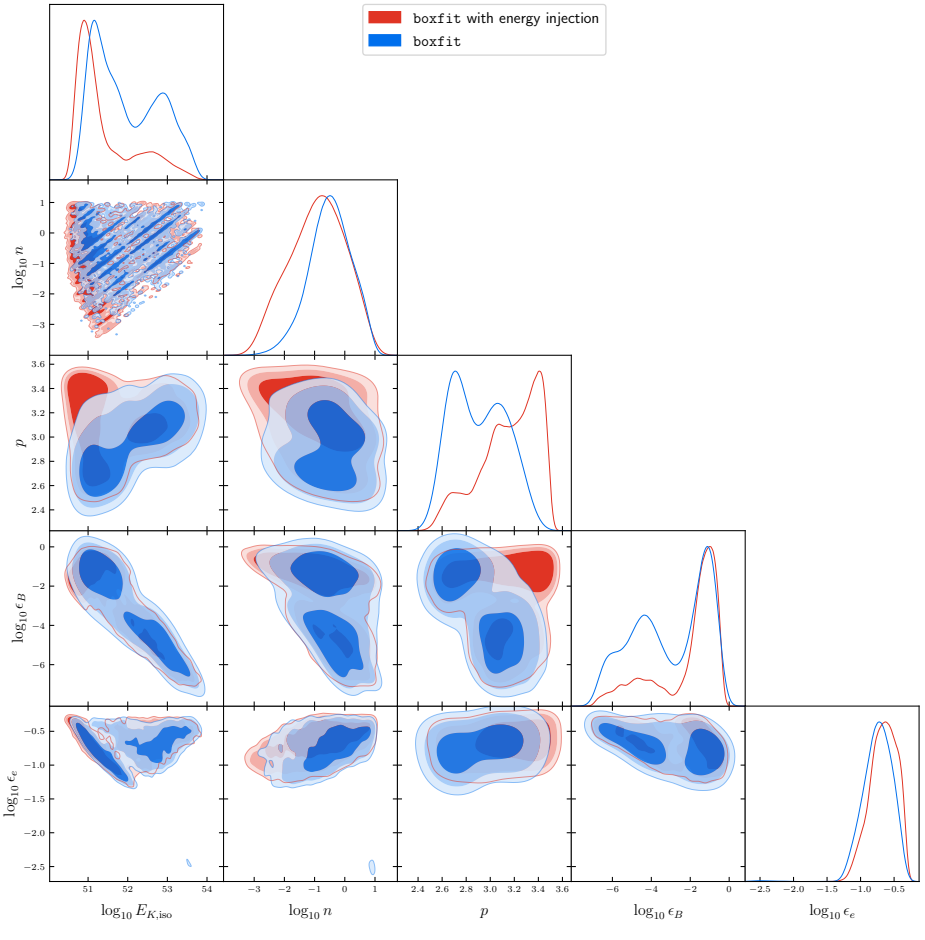

Figure 5.7: As for Figure 5.5, however, in this case both presented parameter distributions include the ATCA data. The red distributions show the modelling results when energy injection is included in the model and the blue distributions show the results without the inclusion of energy injection. Although including energy injection increases the complexity of the model, it can be seen that ϵ_e is well constrained in either case when ATCA data are included. The additional parameters for the energy injection case (t_{inj}, dt_{inj} and α) are omitted in this plot for clarity.

Chapter 6

MeerKAT observations and broadband modelling of "MAGIC" GRB 190114C

M. D. Aksulu, R. Diretse, A. J. van der Horst, E. Tremou, P. Woudt, R. A. M. J. Wijers, H. J. van Eerten

To be submitted to the Monthly Notices of the Royal Astronomical Society

Abstract

The "MAGIC" GRB 190114C is the first GRB detected in TeV energies. The afterglow of this GRB was detected over a record breaking range of observational bands, spanning from 650 MHz to TeV energies, which demonstrates that the physics governing the afterglow phase is able to generate very high-energy radiation. In this study, we present afterglow observations at 1.28 GHz obtained by the Meer Karoo Array Telescope. Furthermore, we perform robust Bayesian inference of the parameters of a forward shock model based on 2D hydrodynamical simulations, and using data over the full available range of frequencies and times. We make use of Gaussian processes to account for additional systematics in the broadband afterglow data set. We compare the inferred parameters with previous studies of GRB 190114C, as well as with a larger population of long GRBs. We perform model selection to determine the density profile around the progenitor, and find that the observations are best fit with a homogeneous environment. We find that the accelerated particle distribution in the shocked plasma is a hard power law with an index, p, well below 2. Moreover, we find that GRB 190114C constitutes an outlier in a broad sample of long GRBs, which might imply that GRBs capable of producing TeV emission are relatively rare.

6.1 Introduction

Gamma-ray bursts (GRBs) are extremely energetic explosions, where an ultra-relativistic collimated outflow is launched by a central compact object. They are initially detected as flashes of gamma rays during the prompt phase, which can last between 0.1 to 1000 s. The exact physical mechanism producing the highly-variable and luminous γ-rays is not well-understood. GRBs are classified as short/long depending on the duration of the prompt emission phase (Kouveliotou et al., 1993). For short GRBs, the duration in which 90% of the energy is emitted in gamma rays is $t_{90} \lesssim 2$ s, and they are associated with compact binary mergers where at least one of the objects is a neutron star (Lattimer & Schramm, 1976; Eichler et al., 1989). For long GRBs, on the other hand, the GRB duration is $t_{90} \gtrsim 2$ s, and they are thought to be the result of core-collapse of massive stars (Woosley, 1993). Once the relativistic outflow starts to interact with the circumburst medium (CBM), a pair of shocks are generated one of which moves into the ejecta (reverse shock) and the other moves into the surrounding medium (forward shock). In these shocks magnetic fields get amplified and charged particles are accelerated which leads to long-lasting, broadband synchrotron emission, which is called the afterglow of the GRB (Rees & Mészáros, 1992).

GRB 190114C was initially detected by the *Neil Gehrels Swift Observatory* (*Swift* from now on) and the *Fermi Gamma-ray Space Telescope*. It was determined to be a long GRB with a burst duration of 25 s (Gropp et al., 2019; Hamburg et al., 2019). This GRB was determined to be relatively close-by at a redshift of $z = 0.425$ (Selsing et al., 2019). The *Major Atmospheric Gamma Imaging Cherenkov* (MAGIC) telescopes started observations 57 s after the initial trigger and they were able to significantly detect TeV energy photons originating from a GRB for the first time (MAGIC Collaboration et al., 2019a). Given that they detected TeV photons up to 40 min after the burst, which is long after the end of the prompt emission phase, this high-energy emission component is most likely originating from the afterglow of the GRB. Such high-energy emission is expected due to the inverse-Compton scattering of the lower energy synchrotron photons by the accelerated high-energy charged particles (MAGIC Collaboration et al., 2019b). Emission resulting from this type of interaction is described as synchrotron self-Compton (SSC) emission.

Misra et al. (2021) have inferred the GRB parameters based on the observed X-ray and radio emission of the afterglow, by employing time-varying shock microphysics within the forward shock framework. In this work, we perform robust Bayesian inference to constrain the physical parameters of GRB 190114C in the context of the standard forward shock model. We make use of the method introduced in Aksulu et al. (2020) to take into account any systematic deviations from the model using Gaussian processes (GPs). We compare the inferred parameter values with the parameter distributions of a large sample of long GRBs presented in Aksulu et al. (2021). Furthermore, we present additional observations at 1.28 GHz obtained by MeerKAT.

In Section 6.2 we present a summary of the afterglow observations and describe the treatment of the afterglow data set. In Section 6.3 we briefly go over the utilized methodology, and in Section 6.4 we present the results of the Bayesian inference procedure. We discuss

the physical implications of our findings in Section 6.5 and compare how the inferred parameters compare to a larger sample of long GRBs (Aksulu et al., 2021). Finally, we present our conclusions in Section 6.6. Throughout this work we assume the cosmology as described in Planck Collaboration et al. (2016).

6.2 Afterglow Data set

In order to infer the burst parameters based on the afterglow emission, a well-sampled, broadband afterglow data set is required. In this section we present an overview of the data set describing the X-ray, optical, and radio afterglow emission of GRB 190114C.

The burst was initially detected by the *Swift* Burst Alert Telescope (*Swift*-BAT) at 20:57:03.19 UT. The X-ray Telescope aboard *Swift* (*Swift*-XRT) began observations 64 s after the initial trigger. We make use of the flux values reported in the *Swift* Burst Analyzer to construct the X-ray light curve (Evans et al., 2009). We collect the reported unabsorbed flux values in the $0.3-10$ keV band along with the reported photon indices. To convert the flux values to mJy units, we calculate the flux at the geometrical center of the observing band (1.73 keV) using the corresponding photon index for each time epoch. The reported photon index values in the burst analyzer show evidence for spectral evolution over time, where there is an increase in the photon index at $\sim 3 \times 10^5$ s after the burst. Note that, in their own analysis, Misra et al. (2021) do not find any evidence for spectral evolution.

The optical data points are compiled from Misra et al. (2021); Jordana-Mitjans et al. (2020) and GCNs (Selsing et al. 2019; Izzo et al. 2019; Bolmer & Schady 2019; Kim et al. 2019; Kumar et al. 2019; Ragosta et al. 2019; D'Avanzo 2019; Im et al. 2019). The collected observations are converted into units of mJy. All data points are corrected for Galactic extinction in the direction of the burst with $E(B-V) = 0.0107$ mag (Misra et al., 2021; Schlafly & Finkbeiner, 2011). de Ugarte Postigo et al. (2020) find that GRB 190114C lies in the nuclear region of an interacting galaxy. They present late-time observations of the host galaxy and its companion throughout the optical spectrum. We approximate the persistent contribution due to the host galaxy using the late-time observations presented in de Ugarte Postigo et al. (2020).

MeerKAT started observations at ~ 1 day after the burst, and performed observations at 13 time epochs up to ~ 35 days after the initial detection of GRB 190114C (Diretse et al. in preparation). The observations were taken at 1.28 GHz and can be seen in Table 6.1. Additionally, we collected data at radio and mm wavelengths from Volvach et al. (2019); Laskar et al. (2019); Misra et al. (2021). Pre-burst images obtained by MeerKAT show that there is significant persistent emission at 1.28 GHz at the location of GRB 190114C, which we correct for prior to our analysis.

Laskar et al. (2019) find that there is a significant contribution from the reverse shock at early times. Since in this study the primary goal is to model the emission from the forward shock, we crop early-time data where the emission from the reverse shock is dominant. Following Laskar et al. (2019), we exclude all optical/X-ray data at time epochs before 0.03 days, and radio/mm-wavelength data before 0.3 days. The forward shock model we will fit also does

Table 6.1: MeerKAT observation log at 1.28 GHz (Diretse et al. in preparation). Host contribution is not subtracted.

Time since burst (seconds)	Flux (mJy)	Error (mJy)
8.12×10^4	1.19×10^{-1}	1.6×10^{-2}
3.34×10^5	9.20×10^{-2}	1.4×10^{-2}
5.21×10^5	1.46×10^{-1}	1.9×10^{-2}
6.77×10^5	4.64×10^{-1}	4.8×10^{-2}
1.53×10^6	1.70×10^{-1}	2.4×10^{-2}
2.13×10^6	1.60×10^{-1}	1.9×10^{-2}
3.19×10^6	2.84×10^{-1}	3.1×10^{-2}
4.54×10^6	1.83×10^{-1}	2.6×10^{-2}
9.46×10^6	2.24×10^{-1}	2.5×10^{-2}
1.19×10^7	1.72×10^{-1}	2.0×10^{-2}
1.76×10^7	9.30×10^{-2}	1.8×10^{-2}
2.48×10^7	9.70×10^{-2}	1.4×10^{-2}
3.04×10^7	1.05×10^{-1}	1.5×10^{-2}

not include the inverse Compton scattering process that generates the TeV gamma rays, so we fit that model to the radio to X-ray data only.

6.3 Method

In this section we describe the employed method to infer the physical properties of GRB 190114C based on the observed afterglow emission. We assume an ultra-relativistic, collimated, blast wave moving into a surrounding medium with a density profile described as,

$$n = n_{\rm ref} \left(\frac{r}{10^{17}\ {\rm cm}} \right)^{-k}, \tag{6.1}$$

where, r is the distance from the explosion center, and $n_{\rm ref}$ is the number density of the circumburst medium (CBM) at a distance of 10^{17} cm. In this study, we only consider cases where the CBM has a homogeneous density profile, i.e., $k = 0$, and where the CBM resembles free stellar-wind type density profile, i.e., $k = 2$. The initial Lorentz factor within the jet opening angle is assumed to be uniform (i.e., top-hat jet model). As the blast wave interacts with the CBM, two pairs of shocks are created; the short-lived reverse shock, which moves into the ejected material, and the forward shock, which moves into the CBM. In these shocks magnetic fields are amplified and charged particles are accelerated which, in turn, emit broadband synchrotron emission (Sari et al., 1998; Wijers & Galama, 1999; Granot & Sari, 2002). In this work, we do not consider the emission arising due to the reverse shock, and therefore omit early-time data which is dominated by the reverse shock emission (see Section 6.2).

We make use of the numerical tool scalefit, which is an afterglow model based on 2D hydrodynamic simulations (Ryan et al. in preparation; Aksulu et al., 2021, 2020; Ryan et al., 2015). scalefit employs pre-calculated tables which include spectral information (peak spectral flux, spectral break frequencies; i.e., self-absorption break, injection break and cooling break) for a range of different opening angles and observer viewing angles calculated on different time epochs. scalefit takes the pre-calculated spectral tables and makes use of scaling rules (van Eerten & MacFadyen, 2012a) to generate spectra and light curves in a computationally efficient manner.

The dynamics of the blast wave is described by the isotropic-equivalent kinetic energy of the explosion ($E_{K,\mathrm{iso}}$), the half-opening angle of the jet (θ_0) and the CBM density (n_{ref}, also see Equation 6.1). Besides the dynamical parameters, the observed emission will also depend on the observer viewing angle (θ_{obs}) and the microphysical parameters of the shock (p, ϵ_e, ϵ_B, and ξ_N). Here, p denotes the power-law index of the energy distribution of the accelerated particles, and ϵ_e denotes the fraction of thermal energy invested in accelerating the particles. ϵ_B denotes the fraction of thermal energy going into amplifying magnetic fields. The ϵ_e parameter is not well defined when $p < 2$, without introducing another parameter γ_{max}, the maximum Lorentz factor of the accelerated particle distribution. In order to avoid adding new parameters, we define $\bar{\epsilon}_e \equiv \frac{p-2}{p-1}\epsilon_e$, and make use of this parameter instead of ϵ_e. ξ_N is the fraction of particles being accelerated in the first place. ξ_N is completely degenerate, and scales proportionally, with respect to $(1/E_{K,\mathrm{iso}}, 1/n_{\mathrm{ref}})$ and (ϵ_e, ϵ_B) (Eichler & Waxman, 2005). Due to this degeneracy, we fix ξ_N to unity throughout this work. We leave the dust extinction in the rest-frame of the host galaxy, A_V, as a free parameter. We make use of the extinction curves defined for the Milky Way (MW), Small Magellanic Cloud (SMC), and Large Magellanic Cloud (LMC) presented in Pei (1992). To summarize, the physical parameters are defined as,

$$\phi = (\theta_0, E_{K,\mathrm{iso}}, n_{\mathrm{ref}}, \theta_{\mathrm{obs}}, p, \epsilon_B, \bar{\epsilon}_e, \xi_N, A_V)^T. \tag{6.2}$$

We follow the exact methodology described in Aksulu et al. (2021) (see also Aksulu et al. 2020; Gibson et al. 2012), and make use of GPs to take into account any systematic deviations from the model.

Following Aksulu et al. (2021, 2020), we make use of nested sampling (Skilling, 2004) to obtain posterior distributions for the physical parameters and hyperparameters of the GP model. We make use of the pymultinest PYTHON package (Buchner et al., 2014; Feroz et al., 2009). Using nested sampling allows us to get an estimate of the Bayesian evidence, which is useful to calculate Bayes factors and perform model selection (see Section 6.4). We assume the same prior distributions for the physical parameters and hyperparameters as in Aksulu et al. (2021), except for the microphysical parameters ϵ_B and $\bar{\epsilon}_e$ (see Table 6.2). We allow these parameters to exceed unity, which is clearly unphysical as they represent fractions, because of the fact that they are completely degenerate with respect to ξ_N. Although we initially assume $\xi_N = 1$ when modelling GRB 190114C, in the cases where $(\epsilon_B, \bar{\epsilon}_e) > 1$, we can easily reduce the assumed value for ξ_N to push these parameters towards physical values. Since ξ_N is also inversely proportional to $(E_{K,\mathrm{iso}}, n_{\mathrm{ref}})$, decreasing ξ_N will also increase

Table 6.2: Assumed priors for the physical parameters.

Parameter range	Prior distribution
$0.01 < \theta_0 < 1.6$	log-uniform
$10^{50} < E_{K,\rm iso} < 10^{56}$	log-uniform
$10^{-3} < n_{\rm ref} < 1000$	log-uniform
$0 < \theta_{\rm obs}/\theta_0 < 2$	uniform
$1.0 < p < 3.0$	uniform
$10^{-10} < \epsilon_B < 100$	log-uniform
$10^{-10} < \bar{\epsilon}_e < 100$	log-uniform
$0 < A_V < 5$	uniform

the values of these parameters. Misra et al. (2021) also reduce the ξ_N value in order to avoid unphysical values for the microphysical parameters.

6.4 Results

We do not make a priori assumptions regarding the CBM density profile; instead, we perform fits both for homogeneous ($k = 0$) and wind-like ($k = 2$) CBM environments. We then perform Bayesian model selection using the obtained evidence values from the nested sampling procedure. The model with homogeneous CBM results in a log-evidence value of $\ln \mathscr{Z} = -72.51 \pm 0.05$, whereas the model with wind-like CBM results in $\ln \mathscr{Z} = -99.24 \pm 0.02$. The quoted error on $\ln \mathscr{Z}$ represents the 1-σ uncertainty. In the end, our analysis suggest a strong preference towards the model assuming homogeneous CBM profile with a Bayes factor of $\mathscr{Z}_{\rm Homogeneous}/\mathscr{Z}_{\rm Wind} \sim 10^{11}$. Besides performing model selection to discern between homogeneous and wind-like CBM, we also compared the evidence values for different extinction curves. We only considered the MW, SMC, and LMC type extinction curves presented in Pei (1992). We were unable to distinguish between these models as each of them results in similar evidence values. For the rest of this paper, we assume an SMC type extinction curve.

The inferred model parameters for both homogeneous and wind-like CBM models can be found in Table 6.3. The obtained posterior distributions of the physical parameters/hyperparameters assuming homogeneous and wind-like models are presented in Figures 6.5 and 6.6. The posterior predictive light curves are presented in Figures 6.1 and 6.2 for homogeneous and wind-like CBM density profiles, respectively.

All of the physical parameters are well-constrained within their respective prior distributions. We infer similar $E_{K,\rm iso}$ values for both homogeneous and wind-like environments, however, the jet-opening angle, θ_0 is smaller for when we assume homogeneous CBM. Therefore the implied beaming-corrected kinetic energy,

$$E_{K,\rm true} \equiv E_{K,\rm iso}(1 - \cos\theta_0), \tag{6.3}$$

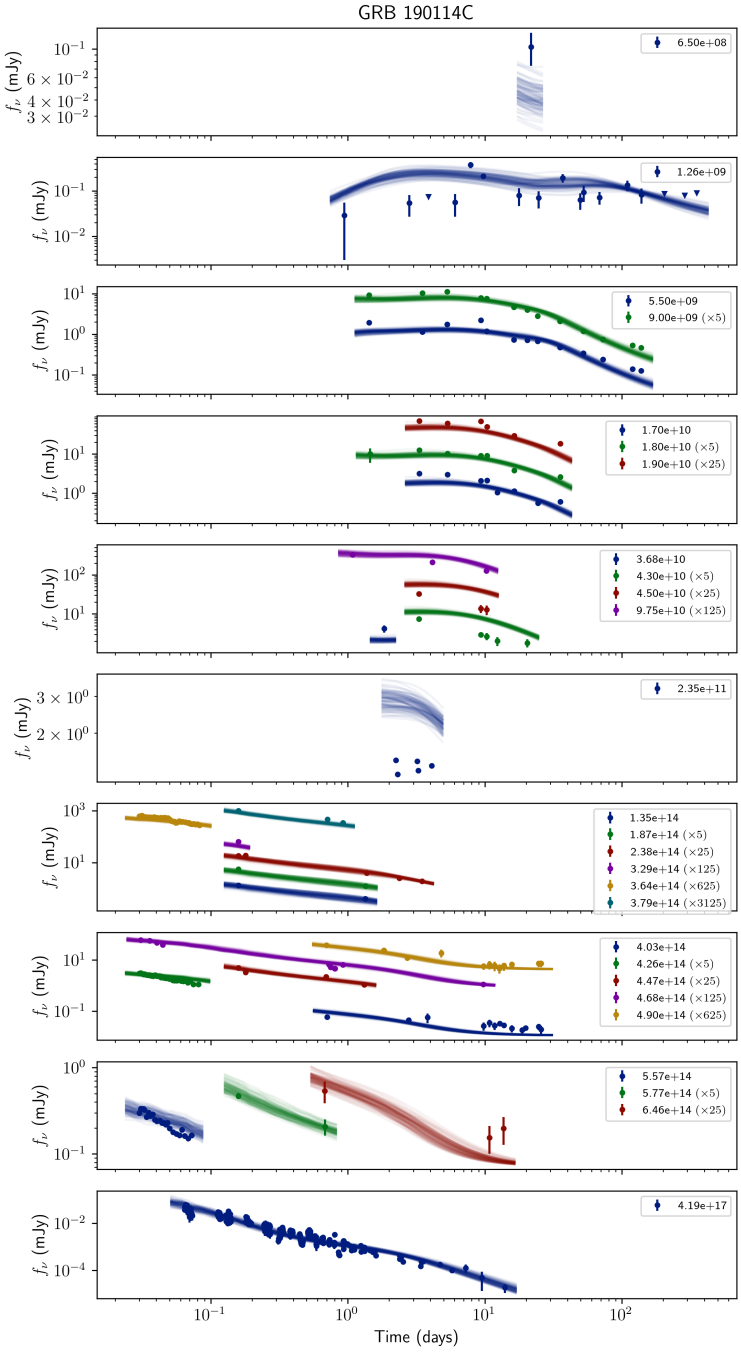

Figure 6.1: Modelling results for GRB 190114C assuming homogeneous circumburst density profile. The posterior predictive light curves for 100 randomly sampled parameter sets are presented.

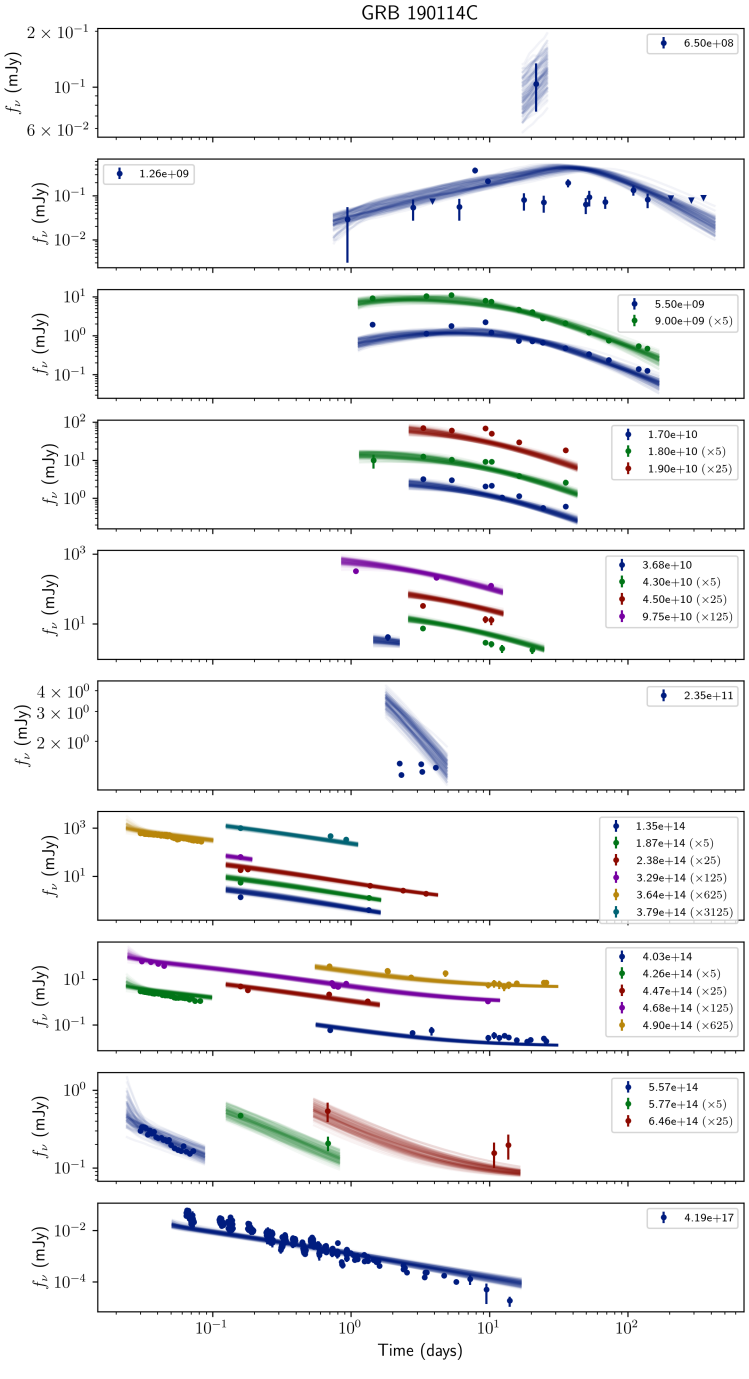

Figure 6.2: Modelling results for GRB 190114C assuming wind-like circumburst density profile. The posterior predictive light curves for 100 randomly sampled parameter sets are presented.

Table 6.3: Modes and uncertainties for the physical parameters. Results for homogeneous ($k = 0$) and wind-like ($k = 2$) environments are presented. The errors represent the 68% credible interval.

Parameter name	$k = 0$	$k = 2$
$\log_{10} \theta_0$ [rad]	$-0.980^{+0.020}_{-0.059}$	$-0.435^{+0.028}_{-0.180}$
$\log_{10} E_{K,\mathrm{iso}}$ [erg]	$52.048^{+0.077}_{-0.052}$	$52.079^{+0.147}_{-0.161}$
$\log_{10} n_{\mathrm{ref}}$ [cm^{-3}]	$-1.531^{+0.084}_{-0.523}$	$0.281^{+0.174}_{-0.161}$
p	$1.578^{+0.024}_{-0.058}$	$1.649^{+0.066}_{-0.035}$
$\theta_{\mathrm{obs}}/\theta_0$	$0.347^{+0.093}_{-0.166}$	$0.791^{+0.080}_{-0.123}$
$\log_{10} \epsilon_B$	$0.833^{+0.309}_{-0.158}$	$-0.693^{+0.308}_{-0.362}$
$\log_{10} \bar{\epsilon}_e$	$-1.680^{+0.070}_{-0.230}$	$-2.099^{+0.269}_{-0.190}$
A_V	$0.667^{+0.092}_{-0.069}$	$0.902^{+0.087}_{-0.077}$

Table 6.4: Mode and uncertainty for the beaming-corrected kinetic energy. Results for homogeneous ($k = 0$) and wind-like ($k = 2$) environments are presented. The errors represent the 68% credible interval.

Parameter name	$k = 0$	$k = 2$
$\log_{10} E_{K,\mathrm{true}}$ [erg]	$49.776^{+0.035}_{-0.055}$	$50.749^{+0.131}_{-0.103}$

is smaller for the homogeneous CBM case (see Table 6.4). We find $\epsilon_B > 1$ for the homogeneous CBM model, which is unphysical given that this parameter represents the fraction of thermal energy invested in amplifying magnetic fields. This is indicative that only a fraction of the electrons in the plasma are being accelerated, i.e., $\xi_N < 1$. Ajello et al. (2020) have measured the isotropic-equivalent energy emitted during the prompt phase ($E_{\gamma,\mathrm{iso}}$ in the 1 keV to 10 GeV band) to be $(3.5 \pm 0.1) \times 10^{53}$ erg. This implies a prompt emission efficiency of $\sim 97\%$ assuming $\xi_N = 1$. Lowering the ξ_N value will also allow for more reasonable gamma-ray efficiencies, because $E_{K,\mathrm{iso}} \propto \xi_N^{-1}$.

6.5 Discussion

In this section, we further elaborate on the physical implications of the inferred parameters. Furthermore, we make comparisons with similar studies conducted for GRB 190114C. Since GRB 190114C is a special case, regarding the detection of TeV photons which indicates efficient SSC emission, we also compare the obtained parameters with a large sample of long GRBs presented in (Aksulu et al., 2021).

The inferred power law index of the accelerated particle distribution, p, is well below 2 for both homogeneous and wind-like CBM models. This indicates a rather hard electron distribution, which may contribute to explaining the fact that TeV photons were detected from GRB 190114C.

Misra et al. (2021) have implemented time-varying microphysics within the context of the forward shock model. They assume that the microphysical parameters, (ϵ_B, ϵ_e), vary as a

Table 6.5: Comparison for the inferred dynamical parameters in this work and Misra et al. (2021) (M21). We scaled the inferred $(E_{K,\rm iso}, n_{\rm ref})$ in this work by multiplying with 50 to accommodate $\xi_N = 0.02$. We express the parameters presented in M21 in the same units as this work.

	$k=0$		$k=2$	
Parameter name	This work	M21	This work	M21
$\log_{10}\theta_0$ [rad]	$-0.980^{+0.020}_{-0.059}$	>-0.25	$-0.435^{+0.028}_{-0.180}$	>-0.47
$\log_{10}E_{K,\rm iso}$ [erg]	$53.747^{+0.077}_{-0.052}$	54.29	$53.778^{+0.147}_{-0.161}$	53.25
$\log_{10}n_{\rm ref}$ [cm^{-3}]	$0.168^{+0.084}_{-0.523}$	1.36	$1.980^{+0.174}_{-0.161}$	1.78

power law with time. They fix $p = 2.01$, so that ϵ_e is well-defined without requiring the introduction of a new parameter $\gamma_{\rm max}$, the maximum Lorentz factor of the accelerated particle distribution. Since we find $p < 2$ for both homogeneous and wind-like CBM, and we keep the microphysical parameters constant over time, it is not straightforward to make comparisons between the microphysical parameters inferred in Misra et al. (2021) and this work. However, it is still insightful to make comparisons for the dynamical parameters. Since they assume $\xi_N = 0.02$ in order to satisfy $\epsilon_e < 1$ at early times, we need to multiply $(E_{K,\rm iso}, n_{\rm ref})$ by a factor of 50 to make a fair comparison. We present the comparison between the dynamical parameters in Table 6.5. Given the different assumptions for the microphysics, one should be cautious before drawing any conclusions from such a comparison. However, for a wind-like CBM, the parameters are remarkably consistent with each other. On the other hand, for a homogeneous CBM (which is the favoured model in this work) the inferred parameters are inconsistent. Furthermore, Misra et al. (2021) favour a MW type extinction curve in their analysis, with a large A_V value in the range of 1.9 to 2.4.

In order to understand where GRB 190114C stands within a large population of long GRBs, we compare the inferred parameters with the results presented in Aksulu et al. (2021). The inferred parameters for GRB 190114C along with the results for the large sample are shown in Figures 6.3 and 6.4, for homogeneous and wind-like CBM models respectively. Since the results in Aksulu et al. (2021) were also obtained assuming $\xi_N = 1$, the presented plots constitute a fair comparison. As can be seen, GRB 190114C is an outlier when compared to the population of long GRBs. The dynamical parameters, besides θ_0, seem to lay on the lower tail of the population. Although there are comparable GRBs in the sample, the majority of GRBs have larger p values than the one inferred for GRB 190114C. GRB 190114C has the largest ϵ_B parameter in the sample for both homogeneous and wind-like CBM models. However, the reader should note that in Aksulu et al. (2021) have not included ϵ_B values larger than unity for the prior distribution. Furthermore, it is possible that the inferred ϵ_B value is over-estimated, due to the additional cooling effects of SSC emission which is not taken into account in our models. This might lead the fitting algorithm to overcompensate by increasing synchrotron cooling via the ϵ_B parameter.

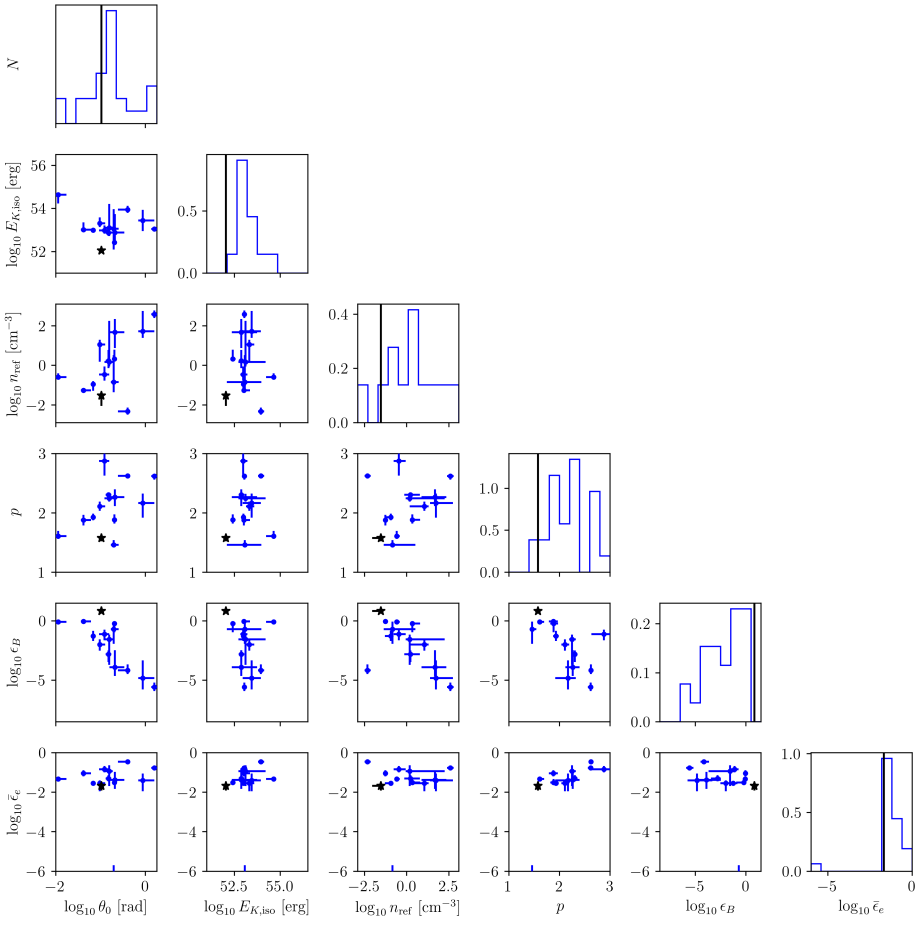

Figure 6.3: Comparison of the inferred parameters for GRB 190114C with the long GRB sample presented in Aksulu et al. (2021). The modes of the posterior distribution and 68% credible intervals are presented. Blue points are long GRBs associated with homogeneous CBM presented in Aksulu et al. (2021), whereas the black point represents the inferred parameters for GRB 190114C assuming homogeneous CBM. GRB 190114C stands out as an outlier in this figure.

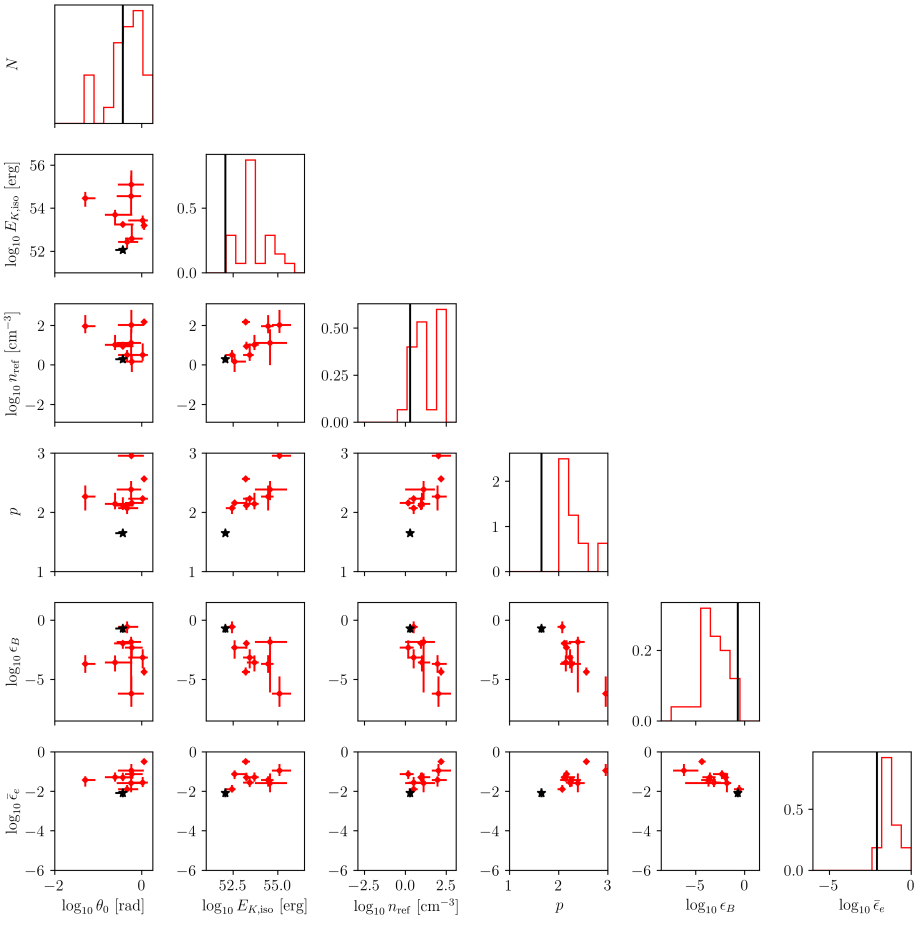

Figure 6.4: Same as Figure 6.3, however for the wind-like CBM case.

6.6 Conclusions

We present new observations of the afterglow of GRB 190114C performed by MeerKAT at 1.28 GHz (Diretse et al. in preparation). We collect observations from the literature in radio/mm-wavelengths, optical, and X-rays to compile a broadband data set for the afterglow of GRB 190114C.

We perform robust Bayesian inference to constrain the physics of this extraordinary GRB based on the broadband afterglow emission. We make use of a forward shock model based on 2D hydrodynamical simulations to capture the dynamics in a realistic fashion. We take into account systematic deviations from our model by utilizing GPs, and robustly infer the dynamics, environment, and shock microphysics of GRB 190114C. When we perform Bayesian model selection to discern between homogeneous and wind-like CBM density profiles, we favour an homogeneous environment with a Bayes factor of $\sim 10^{11}$.

We compare our results with similar studies performed for GRB 190114C, and also see how the inferred parameters compare to a large sample of long GRBs. We find that GRB 190114C possesses unusual microphysical parameters and is an outlier within a broader population of GRBs. The unusual characteristics of this GRB might be a factor in generating TeV photons.

Appendices

6.A Posterior distribution for the physical parameters and hyperparameters

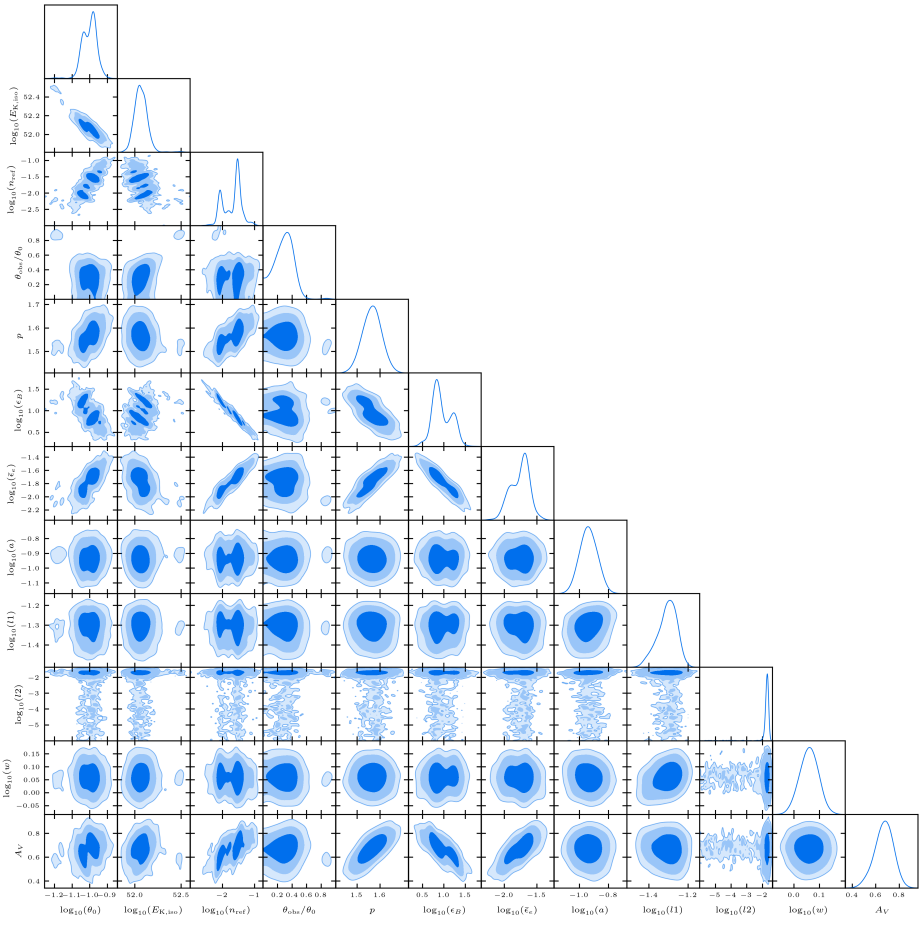

Figure 6.5: Corner plot for the obtained posterior distribution from the Bayesian inference procedure assuming homogeneous CBM. The parameter descriptions can be found in Section 6.3. The parameters (A, l_1, l_2, w) are the hyperparameters of the GP, and the reader is referred to Aksulu et al. (2021, 2020) for detailed descriptions of these parameters.

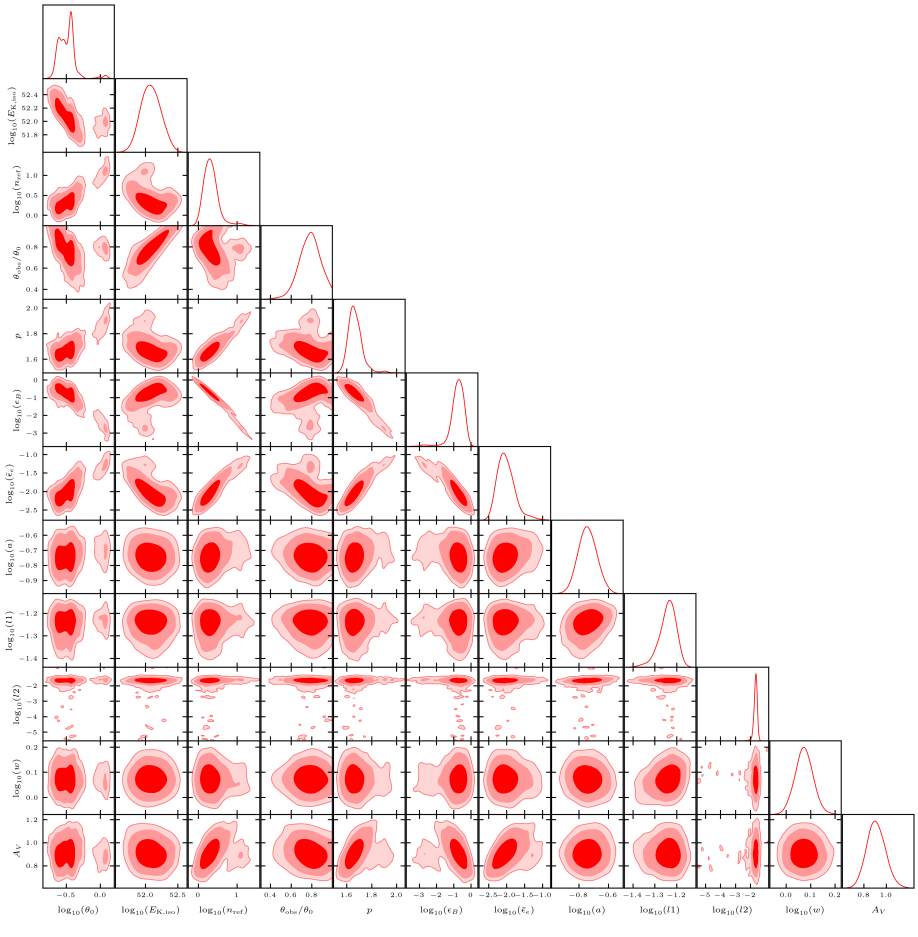

Figure 6.6: Same as Figure 6.5, however, assuming wind-like CBM.

Bibliography

Abbott, B. P., Abbott, R., Abbott, T. D., et al. 2017a, *Gravitational Waves and Gamma-Rays from a Binary Neutron Star Merger: GW170817 and GRB 170817A*, ApJ, 848, L13

Abbott, B. P., Abbott, R., Abbott, T. D., et al. 2017b, *GW170817: Observation of Gravitational Waves from a Binary Neutron Star Inspiral*, Phys. Rev. Lett., 119, 161101

Abbott, B. P., Abbott, R., Abbott, T. D., et al. 2017c, *Multi-messenger Observations of a Binary Neutron Star Merger*, ApJ, 848, L12

Ajello, M., Arimoto, M., Axelsson, M., et al. 2020, *Fermi and Swift Observations of GRB 190114C: Tracing the Evolution of High-energy Emission from Prompt to Afterglow*, ApJ, 890, 9

Aksulu, M. D., Wijers, R. A. M. J., van Eerten, H. J., & van der Horst, A. J. 2020, *A new approach to modelling gamma-ray burst afterglows: using Gaussian processes to account for the systematics*, MNRAS, 497, 4672

Aksulu, M. D., Wijers, R. A. M. J., van Eerten, H. J., & van der Horst, A. J. 2021, *Exploring the GRB population: Robust afterglow modelling*, arXiv e-prints, arXiv:2106.14921

Amati, L., Frontera, F., Tavani, M., et al. 2002, *Intrinsic spectra and energetics of BeppoSAX Gamma-Ray Bursts with known redshifts*, A&A, 390, 81

Ambikasaran, S., Foreman-Mackey, D., Greengard, L., Hogg, D. W., & O'Neil, M. 2015, *Fast Direct Methods for Gaussian Processes*, IEEE Transactions on Pattern Analysis and Machine Intelligence, 38, 252

Anderson, G. E. 2021, *Image fits files for Rapid-response radio observations of short GRB 181123B with the Australia Telescope Compact Array*

Anderson, G. E., Bell, M. E., Stevens, J., et al. 2018a, *GRB 181123B: ATCA 5/9 GHz rapid-response radio observation.*, GRB Coordinates Network, 23467, 1

Anderson, G. E., Staley, T. D., van der Horst, A. J., et al. 2018b, *The Arcminute Microkelvin Imager catalogue of gamma-ray burst afterglows at 15.7 GHz*, MNRAS, 473, 1512

Anderson, G. E., van der Horst, A. J., Staley, T. D., et al. 2014, *Probing the bright radio flare and afterglow of GRB 130427A with the Arcminute Microkelvin Imager*, MNRAS, 440, 2059

Andreoni, I., Ackley, K., Cooke, J., et al. 2017, *Follow Up of GW170817 and Its Electromagnetic Counterpart by Australian-Led Observing Programmes*, PASA, 34, e069

Astropy Collaboration, Price-Whelan, A. M., Sipőcz, B. M., et al. 2018, *The Astropy Project: Building an Open-Science Project and Status of the v2.0 Core Package*, The Astronomical Journal, 156, 123

Atwood, W. B., Abdo, A. A., Ackermann, M., et al. 2009, *The Large Area Telescope on the Fermi Gamma-Ray Space Telescope Mission*, ApJ, 697, 1071

Band, D., Matteson, J., Ford, L., et al. 1993, *BATSE observations of gamma-ray burst spectra. I-Spectral diversity*, The Astrophysical Journal, 413, 281

Bannister, K. W., Murphy, T., Gaensler, B. M., & Reynolds, J. E. 2012, *Limits on Prompt, Dispersed Radio Pulses from Gamma-Ray Bursts*, ApJ, 757, 38

Barthelmy, S. D., Barbier, L. M., Cummings, J. R., et al. 2005, *The Burst Alert Telescope (BAT) on the SWIFT Midex Mission*, Space Sci. Rev., 120, 143

Bell, A. R. 1978, *The acceleration of cosmic rays in shock fronts - I.*, MNRAS, 182, 147

Beniamini, P., Nava, L., Duran, R. B., & Piran, T. 2015, *Energies of GRB blast waves and prompt efficiencies as implied by modelling of X-ray and GeV afterglows*, MNRAS, 454, 1073

Beniamini, P. & van der Horst, A. J. 2017, *Electrons' energy in GRB afterglows implied by radio peaks*, MNRAS, 472, 3161

Berger, E. 2014, *Short-Duration Gamma-Ray Bursts*, ARA&A, 52, 43

Berger, E., Kulkarni, S. R., & Frail, D. A. 2003, *A Standard Kinetic Energy Reservoir in Gamma-Ray Burst Afterglows*, ApJ, 590, 379

Berger, E., Price, P. A., Cenko, S. B., et al. 2005, *The afterglow and elliptical host galaxy of the short γ-ray burst GRB 050724*, Nature, 438, 988

Blandford, R. D. & McKee, C. F. 1976, *Fluid dynamics of relativistic blast waves*, Physics of Fluids, 19, 1130

Blandford, R. D. & Znajek, R. L. 1977, *Electromagnetic extraction of energy from Kerr black holes.*, MNRAS, 179, 433

Bloom, J. S., Frail, D. A., Kulkarni, S. R., et al. 1998a, *The Discovery and Broadband Follow-up of the Transient Afterglow of GRB 980703*, ApJ, 508, L21

Bloom, J. S., Frail, D. A., & Sari, R. 2001, *The Prompt Energy Release of Gamma-Ray Bursts using a Cosmological k-Correction*, AJ, 121, 2879

Bloom, J. S., Kulkarni, S. R., Harrison, F., et al. 1998b, *Expected Characteristics of the Subclass of Supernova Gamma-Ray Bursts*, ApJ, 506, L105

Bolmer, J. & Schady, P. 2019, *GRB 190114C: GROND detection of the afterglow.*, GRB Coordinates Network, 23702, 1

Buchner, J., Georgakakis, A., Nandra, K., et al. 2014, *X-ray spectral modelling of the AGN obscuring region in the CDFS: Bayesian model selection and catalogue*, A&A, 564, A125

Calzetti, D., Armus, L., Bohlin, R. C., et al. 2000, *The Dust Content and Opacity of Actively Star-forming Galaxies*, ApJ, 533, 682

Cavallo, G. & Rees, M. J. 1978, *A qualitative study of cosmic fireballs and gamma -ray bursts.*, MNRAS, 183, 359

Cenko, S. B., Frail, D. A., Harrison, F. A., et al. 2011, *Afterglow Observations of Fermi Large Area Telescope Gamma-ray Bursts and the Emerging Class of Hyper-energetic Events*, ApJ, 732, 29

Chandra, P. & Frail, D. A. 2012, *A Radio-selected Sample of Gamma-Ray Burst Afterglows*, ApJ, 746, 156

Chevalier, R. A. & Li, Z.-Y. 2000, *Wind Interaction Models for Gamma-Ray Burst Afterglows: The Case for Two Types of Progenitors*, ApJ, 536, 195

Chornock, R., Fong, W., & Fox, D. B. 2014, *GRB 141212A: Gemini-N spectroscopy and photometry.*, GRB Coordinates Network, 17177, 1

Costa, E., Frontera, F., Heise, J., et al. 1997, *Discovery of an X-ray afterglow associated with the γ-ray burst of 28 February 1997*, Nature, 387, 783

Cucchiara, A., Cenko, S. B., Perley, D. A., Capone, J., & Toy, V. 2014, *GRB 140903A: tentative spectroscopic redshift.*, GRB Coordinates Network, 16774, 1

Curran, P. A., Evans, P. A., de Pasquale, M., Page, M. J., & van der Horst, A. J. 2010, *On the Electron Energy Distribution Index of Swift Gamma-ray Burst Afterglows*, ApJ, 716, L135

Curran, P. A., Starling, R. L. C., van der Horst, A. J., & Wijers, R. A. M. J. 2009, *Testing the blast wave model with Swift GRBs*, MNRAS, 395, 580

Dalal, N., Griest, K., & Pruet, J. 2002, *The Difficulty in Using Orphan Afterglows to Measure Gamma-Ray Burst Beaming*, ApJ, 564, 209

D'Avanzo, P. 2019, *GRB 190114C: REM optical/NIR detection (CORRECTION).*, GRB Coordinates Network, 23754, 1

De Colle, F., Ramirez-Ruiz, E., Granot, J., & Lopez-Camara, D. 2012, *Simulations of Gamma-Ray Burst Jets in a Stratified External Medium: Dynamics, Afterglow Light Curves, Jet Breaks, and Radio Calorimetry*, ApJ, 751, 57

De Pasquale, M., Page, M. J., Kann, D. A., et al. 2016, *The 80 Ms follow-up of the X-ray afterglow of GRB 130427A challenges the standard forward shock model*, MNRAS, 462, 1111

de Ugarte Postigo, A., Horváth, I., Veres, P., et al. 2011, *Searching for differences in Swift's intermediate GRBs*, A&A, 525, A109

de Ugarte Postigo, A., Thöne, C. C., Martín, S., et al. 2020, *GRB 190114C in the nuclear region of an interacting galaxy. A detailed host analysis using ALMA, the HST, and the VLT*, A&A, 633, A68

de Ugarte Postigo, A., Thöne, C. C., Rowlinson, A., et al. 2014, *Spectroscopy of the short-hard GRB 130603B. The host galaxy and environment of a compact object merger*, A&A, 563, A62

Dessenne, C. A.-C., Green, D. A., Warner, P. J., et al. 1996, *Searches for prompt radio emission at 151 MHz from the gamma-ray bursts GRB 950430 and GRB 950706.*, MNRAS, 281, 977

Dezalay, J. P., Barat, C., Talon, R., et al. 1992, *Short Cosmic Events: A Subset of Classical GRBs?*, in American Institute of Physics Conference Series, Vol. 265, American Institute of Physics Conference Series, ed. W. S. Paciesas & G. J. Fishman, 304

Duffell, P. C. & Laskar, T. 2018, *On the Deceleration and Spreading of Relativistic Jets. I. Jet Dynamics*, ApJ, 865, 94

Eichler, D., Livio, M., Piran, T., & Schramm, D. N. 1989, *Nucleosynthesis, neutrino bursts and γ-rays from coalescing neutron stars*, Nature, 340, 126

Eichler, D. & Waxman, E. 2005, *The Efficiency of Electron Acceleration in Collisionless Shocks and Gamma-Ray Burst Energetics*, ApJ, 627, 861

Evans, P. A., Beardmore, A. P., Page, K. L., et al. 2009, *Methods and results of an automatic analysis of a complete sample of Swift-XRT observations of GRBs*, MNRAS, 397, 1177

Evans, P. A., Willingale, R., Osborne, J. P., et al. 2010, *The Swift Burst Analyser. I. BAT and XRT spectral and flux evolution of gamma ray bursts*, A&A, 519, A102

Falcke, H. & Rezzolla, L. 2014, *Fast radio bursts: the last sign of supramassive neutron stars*, A&A, 562, A137

Fender, R. P., Anderson, G. E., Osten, R., et al. 2015, *A prompt radio transient associated with a gamma-ray superflare from the young M dwarf binary DG CVn*, MNRAS, 446, L66

Feroz, F., Hobson, M. P., & Bridges, M. 2009, *MULTINEST: an efficient and robust Bayesian inference tool for cosmology and particle physics*, MNRAS, 398, 1601

Feroz, F., Hobson, M. P., Cameron, E., & Pettitt, A. N. 2019, *Importance Nested Sampling and the MultiNest Algorithm*, The Open Journal of Astrophysics, 2, 10

Fishman, G. J., Meegan, C. A., Wilson, R. B., et al. 1994, *The First BATSE Gamma-Ray Burst Catalog*, ApJS, 92, 229

Fong, W. & Berger, E. 2013, *The Locations of Short Gamma-Ray Bursts as Evidence for Compact Object Binary Progenitors*, ApJ, 776, 18

Fong, W., Berger, E., Blanchard, P. K., et al. 2017, *The Electromagnetic Counterpart of the Binary Neutron Star Merger LIGO/Virgo GW170817. VIII. A Comparison to Cosmological Short-duration Gamma-Ray Bursts*, ApJ, 848, L23

Fong, W., Berger, E., Margutti, R., & Zauderer, B. A. 2015, *A Decade of Short-duration Gamma-Ray Burst Broadband Afterglows: Energetics, Circumburst Densities, and Jet Opening Angles*, ApJ, 815, 102

Fong, W., Berger, E., Metzger, B. D., et al. 2014, *Short GRB 130603B: Discovery of a Jet Break in the Optical and Radio Afterglows, and a Mysterious Late-time X-Ray Excess*, ApJ, 780, 118

Fong, W., Laskar, T., Rastinejad, J., et al. 2021, *The Broadband Counterpart of the Short GRB 200522A at $z = 0.5536$: A Luminous Kilonova or a Collimated Outflow with a Reverse Shock?*, ApJ, 906, 127

Fong, W., Metzger, B. D., Berger, E., & Özel, F. 2016, *Radio Constraints on Long-lived Magnetar Remnants in Short Gamma-Ray Bursts*, ApJ, 831, 141

Fong, W., Tanvir, N. R., & Levan, A. J. 2018, *GRB 181123B: Gemini-North optical detection.*, GRB Coordinates Network, 23439, 1

Fox, D. B., Frail, D. A., Price, P. A., et al. 2005, *The afterglow of GRB 050709 and the nature of the short-hard γ-ray bursts*, Nature, 437, 845

Frail, D. A., Bertoldi, F., Moriarty-Schieven, G. H., et al. 2002, *GRB 010222: A Burst within a Starburst*, ApJ, 565, 829

Frail, D. A., Kulkarni, S. R., Sari, R., et al. 2001, *Beaming in Gamma-Ray Bursts: Evidence for a Standard Energy Reservoir*, ApJ, 562, L55

Fryer, C. L., Rockefeller, G., & Young, P. A. 2006, *The Environments around Long-Duration Gamma-Ray Burst Progenitors*, ApJ, 647, 1269

Fynbo, J. P. U., Jakobsson, P., Prochaska, J. X., et al. 2009, *Low-resolution Spectroscopy of Gamma-ray Burst Optical Afterglows: Biases in the Swift Sample and Characterization of the Absorbers*, ApJS, 185, 526

Galama, T. J., Vreeswijk, P. M., Pian, E., et al. 1998a, *GRB 980425*, IAU Circ., 6895, 1

Galama, T. J., Vreeswijk, P. M., van Paradijs, J., et al. 1998b, *An unusual supernova in the error box of the γ-ray burst of 25 April 1998*, Nature, 395, 670

Galama, T. J., Wijers, R. A. M. J., Bremer, M., et al. 1998c, *The 1.4 GHz Light Curve of GRB 970508*, ApJ, 500, L101

Gehrels, N., Chincarini, G., Giommi, P., et al. 2004, *The Swift Gamma-Ray Burst Mission*, ApJ, 611, 1005

Ghirlanda, G., Ghisellini, G., Salvaterra, R., et al. 2012, *The faster the narrower: characteristic bulk velocities and jet opening angles of gamma-ray bursts*, Monthly Notices of the Royal Astronomical Society, 428, 1410

Ghirlanda, G., Salafia, O. S., Paragi, Z., et al. 2019, *Compact radio emission indicates a structured jet was produced by a binary neutron star merger*, Science, 363, 968

Ghirlanda, G., Salvaterra, R., Burlon, D., et al. 2013, *Radio afterglows of a complete sample of bright Swift GRBs: predictions from present days to the SKA era*, MNRAS, 435, 2543

Ghirlanda, G., Salvaterra, R., Campana, S., et al. 2015, *Unveiling the population of orphan γ-ray bursts*, A&A, 578, A71

Gibson, N. P., Aigrain, S., Roberts, S., et al. 2012, *A Gaussian process framework for modelling instrumental systematics: application to transmission spectroscopy*, MNRAS, 419, 2683

Gompertz, B. P., Fruchter, A. S., & Pe'er, A. 2018, *The Environments of the Most Energetic Gamma-Ray Bursts*, ApJ, 866, 162

Gompertz, B. P., van der Horst, A. J., O'Brien, P. T., Wynn, G. A., & Wiersema, K. 2015, *Broadband modelling of short gamma-ray bursts with energy injection from magnetar spin-down and its implications for radio detectability*, MNRAS, 448, 629

Goodman, J. 1986, *Are gamma-ray bursts optically thick?*, ApJ, 308, L47

Gorosabel, J., Klose, S., Christensen, L., et al. 2003, *The blue host galaxy of the red GRB 000418*, A&A, 409, 123

Gottlieb, O., Bromberg, O., Levinson, A., & Nakar, E. 2021a, *Intermittent mildly magnetized jets as the source of GRBs*, arXiv e-prints, arXiv:2102.00005

Gottlieb, O., Levinson, A., & Nakar, E. 2019, *High efficiency photospheric emission entailed by formation of a collimation shock in gamma-ray bursts*, MNRAS, 488, 1416

Gottlieb, O., Levinson, A., & Nakar, E. 2020, *Intermittent hydrodynamic jets in collapsars do not produce GRBs*, MNRAS, 495, 570

Gottlieb, O., Nakar, E., & Bromberg, O. 2021b, *The structure of hydrodynamic γ-ray burst jets*, MNRAS, 500, 3511

Granot, J. & Kumar, P. 2003, *Constraining the Structure of Gamma-Ray Burst Jets through the Afterglow Light Curves*, ApJ, 591, 1086

Granot, J. & Kumar, P. 2006, *Distribution of gamma-ray burst ejecta energy with Lorentz factor*, MNRAS, 366, L13

Granot, J., Piran, T., & Sari, R. 1999, *Synchrotron Self-Absorption in Gamma-Ray Burst Afterglow*, ApJ, 527, 236

Granot, J. & Sari, R. 2002, *The Shape of Spectral Breaks in Gamma-Ray Burst Afterglows*, ApJ, 568, 820

Granot, J. & van der Horst, A. J. 2014, *Gamma-Ray Burst Jets and their Radio Observations*, PASA, 31, e008

Green, D. A., Dessenne, C. A.-C., Warner, P. J., et al. 1995, *A Search for Prompt Radio Emission from GRBs*, Ap&SS, 231, 281

Gropp, J. D., Kennea, J. A., Klingler, N. J., et al. 2019, *GRB 190114C: Swift detection of a very bright burst with a bright optical counterpart.*, GRB Coordinates Network, 23688, 1

Guidorzi, C., Mundell, C. G., Harrison, R., et al. 2014, *New constraints on gamma-ray burst jet geometry and relativistic shock physics*, MNRAS, 438, 752

Güver, T. & Özel, F. 2009, *The relation between optical extinction and hydrogen column density in the Galaxy*, MNRAS, 400, 2050

Hamburg, R., Veres, P., Meegan, C., et al. 2019, *GRB 190114C: Fermi GBM detection.*, GRB Coordinates Network, 23707, 1

Helfand, D. J., White, R. L., & Becker, R. H. 2015, *The Last of FIRST: The Final Catalog and Source Identifications*, ApJ, 801, 26

Higgins, A. B., van der Horst, A. J., Starling, R. L. C., et al. 2019, *Detailed multiwavelength modelling of the dark GRB 140713A and its host galaxy*, MNRAS, 484, 5245

Hogg, D. W., Myers, A. D., & Bovy, J. 2010, *Inferring the Eccentricity Distribution*, ApJ, 725, 2166

Horváth, I. 1998, *A Third Class of Gamma-Ray Bursts?*, ApJ, 508, 757

Hotokezaka, K., Nissanke, S., Hallinan, G., et al. 2016, *Radio Counterparts of Compact Binary Mergers Detectable in Gravitational Waves: A Simulation for an Optimized Survey*, ApJ, 831, 190

Huja, D., Mészáros, A., & Řípa, J. 2009, *A comparison of the gamma-ray bursts detected by BATSE and Swift*, A&A, 504, 67

Hunter, J. D. 2007, *Matplotlib: A 2D graphics environment*, Computing In Science & Engineering, 9, 90

Im, M., Paek, G. S. H., & Choi, C. 2019, *GRB 190114C: UKIRT JHK observation (CORRECTIONS).*, GRB Coordinates Network, 23757, 1

Izzo, L., Noschese, A., D'Avino, L., & Mollica, M. 2019, *GRB 190114C: OASDG optical observations.*, GRB Coordinates Network, 23699, 1

Jacovich, T. E., Beniamini, P., & van der Horst, A. J. 2021, *Modeling Synchrotron Self-Compton and Klein-Nishina effects in Gamma-Ray Burst afterglows*, MNRAS

Johnston, S., Taylor, R., Bailes, M., et al. 2008, *Science with ASKAP. The Australian square-kilometre-array pathfinder*, Experimental Astronomy, 22, 151

Jones, E., Oliphant, T., Peterson, P., & Others. 2001, *SciPy: Open source scientific tools for Python*

Jordana-Mitjans, N., Mundell, C. G., Kobayashi, S., et al. 2020, *Lowly Polarized Light from a Highly Magnetized Jet of GRB 190114C*, ApJ, 892, 97

Kaneko, Y., Preece, R. D., Briggs, M. S., et al. 2006, *The complete spectral catalog of bright BATSE gamma-ray bursts*, The Astrophysical Journal Supplement Series, 166, 298

Kangas, T., Fruchter, A. S., Cenko, S. B., et al. 2020, *The Late-time Afterglow Evolution of Long Gamma-Ray Bursts GRB 160625B and GRB 160509A*, ApJ, 894, 43

Kaplan, D. L., Rowlinson, A., Bannister, K. W., et al. 2015, *A Deep Search for Prompt Radio Emission from the Short GRB 150424A with the Murchison Widefield Array*, ApJ, 814, L25

Kass, R. E. & Raftery, A. E. 1995, *Bayes Factors*, Journal of the American Statistical Association, 90, 773

Kim, J., Im, M., Lee, C. U., et al. 2019, *GRB 190114C: KMTNet optical observation.*, GRB Coordinates Network, 23734, 1

Klebesadel, R. W., Strong, I. B., & Olson, R. A. 1973, *Observations of Gamma-Ray Bursts of Cosmic Origin*, ApJ, 182, L85

Kobayashi, S., Piran, T., & Sari, R. 1999, *Hydrodynamics of a Relativistic Fireball: The Complete Evolution*, ApJ, 513, 669

Kouveliotou, C., Meegan, C. A., Fishman, G. J., et al. 1993, *Identification of Two Classes of Gamma-Ray Bursts*, ApJ, 413, L101

Kulkarni, S. R., Frail, D. A., Sari, R., et al. 1999, *Discovery of a Radio Flare from GRB 990123*, ApJ, 522, L97

Kumar, B., Pandey, S. B., Singh, A., et al. 2019, *GRB 190114C: Optical detection from HCT.*, GRB Coordinates Network, 23742, 1

Kumar, P. & Granot, J. 2003, *The Evolution of a Structured Relativistic Jet and Gamma-Ray Burst Afterglow Light Curves*, ApJ, 591, 1075

Kumar, P. & Zhang, B. 2015, *The physics of gamma-ray bursts & relativistic jets*, Phys. Rep., 561, 1

Kyutoku, K., Ioka, K., & Shibata, M. 2014, *Ultrarelativistic electromagnetic counterpart to binary neutron star mergers*, MNRAS, 437, L6

Lamb, G. P., Tanvir, N. R., Levan, A. J., et al. 2019, *Short GRB 160821B: A Reverse Shock, a Refreshed Shock, and a Well-sampled Kilonova*, ApJ, 883, 48

Laskar, T., Alexander, K. D., Gill, R., et al. 2019, *ALMA Detection of a Linearly Polarized Reverse Shock in GRB 190114C*, ApJ, 878, L26

Lattimer, J. M. & Schramm, D. N. 1976, *The tidal disruption of neutron stars by black holes in close binaries.*, ApJ, 210, 549

Lee, H. K., Wijers, R. A. M. J., & Brown, G. E. 2000, *The Blandford-Znajek process as a central engine for a gamma-ray burst*, Phys. Rep., 325, 83

Leventis, K., Wijers, R. A. M. J., & van der Horst, A. J. 2014, *The plateau phase of gamma-ray burst afterglows in the thick-shell scenario*, MNRAS, 437, 2448

Li, L.-X. 2008, *Star formation history up to z= 7.4: implications for gamma-ray bursts and cosmic metallicity evolution*, Monthly Notices of the Royal Astronomical Society, 388, 1487

Liang, E., Zhang, B., Virgili, F., & Dai, Z. G. 2007, *Low-Luminosity Gamma-Ray Bursts as a Unique Population: Luminosity Function, Local Rate, and Beaming Factor*, ApJ, 662, 1111

Lien, A., Sakamoto, T., Barthelmy, S. D., et al. 2016, *The Third Swift Burst Alert Telescope Gamma-Ray Burst Catalog*, ApJ, 829, 7

Lien, A. Y., D'Avanzo, P., & Palmer, D. M. 2018, *GRB 181123B: Swift detection of a short burst.*, GRB Coordinates Network, 23432, 1

MAGIC Collaboration, Acciari, V. A., Ansoldi, S., et al. 2019a, *Teraelectronvolt emission from the γ-ray burst GRB 190114C*, Nature, 575, 455

MAGIC Collaboration, Acciari, V. A., Ansoldi, S., et al. 2019b, *Observation of inverse Compton emission from a long γ-ray burst*, Nature, 575, 459

McBreen, S., Krühler, T., Rau, A., et al. 2010, *Optical and near-infrared follow-up observations of four Fermi/LAT GRBs: redshifts, afterglows, energetics, and host galaxies*, A&A, 516, A71

McKinney, J. C. 2005, *Total and Jet Blandford-Znajek Power in the Presence of an Accretion Disk*, ApJ, 630, L5

Meegan, C., Lichti, G., Bhat, P. N., et al. 2009, *The Fermi Gamma-ray Burst Monitor*, ApJ, 702, 791

Meegan, C. A., Fishman, G. J., Wilson, R. B., et al. 1992, *Spatial distribution of γ-ray bursts observed by BATSE*, Nature, 355, 143

Melandri, A., Covino, S., Rogantini, D., et al. 2014, *Optical and X-ray rest-frame light curves of the BAT6 sample*, A&A, 565, A72

Mészáros, P., Rees, M. J., & Papathanassiou, H. 1994, *Spectral Properties of Blast-Wave Models of Gamma-Ray Burst Sources*, ApJ, 432, 181

Metzger, B. D., Martínez-Pinedo, G., Darbha, S., et al. 2010, *Electromagnetic counterparts of compact object mergers powered by the radioactive decay of r-process nuclei*, MNRAS, 406, 2650

Metzger, M. R., Djorgovski, S. G., Kulkarni, S. R., et al. 1997, *Spectral constraints on the redshift of the optical counterpart to the γ-ray burst of 8 May 1997*, Nature, 387, 878

Misra, K., Resmi, L., Kann, D. A., et al. 2021, *Low frequency view of GRB 190114C reveals time varying shock micro-physics*, MNRAS, 504, 5685

Mooley, K. P., Deller, A. T., Gottlieb, O., et al. 2018, *Superluminal motion of a relativistic jet in the neutron-star merger GW170817*, Nature, 561, 355

Mukherjee, S., Feigelson, E. D., Jogesh Babu, G., et al. 1998, *Three Types of Gamma-Ray Bursts*, ApJ, 508, 314

Nakar, E. & Piran, T. 2011, *Detectable radio flares following gravitational waves from mergers of binary neutron stars*, Nature, 478, 82

Nandra, K., Barret, D., Barcons, X., et al. 2013, *The Hot and Energetic Universe: A White Paper presenting the science theme motivating the Athena+ mission*, arXiv e-prints, arXiv:1306.2307

Narayan, R., Paczyński, B., & Piran, T. 1992, *Gamma-Ray Bursts as the Death Throes of Massive Binary Stars*, ApJ, 395, L83

Nava, L., Salvaterra, R., Ghirlanda, G., et al. 2012, *A complete sample of bright Swift long gamma-ray bursts: testing the spectral-energy correlations*, MNRAS, 421, 1256

Norris, J. P., Cline, T. L., Desai, U. D., & Teegarden, B. J. 1984, *Frequency of fast, narrow γ-ray bursts*, Nature, 308, 434

Oates, S. R. & Lien, A. Y. 2018, *GRB 181123B: Swift/UVOT Upper Limits.*, GRB Coordinates Network, 23437, 1

Ochsenbein, F., Bauer, P., & Marcout, J. 2000, *The VizieR database of astronomical catalogues*, A&AS, 143, 23

O'Connor, B., Beniamini, P., & Kouveliotou, C. 2020, *Constraints on the circumburst environments of short gamma-ray bursts*, MNRAS, 495, 4782

Osborne, J. P., Beardmore, A. P., Evans, P. A., & Goad, M. R. 2018, *GRB 181123B: Enhanced Swift-XRT position.*, GRB Coordinates Network, 23434, 1

Paczyński, B. 1986, *Gamma-ray bursters at cosmological distances*, ApJ, 308, L43

Palaniswamy, D., Wayth, R. B., Trott, C. M., et al. 2014, *A Search for Fast Radio Bursts Associated with Gamma-Ray Bursts*, ApJ, 790, 63

Panaitescu, A. & Kumar, P. 2001a, *Fundamental Physical Parameters of Collimated Gamma-Ray Burst Afterglows*, ApJ, 560, L49

Panaitescu, A. & Kumar, P. 2001b, *Jet Energy and Other Parameters for the Afterglows of GRB 980703, GRB 990123, GRB 990510, and GRB 991216 Determined from Modeling of Multifrequency Data*, ApJ, 554, 667

Panaitescu, A. & Kumar, P. 2002, *Properties of Relativistic Jets in Gamma-Ray Burst Afterglows*, ApJ, 571, 779

Panaitescu, A. & Kumar, P. 2003, *The Effect of Angular Structure of Gamma-Ray Burst Outflows on the Afterglow Emission*, ApJ, 592, 390

Pandey, S. B., Hu, Y., Castro-Tirado, A. J., et al. 2019, *A multiwavelength analysis of a collection of short-duration GRBs observed between 2012 and 2015*, MNRAS, 485, 5294

Paterson, K. & Fong, W. 2018, *GRB 181123B: Keck near-infrared imaging.*, GRB Coordinates Network, 23440, 1

Paterson, K., Fong, W., de, K., et al. 2018, *GRB 181123B: Keck further near-infrared imaging.*, GRB Coordinates Network, 23461, 1

Paterson, K., Fong, W., Nugent, A., et al. 2020, *Discovery of the Optical Afterglow and Host Galaxy of Short GRB 181123B at $z = 1.754$: Implications for Delay Time Distributions*, ApJ, 898, L32

Pei, Y. C. 1992, *Interstellar Dust from the Milky Way to the Magellanic Clouds*, ApJ, 395, 130

Peng, F., Königl, A., & Granot, J. 2005, *Two-Component Jet Models of Gamma-Ray Burst Sources*, ApJ, 626, 966

Perley, D. A., Tanvir, N. R., Hjorth, J., et al. 2016, *The Swift GRB Host Galaxy Legacy Survey. II. Rest-frame Near-IR Luminosity Distribution and Evidence for a Near-solar Metallicity Threshold*, ApJ, 817, 8

Piran, T. 2004, *The physics of gamma-ray bursts*, Reviews of Modern Physics, 76, 1143

Planck Collaboration, Ade, P. A. R., Aghanim, N., et al. 2016, *Planck 2015 results. XIII. Cosmological parameters*, A&A, 594, A13

Prochaska, J. X., Bloom, J. S., Chen, H. W., et al. 2005, *GRB 050724: secure host redshift from Keck.*, GRB Coordinates Network, 3700, 1

Racusin, J. L., Liang, E. W., Burrows, D. N., et al. 2009, *Jet Breaks and Energetics of Swift Gamma-Ray Burst X-Ray Afterglows*, ApJ, 698, 43

Ragosta, F., Olivares, F., D'Avanzo, P., et al. 2019, *GRB 190114C: ePESSTO NTT optical observations.*, GRB Coordinates Network, 23748, 1

Ramirez-Ruiz, E., Celotti, A., & Rees, M. J. 2002, *Events in the life of a cocoon surrounding a light, collapsar jet*, MNRAS, 337, 1349

Rasmussen, C. E. & Williams, C. K. I. 2006, Gaussian Processes for Machine Learning

Rees, M. J. & Mészáros, P. 1992, *Relativistic fireballs - Energy conversion and time-scales.*, MNRAS, 258, 41

Rees, M. J. & Mészáros, P. 1994, *Unsteady Outflow Models for Cosmological Gamma-Ray Bursts*, ApJ, 430, L93

Rhoads, J. E. 1999, *The Dynamics and Light Curves of Beamed Gamma-Ray Burst Afterglows*, ApJ, 525, 737

Roming, P. W. A., Kennedy, T. E., Mason, K. O., et al. 2005, *The Swift Ultra-Violet/Optical Telescope*, Space Sci. Rev., 120, 95

Rossi, E., Lazzati, D., & Rees, M. J. 2002, *Afterglow light curves, viewing angle and the jet structure of γ-ray bursts*, MNRAS, 332, 945

Rossi, E. M., Lazzati, D., Salmonson, J. D., & Ghisellini, G. 2004, *The polarization of afterglow emission reveals γ-ray bursts jet structure*, MNRAS, 354, 86

Rowlinson, A. & Anderson, G. E. 2019, *Constraining coherent low-frequency radio flares from compact binary mergers*, MNRAS, 489, 3316

Rowlinson, A., Bell, M. E., Murphy, T., et al. 2016, *Limits on Fast Radio Bursts and other transient sources at 182 MHz using the Murchison Widefield Array*, MNRAS, 458, 3506

Rowlinson, A., O'Brien, P. T., Metzger, B. D., Tanvir, N. R., & Levan, A. J. 2013, *Signatures of magnetar central engines in short GRB light curves*, MNRAS, 430, 1061

Rowlinson, A., Starling, R. L. C., Gourdji, K., et al. 2020, *LOFAR early-time search for coherent radio emission from Short GRB 181123B*, arXiv e-prints, arXiv:2008.12657

Ryan, G., van Eerten, H., MacFadyen, A., & Zhang, B.-B. 2015, *Gamma-Ray Bursts are Observed Off-axis*, ApJ, 799, 3

Ryan, G., van Eerten, H., Piro, L., & Troja, E. 2020, *Gamma-Ray Burst Afterglows in the Multimessenger Era: Numerical Models and Closure Relations*, ApJ, 896, 166

Sakamoto, T., Barthelmy, S., Baumgartner, W., et al. 2011, *The second Swift Burst Alert Telescope gamma-ray burst catalog*, The Astrophysical Journal Supplement Series, 195, 2

Salmonson, J. D. 2003, *Perspective on Afterglows: Numerically Computed Views, Light Curves, and the Analysis of Homogeneous and Structured Jets with Lateral Expansion*, ApJ, 592, 1002

Salvaterra, R., Campana, S., Vergani, S., et al. 2012, *A complete sample of bright Swift long gamma-ray bursts. I. Sample presentation, luminosity function and evolution*, The Astrophysical Journal, 749, 68

Sari, R., Piran, T., & Halpern, J. P. 1999, *Jets in Gamma-Ray Bursts*, ApJ, 519, L17

Sari, R., Piran, T., & Narayan, R. 1998, *Spectra and Light Curves of Gamma-Ray Burst Afterglows*, ApJ, 497, L17

Sarin, N., Lasky, P. D., & Ashton, G. 2020, *Gravitational waves or deconfined quarks: What causes the premature collapse of neutron stars born in short gamma-ray bursts?*, Phys. Rev. D, 101, 063021

Sault, R. J., Teuben, P. J., & Wright, M. C. H. 1995, *A Retrospective View of MIRIAD*, in Astronomical Society of the Pacific Conference Series, Vol. 77, Astronomical Data Analysis Software and Systems IV, ed. R. A. Shaw, H. E. Payne, & J. J. E. Hayes, 433

Schlafly, E. F. & Finkbeiner, D. P. 2011, *Measuring Reddening with Sloan Digital Sky Survey Stellar Spectra and Recalibrating SFD*, ApJ, 737, 103

Scholz, F. W. & Stephens, M. A. 1987, *K-sample Anderson–Darling tests*, Journal of the American Statistical Association, 82, 918

Schulze, S., Klose, S., Björnsson, G., et al. 2011, *The circumburst density profile around GRB progenitors: a statistical study*, A&A, 526, A23

Seaman, R., Williams, R., Allan, A., et al. 2011, *Sky Event Reporting Metadata Version 2.0*, IVOA Recommendation 11 July 2011

Sedov, L. 1946, *Propagation of strong shock waves (Translated from Russian)*, Prikl Mat Mekh, 10, 241

Sellentin, E. & Starck, J.-L. 2019, *Debiasing inference with approximate covariance matrices and other unidentified biases*, J. Cosmology Astropart. Phys., 2019, 021

Selsing, J., Fynbo, J. P. U., Heintz, K. E., & Watson, D. 2019, *GRB 190114C: NOT optical counterpart and redshift.*, GRB Coordinates Network, 23695, 1

Sironi, L. & Spitkovsky, A. 2011, *Particle Acceleration in Relativistic Magnetized Collisionless Electron-Ion Shocks*, ApJ, 726, 75

Skilling, J. 2004, *Nested Sampling*, in American Institute of Physics Conference Series, Vol. 735, Bayesian Inference and Maximum Entropy Methods in Science and Engineering: 24th International Workshop on Bayesian Inference and Maximum Entropy Methods in Science and Engineering, ed. R. Fischer, R. Preuss, & U. V. Toussaint, 395–405

Snelson, E., Ghahramani, Z., & Rasmussen, C. E. 2004, in Advances in Neural Information Processing Systems 16, ed. S. Thrun, L. K. Saul, & B. Schölkopf (MIT Press), 337–344

Soderberg, A. M., Berger, E., Kasliwal, M., et al. 2006, *The Afterglow, Energetics, and Host Galaxy of the Short-Hard Gamma-Ray Burst 051221a*, ApJ, 650, 261

Staley, T. D. 2014, *voevent-parse: Parse, manipulate, and generate VOEvent XML packets*, Astrophysics Source Code Library, record ascl:1411.003

Staley, T. D. & Fender, R. 2016, *The 4 Pi Sky Transient Alerts Hub*, ArXiv e-prints

Staley, T. D., Titterington, D. J., Fender, R. P., et al. 2013, *Automated rapid follow-up of Swift gamma-ray burst alerts at 15 GHz with the AMI Large Array*, Monthly Notices of the Royal Astronomical Society, 428, 3114

Starling, R. L. C., van der Horst, A. J., Rol, E., et al. 2008, *Gamma-Ray Burst Afterglows as Probes of Environment and Blast Wave Physics. II. The Distribution of p and Structure of the Circumburst Medium*, ApJ, 672, 433

Swinbank, J. J. 2014, *Comet: A VOEvent Broker*, Astronomy and Computing, 7, 12

Tanvir, N. R., Levan, A. J., Fruchter, A. S., et al. 2013, *A 'kilonova' associated with the short-duration γ-ray burst GRB 130603B*, Nature, 500, 547

Taylor, G. 1950a, *The Formation of a Blast Wave by a Very Intense Explosion. I. Theoretical Discussion*, Proceedings of the Royal Society of London Series A, 201, 159

Taylor, G. 1950b, *The Formation of a Blast Wave by a Very Intense Explosion. II. The Atomic Explosion of 1945*, Proceedings of the Royal Society of London Series A, 201, 175

The Astropy Collaboration, Robitaille, T. P., Tollerud, E. J., et al. 2013, *Astropy: A Community Python Package for Astronomy*, Astronomy & Astrophysics, 558, 9

Tingay, S. J., Goeke, R., Bowman, J. D., et al. 2013, *The Murchison Widefield Array: The Square Kilometre Array Precursor at Low Radio Frequencies*, PASA, 30, e007

Troja, E., Castro-Tirado, A. J., Becerra González, J., et al. 2019a, *The afterglow and kilonova of the short GRB 160821B*, MNRAS, 489, 2104

Troja, E., Sakamoto, T., Cenko, S. B., et al. 2016, *An Achromatic Break in the Afterglow of the Short GRB 140903A: Evidence for a Narrow Jet*, ApJ, 827, 102

Troja, E., van Eerten, H., Ryan, G., et al. 2019b, *A year in the life of GW 170817: the rise and fall of a structured jet from a binary neutron star merger*, MNRAS, 489, 1919

Ukwatta, T. N., Ambrosi, E., D'Elia, V., et al. 2019, *GRB 190519A: Swift detection of a burst.*, GRB Coordinates Network, 24595, 1

Usov, V. V. 1992, *Millisecond pulsars with extremely strong magnetic fields as a cosmological source of gamma-ray bursts*, Nature, 357, 472

van der Horst, A. J., Kamble, A., Resmi, L., et al. 2008, *Detailed study of the GRB 030329 radio afterglow deep into the non-relativistic phase*, A&A, 480, 35

van der Horst, A. J., Kamble, A. P., Paragi, Z., et al. 2011, *Detailed Radio View on Two Stellar Explosions and Their Host Galaxy: XRF 080109/SN 2008D and SN 2007uy in NGC 2770*, ApJ, 726, 99

van der Horst, A. J., Levan, A. J., Pooley, G. G., et al. 2015, *Detailed afterglow modelling and host galaxy properties of the dark GRB 111215A*, MNRAS, 446, 4116

van der Horst, A. J., Paragi, Z., de Bruyn, A. G., et al. 2014, *A comprehensive radio view of the extremely bright gamma-ray burst 130427A*, MNRAS, 444, 3151

van der Walt, S., Colbert, S. C., & Varoquaux, G. 2011, *The NumPy Array: A Structure for Efficient Numerical Computation*, Computing in Science & Engineering, 13, 22

van Eerten, H. 2018, *Gamma-ray burst afterglow blast waves*, International Journal of Modern Physics D, 27, 1842002

van Eerten, H. & MacFadyen, A. 2013, *Gamma-Ray Burst Afterglow Light Curves from a Lorentz-boosted Simulation Frame and the Shape of the Jet Break*, ApJ, 767, 141

van Eerten, H., van der Horst, A., & MacFadyen, A. 2012, *Gamma-Ray Burst Afterglow Broadband Fitting Based Directly on Hydrodynamics Simulations*, ApJ, 749, 44

van Eerten, H., Zhang, W., & MacFadyen, A. 2010, *Off-axis Gamma-ray Burst Afterglow Modeling Based on a Two-dimensional Axisymmetric Hydrodynamics Simulation*, ApJ, 722, 235

van Eerten, H. J. 2014, *Gamma-ray burst afterglow plateau break time-luminosity correlations favour thick shell models over thin shell models*, MNRAS, 445, 2414

van Eerten, H. J. & MacFadyen, A. I. 2012a, *Gamma-Ray Burst Afterglow Scaling Relations for the Full Blast Wave Evolution*, ApJ, 747, L30

van Eerten, H. J. & MacFadyen, A. I. 2012b, *Observational Implications of Gamma-Ray Burst Afterglow Jet Simulations and Numerical Light Curve Calculations*, ApJ, 751, 155

van Paradijs, J., Groot, P. J., Galama, T., et al. 1997, *Transient optical emission from the error box of the γ-ray burst of 28 February 1997*, Nature, 386, 686

Vink, J. S. & de Koter, A. 2005, *On the metallicity dependence of Wolf-Rayet winds*, A&A, 442, 587

Vink, J. S., de Koter, A., & Lamers, H. J. G. L. M. 2001, *Mass-loss predictions for O and B stars as a function of metallicity*, A&A, 369, 574

Virtanen, P., Gommers, R., Oliphant, T. E., et al. 2020, *SciPy 1.0: Fundamental Algorithms for Scientific Computing in Python*, Nature Methods, 17, 261

Volvach, A. E., Volvach, L. N., & Pozanenko, A. 2019, *GRB 190114C: RT-22 detection at 36.8 GHz.*, GRB Coordinates Network, 23750, 1

Vreeswijk, P. M., Galama, T. J., Owens, A., et al. 1999, *The X-Ray, Optical, and Infrared Counterpart to GRB 980703*, ApJ, 523, 171

Wenger, M., Ochsenbein, F., Egret, D., et al. 2000, *The SIMBAD astronomical database. The CDS reference database for astronomical objects*, A&AS, 143, 9

Wijers, R. A. M. J. & Galama, T. J. 1999, *Physical Parameters of GRB 970508 and GRB 971214 from Their Afterglow Synchrotron Emission*, ApJ, 523, 177

Wijers, R. A. M. J., Rees, M. J., & Mészáros, P. 1997, *Shocked by GRB 970228: the afterglow of a cosmological fireball*, MNRAS, 288, L51

Wilson, W. E., Ferris, R. H., Axtens, P., et al. 2011, *The Australia Telescope Compact Array Broad-band Backend: description and first results*, MNRAS, 416, 832

Woosley, S. E. 1993, *Gamma-Ray Bursts from Stellar Mass Accretion Disks around Black Holes*, ApJ, 405, 273

Wu, Y. & MacFadyen, A. 2018, *Constraining the Outflow Structure of the Binary Neutron Star Merger Event GW170817/GRB170817A with a Markov Chain Monte Carlo Analysis*, ApJ, 869, 55

Wygoda, N., Waxman, E., & Frail, D. A. 2011, *Relativistic Jet Dynamics and Calorimetry of Gamma-ray Bursts*, ApJ, 738, L23

Yost, S. A., Harrison, F. A., Sari, R., & Frail, D. A. 2003, *A Study of the Afterglows of Four Gamma-Ray Bursts: Constraining the Explosion and Fireball Model*, ApJ, 597, 459

Yu, Y. & Huang, Y.-F. 2007, *Shallow Decay of X-ray Afterglows in Short GRBs: Energy Injection from a Millisecond Magnetar?*, Chinese J. Astron. Astrophys., 7, 669

Zhang, B. 2014, *A Possible Connection between Fast Radio Bursts and Gamma-Ray Bursts*, ApJ, 780, L21

Zhang, B. & Mészáros, P. 2001, *Gamma-Ray Burst Afterglow with Continuous Energy Injection: Signature of a Highly Magnetized Millisecond Pulsar*, ApJ, 552, L35

Zhang, B.-B., van Eerten, H., Burrows, D. N., et al. 2015, *An Analysis of Chandra Deep Follow-up Gamma-Ray Bursts: Implications for Off-axis Jets*, ApJ, 806, 15

Zhang, S., Jin, Z.-P., Wang, Y.-Z., & Wei, D.-M. 2017, *The Interpretation of the Multi-wavelength Afterglow Emission of Short GRB 140903A*, ApJ, 835, 73

Zhang, W. & MacFadyen, A. 2009, *The Dynamics and Afterglow Radiation of Gamma-Ray Bursts. I. Constant Density Medium*, ApJ, 698, 1261

Contribution from co-authors

Here we list bibliographic information of the papers included in this thesis. The relative contribution of every coauthor is represented by their place in the author list. All chapters of this thesis were written under the supervision of prof. dr. Ralph A.M.J. Wijers and dr. Hendrik J. van Eerten.

Chapter 2: A new approach to modelling gamma-ray burst afterglows: Using Gaussian processes to account for the systematics
M. D. Aksulu, R. A. M. J. Wijers, H. J. van Eerten, A. J. van der Horst
Monthly Notices of the Royal Astronomical Society, 2020, 497, 4, p.4672–4683

Chapter 3: Exploring the GRB population: Robust afterglow modelling
M. D. Aksulu, R. A. M. J. Wijers, H. J. van Eerten, A. J. van der Horst
Submitted to the *Monthly Notices of the Royal Astronomical Society*

Chapter 4: Exploring the long GRB population: A population synthesis study
M. D. Aksulu, M. De Pasquale, J. Japelj, H. J. van Eerten, R. A. M. J. Wijers
Submitted to the *Monthly Notices of the Royal Astronomical Society*

Chapter 5: Rapid-response radio observations of short GRB 181123B with the Australia Telescope Compact Array
G. E. Anderson, M. E. Bell, J. Stevens, **M. D. Aksulu**, J. C. A. Miller-Jones, A. J. van der Horst, R. A. M. J. Wijers, A. Rowlinson, A. Bahramian, P. J. Hancock, J.-P. Macquart, S. D. Ryder, R. M. Plotkin
Monthly Notices of the Royal Astronomical Society, 2021, 503, 3, p.4372–4386

- In this study I lead the modelling efforts for the afterglow of GRB 181123B. I also lead the discussions on the interpretation of the modelling results.

Chapter 6: MeerKAT observations and broadband modelling of "MAGIC" GRB 190114C
M. D. Aksulu, R. Diretse, A. J. van der Horst, E. Tremou, P. Woudt, R. A. M. J. Wijers, H. J. van Eerten
To be submitted to the *Monthly Notices of the Royal Astronomical Society*

English summary

Astrophysical jets are directional, beamed ejecta which are powered by a central engine. Much of the non-thermal emission we observe in the Universe is powered by astrophysical jets. Astrophysical jets have been observed over scales varying by many orders of magnitude, from Active Galactic Nuclei (AGN), where the central engine is a supermassive black hole with the mass of the order of 10^8 solar masses, to low mass X-ray binaries where the central engine is either a very dense remnant of a star (i.e., neutron star) or a stellar mass black hole. Despite much dedicated research we still lack the exact understanding of how such jets are formed.

Gamma-ray bursts (GRBs) are astrophysical jets with extreme properties. They are the most energetic explosions in the Universe, where a jet is ejected at nearly the speed of light. They are the resulting outflow from either the merger of neutron stars or the violent deaths of massive stars. GRBs were first discovered during the Cold War, when the U.S. launched the Vela satellites to enforce the treaty against testing nuclear weapons above ground. These satellites carried gamma-ray instruments to detect any illegal nuclear detonations. Officially, the Vela satellites did not detect any nuclear explosions, however, they accidentally discovered the GRB phenomenon.

GRBs are initially detected as bright flashes of high-energy radiation (i.e., γ rays) which can last between 0.1 to 1000 seconds. Given that GRBs originate from outside of our Galaxy, the observations of such bright flashes of γ rays imply enormous energies for these catastrophic events. The observed γ-ray emission is called the prompt emission of a GRB. GRBs are categorized as short and long GRBs depending on the observed duration of the prompt emission. Short GRBs are associated with neutron star mergers, and long GRBs are associated with supernovae of massive stars. The exact physical mechanism which is responsible for the observed flashes of gamma-rays is still debated. Following the prompt emission, when the ultra-relativistic jet of a GRB starts to interact with its surrounding medium and sweeps up material, external shocks are formed. In these shocks charged particles are accelerated and magnetic fields are amplified, which results in synchrotron radiation observable throughout the whole electromagnetic spectrum. This multi-wavelength radiation is called the afterglow of the GRB. An illustration representing the various stages of GRBs can be seen in Figure A. For a more detailed description of GRBs the reader is referred to Chapter 1.

The observed properties of the afterglow emission depend on the energy of the explosion, the opening angle of the jet, the density of the surrounding medium with which the jet interacts,

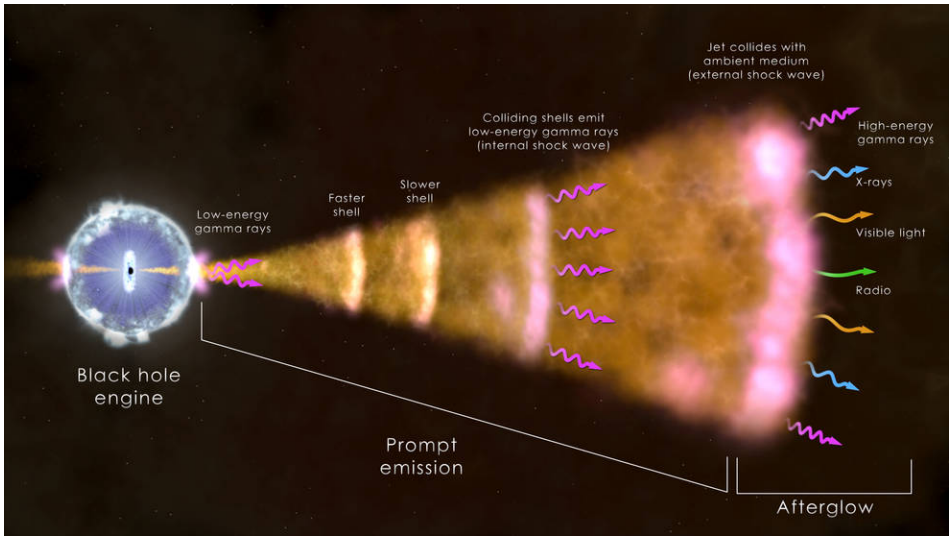

Figure A: Illustration of the different stages of GRBs. They are initially detected as flashes of γ rays (the prompt emission) followed by a long-lived broadband afterglow. Image credit: NASA's Goddard Space Flight Center.

and the physics which govern how particles are accelerated in ultra-relativistic shocks. We are able to capture the dynamical evolution of the jet thanks to recent advances in numerical hydrodynamic simulations. Moreover, we are able to predict the observed afterglow emission based on these simulations for given physical conditions. Utilizing such numerical afterglow models and comparing the predictions with afterglow observations allows us to expand our understanding of GRBs. In this thesis I make extensive use of Bayesian inference techniques, with state-of-the-art numerical afterglow models, to measure the physical properties of GRBs. These properties are described by certain quantities, which we call physical parameters, such as the explosion energy, opening angle of the jet, density of the surrounding environment, and the fraction of the explosion energy spent for accelerating the particles and amplifying magnetic fields in the shocks. For each set of values of these parameters, one gets different predicted light curves. The Bayesian inference technique is a statistical method of finding, given all the measurements made of a specific GRB afterglow, which values of the physical parameters lead to the best match between those measurements and the model, as well as how much uncertainty remains in these values. A large fraction of the work for this thesis was developing a method of doing so that was practical and robust. The overarching aim of this thesis is to provide insights regarding the physics of GRBs by constraining their physical parameters, and to probe how these parameters are distributed across the GRB population.

Although the numerical models are able to explain the general trends in the observed afterglow emission, the observations exhibit a more complex evolution and can deviate from the predicted general trends. Such systematic deviations can be the result of additional emission mechanisms which are not included in the models. Also, as light travels toward the observer

it can get absorbed by interstellar dust, and interact with the interstellar medium to increase the observed variability. Moreover, as we need many different observatories with different characteristics to capture the broadband evolution of the afterglow emission, instrumental systematics also complicate the afterglow data sets. All these different processes introduce systematic deviations to the observed afterglow emission. In Chapter 2, we introduce a new method for modelling the afterglow emission of GRBs. We find that traditional modelling methods result in unrealistic parameter estimates when systematics are present in the data sets. We make use of Gaussian processes (GP) to take into account any systematic deviations from the models. GPs are stochastic processes which allow us to identify any correlations between the data points, and make predictions accordingly. Since we do not have an exact description of the processes contributing to the systematics, we make use of GPs to model any deviations from the afterglow model in a non-parametric fashion. Using synthetic data sets, we demonstrate that the proposed method leads to more robust parameter estimates. Furthermore, we apply this new method on well-studied, archival GRB afterglow data sets, and compare our results with previous studies.

In Chapter 3, we make use of the above-mentioned method to model a sample of 26 GRBs. Our sample consists of 22 long GRBs and 4 short GRBs with available, well-sampled, broadband afterglow data sets. In this study we aim to understand how the various GRB parameters (such as the explosion energy, opening angle, environment density and shock properties) are distributed across the population. We accomplish this by modelling each individual GRB in the sample using the method introduced in Chapter 2. We present the inferred parameters of the GRB sample and comment on how these parameters are distributed across the population. We find that, despite the fact that the observed prompt emission of short GRBs is fainter than long GRBs, they have similar explosion energies. This suggests that the emission mechanism producing the γ rays is less efficient in the case of short GRBs.

In Chapter 4, we take a different approach to probe the parameter distributions of the GRB population. Instead of modelling individual GRBs, we conduct a population study based on a limited sample of long GRBs. We build a numerical tool which is able to generate a synthetic population of GRBs for given parameter distributions, and output distributions of the observables. In order to make a fair comparison between the synthetic population and the observed sample, it is crucial to take into account the selection effects, which we accomplish by only including GRBs over a certain brightness in our sample. We make use of Bayesian inference in order to infer the distribution parameters of the synthetic population, which successfully reproduces the observed properties of the long GRB sample. Furthermore, we compare the inferred synthetic population to the above-mentioned modelling results of individual GRBs, which is presented in Chapter 3, and find that the parameter distributions agree with each other. Based on the inferred properties of the GRB population, we also briefly comment on how future observatories can help us to gain a better understanding of GRB physics.

In Chapter 5, we present the first results for the *Australia Telescope Compact Array* (ATCA) rapid-response mode observations triggered on a short GRB (GRB 181123B). With the beginning of the multi-messenger era in Astronomy it has become important to quickly follow-up

on gravitational wave (GW) events. ATCA started observations ~ 12.6 hours after the initial trigger of short GRB 181123B. Although there were no significant detections, ATCA was able to obtain upper limits on the afterglow emission. In this study, I led the modelling efforts to understand how such early-time observations can help constrain the physics of GRBs. We demonstrate that even upper limits help to constrain the model parameters. We show that, especially, the required amount of energy to accelerate particles in GRB shocks can be constrained using these observations.

In Chapter 6, we derive the physical parameters of the "MAGIC" GRB 190114C, which is the first GRB detected at extremely high (TeV) photon energies. We present new radio follow-up observation obtained by the *Meer Karoo Array Telescope* (MeerKAT) and collect additional observations from the literature in radio/mm-wavelengths, optical, and X-ray bands in order to compile a broadband data set for the afterglow of GRB 190114C. Furthermore, we make use of the method introduced in Chapter 2 to robustly infer the physical parameters of this exceptional GRB. We find that the particle are accelerated to higher energies than expected from canonical GRBs, which might be one of the reasons that this GRB emitted TeV photons. We compare the inferred parameters of GRB 190114C with a large sample of long GRBs (see Chapter 3) and find that this GRB constitutes an outlier within the GRB population. This might indicate that TeV emitting GRBs are relatively rare.

Nederlandse samenvatting

Astrofysische jets zijn gerichte, uitgestraalde ejecta die worden aangedreven door een centrale 'motor'. Een groot deel van de niet-thermische straling die we in het heelal waarnemen, wordt veroorzaakt door astrofysische jets. Astrofysische jets zijn waargenomen op schalen die vele orden van grootte kunnen variëren, van actieve melkwegkernen (AGN), waar de centrale motor een superzwaar zwart gat is met een massa in de orde van 10^8 zonsmassa's, tot een lage-massa röntgendubbelster, waar de centrale motor ofwel een zeer dicht overblijfsel van een ster (neutronenster) is, ofwel een zwart gat met een stellaire massa. Ondanks veel doelgericht onderzoek weten we nog steeds niet precies hoe zulke jets worden gevormd.

Gammaflitsen (GRBs) zijn astrofysische jets met extreme eigenschappen. Het zijn de meest energetische explosies in het heelal, waarbij een jet wordt uitgestoten met bijna de snelheid van het licht. Ze zijn het resultaat van de fusie van neutronensterren of de gewelddadige dood van zware sterren. GRBs werden voor het eerst ontdekt tijdens de Koude Oorlog, toen de V.S. de Vela-satellieten lanceerden satellieten lanceerden om naleving van het verdrag tegen het testen van kernwapens boven de grond te bewaken. Deze satellieten waren uitgerust met gammastraalinstrumenten om illegale nucleaire detonaties op te sporen. Officieel hebben de Vela-satellieten geen nucleaire explosies gedetecteerd, maar ze ontdekten per ongeluk het GRB fenomeen.

GRBs worden het eerst waargenomen als heldere flitsen van hoogenergetische straling (d.w.z. gammastralen) die tussen 0.1 en 1000 seconden kunnen duren. Aangezien GRBs van buiten ons melkwegstelsel komen, impliceren de waarnemingen van zulke heldere flitsen enorme energieën voor deze catastrofale gebeurtenissen. De waargenomen emissie van gammastralen wordt de "prompt emission"van een GRB genoemd. GRBs worden ingedeeld in korte en lange GRBs, afhankelijk van de waargenomen duur van de prompt emission. Korte GRBs worden in verband gebracht met fusies van neutronensterren, en lange GRBs met supernovae van zware sterren. Het precieze fysische mechanisme dat verantwoordelijk is voor de waargenomen flitsen van gammastraling is nog steeds onderwerp van discussie. Wanneer de ultra-relativistische jet van een GRB in wisselwerking treedt met het omringende medium en materiaal opveegt, worden externe schokken gevormd. In deze schokken worden geladen deeltjes versneld en worden magnetische velden versterkt, hetgeen resulteert in synchrotronstraling die over het gehele elektromagnetische spectrum kan worden waargenomen. Deze multigolflengtestraling wordt de nagloeier van de GRB genoemd. Een illustratie van de verschillende stadia van GRBs is te zien in Figuur A. Voor een meer gedetailleerde beschrijving van GRBs wordt de lezer verwezen naar Hoofdstuk 1.

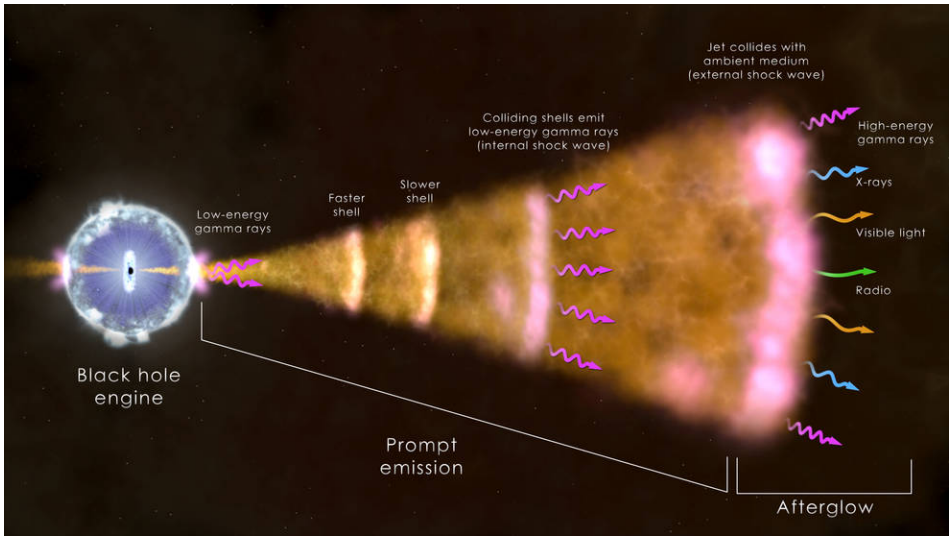

Figuur A: Illustratie van de verschillende stadia van GRBs. Ze worden aanvankelijk waargenomen als flitsen van *gamma*-stralen (de prompt emissie), gevolgd door een langlevende breedbandige nagloei. Afbeelding credit: NASA's Goddard Space Flight Center.

De eigenschappen van de nagloei-emissie hangen af van de energie van de explosie, de openingshoek van de jet, de dichtheid van het omringende medium waarmee de jet wisselwerkt, en de fysica die bepaalt hoe deeltjes versneld worden in ultra-relativistische schokken. We zijn in staat om de dynamische evolutie van de jet te beschrijven dankzij recente vooruitgang in numerieke hydrodynamische simulaties. Bovendien zijn we in staat om de waargenomen nagloei-emissie te voorspellen op basis van deze simulaties voor gegeven fysische condities. Het gebruik van zulke numerieke nagloeimodellen en het vergelijken van de voorspellingen met nagloeiwaarnemingen stelt ons in staat om ons begrip van GRBs te vergroten. In dit proefschrift maak ik uitgebreid gebruik van Bayesiaanse inferentietechnieken, met state-of-the-art numerieke nagloeimodellen, om de fysische eigenschappen van GRBs te meten. Deze eigenschappen worden beschreven door bepaalde grootheden, die we fysische parameters noemen, zoals de explosie-energie, de openingshoek van de jet, de dichtheid van de omgeving, en de fractie van de explosie-energie die besteed wordt aan het versnellen van de deeltjes en het versterken van magnetische velden in de schokken. Voor elke reeks waarden van deze parameters krijgt men verschillende voorspelde lichtkrommen. De Bayesiaanse inferentietechniek is een statistische methode om, gegeven alle metingen die aan een specifieke GRB nagloeier zijn gedaan, te vinden welke waarden van de fysische parameters leiden tot de beste overeenkomst tussen die metingen en het model, alsmede hoeveel onzekerheid er in die waarden overblijft. Een groot deel van het werk voor dit proefschrift bestond uit het ontwikkelen van een methode om dit te doen die praktisch en robuust is. Het overkoepelende doel van dit proefschrift is inzicht te verschaffen in de fysica van GRBs

door hun fysische parameters te bepalen, en te onderzoeken hoe deze parameters verdeeld zijn over de GRB-populatie.

Hoewel de numerieke modellen in staat zijn de algemene trends in de waargenomen nagloeiemissie te verklaren, vertonen de waarnemingen een complexere evolutie en kunnen zij afwijken van de voorspelde algemene trends. Dergelijke systematische afwijkingen kunnen het gevolg zijn van extra emissiemechanismen die niet in de modellen zijn opgenomen. Bovendien kan het licht op zijn weg naar de waarnemer geabsorbeerd worden door interstellair stof en wisselwerken met het interstellaire medium, waardoor de waargenomen variabiliteit toeneemt. Omdat we veel verschillende observatoria met verschillende eigenschappen nodig hebben om de breedbandige evolutie van de nagloeier vast te leggen, bemoeilijkt de instrumentele systematiek ook de nagloei-datasets. Al deze verschillende processen leiden tot systematische afwijkingen van de waargenomen nagloeier. In Hoofdstuk 2 introduceren we een nieuwe methode voor het modelleren van de nagloei-emissie van GRBs. We vinden dat traditionele modelleringsmethoden resulteren in onrealistische parameterschattingen wanneer er systematiek in de datasets aanwezig is. Wij maken gebruik van Gaussische processen (GP) om rekening te houden met eventuele systematische afwijkingen van de modellen. GPs zijn stochastische processen die ons in staat stellen eventuele correlaties tussen de datapunten te identificeren, en dienovereenkomstig voorspellingen te doen. Aangezien wij niet beschikken over een exacte beschrijving van de processen die bijdragen tot de systematiek, maken wij gebruik van GPs om afwijkingen van het nagloeimodel op een niet-parametrische manier te modelleren. Met behulp van synthetische datasets tonen we aan dat de voorgestelde methode leidt tot robuustere parameterschattingen. Verder passen we deze nieuwe methode toe op datasets van goed bestudeerde GRB-nagloeiers, en vergelijken onze resultaten met eerdere studies.

In Hoofdstuk 3 maken we gebruik van de hierboven vermelde methode om een steekproef van 26 GRBs te modelleren. Onze steekproef bestaat uit 22 lange GRBs en 4 korte GRBs met beschikbare, goed bemonsterde, breedbandige nagloei-datasets. In deze studie willen we begrijpen hoe de verschillende GRB-parameters (zoals de explosie-energie, openingshoek, omgevingsdichtheid en schok-eigenschappen) verdeeld zijn over de populatie. We doen dit door een model te maken van elke individuele GRB in de steekproef met behulp van de methode geïntroduceerd in Hoofdstuk 2. We presenteren de afgeleide parameters van de GRB steekproef en bespreken hoe deze parameters verdeeld zijn over de populatie. We vinden dat, ondanks het feit dat de waargenomen prompt emission van korte GRBs zwakker is dan die van lange GRBs, ze vergelijkbare explosie-energieën hebben. Dit suggereert dat het emissiemechanisme dat de gammastraling produceert minder efficiënt is in het geval van korte GRBs.

In Hoofdstuk 4 kiezen we een andere aanpak om de parameterverdelingen van de GRB-populatie te onderzoeken. In plaats van individuele GRBs te modelleren, voeren we een populatiestudie uit op basis van een beperkte steekproef van lange GRBs. We bouwen een numeriek instrument dat in staat is om een synthetische populatie van GRBs te genereren voor gegeven parameterverdelingen, en uitgangsverdelingen van de waarneembare grootheden. Om een eerlijke vergelijking te kunnen maken tussen de synthetische populatie en

de waargenomen steekproef, is het cruciaal om rekening te houden met selectie-effecten, wat we bereiken door alleen GRBs boven een bepaalde helderheid in onze steekproef op te nemen. We maken gebruik van Bayesiaanse inferentie om de distributieparameters van de synthetische populatie af te leiden, die met succes de waargenomen eigenschappen van de lange GRB steekproef reproduceert. Verder vergelijken we de afgeleide synthetische populatie met de bovengenoemde modelresultaten van individuele GRBs, die worden gepresenteerd in Hoofdstuk 3, en vinden dat de parameterverdelingen met elkaar overeenkomen. Op basis van de afgeleide eigenschappen van de GRB populatie, geven we ook kort commentaar op hoe toekomstige observatoria ons kunnen helpen om een beter begrip te krijgen van de GRB fysica.

In Hoofdstuk 5 presenteren we de eerste resultaten van de snelle-reactie waarnemingen van de *Australia Telescope Compact Array* (ATCA) naar aanleiding van een korte GRB (GRB 181123B). Met het begin van het multi-messenger tijdperk in de astronomie is het belangrijk geworden om gebeurtenissen met zwaartekrachtgolven (GW) snel op te volgen. ATCA begon met waarnemingen ~ 12.6 uur na de eerste trigger van de korte GRB 181123B. Hoewel er geen significante detecties waren, was ATCA in staat om bovengrenzen te stellen aan de nagloei-emissie. In deze studie leidde ik de modelleringsinspanningen om te begrijpen hoe zulke vroege waarnemingen de fysica van GRBs kunnen helpen inperken. We tonen aan dat zelfs bovengrenzen helpen om de modelparameters in te perken. We tonen aan dat, in het bijzonder, de hoeveelheid energie die nodig is om deeltjes in GRB-schokken te versnellen, beter kan worden ingeperkt met behulp van deze waarnemingen.

In Hoofdstuk 6 leiden we de fysische parameters af van de “MAGIC” GRB 190114C, die de eerste GRB is die gedetecteerd werd bij extreem hoge (TeV) fotonenergieën. We presenteren nieuwe radio follow-up waarnemingen, verkregen door de *Meer Karoo Array Telescope* (MeerKAT) en verzamelen aanvullende waarnemingen uit de literatuur in radio/mm-golflengten, optische, en röntgenbanden om een breedbandige dataset samen te stellen voor de nagloeier van GRB 190114C. Verder maken we gebruik van de methode geïntroduceerd in Hoofdstuk 1 om de fysische parameters van deze uitzonderlijke GRB op een robuuste manier af te leiden. We vinden dat de deeltjes versneld zijn tot hogere energieën dan verwacht wordt van canonieke GRBs, wat een van de redenen zou kunnen zijn dat deze GRB TeV fotonen heeft uitgezonden. We vergelijken de afgeleide parameters van GRB 190114C met een grote steekproef van lange GRBs (zie Hoofdstuk 3) en vinden dat deze GRB een uitschieter is binnen de GRB-populatie. Dit zou erop kunnen wijzen dat GRBs die TeV uitzenden relatief zeldzaam zijn.

Acknowledgements

Can't believe
How strange it is to be anything at all.
Jeff Mangum

It has been a challenging, rewarding, and unforgettable 4 and a half years! API is truly a unique workplace, where I felt like I'm at home, and everyone knows that what makes a place special are the people within. In this section I would like to thank all the people without whom I wouldn't be able to get this far in my Ph.D. journey.

First of all, I would like to thank Ralph, my supervisor/promotor, for giving me the opportunity to become an astrophysicist. Ralph, it has truly been a pleasure to work with you. Under your supervision I have grown as an astrophysicist and scientist. I will always cherish the interesting conversations we had. I would also like to thank Hendrik, my co-supervisor, for all his support. Hendrik, without your expertise I would not be able to achieve many of the results presented in this thesis. It was a lot of fun working with you. Alexander, I would like to thank you for your support throughout my Ph.D.. It was a great experience visiting you at D.C., where I met a lot of new friends. Whenever I had a question about GRB observations/theory, you were ready with an answer. I would also like to thank Sera for welcoming me into her group meetings. I have learnt so much from you, especially on how to give presentations.

Second, I would like to thank Vatsal and Alex, my paranymphs. Vatsal, you are the first person I interacted with at API. You were one of the best flatmates one could wish for and I will truly miss our times back in Ijburg. Also, you were a huge help both scientifically and mentally throughout my Ph.D.! Alex, we met when you were still a M.Sc. student at Sera's group and I remember answering your questions regarding Ph.D. life at API. I'm glad I was able to convince you that day to join our research group. You are a great friend and I am glad we ended up being desk mates. You have been a source of inspiration with your never ending passion for theory. You both have been very supportive throughout the rough times in my Ph.D. and I am happy to have gained such great friendships. Of course, Alicia also deserves a big thanks for all her support over the years and also for all the delicious food

she would bring me when I was deep into my Ph.D. studies.
I would also like to thank all the people in our research group. Mark, thank you for all the interesting and fun conversations. You have been very supportive whenever I needed life advice. Kelly, besides throwing the best parties ever, you have also been an amazing friend. Having you around during the observation course, made those sleepless nights endurable. Aleksandar, you were for sure the best chair for our group meetings. You brought joy to our meetings by initiating interesting discussions on art, science and politics. Antonia, it has always been a pleasure to discuss GRB physics with you. Iris and David, you both are great additions to the research group and I have no doubt that you will become very successful in your studies. Your passion for astronomy and machine learning has been inspiring. Vincent, we have started to work together at the end of my Ph.D., however, I have no doubt that you will be very successful in your endeavours.
Of course I owe a big thanks to the Secretariat of API: Milena, Susan and Renee. You have been extremely supportive all these years, and you have made API feel like home! I would also like to thank Martin, both for his support scientifically and for all the good times we have spent at Oerknal!

I am extremely happy to have such a great Ph.D. cohort. Eva, Dimitris, Eleanor, Sarah: We have started to learn the ins and outs of Ph.D. life together and I am very grateful for all your friendships. Vlad, you have been a lifeline for the social life at API and I appreciate all the fun times we had! Jure, it's been a great pleasure working with you, thank you for all your support! Ben, you have been a source of joy for everyone at API. I will never forget all the trips you have organized and the hilarious movies and pictures. Frank, you deserve a special thanks. Besides being an amazing friend, you have also helped me in translating the summary of this thesis into Dutch. May you always win the day! David, it's been a privilege getting to know you and I appreciate all the fun times we had. Kenzie, you have such a bright personality, and it was great having you as an office mate!
Şevket, throughout our almost decade-long friendship you have always supported me. I consider myself lucky that we both ended up in the Netherlands at the same time! I know that I can always count on you, and I thank you for your friendship.

At last but not least, I would like to thank my family. Sinem, my lovely fiancée, thank you for being so patient with me during this 4-year long journey. You have always been very supportive and loving towards me. I wouldn't have been able to finish my Ph.D. without your love and moral support. My parents have always supported me in all of my endeavours. They have sparked my interest in science from very early on in my childhood and I am eternally grateful for that. I am also very lucky to have such awesome sisters, Aslı and Ayça! They have been a huge moral support for me throughout my whole life. I would also like to thank Onur and Mutluhan for their loving support. I love you all!

Mehmet Deniz Aksulu,
3 November 2021